Prediction of the Mechanical Properties of Molecular Crystals Based Upon Their Crystallographic Structure

Siti Fatimah Binti Ibrahim

Submitted in accordance with the requirements for the degree of

DOCTOR OF PHILOSOPHY

THE UNIVERSITY OF LEEDS

School of Chemical and Process Engineering

March 2016

The candidate confirms that the work submitted is her own, and that appropriate credit has been given where reference has been made to the work of others. This copy has been supplied on the understanding that it is copyright material and that no quotation from the thesis may be published without proper acknowledgement.

Acknowledgements

Abstract

The APIs mechanical properties particularly, tabletability and flowability are of significant interest in the drug dosage tabletting. Insights into the APIs mechanical behaviour not only assist in the selection of optimum tabletting process but the choice of suitable excipients for dosage blend. Prediction of the mechanical properties of seven solid forms was described in this study two of which were used at the initial stage to develop the model. The objective of the model is to test the reliability of applying molecular and crystallographic modelling to predict the slip behaviour of APIs which will provide a quick tool for observing the mechanical properties. Plane rugosity and interlock properties were calculated for the first time by taking the crystallographic properties of each compound.

The prediction model comprises of three main components. Firstly, the identification of likely dislocation Burgers vectors based on lattice geometry and dependency to line dislocation; secondly, selection of slip planes for plastic deformation using the calculation of interplanar interactions, rugosity and surface energy and thirdly, characterisations of slip systems or propensity for cleavage and fracture.

The pentaerythritol and its derivative, pentaerythritol tetranitrate were selected as the basis structure during development of model because of known cleave and plastic behaviour. From the calculation, the primary Burgers vector for pentaerythritol was identified as ½ [111], and the prominent slip plane for pentaerythritol is a non-habit plane of (001). The (001) was 94% behaving as an ideal slip plane. However, the primary slip system of pentaerythritol was inactive because the Burgers vector was not in the (001) plane. Pentaerythritol was predicted to cleave at (001) because of strong intraplanar intermolecular interactions. In contrast, pentaerythritol tetranitrate was predicted to undergo deformation by slipped on the plane (110) and in the direction of [001]. The (110) was behaving with 82% of ideal slip plane. The predicted slip behaviour was agreeing with the micro-indentation measurements in the literature.

Five solid forms of paracetamol, namely polymorph I and II, paracetamol theophylline, paracetamol trihydrates and paracetamol hydrochloride monohydrate were tested using the developed model to verify the prediction robustness. The influence of each component towards the mechanical behaviour of paracetamol varies depending on intermolecular interactions present in the crystal system.

Table of contents

CHAPTER 7   PREDICTION OF THE MECHANICAL PROPERTIES FOR FIVE DIVERSE SOLID FORMS OF PARACETAMOL

CHAPTER 8   INFLUENCE OF SOLID FORM PROPERTIES ON THE SOLID FORMS TABLETABILITY OF MICROCRYSTALS OF PARACETAMOL

CHAPTER 9   CONCLUSIONS AND SUGGESTIONS FOR FUTURE WORK

List of table

List of figures

Chapter One

Introduction

This chapter sets the background for this research, outlines the research question, objectives, and a schematic of the overall structure for this report. The project management team in which this research involves is also included

Chapter 1   Introduction

1.1   Motivation of study

Pharmaceutical solid dosage is one of the commonly used mechanisms for drug delivery to the patient target organ. Solid dosage forms demand component particulates to blend readily by flowing well [1] to ensure formulation uniformity. They must also be robust enough to undergo a particular manufacturing process without changing physical, chemical and mechanical properties. Particle size and shape describe the uniformity and flowability activities [2], morphology and surface chemistry [3] that will impact the processability and devolopability of solid particulates. Leane et.al [4] have come up with a framework namely Manufacturing Classification System (MCS) with aims to assist the selection of optimal solid dosage processing route by adapting the percolation concept. The framework provides a guideline for understanding processing route by physical properties from previous knowledge of people working in the manufacturing of solid dosage. Hence, it complements the existing Biopharmaceutics Classification System (BCS) [5] that is implemented to rank drugs based on solubility, permeability in combination with *in vitro* dissolution characteristics.
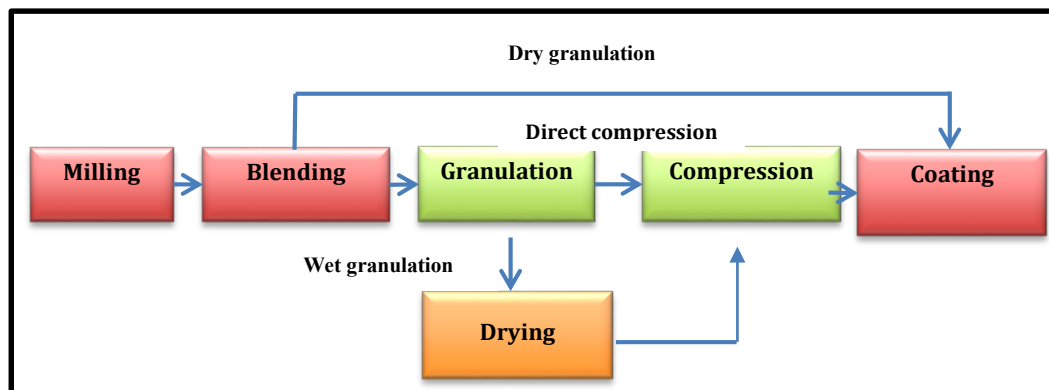
Figure 1-1 Schematic diagram showing standard route to manufacture pharmaceutical solid dosage forms. Red boxes are unit operations that are identical for all routes, green boxes are unit operations for dry granulation and orange box is for wet granulation

The common routes for processing solid dosage forms are direct compression also dry or wet granulation. Direct compression has always been the preferred way for solid dose drug production [6]. It is the simplest, easy-to-handle and cost-saving manufacturing process [7]. Direct compression consists of fewer unit operations, and uses a small amount of raw material, which reduces the processing cost as observed in Figure 1-1 [8]. In comparison to the granulation process, which has more unit operations and is susceptible to contamination [6], direct compression seems to be the most promising route for drug tablet production for the industry. The identification of optimal solid dosage route starts with the solid form selection [9]. The standard practices for solid form selection to suit tablet production route are considering the flowability and compressibility of particulates represented best as a matrix shown in Table 1-1. The solid form needs to have a high compressibility and flowability behaviour to be suitable for direct compression [6].

Table 1-1 Matrix showing criteria of solid form selection for use in pharmaceutical solid dosage production. The matrix shows key properties of production, flowability, and compressibility of powder particulates [19]

Flowability	*Compressibility*	
	High	**Low**
High	Direct compression	Wet granulation
Low	Dry granulation	Wet granulation

Despite its optimum operation, direct compression suffers from several significant drawbacks, that are the ability of the formulation to withstand the direct force during compaction [3] and the assurance of formulation drug uniformity [8]. Consequently, the development of the formulation technique for direct compression in the industry becomes delicate and time consuming. Tablet dosages consist of two main components, the active pharmaceutical ingredients (API) and the inactive components (excipients). Excipients can be binders, lubricants, glidants, coatings and other bulking agents. The role of excipients includes to improve homogeneity and stability of tablet, assist for dosage transportation to target organ and facilitate bioavailability. The general properties of excipients are safe, palatable and cost effective. When the composition of active pharmaceutical ingredients (API) governs, API mechanical properties affect observed tablet performance.

API is known to have poor mechanical properties causing a setback, for example, sticking and capping [10–12]. Only a few APIs have the flow, cohesion, lubricating properties [10] that are essential for direct compression. Hence, any extreme forces from direct compaction may induce phase transformation, for instance, polymorphism and utterly change the

toxicity or bioavailability of the API [13]. It is clear that the mechanical properties of API are hindering direct compression to be the default drug-tabletting route in the industry.

Summary of interest for earlier research to date for direct compression ranging from process optimisation, instrument development, particles engineering and computational analysis is shown in Figure 1-2[3, 14-17]. Process optimisation and instrument development may resolve issues during direct compression, physically, for instance, picking, and capping but the problem persists if formulations cannot withstand compaction pressure. Therefore, appreciation of APIs' mechanical properties and their characterisation is the best measure to promote direct compression as the default tablet dosage manufacturing route. About the previous research interest, a considerable amount of literature has been published on studying mechanical properties for direct compression experimentally [6,15,18–22]. However, only a few studies are focusing on the understanding of mechanical properties of API interaction, based on its molecular crystallographic structure. The small number of studies with regards to the crystallographic structure led to an imprecise mechanical properties prediction, and this issue triggers the idea for the current research.
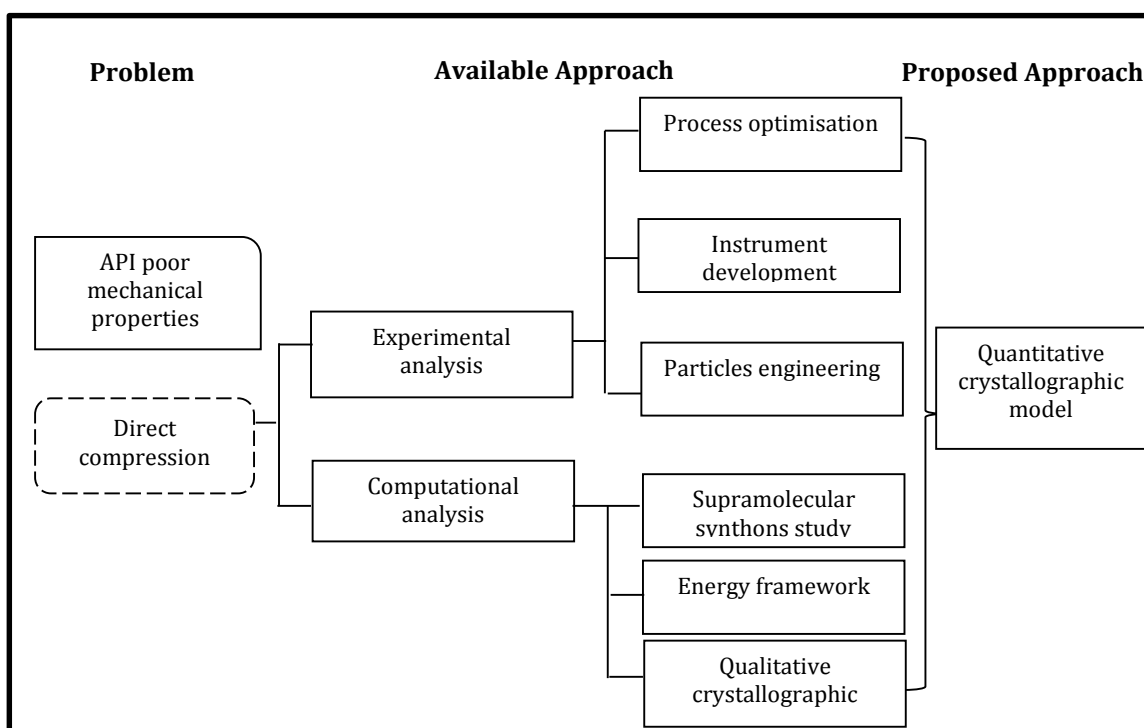
Figure 1-2 Summary of previous study done in the field for studying the mechanical properties of pharmaceutical powders. It is seen that there is lacking of study using crystallographic structure for modelling the mechanical properties during tableting. A lot of the model is based on experimental study

Most researchers have developed the mechanical properties (flow and compressibility) prediction model by focusing on the experimental analysis of the active pharmaceutical ingredient (API) deformation behaviour during compaction. One of the most significant drawbacks of the available crystallographic-based prediction models it is conducted by evaluating the crystal packing qualitatively to identify the availability of the slip system. The questions that arise from this downside are:

1. What are the crystallographic dimensions with regards to mechanical properties that best describe deformation behaviour during direct compression?

2. How can the crystallographic dimensions with regards to the deformation be measured?

The drawback thus creates an urge to develop a framework that provides quantitative analysis of the slip deformation in crystal packing alongside the qualitative evaluation.

A schematic shown in Figure 1-2 has become the basis for this research by depicting the summaries of previous approaches to resolving issues of direct compression. From the summary, the problem that is hindering the effort of making direct compression as the default route for drug solid dosage processing is shown. The summary delineates only a few analyses of mechanical properties based on its crystallographic structure. It thus speculates the limited understanding of the API molecular structures, how widely they can be applied, also how and why they are limited. Hence, this research will try to address several problems:

1. A small number of frameworks to understand the crystal mechanical properties based on its crystallographic structure.

2. A few amounts of guidance to develop a crystallographic-based model to predict mechanical properties

Inferring from the previous work done, the intention of this study is to design and demonstrate a simple computational chemistry tool to predict crystallographic deformation occurrence. This is to be achieved by exploring solid form mechanical properties, for instance, elasticity and plasticity occurrence by in-silico modelling.

1.2 Research question and objectives

The developed tool is anticipated to link between observed properties of solid form to its molecular behaviour while undergoing tabletting. In short, the tool captures mechanical properties, appreciation of crystallographic structure, their descriptions and the way they are related. Because of its simplicity, the tool is hoped to provide a fast and sensible prediction, also understandable data for use by the formulation scientists. This research aims to answer the following question:

Can the molecular and synthonic modelling predict mechanical properties of pharmaceutical particulates using the crystallographic structure?

Specific research objectives are as follows:

1. Identify sets of suitable molecular crystals that differ in its physicochemical and mechanical properties for computational tool development and case study structures

2. Elucidate the molecular crystal chemistry of the active pharmaceutical ingredients (API) to understand its mechanical properties by molecular modelling

3. Predict defects of the active pharmaceutical ingredient (API) system with regards to its crystallographic structures

4. Develop a molecular scale crystallographic defect prediction model for the advantage in pharmaceutical tablet industry

5. Validated prediction model developed through experimental studies on representative crystal molecular systems

6. Evaluate particulate's properties in pharmaceutical solid dosage during the manufacturing process, particularly flowability and compressibility

Following the defined research question and objectives, a case-study approach is adopted to conduct this research. The approach can assist in developing model besides providing in-depth information on the mechanical properties of solid forms.

1.3   The solid forms and method selection

Diverse organic solid forms were selected to achieve the objectives of the study. The solid forms comprise of pentaerythritol and pentaerythritol tetranitrate for method development and paracetamol for method testing. Both solid forms systems have been chosen because of the distinct mechanical properties representing slip deformation, cleavage, and fragmentation. Molecular and synthonic modelling was selected for studying the crystallographic properties of materials. The advantage of using computer simulations is that it allows for quick calculations that provide ample data for evaluating the mechanical behaviour.

Diverse solid forms of different molecular systems were selected. The development of the prediction model is done using pentaerythritol, a polyhydric alcohol and pentaerythritol tetranitrate, a nitrate ester of it. The developed model was then tested using varying solid forms of paracetamol. Five solid forms of paracetamol for model testing consist of two polymorphs (FI and FII), a co-crystal (PTHEO), a hydrate (PTRI) and a salt (PHM).

Pentaerythritol (PET) and pentaerythritol tetranitrate (PETN) are of interest because of their different mechanical properties in which when subjected to the same stress PET cleaves, but PETN slips. Additionally, PET and its derivatives are well-studied systems with experimental data available to cross check molecular computational analysis. Paracetamol diverse solid forms were selected on the similar basis as the PET and PETN. Besides that, paracetamol is available at a low cost for crystallisation and mechanical properties measurement experiments. Paracetamol too is the common solid forms for developing technique concerning to direct compression. In short, the reasons entailing the selection of all studied systems are based on:

1. Distinct observed macro properties specifically related to the compressibility.
2. Well explored solid forms, providing diverse system
3. Dissimilar micro properties related in molecular structure, specifically brittle and ductile behaviour
4. Molecular and intermolecular interaction trait of the solid forms
5. Practical cost for the raw materials

1.4 Project management

This work forms part of the synthonic engineering research collaboration with Elna Pidcock and Jason Cole at the Cambridge Crystallographic Data Centre, which aims to provide enhancement for the current range of solid-state and surface property prediction of organic crystals. This was initially supported through an ESPRC follow-on grant and subsequently by the synthonic engineering research consortium funded by Boehringer Ingelheim, Novartis, Pfizer, and Syngenta.

I am gratefully acknowledging Robert Docherty and Klimentina Pencheva from Pfizer Ltd Sandwich and Robert Hammond from the University of Leeds for the support to this work and many helpful and stimulating discussions. Furthermore, I would like to thank Dawn Geatches from Hartree Centre Warrington for the density functional theory (DFT) elastic tensor calculations.

1.5 Thesis structure

This thesis is constructed in the utmost possible best manner to describe the research in a concise and clear structure. The diagram as in Figure 1-3 represents the general scheme of this thesis consisting of nine chapters. Summaries of content in each chapter are as follows:

Chapter 1: This chapter sets the background for the research. The introduction defines any critical components for the thesis, specifically research question, objectives and the project management.

Chapter 2: This chapter outlines the theoretical crystal science and crystallisation aspects underpinning the mechanical properties. The aspects include the perfect and imperfect crystal behaviour and computational functions to model the molecular properties.

Chapter 3: This chapter provides an overview of the available mechanical properties studies of pharmaceutical's particulates. Inferring from the literature study, the gap in the research was distinguished.

Chapter 4: The materials used, and steps are taken to carry out the crystallisation and computation are described here.

Chapter 5: This chapter sets the foundation for the mechanical prediction model. The development of the model was exploiting prior knowledge and study of mechanical behaviour for pentaerythritol (PET) and pentaerythritol tetranitrate (PETN).

Chapter 6: This chapter presents the result of the five selected paracetamol solid forms. The chapter starts with structure conformational analysis followed by the fitting of the force field and crystal chemistry computation.

Chapter 7: The chapter provides detail mechanical properties prediction of the five paracetamol solid forms. Each of the five sections contains the characterisation of slip plane, identification of slip directions and finally recognition of slip systems.

Chapter 8: The results from tabletability and flowability measurements are presented to validate the predicted mechanical properties.

Chapter 9: Findings are concluded, and suggestion for future work is included.
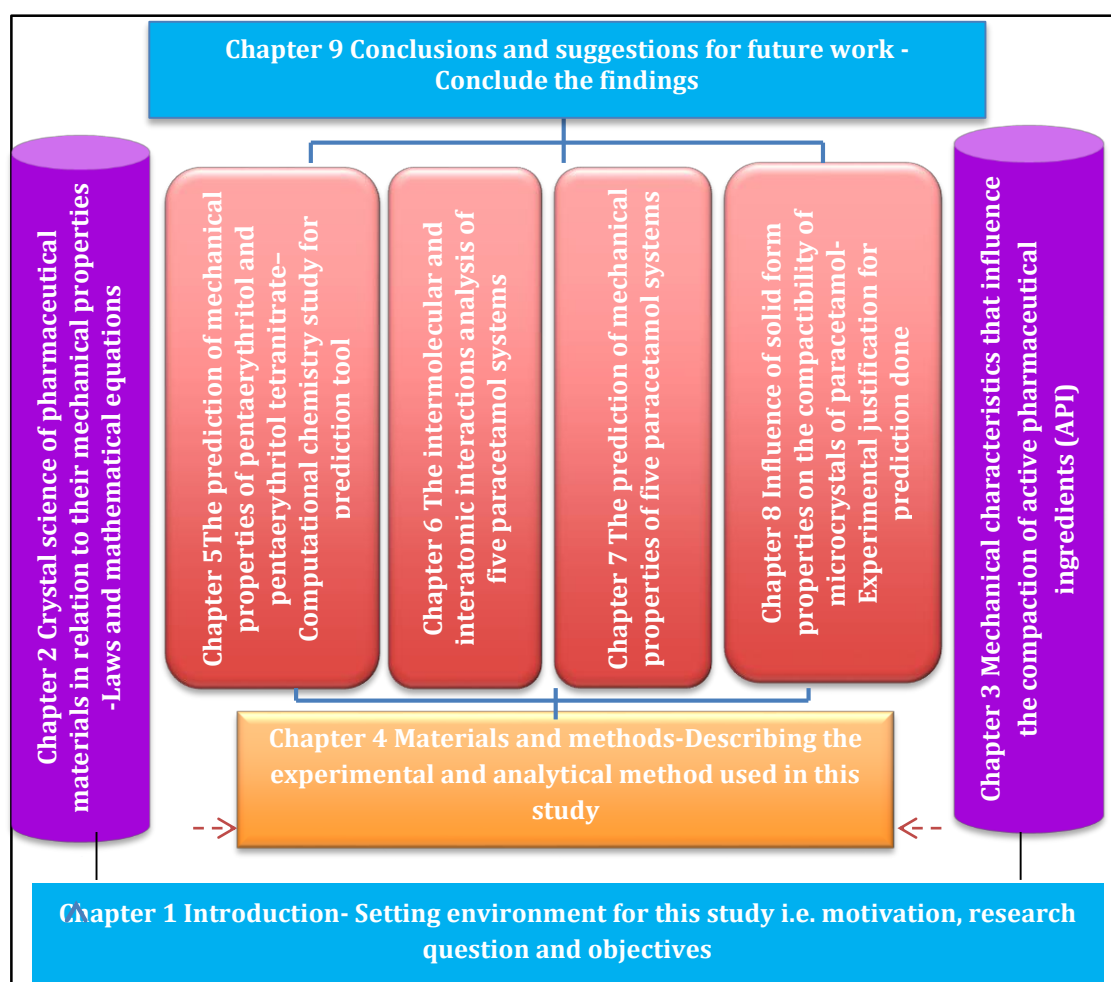
Figure 1-3 Thesis structure

References

[1]   M.P. Mullarney, B.C. Hancock, G.T. Carlson, D.D. Ladipo, B.A. Langdon, The powder flow and compact mechanical properties of sucrose and three high-intensity sweeteners used in chewable tablets, International Journal of Pharmaceutics. 257 (2003) 227–236.

[2]   N. Rasenack, B.W. Müller, Crystal habit and tabletting behavior, International Journal of Pharmaceutics. 244 (2002) 45–57.

[3]   L. Shi, C.C. Sun, Overcoming Poor Tabletability of Pharmaceutical Crystals by Surface Modification, Pharmaceutical Research. (2011) 1–8.

[4]   M. Leane, K. Pitt, G. Reynolds, A proposal for a drug product Manufacturing Classification System (MCS) for oral solid dosage forms, Pharmaceutical Development and Technology. (2014) 1–10.

[5]   The Biopharmaceutics Classification System (BCS) Guidance, Available from: http://www.fda.gov/AboutFDA/CentersOffices/OfficeofMedicalProductsandTobacc o/CDER/ucm128219.htm.

[6]   D. McCormick, Evolutions in direct compression, Pharmaceutical Technology. 17 (2005) 52–62.

[7]   B.S. Barot, P.B. Parejiya, T.M. Patel, R.K. Parikh, M.C. Gohel, Compactibility improvement of metformin hydrochloride by crystallization technique, Advanced Powder Technology. (2011).

[8]   J.K. Prescott, R.J. Hossfeld, Maintaining product uniformity and uninterrupted flow to direct-compression tabletting presses, Pharmaceutical Technology. 18 (1994) 98–115.

[9]   M.D. Ticehurst, I. Marziano, Integration of active pharmaceutical ingredient solid form selection and particle engineering into drug product design, Journal of Pharmacy and Pharmacology. 67 (2015) 782–802.

[10]   D. Olusanmi, K. Roberts, M. Ghadiri, Y. Ding, The breakage behaviour of Aspirin under quasi-static indentation and single particle impact loading: Effect of crystallographic anisotropy, International Journal of Pharmaceutics. (2011).

[11]   A.G. Ogienko, E.V. Boldyreva, A. Yu Manakov, V.V. Boldyrev, A.S. Yunoshev, A.A. Ogienko, et al., A new method of producing monoclinic paracetamol suitable for direct compression, Pharmaceutical Research. (2011) 1–12.

[12]   H.A. Garekani, J.L. Ford, M.H. Rubinstein, A.R. Rajabi-Siahboomi, Highly compressible paracetamol: I: crystallization and characterization, International Journal of Pharmaceutics. 208 (2000) 87–99.

[13]   J.V. Santos, L.A.E. Batista de Carvalho, M.E.T. Pina, The Influence of the Compression force on Zidovudine release from matrix tablets, AAPS PharmSciTech. 11 (2010) 1442–1448.

[14] H. Nakamura, Y. Sugino, T. Iwasaki, S. Watano, Development of a Novel Tablet Machine for a Tiny Amount of Powder and Evaluation of Capping Tendency, Chemical and Pharmaceutical Bulletin. 59 (2011) 1518–1522.

[15] E. Joiris, P. Di Martino, C. Berneron, A.-M. Guyot-Hermann, J.-C. Guyot, Compression behavior of orthorhombic paracetamol, Pharmaceutical Research. 15 (1998) 1122–1130.

[16] I. Akseli, N. Ladyzhynsky, J. Katz, X. He, Development of Predictive Tools to Assess Capping Tendency of Tablet Formulations, Powder Technology. 236 (2013) 139–148.

[17] I. Sinka, F. Motazedian, A. Cocks, K. Pitt, The effect of processing parameters on pharmaceutical tablet properties, Powder Technology. 189 (2009) 276–284.

[18] J. Fachaux, A. Guyot Hermann, J. Guyot, P. Conflant, M. Drache, J. Huvenne, et al., Compression ability improvement by solvation desolvation process: application to paracetamol for direct compression, International Journal of Pharmaceutics. 99 (1993) 99–107.

[19] P. Di Martino, A.M.Guyot-Hermann, P.Conflant, M.Drache and J.C.Guyot, Preparation and physical characterization of Forms II and III of paracetamol, Journal of Thermal Analysis. 48 (1997) 447-458.

[20] R. Roopwani, I.S. Buckner, Understanding deformation mechanisms during powder compaction using principal component analysis of compression data, International Journal of Pharmaceutics. 418 (2011) 227–234.

[21] P. Di Martino, A.M.Guyot-Hermann, P.Conflant, M.Drache and J.C.Guyot, A new pure paracetamol for direct compression: The orthorhombic form, International Journal of Pharmaceutics. 1, 128 (1996) 1-8.

[22] Joiris Etienne, P.Di Martino, Christophe Berneron, A.M. Guyot-Hermann and J.C. Guyot, Compression behavior of orthorhombic paracetamol, Pharmaceutical Research, 15 (1998) 1122-1130.

Chapter Two

Crystal Science of Pharmaceutical Materials in Relation to Their Mechanical Properties

Theoretical crystal science, and crystallisation principles underpinning the mechanical properties of solid are delineated. The associated commons in silico modelling approach used for this study are described against the theories

Chapter 2 Crystal Science of Pharmaceutical Materials in Relation to Their Mechanical Properties

2.1 Introduction

This section will describe briefly the concept that leads to the formation of solid forms, starting from the state of matter. The context of this section is set against the pharmaceutical industry. The crystallisation process that is the path to the formation of the solid form is also explained. This chapter also highlights the crystallography principle and its importance for in silico modelling during the formulation of the tablet. It is important to study the solid-state form because at room temperature, the active pharmaceutical ingredients (APIs) and excipients are in the solid form. Besides the concept of a perfect crystal, the event of crystal imperfection too is elaborated. These theories are further correlated with the essential parameters for drugs tabletting, namely flowability and compressibility. Summary of the whole chapter is illustrated in Figure 2-1.
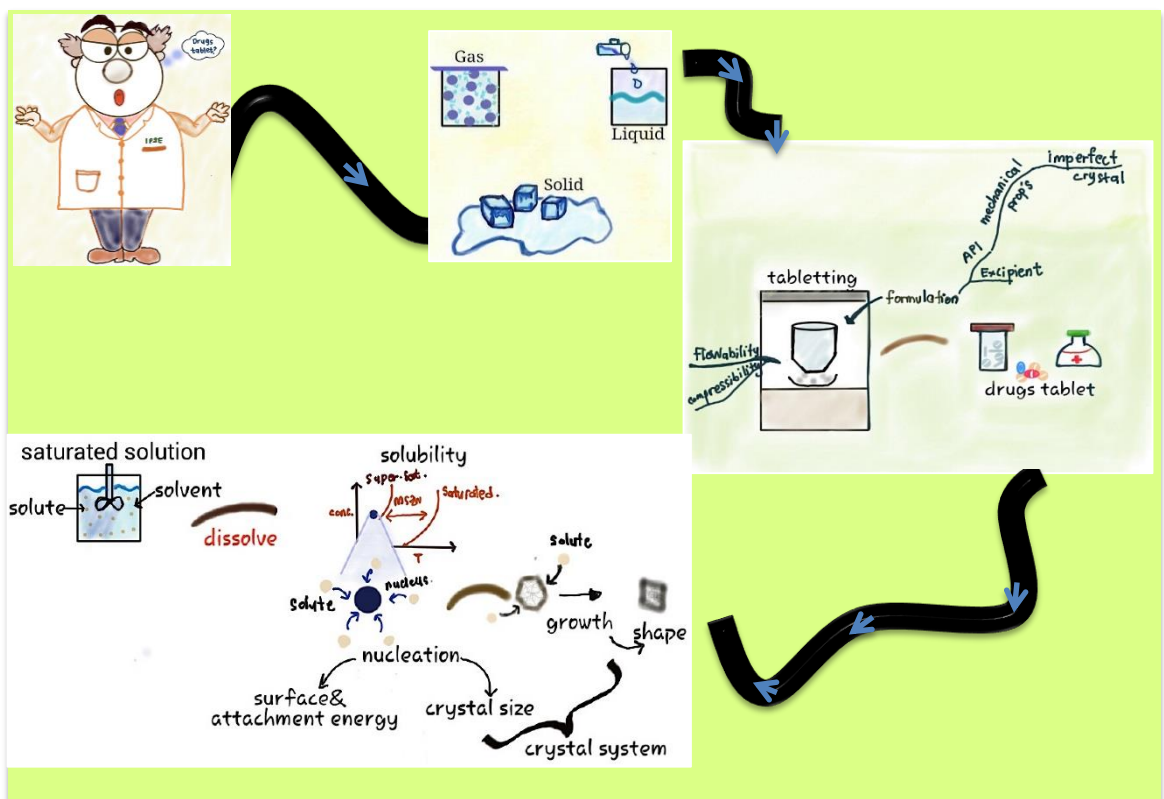
Figure 2-1 Route map of summary for chapter two consisting theories for the study, starting from the state of matters up to the mechanical properties for materials

2.2 Building from matters to crystalline

The common states of matter are gas, liquid and solid. Commonly, the general differences between states are mobility and intermolecular distances. Gas has the most mobility and largest intermolecular distance, allowing the atoms to disperse freely occupying space. The liquid is having medium mobility and intermolecular distance closer than gas. Both gas and liquid are examples of disordered systems. Lastly, solid state has very low mobility, limited to vibration and the intermolecular distances are at a minimum. The mobility, vibration and distances' limitation hence, makes the atom in a fixed position, retaining the original shape unless an external force was employed for alteration.

The conversion between different states of matters involves a thermodynamic relationship to represent the ordering and disordering of the molecule system. The states' transition brings about changes in the physical properties, specifically volume and density. The transitioning encompasses a phase transformation crossing the equilibrium lines separating the different phases. The driving forces for the phase transformation are temperature and pressure.

As mentioned in the earlier section, the APIs and excipients at room ambient are solid forms. Solid forms exist in two forms, notably crystalline and amorphous depending on the thermodynamic stability. Crystals are the building block for crystalline. Crystalline is constructed by a considerable number of minute's units of crystal resembling the larger crystalline shape. On another note, the amorphous forms are thermodynamically unstable, and potentially transforming into crystalline if the kinetics' barrier is not too immense. The metastable conditions correlate to the disordered state, makes it having similar properties as a liquid.

2.2.1 Crystal chemistry – structure-property relationships

Comprehensive knowledge of the structure provides invaluable information for predicting the macro properties, for example, strength and stability of materials [3]. The concept of structure-property is the core process during the selection of APIs for formulation. This concept has been extended, by materials science tetrahedron (MST) [4] that considers parameters for evaluating the process and performance for a specific solid form. The MST brings together four key considerations for materials understanding which are structure, property, process and performance. The MST describes the observed crystal behaviour and the impact during solid form selection. This section will focus on the structure-property

relationship, and the subsequent section will describe the gain for understanding structure-property holistically based upon the MST concept.

For solid form, the macro properties are more predictable and correlate well to the molecular properties (single crystal) [5]. In contrast, for a disordered system; the macro properties are based on the average values instead of the individual molecules making the calculation intensive. Pharmaceuticals compounds, which are organic, usually are molecular in nature. The solid forms are held together by cohesive force between the atoms forming the molecules. The equilibrium between these forces will determine the configurations and positions (structural perspective) for the molecules. The creation of multi-type bonds helps to class physically distinct molecules' behaviours [6]. The physical properties of solid forms can also be evaluated based on geometry, involving the crystallography viewpoint.

The familiarity with the APIs candidates, in particular, structure-property relationships assure that probable risk after dispensing the drugs dosages are well regarded [7]. A famous case of the effects of molecular structure changes on material's physicochemical properties within the pharmaceutical workspace is the Ritonavir incident [8]. Ritonavir is a drug originally discovered for inhibiting HIV protease for treating AIDS and HIV. It is manufactured by Abbott (now known as AbbVie.Inc) as a normal capsule known as Norvir, with no needs of refrigeration in 1996. In 1998, a more stable polymorph (form II) of Ritonavir was identified causing the Norvir to be recalled from counters [9]

Polymorphism is a transition of molecules into different form while maintaining its chemical compound but exhibiting completely different physicochemical behaviours. The physicochemical differences were caused by dissimilarities of the molecular packing arrangements. Polymorphs may take place in two distinct conditions, monotropic and enantiotropic with the latter is reversible. The form II Ritonavir has a much lower solubility, compromising the therapeutic efficiency relating to bioavailability of dosage after dispensing. As a temporary solution, Ritonavir is supplied as suspension form, and refrigerated gelcaps replace the capsule. Finally, in 2000, researchers in Abbott [10], found a solution to avoid the polymorphism occurrence by producing Ritonavir as the tablet is known as Kaletra eliminating the needs for refrigeration. The ritonavir incident was one circumstance when the molecular structural failed the crystal properties of chemical compounds.

2.2.1.1 Intermolecular bond

The molecular crystal lattice is built from a group of molecules that are packed densely. The lattice is held together by intermolecular bonds interactions resulting in binding energy. Knowledge of intermolecular bond is crucial because alterations will impact directly or indirectly the physicochemical properties of the APIs such as melting point, mechanical properties and crystal form itself [11]. The nature of molecular crystals behaviour can be best shown by its' type of bond. Bonding of molecules involves the interaction of bonded atoms and valence electrons. The likelihood of valence electron interactions is measured by electronegativity. The strength of interaction between the valence electrons and bonded atoms will determine the nature of a particular bond. Interactions between two atoms, for example, atom A and B is best described using the van Arkel-Ketelaar triangles or bond triangle in Figure 2-2 [12].
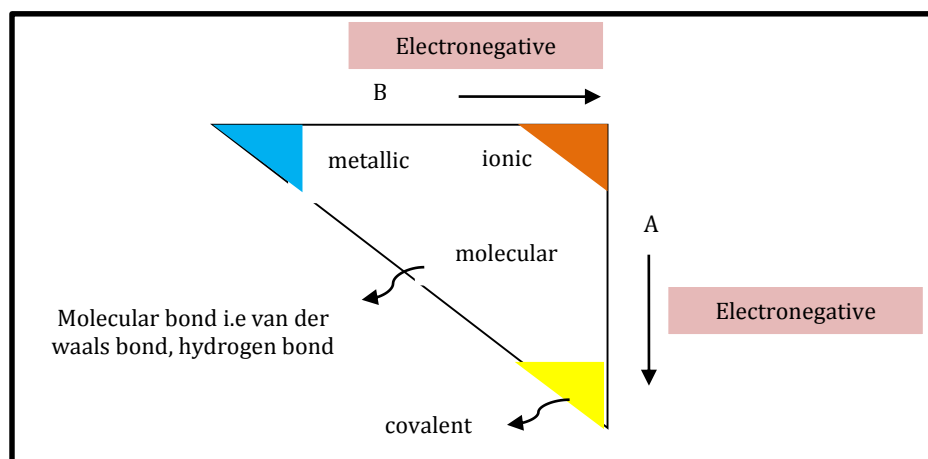
Figure 2-2 The variation of electronegativity with respect to the ideal bond. A and B are two atoms in a binary molecules, with varying electron movement that results in the ideal bond types and the molecular bonds [12]

Referring to the bond triangle in Figure 2-2, the ideal bonds are occupying the corner of the triangle. Meanwhile, the molecular bonds notably, van der Waals and hydrogen are floating in the centre of the triangle. The different electron concentrations from one corner of the bond triangle to another cause an electron shift. When both atoms (A and B) are electropositive, the electrons are lost from the individual atom. The electrons then travel freely within the solid. Thus, create a metallic bonding. The metallic bond is a non-directional bonding as the electron can travel freely during the bonding creation.

In contrast, two electronegative atoms will create the covalent bonds. Sharing of valence electrons of two atoms creates the covalent bonds. A covalent bond is a directional bonding. When the bonds interact in a network, it is robust and hardly breaks. The ionic bonding is

created when two atoms have different ions creating an electrostatic attraction. The ionic bond has similar directionality as the covalent. The property that is setting ionic and covalent apart is on ways the bond is taking place. The covalent involves sharing of electrons while the ionic transfers the electrons causing ions formation.

Van der Waals bonds are weak repulsive and attractive forces between two molecules that are distance dependent. The movement of electrons follow Pauli's principle and act on the basis of incompressibility behaviour of matter. The van der Waals bond results in three types of forces that are Keesom forces (permanent dipoles), Debye forces (between the permanent and induced dipole), and London force (instantaneously induced dipoles). The van der Waals is significant for molecular mechanics study because of its effect on the conformational energies and selection of preferred geometries over another. In this study, the van der Waals forces play a significant role in representing the intermolecular interactions occurring in molecular crystals. Another type of molecular bonding is the hydrogen bond. A hydrogen bond is necessary for bonds formation of polar molecules. Creation of hydrogen bonds involves the exchange of proton of a hydrogen atom in one molecule to a highly electronegative atom attached to the other molecule. The different type of intermolecular bonds is characterised and summarised in Table 2-1.

Table 2-1 Summary of different type of bonds, consisting of metallic, ionic, covalent and molecular bonding. The molecular bonding is necessary for this study. *Directional* and *non-directional* shows the characteristic of the bond. Directional bond is having a particular direction during the formation of bond while non-directional is the opposite [12]

Type of bond	Description
Metallic bond (*non-directional*)	It triggers by the free electrons and metal ions. These create a maximum density of electrons and metal atoms. Evaluation of energy done qualitatively by empirical correlation
Ionic bond (*directional*)	Triggers by the different charge of ions between atoms creating an electrostatic attraction. Energy is correlated qualitatively to ion size
Covalent bond (*directional*)	Triggers by the electronegative atom at the valence shell forcing it to share the valence electron to become stable. The geometry will be affected by the number of electrons and energy quantification is related to the number of bonding electrons
Van der Waals bond (*non-directional*)	The force originated from electrostatic and resulted in a weak force. Plays significant role in crystal geometry
Hydrogen bond (*directional*)	The force originated from the proton transfer bond creation. The bond strength increased when the distance of bonding shorter. It also plays significant role in dictating the crystal geometry

17

2.2.1.2 Modelling van der Waals interactions using Lennard-Jones 12-6 potentials

In modelling the van der Waals interactions, a simple empirical expression is used. The function must be able to calculate repeatedly the large number of van der Waals interactions in the molecular crystal studied. It is suggested that Lennard-Jones 12-6 given in Equation 2-1 [13] is the most suitable function to show the van der Waals interactions between two atoms. Another possible potential is the Buckingham, which has three adjustable parameters. In Buckingham, during computational calculations, as the distance between the atoms decrease, the attraction strength increases causing the atomic nuclei to fuse. Therefore, Lennard-Jones 12-16 is the commonly used potentials for molecular crystal modelling.

$$v(r) = 4\varepsilon\left[\left(\frac{CD}{r}\right)^{12} - \left(\frac{CD}{r}\right)^6\right] \tag*{(Equation \textit{2-1})}$$

There are two adjustable parameters, the collision diameter CD (the separation for which the energy is zero) and the well depth ε. The Lennard-Jones can also be represented by using A and C constants representing the repulsive and attractive forces as in Equation2-2. The A and C constants result from the first degree derivatives of the initial equation at internuclear distance of zero (i.e $\frac{\partial v}{\partial r} = 0$) with regards to a minimum point r_m. By substituting the σ with $r_m = 2^{1/6}CD$ to above, or

$$v(r) = \varepsilon\left\{\left(\frac{r_m}{r}\right)^{12} - 2\left(\frac{r_m}{r}\right)^6\right\} \tag*{(\textit{Equation 2-2})}$$

$$v(r) = \frac{A}{r^{12}} - \frac{C}{r^6} \tag*{(\textit{Equation 2-3})}$$

moreover, will give A is εr_m^{12} (or $4\varepsilon\sigma^{12}$) and C is $2\varepsilon r_m^6$ (or $4\varepsilon\sigma^6$)

The Lennard-Jones potential attractive part is r^{-6} and repulsive is r^{-12}. Figure 2-3 shows the relation of the two components, repulsive and attractive. The Lennard-Jones 12-6 potential is usually used to calculate large systems at which the twelfth power term and be calculated by squaring the r^{-6} term. Moreover, the r^{-6} term can also be calculated from the square of the distance. Besides that, the power for repulsive part varies in giving the curve lesser steepness, which is used as force fields.
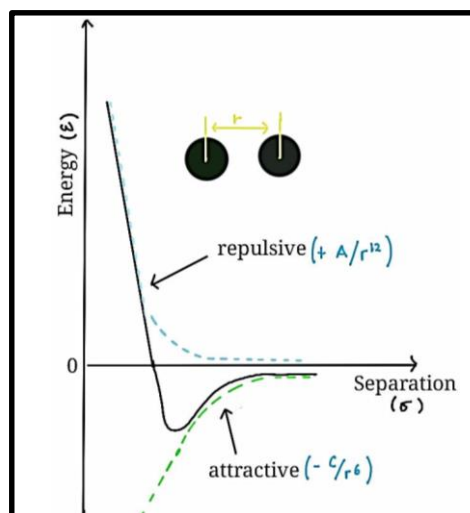
Figure 2-3 Lennard-Jones potentials illustration. The separation distance between two atoms are set against the energy created. Interactions are repulsions and attractions as the distance been manipulated

The van der Waals makes up the non-bonded interaction for a molecular system. Other non-bonded interactions are that involving the electrostatic charges. As the relations are not bond specific, it will have 'through space' notion with analysis usually by a mathematical function of some inverse power of distance.

2.2.1.3 Electrostatic interactions –semi-empirical methods and atomic charges

Besides van der Waals, the non-bonded interactions also involve electrostatic forces. Electrostatic is the effect of unbalance distribution of charges during electron transfer between two molecules. There are several models to represent the electrostatic contribution, for instance, the multipole expansion, point-charge and partial atomic charge. There is also the semi-empirical method that is developed to provide quick calculation in ab-initio by regarding only the charges at atomic valence. An example of the partial atomic charge is Gasteiger and for the semi-empirical method is MOPAC [13]. Comparison of various electrostatic models is shown in Table 2-2 consisting the way the calculation is carried out with regards to a specific model.

Table 2-2 Comparison of electrostatic model for calculating non-bonded interaction in molecular modelling include MOPAC and semi-empirical model [13]

ELECTROSTATIC MODEL	DESCRIPTION
Multipole expansion	The calculation is based on electric moments. Treat molecule as one exclusive unit and simplify calculation in comparison to partial charges. The disadvantage is when the distance between molecules is comparable with the molecular dimensions
Point charge	Complete application of each point charges can reproduce the interaction energy calculated using multipole and coulombs. The disadvantage is when dealing with dipole moment, tends to oversimplify
Partial atomic charge	Electrostatic field related to the electronegativity occurrence. Two components contribution, nuclei (positive charge) and electron distribution (negative charge). Partial atomic charge can also be calculated based on population balance
Gasteiger-Marsili	Adopt concept of partial equalisation of orbital electron electronegativity. The calculation involves iteration to balance the electron transfer. The electron transfer will reduce in each iteration step
MOPAC- Modified Neglect of Diatomic Overlap (MNDO)	Adopt the Fock matrix and have special treatment for hydroxyl (OH) and an amine group (NH) for the core-core repulsion. This model is used throughout the monatomic parameters. Disadvantages include overestimating repulsion between atoms when separated and extreme energy values depending on size of molecules.
MOPAC- Austin Model 1 (AM1)	Second derivatives of the MNDO, with modification of core-core term using Gaussian function. This addition eliminates overestimating repulsions between atoms that have distance equally to their van der Waals radii. The disadvantage is increasing the number of parameters for calculation
MOPAC- Extension of AM1 (PM3)	Third parametisation of MNDO. It uses the Hamiltonian elements same as in AM1 only, here the parameters is derived using automated parametisation steps. The disadvantage is during rotational barrier calculation and can be corrected using torsional potential

For a large molecular system, the Gasteiger and semi-empirical is used to provide a quick electrostatic calculation. Gasteiger calculation is based upon the polynomial relationship between atom orbital electronegativity (χ_A) and charge (Q_A) as represented in Equation 2-4.

$$\chi_{\mu A} = a_\mu + b_{\mu A} Q_A + c_{\mu A} Q_A{}^2 \qquad\qquad (\textit{Equation 2-4})$$

where a, b and c are elements in their valence state.

Recall that electrostatic is about electronegativity and follow the Pauling Principle. Gasteiger represents electron decrease by an iterative procedure. From Equation 2-4 above, the charge (Q_A) is given by iteration following Equation 2-5.

$$Q^{\langle k \rangle} = \frac{\chi_B^{\langle K \rangle} - \chi_A^{\langle K \rangle}}{\chi_A^+} \alpha^k \qquad\qquad (\textit{Equation 2-5})$$

where α^k is the damping factor and set as 0.5 in Gasteiger-Marsili. The damping factor is reducing the effect of more electronegative atoms in the calculation. Having to describe crystal behaviour molecularly, next subsection will convey theories to describe crystal behaviour geometrically.

2.2.2 Crystallography

The geometrical law that governs the formation of the crystal is known as crystallography. Crystallography describes the arrangement of atoms and molecules that form a lattice which is the basis for analysing the x-ray diffraction. Lattice is imaginary sets of points in space as such that the atomic arrangement of motif looks the same in every aspect when viewed from any point within the designated space [2] [14]. The concept of the lattice can simply be described in two-dimensional before extending to the three-dimensional using motif repetition. A tulip motif is selected as depicted in Figure 2-4 to illustrate the lattice concept. The motif is repeated in a specific manner forming an array of tulips. This array is the lattice. The pattern of repetition can be traced by having circles overlaid by tulips. The removal of tulips motifs will show the circles in the array. These are the lattice points.
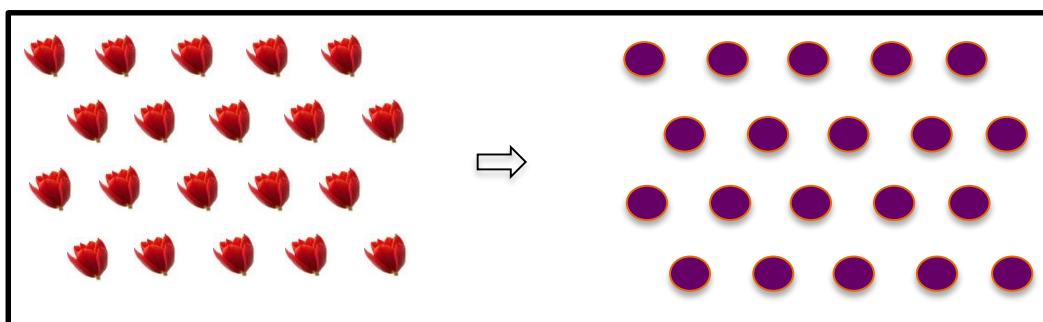
Figure 2-4 Illustration of motif repetition creating array know as lattice. The circle on the right represents the lattice points showing the pattern of repetition

Crystal is three-dimensional systems generated from three primitive translation vectors a_i, a_j and a_k adopting the same repetition principle described earlier. The array can be cut carefully so that it still contains the information needed to represent the pattern. The cut pattern is the unit cell. The vectors and angle together form a unit cell. The unit cell properties are called lattice parameters or unit cell constants. Lattice points enclosed within a unit cell are contributing towards a different fraction of the total points in each cell (Figure 2-5). The position of lattice points is described in fractional coordinates with regards to the crystallographic axes. The practice for in silico modelling of molecular APIs is taking unit cell as the basis [15]. A mole of sample APIs powder physically will consist of 6×10^{23} molecules, resulting in an expensive computational calculation. Taking only a unit cell, which typically, having four to eight molecules will reduce substantially the computational cost needed to carry out the calculation.
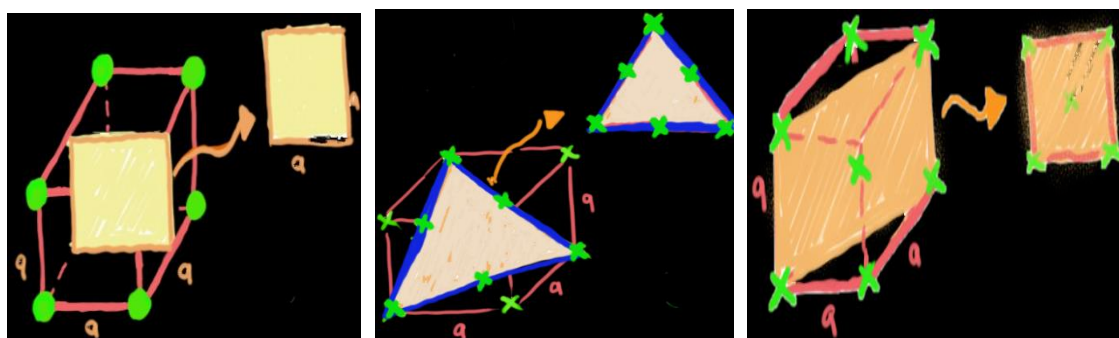
Figure 2-5 Showing three different arrangements of lattice points in crystal systems. There are primitive, body and face centred

In the lattice, atoms are arranged in the equal distance creating imaginary sheets forming layers known as the lattice planes. Each lattice plane has the same orientation that is held together by the intermolecular bond. These layers are identical and parallel consisting of lines and nodes regularly spaced in intervals. The importance of the plane will be for planes with highest nodes per unit length measured as reticular density. The plane will naturally intersect forming rows. The rows can intercept with planes parallel to it creates edges known as axes. The consistency of internal structure of this solid system will result in the crystal habit. The habit of the crystal consists of the development of shape and faces as the crystal grows and the planes of these faces are parallel to atomic planes in lattice [2].

For the crystal, there are seven distinct shapes of unit cells. These shapes can be arranged uniquely in space lattice according to 14 types of Bravais lattices. The APIs molecular crystals are typically simple primitive of triclinic, orthorhombic and monoclinic. APIs molecular crystals are complex makes it hard to be packed into the cubic system. The complexity of API's molecular crystal contributes to its anisotropic behaviour. The physicochemical properties of the APIs will depend on the orientation of interactions.

The types of crystal systems dictate the crystal habit whereby the crystal habit can be predicted numerically. The equilibrium relation between the interfaces of crystal and solvent phases [16] is developed by Gibbs in 1948 with Wulff in 1901 develops the geometrical representation of the crystal shape at that equilibrium state. The Gibbs-Thomson formula (Equation 2-6) relates surface free energy (γ_i) with area (A_i) at facet i to the volume (v) to give the total surface free energy (ΔGs). Increasing surface free energy resulting in decreasing importance of morphology of that particular face. The equilibrium is occurring when the surface free energy and area is at minimum value.

$$\Delta Gs = -\frac{V \Delta c}{V_m} + \sum_i \gamma_i A_i \qquad\qquad (Equation\ 2\text{-}6)$$

$\Delta c \ concentration, V_m \ Volume \ at \ equilibrium$

Further improvement in the formula is made by Frank-Chernov by considering the kinetic for a steady state growing crystal. At steady state, the shape will be independent of equilibrium shape. Frank-Chernov considers the growth rate (H_i) that is perpendicular to the face of crystal rather than the surface energy. Bravais then observed the relationship between the growth rates of the face with interplanar spacing in the crystal. The relationship (Equation 2-7) identifies that the growth rate of faces is inversely proportional to the interplanar spacing (d_{hkl}) [17]. Bravais suggested that the surface energies and the

rates of growth should be inversely proportional to the reticular densities. Donnay and Harker then refine the Bravais morphology formula by including the symmetry extinction condition that reduction of inter-planar spacing.

$$G_{hkl} \propto \frac{1}{d_{hkl}} \qquad\qquad (Equation\ 2\text{-}7)$$

Both the BFDH and surface free energy approach only consider the geometrical factor without regard to the internal crystal interactions. Hartman Perdock [18-19] then developed an attachment energy model for predicting crystal morphology by taking into account the intermolecular interaction. Attachment energy is the bonding energy when a face-building unit is attached to the surface of a crystal represented by Equation 2-8. Hence, the displacement velocity of the crystal face increases with increasing of attachment energy. The additional of growth layer based on the attachment energy model is perpendicular to the crystal face (Equation 2-8). The attachment energy can be calculated from the total intermolecular interaction energy per mole in a crystal that is lattice energy E_{latt} in relation with the intermolecular interaction within a layer of thickness d_{hkl}, E_{hkl}^{slice} (Equation 2-10). Linearity relationship of E_{hkl}^{att} and G_{hkl} will give a perpendicular growth rate as in Equation 2-9.

$$E_{att} = \sum_{[i=1}^{\infty} E_i(hkl) \qquad\qquad (Equation\ 2\text{-}8)$$

$$E_m^{att} > E_n^{att} \Rightarrow G_m > G_n \qquad\qquad (Equation\ 2\text{-}9)$$

$$E^{latt} = E_{hkl}^{slice} + E_{hkl}^{att} \qquad\qquad (Equation\ 2\text{-}10)$$

The attachment energy model only considers the internal interaction within the crystal and excluding the external factor that may impact the crystal growth such as solvent interaction, additives, and supersaturation. This study applies an atom-atom distance calculation to calculate the attachment energy. The atom-atom approach averages the intermolecular interactions between atoms that limited by specific radii. The surface energy can be calculated using attachment energy of molecule in a unit cell for a specific reticular area (Equation 2-11)

$$\gamma \simeq Z E_{att} d_{hkl}/2V \qquad\qquad (Equation\ 2\text{-}11)$$

2.2.2.1 Crystallographic symmetry

The geometric shapes that appear in crystal possess some degree of symmetry, and this fact can be used as a way for crystal classification. The three simple elements of crystal symmetry according to the law of constancy are a plane, axes and centre of symmetry. Crystal properties may differ according to the type of symmetry operators of the crystal lattice. Hypothetically, any two points in a lattice may have an identical property as they are in line with translation vector except for points lying near to the surface.

The full symmetry of given crystal structure is important for the physical properties of a crystal. Symmetry is evident in properties such as crystal growth rates and crystal shape, mechanical properties, and surface chemistries. Crystal may not have any symmetry at all, creating a complex and an oblique crystal with a high number of parameters to describe it. The low number of symmetry or no symmetry is one of the mechanical defects criterion and one of the hypotheses for the study. The external development of smooth faces of a crystal arises from some regularity in the internal arrangement of the constituent ions, atoms, or molecules. Any account of crystal, therefore, should include some references to the internal crystal structures.

The common symmetry operations are rotation, translation, reflection and inversion as shown in Figure 2-6. The rotation symmetry upon a crystal is demonstrated by the way crystal rotates 360 degrees around any axis to its original position that is denoted by n. If the crystal appears to have reached its initial position more than once during its complete rotation, the chosen axis is an axis of symmetry. If the crystal has to be rotated through 180 before coming into coincidence with its original position, the axis is one of two-fold symmetry. Lattices can be found such that one-, two-, three-, four-, and six-fold rotation axes are corresponding to 360/n. The rotation axes are denoted by the symbols 1 to 6. The translational operation is a repetition of motifs without alteration. The translational symmetry operation gives rise to two other symmetry elements, screw axis and glide plane. The glide symmetry reflects and shifts the mirror related component by half lattice spacing. The screw axis is resulting from translational and rotational of the component about an axis. These two additional symmetry operations are illustrated in Figure 2-6[20].
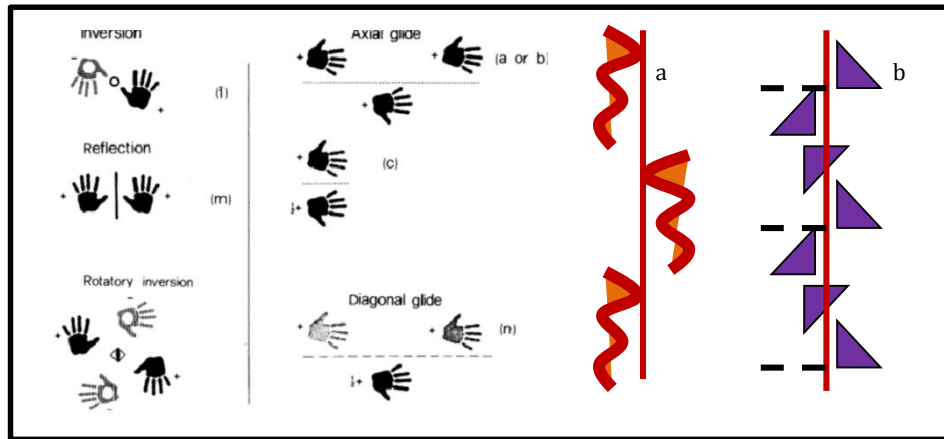
Figure 2-6 Left figure is showing the general symmetry operations. Figure a showing the glide plane of a helical pattern with ½ lattice distance shifted b) Figure showing triangle rotating about an axis at 90 degrees and shifted ½ lattice distance (Figure from [32])

The reflection symmetry is similar to the mirror effects. The motifs will be unaltered but in the opposite orientation, and best shown by our left and right hands. The inversion operation is when crystal system has an inversion centre. All points will have associated points on a line that passes through the inversion point. The combination of rotation and inversion may result in the molecular having the initial form after undergoing the symmetry operation.

2.2.2.2 Miller indices

The Miller indices are used to index planes and directions vectors within the lattice crystal. The Miller indices steps for indexing a set of parallel lattice planes are essentially a two-step process. Firstly, keep only three numerical factors for the three points or intercepts on lattice axes. Secondly, inverse these three numerical factors to corresponding smallest three integers to give the Miller indices of (hkl). Essential guidelines regarding the Miller indices indexing the lattice plane are Important lattice planes in a crystal are those with low Miller indices since these are the planes that will have the highest concentrations atoms (per unit area) [21]

Steps to index directions in the lattice are similar to indexing the planes, except in indexing direction vectors all components numerical factor is not inverted but being multiplied by their common denominator. The significance of indexing is the influences it has on optical properties, the reactivity of crystal, surface tensions and dislocations in the crystal. Within this study, the planes are used alternatively together with faces. Both are referring to the same thing. Within this study, the planar planes also been referred to as faces.

26

2.2.2.3 Point and space groups

Deriving from the symmetry operations described above, the properties of each lattice points passing through the symmetry elements form a mathematical group known as the point group. Because component in the crystal system must have the same environment throughout, making the crystallographic point groups restricted to 32 only. Two common methods for denoting point group are Hermann-Manguin and Schoenflies notation. The Schoenflies is commonly used for spectroscopy. The Hermann-Manguin consist the list of symmetry operators for the point groups with the order indicating relative orientation that takes place.

The space group arises from the combination of Bravais lattices, and point groups is another way to describe crystal structure. Recall that Bravais lattices provide the scheme for lattice point's repetition while the point groups correlate to the symmetry operators present at each lattice points. The combination of both Bravais and point groups provide a thorough geometrical view on symmetry operator for the crystal systems from its notations. The unique combination of Bravais lattices and point groups give rise to 230 different space groups. The notation of space group consists of the first letter of P, C, I, F or R which represents the Bravais lattices follows with a statement describing the symmetry operators present.

2.3 Crystal imperfections

This section will introduce the defects that occurred in the crystal. In reality, crystals are hardly perfect. There will always be impurities presence that is affecting the crystal structure. The succeeding subsection presents the common defects of materials in different dimensions specifically zero up to three dimensions. Following the types of the defect is the mechanical properties definitions according to materials' respond when under force.

2.3.1 Lattice defects

Imperfections are irregularities resulting from distortions that crystal suffers. The occurrence of defects in the crystal is small, but the impact is significant towards crystal physical properties [22]. In general, defects in the crystal are classified into point defects, line defects and planar defects. Two common point defects are vacancy and interstitial that can enhance diffusion in the crystal. The line defects such as dislocations allow the plastic deformation to occur while planar defect for example grain boundaries will promote

hardening of the crystal [23]. The different types of defects in the crystal are presented in Table 2-3 together with a description of the conditions resulting from the defects.

2.3.1.1 Point defects

The point defects relate to the movement of an atom in the lattice that eventually affect the energy required for the movement for example the internal energy. The difference between the vacancy defect and interstitial is between missing and having extra atoms in the lattice illustrated in Figure 2-7.

Table 2-3 Types of lattice defects showing a point, line and volume defects. The similar conditions with regards to the types of defects are shown to be vacancies, interstitials, impurities, dislocations, stacking faults and inclusions

Point (0 dimension)	Line (1 dimension)	Area (2 dimensions)	Volume (3 dimensions)
Vacancies: Occurrence of vacant lattice sites	Dislocations: Gliding motions with combination of slip plane and Burgers vector	Stacking faults: Additional of odd atoms sequence (twin) compared to original	Inclusions and precipitations
Interstitials/substitutionals: Inclusions of atoms not on lattice sites			
Impurities: Occurrence of foreign particles in the lattice			

It is possible to determine the vacancy in the crystal with a given temperature at equilibrium, using the exponential law (Equation 2-12). The occurrence of the vacancy and interstitial at the same time is Frenkel defect whereas the occurrence of a vacancy on its own is Schottky defect. Besides interstitial defects, if the impurities are similar size as the host atom, then substitutional defects take place. Impurities may be an inclusion that includes during the crystallisation process. The occurrence of impurities affects the functionality of crystal that lower the purity and performance of the pure crystal.

$$n = \alpha N e^{-E_f/RT}$$
 (Equation 2-12)

n: number of a vacancy among N crystal sites, E_f: energy for the vacancy formation in dilute solution, α : numerical factor, (≈ 10)
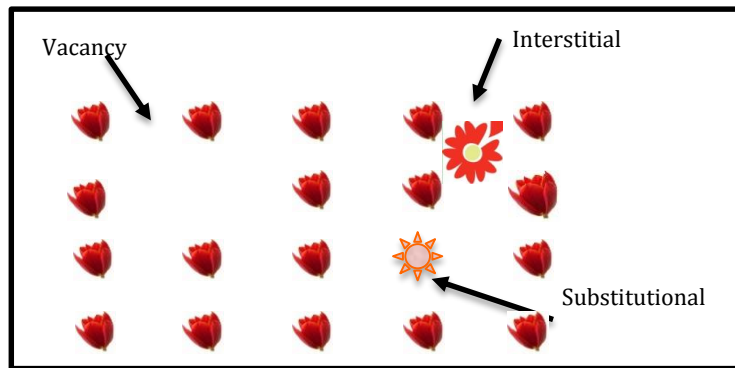
Figure 2-7 The illustration of a lattice pattern with a vacancy and interstitial. Availability of vacancy increase the internal energy at a low condition while the interstitial is of the same size, hence the energy required to eject the atom from one space to another is more

2.3.1.2 Stacking and twinning faults

Besides point defects, the crystal can also have imperfections that change its lattice pattern, for example, stacking faults [21]. The stacking faults are planar imperfections. It occurred when one layer from the lattice sequence was omitted, or added. The omission of one layer is giving intrinsic stacking faults, while the addition is extrinsic. Both stacking conditions are as seen in Figure 2-8. The stacking faults can cause sliding between layers of atoms during plastic deformation.
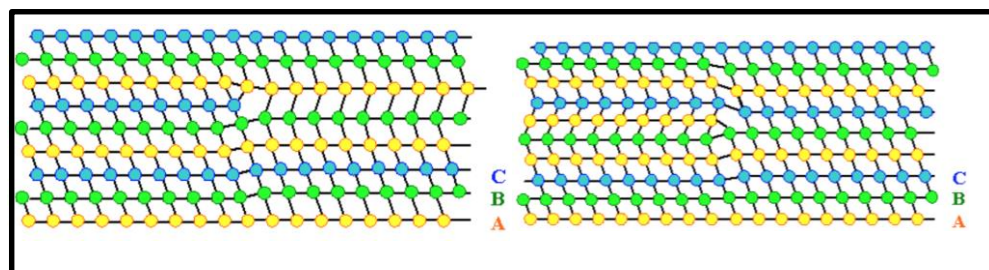
Figure 2-8 Intrinsic and extrinsic stacking faults represented by three sequence, a, b and c. The intrinsic stacking faults are with omission of half b-sequence and the extrinsic with an extra c sequence inserted within the layers (Figure from [36])

The presence of extra-planar makes the adjacent layer to be shifted creating an orifice-like pattern when being observed. Different types of crystal will undergo the stacking faults differently. Stacking faults is a partial defect. The stacking faults can also lead to the twinning faults, at which the stacking sequence inverts itself creating a mirror-image orientation. Twinning faults are easily recognisable because it will create boundaries between the twin crystals and create a huge lattice orientation difference. Twin boundaries occurred when a region undergoes homogeneous shear that produces the original crystal

structure in a new orientation. The parent is the original crystal, and the product is the mirror image of the parent as seen in Figure 2-9.

Figure 2-9 Twinning in Pyrite crystal showing clear mirroring of parent structure (Figure from [37])

2.3.1.3 Grain boundaries

Crystals are commonly crystallised in irregular shapes known as grains and concentrated grains in the same area is bound by grain boundaries [24]. Each grain contains any of defects described earlier. Large grains disorientation made the atomic arrangement at the boundary become complicated and varies significantly. The best way to observe the grain boundaries is by using raft bubble model. Figure 2-10 showed grains boundaries of several defects showing the surrounding area that is perfect and within the boundaries is imperfection. The region of the disorder is observed to be very narrow, being limited to one or two atoms at each side of the boundary.
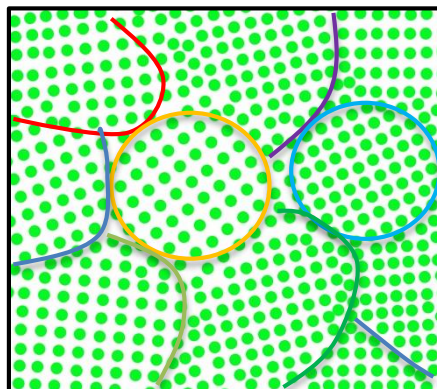
Figure 2-10 Raft of bubbles showing grain boundaries of several grains that have imperfections [23]

2.3.2 Dislocations

In organic materials, the dislocation occurs in a more complex manner in comparison to the elemental materials. Dislocations are linear defect corresponding to a disturbance in the structure that caused a systematic deviation of the positions of atoms from their normal sites [22]. It is the largest crystal imperfections in defining the crystal growth, chemical

reactivity and also vitally affecting the mechanical strength and plasticity of crystals. Dislocations in crystal may be developed by two ways either during the early stage of growth or induced mechanically after crystal formation [25] in which the former is affected heavily by crystallisation techniques.

Components of dislocation are dislocation line and the slip system, comprises of Burgers vector (dislocation vector) and slip plane (the surface where the dislocation take place). The dislocations aid the plastic deformation by having the movement layer by layer. In organic materials, the dislocation occurs in the more complex manner in comparison to the elemental materials. The total energy for dislocation (E_{disloc}) is represented by two parts, which are core dislocation (E_{core}) and line dislocation (E_{line}) given in Equation 2-13. The core dislocation is difficult to be calculated but usually is estimated to be at least a magnitude smaller than the line direction. Disregarding the core dislocation energy will not cause a significant error.

$$E_{disloc} = E_{core} + E_{line} \hspace{4cm} (\textit{Equation 2-13})$$

The line direction bound the slipped area where the dislocation occurs. The movement of the slip is burgers vector. For the dislocation to move, the burgers vector and dislocation line must lie in the same slip plane. The energy of dislocation represents the barrier needed for the deformation and displacement to occur. A dislocation is simply describing the weakening of materials about their theoretical strength.

2.3.2.1 Burgers vector

The direction at which the dislocations move is the Burgers vector. The dislocations path taken by atoms in imperfect crystals is the Burgers circuit [26]. The Burgers circuit as illustrated in Figure 2-11 showed that in a perfect crystal, the path is fully closed. Now, incorporating the same route into an imperfect crystal, the Burgers circuit is incomplete. The vector needed to complete the circuit is Burgers vector. Burgers vector is usually the shortest lattice translation. Burgers vector is the magnitude of dislocation and act as a connector to complete the circuit surrounding dislocation. The Burgers vector is independent of crystal shapes. The shortest Burgers vector will have the lowest energy and will likely dominate the plastic deformation. For instance, in a body-centered cubic crystal it is ½ [111]. If Burgers vector is connecting two equivalent lattice points, it is called perfect dislocation or complete dislocation. Noteworthy, the circuit must be in a small strain as when it gets larger, it will defy the Hooke's law [27].
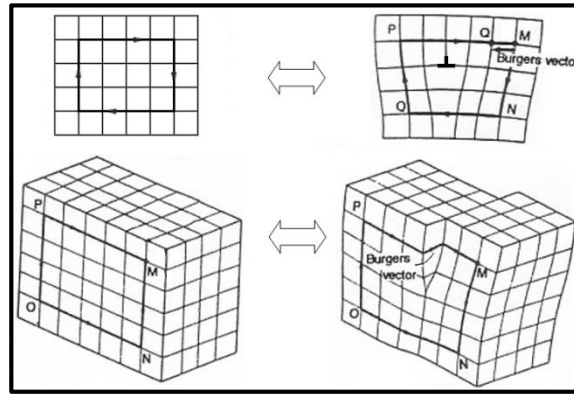
Figure 2-11 Comparison of perfect crystal and imperfect crystal showing the Burgers circuit. As the Burgers circuit is transferred into the perfect crystal, incomplete circuit is observed. The vector needed to complete the circuit is Burgers vector [22]

2.3.2.2 Slip plane

The surface where dislocations slip takes place is known as slip plane. Slip plane is where dislocation line and Burgers vector lies. The slip plane is usually the densest lattice plane. Collectively, Burgers vector and slip plane make a slip system. Slip in molecular structure will start from a small area and spread outwards [28] making the slip front or the line that separates the slipped and the unslipped region as essential characteristics during plastic deformation. Figure 2-12 represented examples of the potential slip planes for three types of Bravais lattice systems namely primitive, body-centered and face-centered.
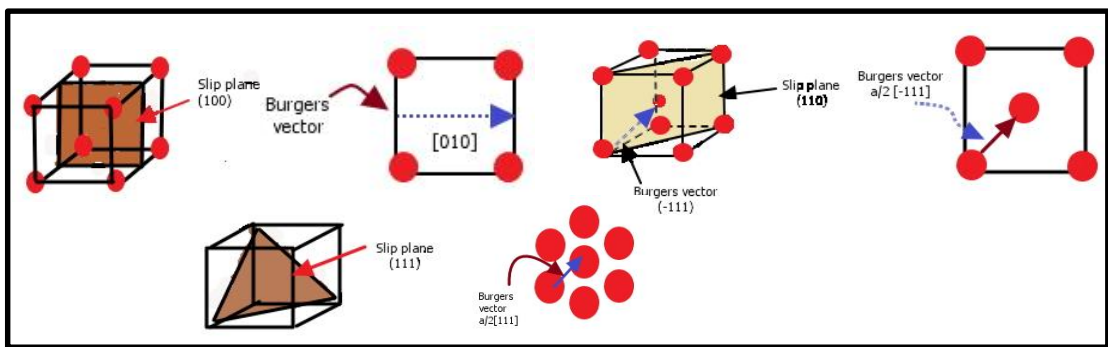
Figure 2-12 Slip planes in different in three common bravais lattice crystal system. The densest plane in crystal is shown to be (100) plane for primitive, (110) plane for body centered and (111) plane for face centered. Shown together is the preferred Burgers vector with respect to Bravais crystal system

For a slip system to occur, both factors Burgers vector [uvw] and slip plane (hkl) must present. The Burgers vector must lie in the slip plane. Simply Equation 2-14 known as Weiss zone law can observe this condition.

hu + kv + lw = 0   (*Equation 2-14*)

2.3.2.3 Edge, screw and mixed dislocations

Dislocation is grouped into two main orientations: screw (Equation 2-15) and edge (Equation 2-16) [22]. The orientations are differing based on the angle created between the dislocation line and Burgers vector. Edge dislocation is when dislocation line and Burgers vector is 90° apart and normal to slip plane. In contrast, screw dislocation is when dislocation line and Burgers vector are parallel with the slip plane. Apart of the two primary orientations, a dislocation that takes place at angles between 0-90° will be a mixed dislocation.

Edge dislocation is best simulated by insertion of an extra half-plane into the crystal structure (Figure 2-13). Insertion of an extra half-plane displaced the atoms from the original positions by one d-spacing gap causing the perfect atoms aligned surrounding the half plane to be disorganised. The atoms around the dislocation area will reorganise itself by atoms movement trying to fill in the gaps created by the half-plane.

Edge dislocation has energy higher than the screw dislocation by $1/(1-\acute{y})$ at which $\acute{y}$ is the Poisson's ratio. Poisson's ratio is the negative ratio of transverse to axial strain. The negative of tranverse occurs when the edge dislocation is compressed with pressure; the solid will expand perpendicularly in the other two directions. Poisson's ratio will be explained further in section 2.3.3. When being stretched, materials will transversely elongate in a direction perpendicular to the force. The elastic energy is calculated based on the integration of each small element of volume [29] representing the energy associated with the strain field around the dislocation line. The equations that represent the elastic energy stored in a specific volume per unit length of dislocation with respect to the orientation are,

Screw dislocation:

$$E_l \ (evm^{-1}) = \frac{G|b|^2}{4\pi} ln \frac{R}{r_0} \hspace{3cm} \textit{(Equation 2-15)}$$

Edge dislocation:

$$E_l(evm^{-1}) = \frac{G|b|^2}{4\pi(1-\acute{y})} ln \frac{R}{r_0} \hspace{3cm} \textit{(Equation 2-16)}$$

33

For anisotropy, G= K

where G is bulk modulus, b is Burgers vector, R and r_o are outer, and inner cut-off radii distance and v' is Poisson ratios. In anisotropic materials, the bulk modulus is represented by elastic tensors; therefore, G is substituted with K, energy constant.
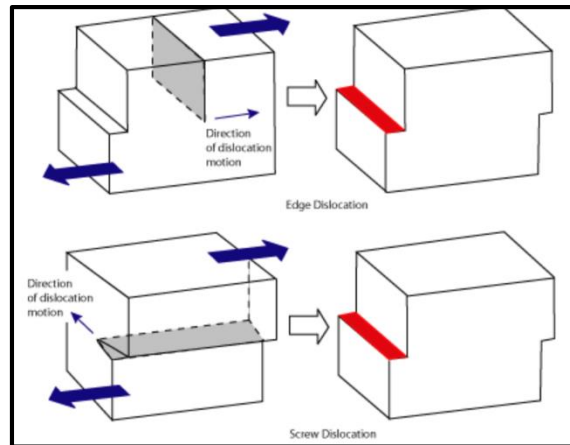
Figure 2-13 Representation of edge and screw dislocation. Half plane is inserted and cause shift within the perfect lattice. If the line and Burgers vector is parallel, an edge dislocation will take place and if it perpendicular, edge dislocation occurs (Figure from [34])

Turning now to the theoretical concept of materials respond to the force. The next subsection describes the mechanical properties of anisotropic materials that include Hooke's law, deformation behaviour and fracture mechanisms.

2.3.3 Mechanical properties- Hooke's Law

In this subsection, the basic science underpinning the deformation of organic anisotropic crystals is presented. This section will describe the theoretical concept for molecular crystal mechanical properties. The subsequent follows that Hooke's law, elastic and plastic properties, and finally the fracture and cleavage.

Under constant application of loads, materials will have changes in shape to accommodate the applied loads. The nature of the load and deformation will lead to different failure mechanisms. The failure mechanism can be characterised as brittle or ductile. In brittle fracture, there is no or very little plastic deformation before or during the failure. The little plastic deformation results in relatively clean fracture by cleavage. In ductile fracture, there is considerable plastic deformation before and during the failure. The fracture forces are often complicated showing evidence of growth by multiple void growth and coalescence. A lot of the active pharmaceutical ingredients (API) are identified as brittle because of their

distinct anisotropic properties and the complicated micro-molecular structure, for instance, paracetamol [29] and aspirin[30].

2.3.3.1 Hooke's law

Materials can be soft and hard depending on their bulk crystal properties particularly symmetry and intermolecular interactions. An organic compound usually crystallises with a low symmetry system, for instance, monoclinic and orthorhombic, has weaker intermolecular interactions giving a soft and anisotropic materials. Under constant application of loads, materials will change in shape to accommodate the applied loads. The nature of materials response and deformation to the loads will lead to different failure mechanisms that are fundamentally described by the Hooke's law [35]. Deforming materials will undergo the elastic region up to its yield stress firstly, before entering the plastic region. In the elastic region, materials will return to its original state once removing the loads.
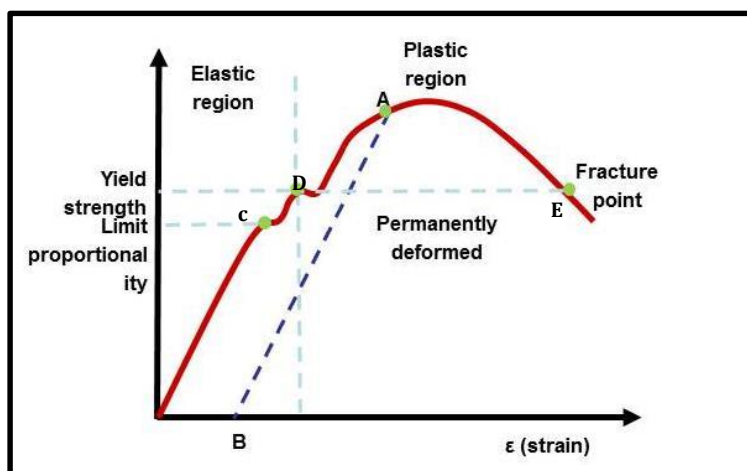
Figure 2-14 The stress and strain respond representing Hooke's law. There is linear respond of strain to stress at low stress. Maximum point at which materials will start to be permanently deformed is the yield stress [35]

The Hooke's Law describes a linear response (point C) of strain to stress up to the yield point that governs the elastic response of materials as shown in Figure 2-14. Yield stress (point D) is the stress above, which the materials will permanently plastically deform (point A), found from the stress-strain curve obtained during the tensile strength test. The negative ratio of transverse to axial strain namely, Poisson's ratio. Poisson's ratio occurs when compressing the deforming area with pressure; the solid will expand perpendicularly in the other two directions that are perpendicular to the stress.

During the displacement of an atom in an equilibrium state, forces (F) in the crystals act to reorganise the atom into its original spatial space (A) [2], this action leads to the generation of stress (σ), from within the crystal as shown in Equation 2-17. The stress generated from the forces acting upon the crystal is balanced by another deformation behaviour that is a strain (ε). The strain, in particular, changes in atom position when force is acting on the crystal. Elongation and shear process are two ideal ideas to describe strain. There can be an infinitesimal or a similar strain in a crystal that depends on the distortion of position in the system. In Equation 2-18, the basic definition for a strain is demonstrated by relating between the changes in length during deformation to the initial length of the rod.

$$\sigma = {}^F\!/_A \qquad\qquad\qquad\qquad\qquad\qquad (Equation\ 2\text{-}17)$$

$$\varepsilon = \frac{\Delta l}{l} \qquad\qquad\qquad\qquad\qquad\qquad (Equation\ 2\text{-}18)$$

From Hooke's law, materials can be divided into two groups, brittle and ductile. Brittle materials will have its total failure once it reaches the yield point, while ductile materials it will undergo permanent displacement called the plastic phase. The plastic phase is assisted by dislocation slip that was defined earlier. The slip consists of burgers vector, slip plane and line direction.

2.3.3.2 Elastic and plastic behaviour

The elasticity of crystal relates to stress and strain as mentioned by Hooke's Law with respect to the second rank tensor [24]. The basis for the elastic constant is the consideration of energy density stored resulting from homogeneous deformation. The elasticity is said to be taking place when the deformation vanishes immediately after removing the external forces. The external forces applied are directly proportional to the deformation in the proportional elastic region [23].

The elastic tensor components (C_{ij}) are the second order derivatives with respect to the strain of the wave function (ε) and normalised by the cell volume (V) as in Equation 2-19 [24].

$$C_{ij} = \frac{1}{V}\left(\frac{\partial^2 U}{\partial \varepsilon_i \partial \varepsilon_j}\right) \qquad\qquad\qquad\qquad (Equation\ 2\text{-}19)$$

The elastic tensors consist of components arranged in arrays represented as C_{11} to C_{66}. Born criteria test molecular system stability with respect to elastic components. The Born

stability [38] will depend on upon crystal systems. Take for example the criteria for tetragonal (I) molecular system that are

$$C_{11} > |C_{12}|; 2C_{13}{}^2 < C_3(C_{11} + C_{12})$$ (*Equation 2-20*)

$$C_{44} > 0; C_{66} > 0$$

while the Born stability criteria for tetragonal(II) are having an extra independent component of C_{16}

$$C_{11} > |C_{12}|; 2C_{13}{}^2 < C_{33}(C_{11} + C_{12})$$ (*Equation 2-21*)

$$C_{44} > 0; 2C_{16}{}^2(C_{11} - C_{12})$$

The elasticity indirectly represents stiffness of materials. In isotropic materials, the elastic component is Young's modulus (E) whereas for anisotropic is by six by six tensors (K). The Young's modulus represent the mechanical properties of linear elastic solid correlating the stress to strain. Hence, the elastic components of molecular crystal are represented as a tensor. The elastic component is dependent on the energy of interaction between molecules and their distance of separation.

2.3.3.3 Plastic deformation

Plastic deformation can take place in several ways, and the common ways are gliding and twinning [22]. The concept of stack faults and twinning mentioned earlier described the plastic deformation occurs by layers of atoms sliding over each other. The obvious different between slip and twinning is twinning took place in the imperfect crystal. Figure 2-15 shows the sliding occurrence at which deforming cylindrical producing steps on the surfaces. For each step formed, it will compose of many smaller steps, which result from the apparent sliding of planes of atoms over one another.
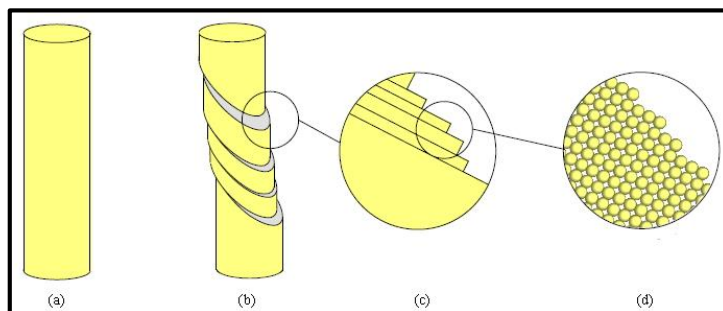
Figure 2-15 Schematic diagram showing the process for deformation by slip (Figure from [33])

Plastic deformation will lead to ductile materials. The sliding process involves three phases. Firstly, the breaking of all bonds between the neighbouring layers. Secondly, displacement of two layers and finally the formation of new bonds between layers. Bonds that formed are characterised by the crystal structure [55]. The following subsection describes the glide and climb.

2.3.3.4 Glide and climb

The movement or slip in dislocations is divided into two; conservative that is the glide and non-conservative that is the climb. For the glide dislocation to move, the Burgers vector and dislocation line must lie in the same slip plane. Dislocations that moved in this manner are known as glissile [28]. Glissile is dominant at low temperature dislocations. Commonly, slip or glide occurred tangentially to the slip plane hence preserving the inter- planar spacing between planes. Sessile is an immobilise dislocations which occurred as stacking faults taking place. The event of the climb for edge and screw dislocations can be observed in Figure 2-16.

Nonetheless, inorganic materials, intermolecular interaction influences the slip occurrence also the surface properties play a significant role for the slip to takes place. Climb take place when there is non-equilibrium vacancy defects presence at low temperature. The presence of vacancy defects makes the system concentrated with vacancies. Once at high temperature, the dislocations can move out of its slip plane. This movement is 'climb' and makes the dislocations line normal to the Burgers vector. Figure 2-16 best illustrates climb in both edge and screw dislocations. Climb movement results in the kink and jog to exist in the crystal system. The climb dislocations movement from one atomic plane to another is characterised as 'jogs' and the steps involved 'kinks'. From the above definition, glissile plays an important role at low temperature while sessile at high temperature.
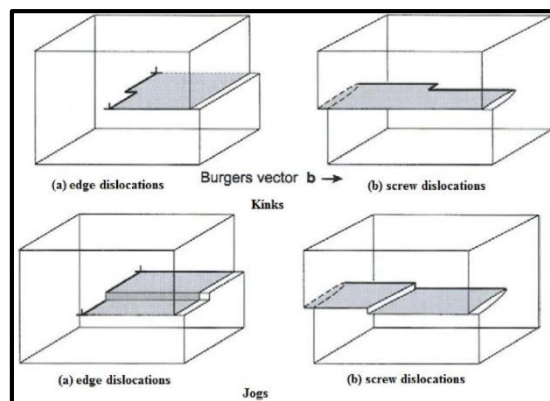
Figure 2-16 Representations of the two conditions of climb movement, showing jogs and kinks in both edge and screw dislocations (Figure from [22])

2.3.3.5 Work hardening

By having many dislocations, deformation flow is halted, causing strengthening of materials. The strengthening can occur as glissile slip when stress increases. These concentrated dislocations at the point of deformation lead to work hardening, a consequence of plastic deformation. Jogs can also occur in work hardening. The application of work hardening can be appreciated taking the example of a paper clip. It is relatively easy to bend steel wire to make the paper clip, but fracture will occur as it strengthened. During the bending, the dislocations moved towards the bending point. As the dislocations concentrated at that specific point, it will be locked, and movement is halt. The available condition to dissipate the stress is by breaking. The next subsection will describe the fracture mechanism.

2.3.4 Fracture mechanism

The fracture mechanism is described by cracks and the way it grows in solid. The strength of a crystal depends on the atomic bond strength. Fracture mechanism is related to the types of materials mechanical properties that are brittleness and ductility. In brittle solids, the fracture is caused by sharp cracks acting as stress concentrators while in ductile solids fracture; plastic deformation causes it. Besides that, fracture of forms is closely related to the yielding and breaking process. The concentrated strain resulting from the deformation promotes the formation of cleavage cracks in which breakage can occur. The bulk strength of material is related to its fracture toughness and depends on mostly upon the ductility.
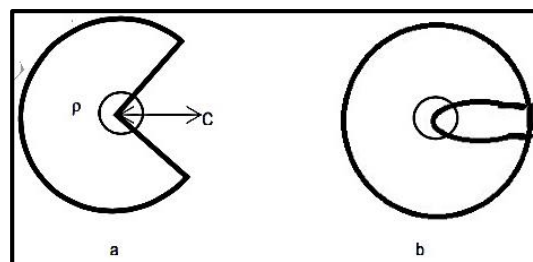
Figure 2-17 Griffith crack propagation showing a: sharp tip b: blunt tip. Sharper tip increase the stress concentration, instigate fracture to takes place at lower stress compared to the blunt tip

Commonly, brittle fracture occurs at a stress far below its theoretical maximum yield stress. A variation of stress for fracture is observed for the same set of sample used. The variation suggests that cracks in the solid act as a concentrator of any applied stress and the basis of Griffith crack model [33]. Griffith crack model (Figure 2-17) relates the crack occurrence to the length (c), of the crack and its radius at the tip of the crack (ρ) as the tip. For an applied stress σ, the maximum stress (σ_m) and the tip is given by

$$\sigma_m \approx 2\sigma \left(\frac{c}{\rho}\right)^{1/2}$$

<div align="right">(Equation 2-22)</div>

From the Equation 2-22, the sharpest crack present in the material wills influenced the occurrence of brittle fracture. Hence, the variation of maximum stress for brittle fracture is caused by the varying crack sharpness.

2.4   Crystallisation – theories and practices

Solution state is consisting two main components, solute and solvent. Crystallisation is a process of depositing of the excessive solid in solution at a supersaturated phase. The susceptibility for the solute to dissolve forming solution is the solubility.

2.4.1   Solubility of organics

Solubility is the measure of the susceptibility of solute to the solvent at a specific temperature during dissolution activity. The susceptible level covers both physical and thermodynamics considerations, notably the enthalpy of dissolution and diffusion activities. The common units to represent solubility are moles of solutes per mass (or volume) of solvent and mass of solute per mass of (or volume) of solvent [31]. Through the dissolution process, the solid-solid interaction can be broken into the formation of solute-solute or solute-solvent bonding. This breakdown, in turn, clarifies reasons for solid-solvent selection in crystallisation. The solubility is also known to represent solid saturation in the solvent or solution. The solubility is essential as this is the first step for designing the crystallisation process of solid forms APIs.

During dissolution process, the solute is to be separated from the solid and transported out into the bulk solution. This process usually occurs by diffusion. Though diffusion may take time, in many processes, it is taken as the rate-determining step. The diffusion activity adopts the same theory to when transporting drug into the systemic circulation. The dissolution begins with the solute at solid surface interacts with the solvent, creating a concentration gradient. As the concentration gradient at the surface increases, solute will slowly diffuse away from the surface moving into the bulk solution. The continuous diffusion at the surface between solute-solvent creates boundary layer, as the surface now

is concentrated with the solute. The diffusion continues until there are no solutes left therefore at equilibrium condition. This activity is illustrated in Figure 2-18.
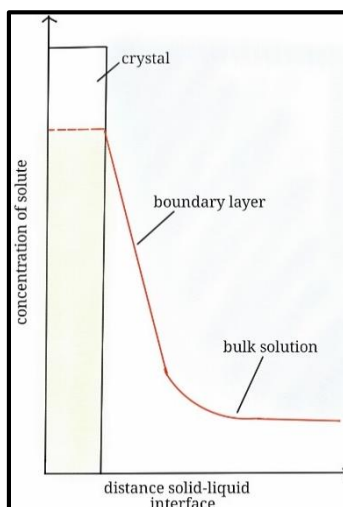
Figure 2-18 Crystal dissolution interaction in the bulk solution. The interaction of solute-solvent forms the boundary layer. As the concentration of solute in crystal decreases, the concentration of solute diffusing into the bulk solution increases

The type of solvent used affects the rates of crystallisation and crystal habit. The solvent has three categories. First is polar protic, secondly dipolar aprotic and thirdly non-polar aprotic. All of the solvents will interact actively with likely behaving solute. For instance, a polar protic solvent creates a strong hydrogen bond between the solvent molecules and readily donates hydrogen to the solute. The solubility will be higher with a protic solute as it can break the hydrogen bond between the solvent and create similar hydrogen bond strength. An example of a polar protic solvent is water, methanol and acetic acid. The solutes with hydroxyl (OH) or a carbonyl group (C=O) are potent to create a bond in the polar solvent.

A dipolar aprotic solvent undergoes dipole-dipole interactions and has a high dielectric constant. Hence, solute must be dipolar aprotic to have an effective interaction with the solvent. A non-polar solute is incapable of creating a bond with dipolar aprotic solvent making it insoluble. The protic solutes may create a strong hydrogen bond with a basic dipolar aprotic solvent. Whereas when interacts with the non-basic dipolar aprotic solvent, the hydrogen bond is replaced with weak dipole-dipole interactions. In a non-polar aprotic solvent, molecules interact through weak van der Waals bond. The solvent is having a low dielectric constant and readily soluble.

Table 2-4 Summary of different type of solvent showing different behaviour relate to the tendency for interaction with the solute. There are three types of solvents, polar, non-polar and dipolar [31]

Type	Description	Example
Polar protic	Solvent readily donates protons (H^+), creating a strong hydrogen bond	water (H-O-H), methanol (CH_3-OH), acetic acid (CH_3-C(=O)OH)
Dipolar aprotic	Solvent interacts by dipole-dipole bond between each other and create a hydrogen bond with protic solute in basic solvent	nitrobenzene ($C_6H_5NO_2$), furfural (OC_4H_3CHO)
Non-polar aprotic	Solvent-solvent interacts by weak van der Waals with a low dielectric constant. A non-polar solute is readily soluble in this type of solvent	hexane (CH_2-CH_3), benzene (C_6H_6), diethyl ether (CH_3CH_2-O-CH_2CH_3)

Besides the different behaviour of solvent-solute interactions, molecules with a different shape and sizes from the solvent will further cause distortion. The smaller the distortion, the more soluble the solute. A low molecular weight solute is more soluble than the high. Table 2-4 provides the summary of available solvent used in crystallisation. In addition to solvent and solute characteristics, other significant parameters that can influence the solubility are process temperature, particle size, environment pH also the common ion effects.

2.4.2 Supersaturation and metastable zone width

The crystallisation can only occur at the supersaturated state, which the solute is in excess and started to form small crystal clusters. These clusters will either dissociate or congregate forming nuclei. The nuclei need to achieve a critical size to grow further into crystals. The point that nuclei started to be visible is the crystallisation temperature. Crystals will grow to form a distinct habit. Stability of crystal clusters is correlated to the Gibbs free energy when the free energy is negative; crystal growth will continue.

Solubility-super solubility diagram can be used to describe the supersaturation of solution. The solubility curve is divided into three phases, the stable phase (unsaturated), metastable phase and unstable phase (labile). The supersaturation occurs at the labile phase at which crystallisation occurs spontaneously. In the metastable phase, crystallisation does not take place spontaneously, but an introduction of crystal seed will trigger crystallisation. At the unstable phase, crystallisation may not happen at all.

Crystallisation can take place in three common ways, firstly by cooling the heated saturated solution, evaporation at constant temperature and finally mix process of both evaporation and cooling. Figure 2-19 depict the phases of solution saturations. If a solution is cooled from point A across the solubility curve, it will only start to crystallise at point C and may need further cooling to be observed. If constant temperature evaporation is done, crystallisation might occur at point C' with longer crystallisation time. For mix methods, the solution temperature is lowered to point B'' before been let to vaporise to initiate crystallisation at point C''.

The metastable zone width (MSZW) is a reactive region which presence of crystal seeds or impurities quickly creates concentration gradient triggering nucleation. The width of the region is dependent on the position of the supersolubility curve. As the supersolubility is related to crystal nucleation, the MSZW than, reflects the nucleation kinetics of a system. A basic empirical relationship to represent nucleation kinetic is as Equation 2-23 with J is the nucleation rate, k_n the nucleation rate constant, and Δc_{max}^n the maximum allowable supersaturation.

$$J = k_n \Delta c_{max}^n \hspace{4cm} \textit{(Equation 2-23)}$$

$$\Delta c_{max} = \left(\frac{dc^*}{d\theta}\right) \Delta \theta_{max} \hspace{3cm} \textit{(Equation 2-24)}$$

The maximum allowable supersaturation can be related to the maximum allowable undercooling($\Delta \theta_{max}$) before nucleation as in Equation 2-24 with dc* and $d\theta$ are concentration and cooling temperature difference. There are two means for measuring MSZW,

1. Cooling to target temperature rapidly and record the time taken for the first nuclei to be visible or when the crystallisation starts. The recorded time will be shorter when the MSZW is near

2. The cooling solution with varying cooling rate. For each rate, the crystallisation (cloud) temperature is recorded. The temperature difference between the solubility (clear) and crystallisation will be the maximum undercooling temperature before nucleation occurs with respect to cooling rate
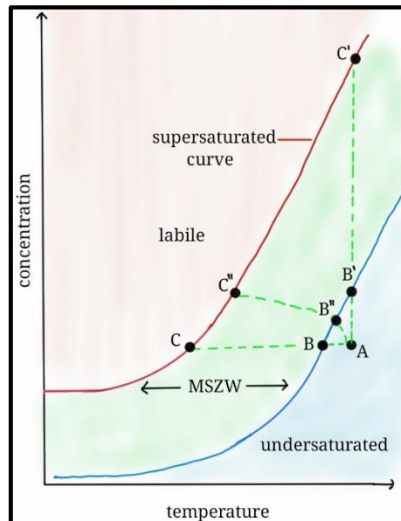
Figure 2-19 The binary solid-liquid system solubility-supersolubility diagram. Three possible crystallisation routes are highlighted. The cooling crystallisation takes place from point A moving to point C. Evaporation at constant temperature is represented by A-B'-C', showed a longer crystallisation time. The final route is A-B''-C'' with the combination of cooling and evaporation taking place together. The region in between the solubility-supersolubility is the metastable zone width [52]

The MSZW is heavily dependent on the temperature activity. The MSZW will be wider for a solution, which is heated far above the saturation temperature and kept for a certain amount of time, compared to a solution heated just above the saturation temperature. The high temperature will increase the supersolubility level. Hence, a longer time is taken for nucleation to happen results in the lower amount of crystals and longer induction time. The MSZW highlights the relationship of nucleation and growth kinetics during crystallisation of a system.

2.4.3 Crystals formation and habit

Crystallisation of a system does not only depend on supersaturation or supercooling condition, but it also needs nuclei acting as the centre of crystallisation. The occurrence of nucleation can be spontaneous or induced. Nucleation of the crystal can be divided into two categories, primary and secondary. Primary nucleation is for a system that nucleates without any solid crystalline presence in the system. Primary nucleation is further class into homogeneous or heterogeneous depending on whether it is undergoing spontaneous or induced by foreign particles nucleation. While, secondary nucleation, it occurs with an existence of crystal in the supersaturated system.

The free energy relationship best describes nucleation that is taking place during the formation of the nucleus. The diffusion of solute from the supersaturated solution to the nucleus solid phase reduces the free energy per solute. When the solute reaches the surface of the forming nucleus (clusters), the free energy increases per unit area of the clusters. Referring to Figure 2-20 the correlation between the free energy and critical nucleus radius lead either nucleation to be preferred to nucleate or growth. The preferred process will dictate the shape and size of crystals that are forming. The different saturation of crystals relates to the size and shape of the forming crystals. Forming crystal will give impact to the processing of tablet. A high supersaturation will particularly form a small size particle. If the crystals are left longer or low supersaturation, the crystal will have a bigger size.
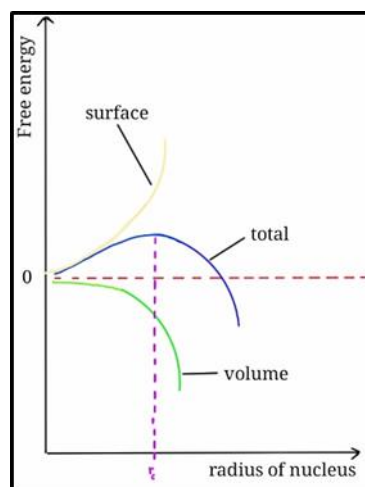
Figure 2-20 The nucleation relationship with Gibbs free energy. The yellow line shows the increasing free energy as the solute in bulk solution bound to the forming solids. The green line represents decreasing free energy and the blue line is the total free energy during the formation of nucleus

2.4.4 Crystal growth

When stable nuclei are achieved from nucleation, crystal growth will take place. Stable nuclei are the particle that has larger crystal size than the critical crystal size in the supersaturation phase. Theories of crystal growth vary from surface energy, adsorption layer, kinematic, diffusion-reaction, to birth and spread models. This study will focus particularly on the surface energy theories.

Crystal faces will grow proportionally to their respective surface energies. The free energy and faces relation can reflect the growth of the crystal. Crystal growth is inversely proportional to reticular density or lattice density. Crystal face with low reticular density will have high growth rate. Higher growth rate makes the face grows out leaving the

importance crystal faces with high reticular density. The determination of crystal growth velocity is based on the rate of outward movement in the direction perpendicular to the specific face (Figure 2-21). The interfacial angles within crystal are maintained by having parallel displacements of the face during growth or dissolution.

(a)   (b)
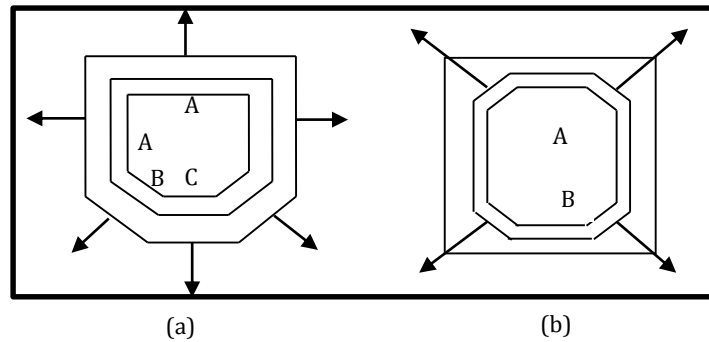
Figure 2-21 The crystal faces growth velocities, (a) invariant crystal (b) overlapping [31]

Figure 2-21 shows the ideal cases of invariant crystal that preserve its geometric pattern as it is growing. The crystal on the left has three faces that are A, B and C. A face grows at an equal rate. Faces B and C is growing slightly faster than A with C having the highest growth rate. The crystal on the right is representing the standard growth in practice; that is overlapping with the fastest growing faces dissolved. Growth and dislocations are related at the surface of the crystal. The presence of kinks as described earlier in climbs subsection will expedite the growth rate of crystal. Dislocations can occur either at growth front or post growth. Both dislocations mechanisms are related to the final condition of the crystal. The screw dislocations may lead to spiral growth. This mechanism is represented in Figure 2-22. The growth-dislocations relationship then presents one of the growth mechanism that is birth spread model.
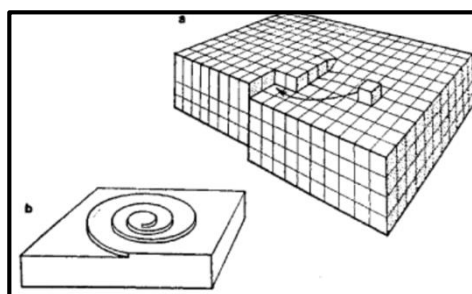
Figure 2-22 Screw dislocations showing the spiral growth toward the surface of the crystal. The presence of the dislocations expedites the kinetics of crystal growth by the presence of extra surfaces at kink [31]

2.5   Conclusions

The purpose of this chapter is to outline all the theoretical concepts for the development of a crystallographic model to analyse mechanical properties of solid forms. It is hoped that this chapter successfully showed the link between intrinsic to the extrinsic behaviour of crystal. The crystal science introduces the basic knowledge of solid-state materials. From the initial building blocks, it is explicable that the crystallographic structure of the crystal is highly structured. This theoretical concept results into a perfect crystal. Nonetheless, practically, the crystal is usually imperfect and contains defects that change the physicomechanical properties of materials.

This relation between the crystallographic structure and observed behaviour of crystal shades some light on the structure-property relationship of materials. The varying mechanical properties of materials of single crystal exhibited its effects on the bulk systems. Drawing from the fundamental knowledge, the compression and flowability properties of the bulk crystal can be predicted. Moreover, the anisotropy behaviour of organic materials is an indicator of the directionality impact towards mechanical properties. Besides the anisotropy impact of crystals, this chapter presented theoretically the consequence of having defects in the crystal that lead to ductility and brittleness of materials.

The following chapter, describe the applications of the theoretical concept mentioned here in the powder tabletting. The previous study of the mechanical properties of powder for making dosage tablet is reviewed. The review, of the previous study, set the background for the whole study. The review includes the identification of gap within the available study for understanding the mechanical properties using empirical and prediction model.

References:

[1]   Andre'Guinier, The structure of matter , 1st , Edward Arnold, 41 Bedford Square, London WC 1B 3DQ, 1984.

[2]   J. I.Gersten, F. W.Smith, The physics and Chemistry of Materials, Wiley-Interscience publication, University of Michigan, 2001.

[3]   M. Salahinejad, T.C. Le, D.A. Winkler, Capturing the crystal: prediction of enthalpy of sublimation, crystal lattice energy, and melting points of organic compounds, Journal of Chemical Information and Modeling. 53 (2013) 223–229.

[4]   C.C. Sun, Materials science tetrahedron—A useful tool for pharmaceutical research and development, Journal of Pharmaceutical Sciences. 98 (2009) 1671–1687.

[5]   C.M. Reddy, G.R. Krishna, S. Ghosh, Mechanical properties of molecular crystals— applications to crystal engineering, CrystEngComm. 12 (2010) 2296–2314.

[6]   G.R. Desiraju, Crystal engineering: from molecule to crystal, Journal of the American Chemical Society. 135 (2013) 9952–9967.

[7]   E. Bharath, S. Manjula, A. Vijaychand, In silico drug design-tool for overcoming the innovation deficit in the drug discovery process, International Journal of Pahrmacy and Pharmaceutical Sciences. 3 (2011) 8-12.

[8]   J. Bauer, S. Spanton, R. Henry, J. Quick, W. Dziki, W. Porter, et al., Ritonavir: an extraordinary example of conformational polymorphism., Pharm. Res. 18 (2001) 859–66.

[9]   D.J. Kempf, H.L. Sham, K.C. Marsh, C.A. Flentge, D. Betebenner, B.E. Green, et al., Discovery of ritonavir, a potent inhibitor of HIV protease with high oral bioavailability and clinical efficacy, Journal of Medicinal Chemistry. 41 (1998) 602–617.

[10] S.R. Chemburkar, J. Bauer, K. Deming, H. Spiwek, K. Patel, J. Morris, et al., Dealing with the impact of ritonavir polymorphs on the late stages of bulk drug process development, Organic Process Research & Development. 4 (2000) 413–417.

[11] H. Dorsett, A. White, Overview of molecular modelling and ab initio molecular orbital methods suitable for use with energetic materials, (2000).

[12] N.W.Alcock, Bonding and Structure, Ellis Horwood, Market Cross HOuse, Cooper Street, Chichester, West Sussex,PO19 1EB, England, 1990.

[13] A. R.Leach, Moelcular Modelling: Principles and Applications, Pearson Education, 2001.

[14] D. Kondrashov, Geometric theory of crystal growth, (1998).

[15] J.G. Peter Bladon, R. Hammond, Molecular modelling computational chemistry Demystified, RSC Publishing, 2012.

[16] R.C. Tolman, Consideration of the Gibbs theory of surface tension, The Journal of Chemical Physics. 16 (1948) 758–774.

[17] M.A. Lovette, A.R. Browning, D.W. Griffin, J.P. Sizemore, R.C. Snyder, M.F. Doherty, Crystal shape engineering, Industrial & Engineering Chemistry Research. 47 (2008) 9812–9833.

[18] P. Hartman, P. Bennema, The attachment energy as a habit controlling factor: I. Theoretical considerations, J. Cryst. Growth. 49 (1980) 145–156.

[19] P. Hartman, W. Perdok, On the relations between structure and morphology of crystals. I, Acta Crystallographica. 8 (1955) 49–52.

[20] W.E.H. and W.E. Parker., Symmetry in chemical bonding and structure, Merrill, Columbus, Ohio, 1974.

[21] K.M. Knowles, A.A. Kelly, Crystallography and Crystal Defects, 2nd Revised edition, John Wiley and Sons Ltd, Hoboken, United States, 2012.

[22] D. Hull, D.J. Bacon, Introduction to dislocations, Pergamon Press Oxford, 1984.

[23] J.F. Nye, Physical properties of crystals: their representation by tensors and matrices, Oxford university press, 1985.

[24] C. Kittel, Introduction to solid state physics, Wiley, 2005.

[25] P. Halfpenny, K. Roberts, J. Sherwood, Dislocations in energetic materials: I. the crystal growth and perfection of pentaerythritol tetranitrate (PETN), J. Cryst. Growth. 67 (1984) 202–212.

[26] J.L. John Price Hirth, Theory of Dislocations, Second, Krieger Publishing Company, Krieger Drive, Malabar, Florida 32950, 1982.

[27] F.R. Nabarro, M.S. Duesbery, Dislocations in solids, Elsevier, 2002.

[28] A.H. Cottrell, The mechanical properties of matter, Krieger Publishing, 1981.

[29] G. Nichols, C.S. Frampton, Physicochemical characterization of the orthorhombic polymorph of paracetamol crystallized from solution, Journal of Pharmaceutical Sciences. 87 (1998) 684–693.

[30] D. Olusanmi, K. Roberts, M. Ghadiri, Y. Ding, The breakage behaviour of Aspirin under quasi-static indentation and single particle impact loading: Effect of crystallographic anisotropy, International Journal of Pharmaceutics. (2011).

[31] J.W. Mullin, Crystallization, Butterworth-Heinemann, 2001.

[32] Space Group Operations, Available at: http://oldwww.iucr.org/iucr-top/comm/cteach/pamphlets/14/node3.html.

[33] K.J. Roberts, Pharmaceutical Product Formulation PEME 5360 Course notes, 2011.

[34] Linear Defects - Dislocations, Available at: https://www.nde-ed.org/EducationResources/CommunityCollege/Materials/Structure/linear_defects.htm.

[35] The Young Modulus (E) - The modulus of elasticity, Available at: http://www.cyberphysics.co.uk/topics/forces/young_modulus.htm.

[36] Partial Dislocations and Stacking Faults, Available at: http://www.tf.uni-kiel.de/matwis/amat/def_en/kap_5/backbone/r5_4_1.html.

[37] Vassil, Macle de trois cristaux de pyrite (2008)

[38] F. Mouhat, F.-X. Coudert, Necessary and sufficient elastic stability conditions in various crystal systems, Physical Review B. 90 (2014) 224104.

Chapter Three

Mechanical Characteristics that Influence the Tabletability of Active Ingredients (API)

This chapter describes the relation between particles, powder up to the formation of the tablet. Contents include tablet administration mechanism, a common problem faced by tabletting and available model for understanding the activity

Chapter 3   Mechanical Characteristics that Influence the Compaction of Active Ingredients (API)

3.1   Introduction

More than 50% of pharmaceutical drugs are produced as tablet or capsules [1]. The preference for a tablet is because of the less complication in term of safety and processing to meet the required efficacy of the drugs. In 2004, the United State Food and Drugs Administration (FDA) introduced the process analytical technique (PAT) for improving ways to manufacture tablet drugs by understanding the behaviour (critical quality attributes, CQA) and also by optimising the process (critical process point, CPP). The PAT is one component of a bigger initiative namely quality by design (QbD), a concept that was implemented within the pharmaceutical processing environment by FDA in 2007 [2] to ensure the sustainability of the manufacturing process. The available systematic guidelines are improving by years with more specification being added to cope with the latest manufacturing technology for the pharmaceutical companies to have better percentages of success for replicating the pre-formulated drugs.

The discovery and manufacturing of new drug entities (NDE) have a linear relation. The cost incurred in both process was staggering that requires the pharmaceutical companies and government to explore a solution to reduce it [3]. It was reported that though there was an amount of success during the pre-clinical stage half of the succeeded NDEs were not able to be replicated for manufacturing [4]. On top of that, the pressure of time for discovering the lead compound instigated the need for having an approach to speed the process. The need for having an explicit approach to ease during pre-formulation stage defined the increasing numbers of the literary amount for in-silico modelling of the pharmaceutical tablet. The growing number of in-silico studies show the advantages of cross-field knowledge, particularly, the materials science and process engineering [5,6,7]. The main concern of the in-silico modelling for tabletting is to understand the powder properties.

The powder properties influence the tabletting process which is believed to relate to the molecular behaviour of the particle [8,9]. Therefore, this chapter is attempting to provide the foundation for this study by considering literature concerning the relation

between particles to powder impact onto final tablet behaviour. The flow of this chapter is following that tablet safety and efficacy, powder functionality, particles mechanical properties and explanation for case study systems and selected methods.

3.2 Basis for drugs administration and distribution pathway

Drugs tablet consists of a combination of majorly API and excipients with formulated amount of each depends on target functionality. The formulation process is carried out in the discovery and development stage at which knowledge of physicochemical properties for the solid form is vital. The selection of solid forms is revolving around three main factors, efficacy once administered, the safety of the final tablet and processability of the formulation. In 2011, the FDA established a regulation that requires a thorough knowledge of all NDE's behaviour before going through stringent interview process [10]. The interview process is to ensure that no alteration occurs during the scale-up process which reflects the stability of NDEs by preserving the safety and efficacy. The understanding of the reason behind any changes occurrence was crucial to allow ease of designing the NDEs that meet a particular purpose. Before looking into the various tabletting process, it is best to review the APIs distribution pathway and mechanism after being consumed into the gastrointestinal tract.

3.2.1 Drugs delivery route

The route for drugs delivery to the target site, when administered into the body, varies from oral, parenteral, rectal, eye, respiratory, nasal and topical. Association of each route with the suitable type of dosage depending on the following corresponding key considerations. The key consideration for selecting the path of administration includes the properties of API's compound, the release rate of the APIs and way of distribution, whether systemic or intravenous. Commonly, drugs are administered orally, as it is convenience. The oral type of dosage can be solution, tablet, powder or capsule, but this study will highlight the properties of tablet dosage.

For the APIs to act, it needs to reach the target site(s) without being metabolised and have a fraction of concentration that meets the effective therapeutic level. This event entails transporting out and distributing the APIs from gastrointestinal fluids to the systemic circulation. Therapeutic level is the range of the effective concentration and below the onset concentration of toxicity. How can the therapeutic level be achieved in the complex human body environment? The pharmacokinetics concept best explains

the process. The pharmacokinetics explicates the APIs pathway by four stages that are *a*bsorption, *d*istribution, *m*etabolisation and *e*limination (ADME) [11]. The dissolved APIs underwent absorption through the gastrointestinal wall or membrane and transferred to the bloodstream for distribution. When APIs reach the target site(s), it is metabolised to express functionality. Finally, the APIs is eliminated from the system. After drugs administration, the ADME cycle and bioavailability concept are used to explain API's property. The preceding aspects construct the general deliberations for tablet dosage design.

3.2.2 Bioavailability of APIs

Before going further into the mechanism theory, it is best to note the means for measuring the API's dose level at the site(s) of action. The notion of the measurement meant is bioavailability. Bioavailability studies the effects of physicochemical, dosage forms and administration route towards the release rate and the extent of absorption of APIs [12]. The APIs is said to be 100% bioavailable if there is no loss of APIs when it reaches the target site(s), and achievable by intravenous administration. For tablet dosage, it is unlikely to achieve hundred percent bioavailable doses because of the pathway that it undergoes to reach the target site(s). By knowing the bioavailability, the optimum efficacy and the therapeutic level can be achieved by having the right dose and release rate capability of APIs in the formulation.

It is about balancing between the kinetics (dissolution) with that transport across cell wall and diffusion through the membrane into the bloodstream. The formulation must be able to hold the APIs before reaching the onset concentration and releasing it at an optimal rate. The description of the mechanism is as seen in Figure 3-1 showing a comparison of the absorption rate for the same dose of APIs for three different types of formulations, namely A, B and C on its concentration in blood. Formulation A has the fastest absorption rate, making the concentration in blood plasma exceed the therapeutic level and hypothetically resulting in toxic side effects. Whereas formulation B, has slow absorption rate, making it reaching the onset concentration for a fair time and maintain within the therapeutic range longer than formulation A. For formulation C, it has the slowest rate resulting in broader absorption peak. The broad peak shows that the absorbed formulation is too little to achieve the optimum onset concentration for effective APIs functionality.
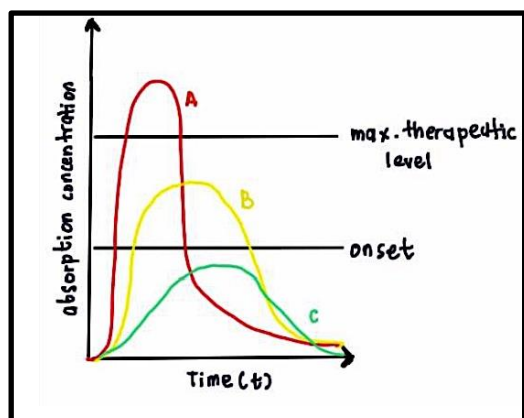
Figure 3-1 Plot showing three different formulation of the same drugs dosage. The absorption rate differs between the three formulations, with 'A' passes the safe therapeutic limit and 'C' does not reach the onset therapeutic level. This plot represents the concept of bioavailability

Once the API is dissolved in the gastrointestinal tract, it needs to be transported out. The process involves passing across the mesenteric wall and absorbed through the biological membrane into the bloodstream. The constructs of biological bilayer membrane are protein and lipid. The nature of the membrane makes it selective for the type of substances that can pass. The bilayer consists of two regions, polar (head) and non-polar hydrocarbon (tail) held intact by van der Waals bond. The polar terminal is arranged outward to expose it to the aqueous solution surrounding the cell membrane. The existence of the hydrophobic tail, facing the inner part of the cell creates a separation and compartmentalisation between aqueous regions within the body.

3.2.3 Mechanism of APIs transportation

Absorption of APIs occurs through two primary mechanisms, transcellular and paracellular. The transcellular process involves transporting the APIs across the membrane while paracellular is when APIs are moving in-between cells as shown in Figure 3-2. Transcellular mechanisms are passive or carrier mediated. Passive movement commonly occurs among small size and lipid soluble molecules and is directly related to the permeability of APIs. The Fick's law best represents the molecule diffusion of the APIs. The Fick's law Equation 3-1 state that the rate of diffusion is the difference in concentration as the driving force for movement, the area at which the diffusion is taking place and specific molecule system diffusion coefficient [63]. These parameters values must be significant enough to overcome the barrier, which is the membrane wall thickness for the diffusion to takes place.

$$\frac{dc}{dt} = \frac{DA(c_{ext} - c_{int})}{d}$$

(Equation 3-1)

where dc/dt is the rate of transfer of drug across the membrane, D is the diffusion coefficient, C_{ext} is the concentration of drug in the external membrane, C_{int} is the concentration of drug at the internal surface of the membrane, A is the area of the membrane, and d is the thickness of the membrane. The carrier-mediated mechanism involves carrier species at the membrane. The APIs will bind to the carrier making one complex, then move across the cell before being released at the other end and the carrier returns to its initial position. An active movement is when energy is supplied, and it can move against concentration while the facilitated movement will not be able to go against the concentration. The significance of knowing the tablet function after administration assists the pre-formulation stage also giving valuable information for solid forms selection to provide efficacy and safety for the tablet.
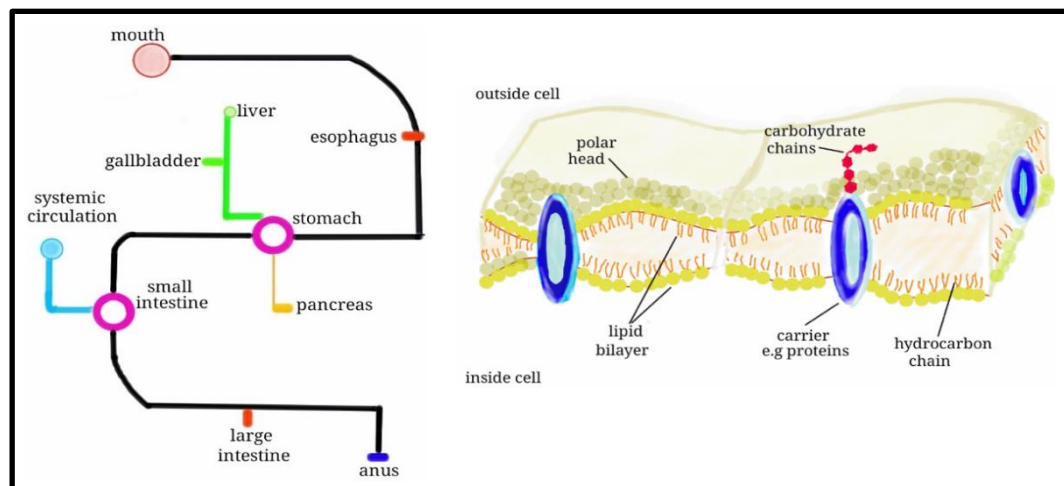
Figure 3-2 Schematic representation for gastrointestinal tract (GI) and cell membrane involve for transporting tablet dosage to the target system. The tablet is administered orally, passing through the oesophagus into the stomach before being absorbed through to the small intestine. The APIs now will transfer through to the systemic circulation. Cell membrane consists of lipid bilayer cell carrier available at the surface to assist transport from inside cell to bulk fluid

Now that the APIs distribution pathway and the mechanism have been described, the process for measuring its efficiency is simplified by having a classification system that groups the APIs based on their bioavailability performance. By understanding the behaviour of the APIs, ease for selecting the processing route suitable for the APIs can be determined.

3.2.4 BCS and MCS relationship with the materials science tetrahedron (MST)

The relationship between solid forms selection and processing factors is represented by the Biopharmaceutics Classification System (BCS) [13] and Manufacturing Classification System (MCS) [14]. The next subsection elaborates the concept adopted by the BCS and MCS and how these two classification systems help to shed some lights for the consequence of structure-property relationship onto the performance of APIs and its tabletting process. The two latter factors were shown to relate to the structure-property by the materials science tetrahedron (MST), a concept applied by the materials scientist for materials elucidation. The application of MST is now being extended by implementation within the pharmaceutical area.

3.2.4.1 Biopharmaceutics Classification System (BCS)

BCS is an approach to represent the in-vivo bioavailability relation towards the in-vitro drugs behaviour. Bioavailability of drugs has three crucial factors that govern the performance, which is permeability through gastrointestinal, solubility and dissolution rate. Referring to the three factors, the BCS describes a drug (APIs) performance by classifying it into four classes (Class 1 to 4) according to the level of permeability and solubility. APIs of class 1 have high permeability and solubility as seen in Figure 3-3, therefore, the easiest to work with in dosage formulation. For the following class 2 to 4, the level of permeability and solubility is decreasing as it moves from left to right of the table. Class 4 is the toughest to formulate as it has a poor level of permeability and solubility, hence commonly being prevented from being used in tablet formulation. An example of class 4 is furosemide and taxol.

Usually, the performance of APIs can be improved by two approaches, firstly by using suitable excipients and secondly, modification of the APIs itself. Class 1 drugs are preferred but not as many is discovered in the real industrial situation. A highly soluble drug are when the highest drugs strength is soluble in 250mL or less of aqueous media over a pH range of 1-6.8 while a high permeability is when 85% or more of an administered dose being absorbed based on a mass balance determination [13].

Class 1 - High permeability & solubility - E.g Propanolol, theophylline	Class 2 - High permeability & low solubility -E.g Carbamazepine, ketoprofen
BCS	
Class 3 -Low permeability & high solubility - E.g Atenolol, ranitidine	Class 4 - Low permeability & low solubility - E.g Furosemide, hydrochlorothiazide
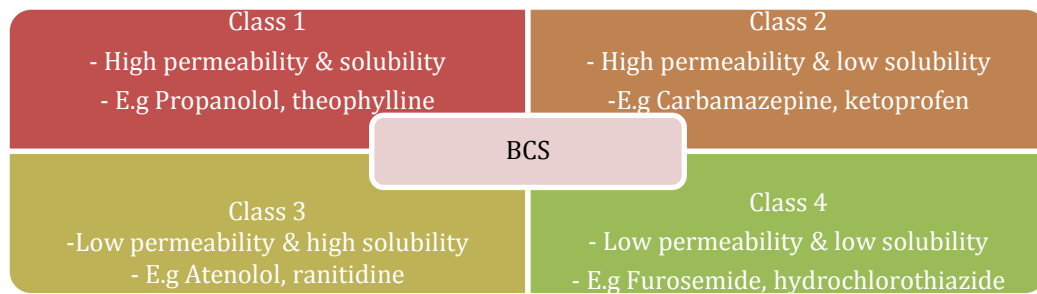
Figure 3-3 BCS matrix showing four classes of drugs based on the permeability and solubility. Class1 is the most preferred behaviour, with optimum bioavailability performance. As the classes get lower, the preferability become lesser

In class 2, the high permeability and low solubility do not create enough concentration gradient for absorption to take place. The low solubility leads to a low dissolution rate hence create a rate dependent condition. Amongst option to improve the solubility is by using a smaller particle size or selecting a higher solubility salt or metastable forms. An example includes ketoprofen, carbamazepine and mefenamic acid. For class 3, the permeability is the rate limiting factor and by having a prodrugs and permeation enhancers improve the situation. The permeation enhancers assist transportation of drugs either by transcellular or paracellular route. An example of class 3 drugs is atenolol, captopril and cimetidine. It is clear that the BCS is useful during solid forms selection. Nevertheless, the BCS does not consider properties beyond permeability and solubility, for instance, mechanical property, morphology and other particle's physical properties that are affecting the choice of tabletting process [15,16]. Therefore, a classification that relates to various tabletting process is useful to help during API's selection to fit selected tabletting route, the Manufacturing Classification System (MCS) can provide this.

3.2.4.2 The Manufacturing Classification System (MCS)

The MCS is a concept proposed based on discussions by focus group involve in the Academy of Pharmaceutical Sciences (APS) to relate the materials science with the manufacturing. If BCS have the permeability and solubility to class the APIs, the MCS uses mainly physical properties that are desired by the three main tabletting routes [14]. The three most important tabletting routes are direct compression (DC), dry granulation (DG) and wet granulation (WG). Referring to Figure 1.1 in chapter 1, DC has the shortest processing route with least unit operation which requires powder to have good flowability and compactibility that's hard to achieve with poor behaving

APIs. As mentioned in chapter one, DC has always been the preferred processing route if the demanding powder properties can be satisfied [17-18].

By having the MCS, the structure of property relationship can be obtained which leads to better understanding of API's behaviour when undergoing respective tabletting process. Both BCS and MCS link between the formulators, materials scientists and process engineers, therefore, improve the process and production from small-scale to large-scale [19]. From the information and data obtained from the classification, development of the best method can be done to the highest standard. Moreover, it can reduce the possibility of out of specification products.

From Figure 3-4, clearly, that BCS is the base classification that separates APIs according to their molecular behaviour. From the BCS separation, the performance of the APIs is well perceived during tabletting process, which was given by the MCS. From BCS and MCS standards, it is observed that structure-property have an impact on the performance and tabletting process. Both BCS and MCS are enclosed within the concept of Materials Science Tetrahedron (MST), a scientific framework for designing and development of new drug products. By now, it is evident that there are four core factors in drugs design and development, namely, structure, property, performance and process. There has been a continuous study to understand better the raw materials for used in the three common tabletting process [20-22].
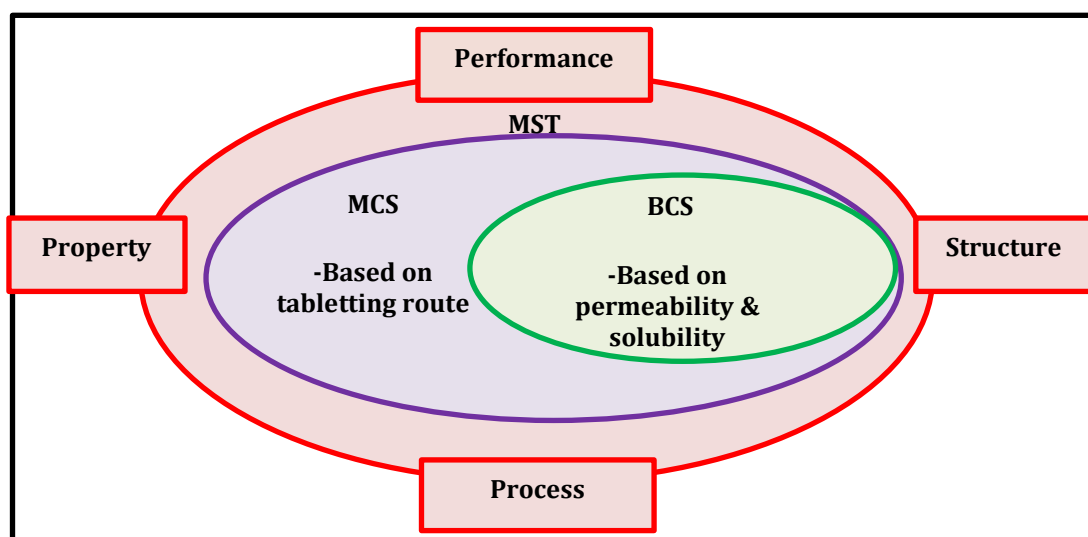
Figure 3-4 Relation between the BCS-MCS to bigger concept of MST. BCS relate to the structure-property relationship while the MCS represent the specific tabletting process. The inter-dependent of each factors assist to improve drugs production

It has been established that interplay between solid forms structure and property affects the final performance of drugs also a selection of optimum tabletting route. Moreover, the tablet strength can directly be correlated to the powder behaviour, for instance, particle size and shape, strength, bonding mechanism and porosity [23-24]. Powder behaviour is posing an impact on the compactibility, compressibility and tabletability [25]. Therefore, powder characterisation is essential for maintaining tablet quality and performance. In the following subsection, key characteristics of powder to form tablet are discussed together with available empirical and prediction model for powder tabletting.

3.3   Principal of powder characteristics for tablet formation

Definition of powder is particles amassing together through interparticle interaction, particularly adhesive and cohesive forces. The interaction between identical particles is regarded as cohesive while different particles as adhesive [24]. By now, it is clear that drugs formulation consists of multicomponent, and it is a challenge to ensure the homogeneity to get an optimum efficacy and prevent out of specification tablet. In this instances, prior knowledge of powder properties is useful. Two essential powder properties were further defined, namely, flow process and compaction. It was selected based on the critical powder properties needed for direct compression to take place.

3.3.1   Flow process of powder

Mixing of powder APIs plays a crucial role, especially in DC process that requires a good powder flow. Physical properties that effect APIs flowability are particle size and shape, moisture [26] and temperature [27- 30]. The API is categorised as good flowing when flows easily by gravitational force without needing of applied stress. In contrast, a bad flowing API will consolidate while in storage and is easily accumulated and causes obstruction in hoppers or silos. The interparticle forces taking place is differing according to the type of powder APIs, for instance, for the dry condition as in DC, the van der Waals is the principal interactions, while in wet granules, the hydrogen bonding created between the moisture towards the particle is dominating. The adhesive and cohesive forces may lead to time consolidation (caking) [31], condition at which powder APIs gained strength when at rest and under compressive stress at a certain length of time. Time consolidation reduces API's powder flow [32].

3.3.1.1 Method for flow measurement

The unconfined yield strength (σ_c/f_c) also known as compressive strength, the force needed to break specimen based on uniaxial compression test, predominantly represents the measurement of flowability. Uniaxial compression test best describes the primary concept for flow measurement. Flow is simply a measure of plastic deformation or when compact starts failing. Illustration of the uniaxial compression test as in Figure 3-5, whereby the powder is filled into a hollow cylinder that is assumed to be frictionless with regards to cylinder wall (Figure 3-5 (a)) with a cross-sectional area, A. Stress employed to fill the powder is the consolidation stress (σ_1). The untapped powder density is the bulk density (ρ_b).
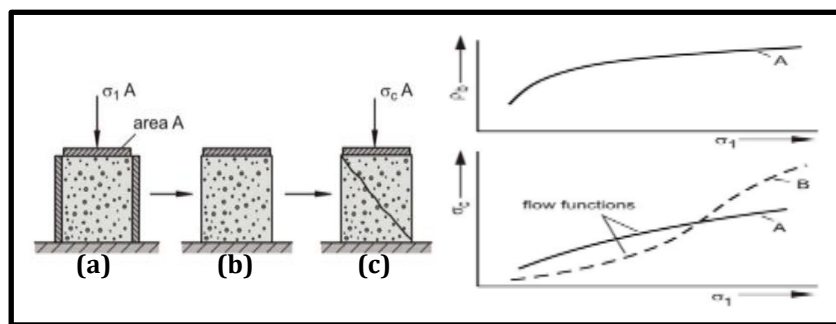
Figure 3-5 Uniaxial compression test showing cylinder filled with powder at three condition, a: confined with consolidation stress (σ_1) applied b: unconfined c: unconfined with continuous compressive stress (f_c) applied [32]. Plot represents the bulk density (ρ_b) and unconfined yield strength (σ_c) increasing with consolidation stress (σ_1) following A and hardly the progressive slope(B) is observed

It was observed in Figure 3-5 that the unconfined yield strength (σ_c/f_c) and bulk density(ρ_b) frequently will be directly proportional to the increasing consolidation stress (σ_1). The volume of powder consolidation is directly proportional to the bulk density and concurrently reflects the compressibility of powder. Applying further vertical stress after removing the wall of the cylinder (Figure 3-5(b-c)), makes the specimen start failing (break) which indicates that flow starts to take place (incipient flow). The flow occurs as the distance between particles are increasing, therefore, dilate the density. However, the uniaxial approach has some shortcomings when dealing with cohesive and fine powder APIs, that are, plausible to have too low unconfined pressure and also the timely manner to get a frictionless condition. Thus, measurement using shear stress is proposed initially by Jenike et.al in 1964 [33] and later by Schulze et.al. [32] with ring shear tester. Shear tester works by measuring yield locus at "shear to failure" point.

3.3.1.2 Ring shear tester

In comparison to the uniaxial test, the shearing tester has two main phase, the preshear, at which the powder consolidates until it achieves constant state flow and the "shear to failure" point as described in Figure 3-6. Powder loading in the normal stress direction (vertical) (σ_{pre}) generates shear stress (τ). Shear stress (τ) increase proportionally with time until it reaches constant condition, preshear. Under this condition, further, shearing will not change the normal shear, shear stress and bulk density. Shear stress at this point is the preshear stress (τ_{pre}) and powder are described as consolidated. If the consolidated powder was shear (σ_{sh}) at a pressure lower than preshear (σ_{pre}) the powder will start to dilate the density, promote shear resistance hence decrease the shear stress (σ_{sh}). The maximum shear stress signifies the failure point (incipient flow). Flow occurring at constant condition is steady-state flow.
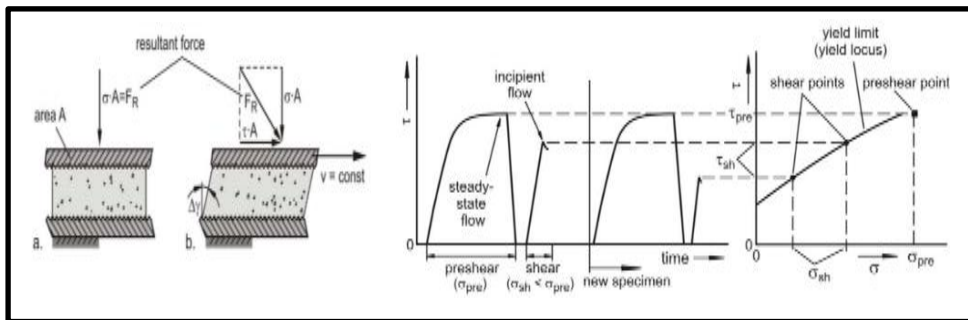
Figure 3-6 Figure (a) and (b) are the shearing tester showing the initial condition before shearing and after shearing at Ϋ angle. FR is resultant force between shear stress and normal stress and v is velocity. (Figure taken from [32]). The plot showed the two main phase for ring-shear test

The difference between Jenike shear test and Schulze ring shear test is the latter run measurement continuously without needing to load a new sample. Continuous measurement then reduces the human-error factor. Representation of the numerical flow boundaries is the ratio between consolidation stress (σ_1) to the yield strength or locus (σ_c/f_c) as in Equation 3-2. Powder flow gets better as the *ff$_c$* values increases. The powder flow boundaries as acquired by Jenike [34] is presented in Figure 3-7 below. The cohesive powder will have *ff$_c$* below one while free-flowing is above ten.

$$ff_c = {}^{\sigma_1}\!/\!_{\sigma_c} \qquad\qquad\qquad\qquad \textit{(Equation 3-2)}$$
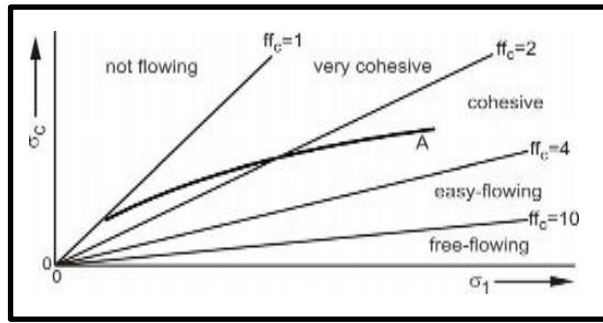
Figure 3-7 Flow index according to Jenike's. As the *ff*_{*c*} increases, the flowability increases [32]

3.3.2 Tabletability of APIs and blends

The tabletability is powder APIs and blend ease and ability to form tablet through compaction. The tabletability may be described through two principal component, compactibility and compressibility [36]. The compactibility is the ability of the powder to withstand stress where the strength is gathered through the interparticle interactions. The strength of powder properties is similar to that impacting the flow, by the neighbouring particulates behaviour [35]. While the compressibility is the ability of the powder to withstand stress about volume reduction hence relate to the total surface area available during compaction.

The interparticle interactions are structure dependent, that is, following the exposed functional groups at the surface which are ready to create bonds. Commonly, the interactions are constant, leaving the surface area solely to determine the compressibility of powder. Both the type of interactions and surface area of interactions are taken as the primary factors affecting during compaction [23]. However, it is difficult to monitor both of these factors experimentally. Therefore, the secondary factors, consisting of mainly the physical properties of the powder, namely, particle size, shape, surface roughness and volume reduction mechanisms become the obvious choice to monitor compaction [27]. Here, the relationship between the interparticle interactions at the surface with the compaction performance showed the micro (particles) behaviour can surely impact the macro (powder).
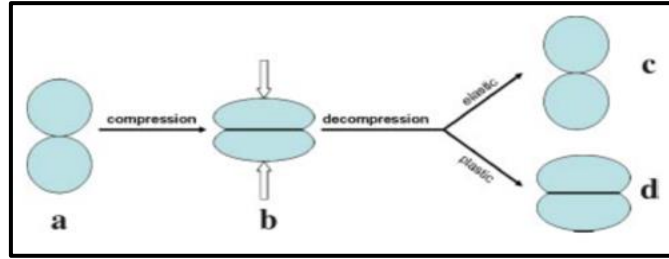
Figure 3-8 Powder activities during and after compaction. Post compaction, particle may return to original form or retain the final form depending on its strength. If elastic recovery takes place, the particle will reduce the surface area and conversely for plastic deforming powder, large contact area is maintained (Figure from [36])

Nystrom (1993) summarised the compaction activities into five stages. Firstly, rearrangement of the particle to fill in vacant space in the tablet die. Secondly, as space become limited, particle undergoes elastic deformation. Thirdly, subsequent compression stress leads to plastic deformation. Next, fragmentation occurs and provide more surface area. Lastly, the fragmented particle with exposed surface area will form inter-particulate bonds. Post compaction, the tablet can either return to original form (elastic) or permanently deformed (plastic). Permanently deformed powder will retain its final state and provide a large surface area as seen in Figure 3-8. Consequently, the strength of tablet can be measured directly by tensile strength gained during compression.

3.3.3 Tensile strength

The tensile strength is representing a mechanical property of tablet. The extent of tensile strength when compressed demonstrates the tabletability of powder. The apparent contribution of bonding strength and surface area to the degree of tensile strength thus justify the needs to differentiate the two. Representation than can be achieved through the resulting powder compressibility and compactibility concept. The compressibility is representing powder ability to reduce in volume on compression pressure while the compactibility is related to volume reduction with regards to tensile strength [20]. The amount of volume reduction demonstrates the porosity of powder. Many drugs powder is viscoelastic demonstrating mechanical property at two extreme, perfectly elastic or perfectly plastic [36-37].

Both powder flowability and tabletability exhibits prominent characteristics for tablet formation. The formation of the tablet is suggested to relate the particle to powder properties. The dependent of flowability and tabletability performance to the type of

powder creates various complications during tabletting [38]. Now that the theoretical factors have been described, complications that are arising from poor behaving powder APIs or blends will be discussed.

3.3.4   Problems encountered during tabletting

The common tabletting problems faced are sticking, picking, capping, and lamination. The problems can be seen on both pure APIs and blends tablet. The root cause can be process parameters or particles property. The major problem faced during tabletting is sticking. Sticking is when powder attaches themselves to the punch surface over time causing weight variation. Causes for sticking are unsuitable punch speed, or the powder itself has weak tensile strength. Mullarney (2011), studied the sticking tendency of ibuprofen and mannitol onto punch surface to relate with the structure-property of both cases. As expected, ibuprofen which is known to be brittle [39] was adhering to the punch surface over time and when the composition is more in the formulation. On the contrary, mannitol that is ductile [27] was showing less sticking propensity at the same test condition as ibuprofen. From this study, an insight of dependency between structure-property to sticking propensity was acquired.

Similar to sticking, picking is when the powder sticks to the embossing of punch. The best way to solve picking is by altering the letters embossed on the punch surface. It can be seen that the problem arising during the tabletting is interdependent with flowability and compressibility of powder.

Another prevalent problem is capping. Capping is when the top cap of table detaches after decompression. Capping is a problem instigated by air entrapment though some say the cause is by insufficient compression force and high elastic energy [40]. Paracetamol is a well-known compound with capping tendency [41]. Capping incidence was shown to be worse as the punch speed increases [40] in Paracetamol. The latter was identified related to elastic recovery.

Inferring from the common problems faced in tabletting, the impact of the interplay between the four core factors namely, structure, property, performance and process is well-defined. However, the underlying cause of the APIs or excipients having distinctive deformation behaviour is not evident. The indistinctive deformation behaviour, urge the need to have a way to link the bulk powder behaviour observed to the individual mechanical properties. The available experimental powder mechanical

properties measurements for example compaction and ring shear tester only define the bulk mechanical properties. Besides, it is the requirement of the FDA as described at earlier section 3.1 that in complying with the QbD concept, there is a need to explicate the property of drugs being formulated inspecting from molecular to bulk.

Referring to Figure 1-2 in the introduction chapter, possible approach to study tabletting properties can be categorised into experimental and computational based. Numerous theoretical models have been developed to link the powder APIs and blends behaviour impact onto compaction hence tackle the tabletting problem. The next subsection will describe the available model to relate the structure, property, process and performance of powder APIs and blends.

3.3.5 Available model for elucidation of the mechanical properties of tablet

Thus far, categories for a possible model for understanding mechanical properties are process-based, instrument-based and interparticle-based. These models are elaborated further in the subsequent subsections.

3.3.5.1 Process-based model

Process-based model is mainly to describe the mechanism at every stage of compaction process, i.e., from the start of the process up to the ejection of the tablet [42]. In particular, these models are looking into interparticles interaction, particles strength and adhesion-cohesion forces (particles-particles or particles-die wall). Another aspect that is explored by these models is the consolidation parameters during compaction [24, 31] that is porosity, density and void ratio. An example of known models are Kawakita model [29], Heckel model as mentioned by Yap et.al (2008) [43] that adapts the Heckel et.al. [44] and Walkers model [45], presented in Table 3-1. The models mentioned above have something in common, that is, trying to predict the deformation via strength properties of tablet specifically stress-strain, elastic, fracture mechanism and bonding interactions.

However, all these models suffer from the same weaknesses that all the models are evaluated by ignoring the possibility of the thermal interaction during friction [46], time-dependent deformation [47] and surface interaction during the compaction [48]. During the compaction, the true form of bonding formed between particles that relate

to surface area between the particles. The surface can be used as a measure reflecting roughness which in short may affect the bonding interaction.

For instance, the thermal interaction during compression, might have been occurring in two ways, die wall-powder (adhesion) or powder-powder (cohesion) interaction itself. A possible outcome resulting from the thermal changes in the thermodynamic behaviour of the particles that might impact the shapes and sizes of the particles. Furthermore, the heat created by the friction may lead to an increase of moisture in the system. The models might have been more accurate if they had considered thermal, surface and time-dependent interaction which then extends the model by including roughness, one of the important parameters to characterize mechanical properties of the tablet.

Table 3-1 List of available process-based model for understanding the powder compaction process

Name of model	Model	Description
Heckel (1961)	$\ln\frac{1}{e} = \ln\frac{1}{e_f} + K\sigma$ e=bed porosity, K= Heckel parameter, σ= stress 1/K=mean yield	Direct dependency between the bulk powder and pressure applied
Kawakita & Ludde (1971)	$\frac{\sigma}{\varepsilon} = \frac{1}{ab} + \frac{\sigma}{a}$ ε=degree of volume reduction, $\frac{h_1-h_0}{h_1}$ that is equal to uniaxial strain a=initial bed voidage	Showing relation for volume reduction when stress is applied. This model is suitable for soft powders and less generic. Kawakita – Heckel is correlated by:
Correlation Kawakita to Heckle	b=failure stress $$\ln\frac{1}{e} = \ln\frac{1}{e_f} + b(1-e_i)\sigma$$ $$\therefore \ b(1-e_i) = K$$	$$b(1-e_i) = K$$
Walker (1923)	$\log\sigma = -L\left(V'/V\right) + C_1$ σ= stress, L= pressing modulus, V_0= volume at zero modulus C= constant	Volume reduction is proportional to pressure applied
Gene Expression Programming (GEP) (2012)	Model is based on the extension of genetic programming with the compliment of mathematical process	Sets of attributes related to direct compression were tested to create a design space for prediction

In more recent study, a model has been suggested by Mariana Landin et.al [49], which inculcates the gene expression programming (GEP) to model the effect of four variables namely, diluent variations, drug type and composition and finally maximum compression force onto direct compression formulations. Interestingly, the model adopts genotype and phenotype concept in the algorithm. In this model, genotype is the structure responsible for a particular observed behaviour particularly drug type and compositions. The phenotype is the observed behaviour in this instance the compression properties. GEP matches several data sets of excipients to list of variables to develop a design space for the formulation. The model shows a faster screening process compared to the conventional statistical method and helpful in establishing the relationship of the multiple variables. Nevertheless, the current GEP model considers only a single excipient data set for the test. The model would have been far more universal if a multiple input (structures) data set were analysed and not only a single set of data.

3.3.5.2 Instrument-based model

The instrumentation-based model is looking into improving tabletting performance by focusing on the tablet machines or newly improved technology. As an example, in quantifying and evaluating sticking tendency, Nakamura et.al [50] developed a novel tablet machine that only uses a small amount of sample, while Mullarney et.al [51] designed tablet tooling with the ability to remove the tip to assess the amount of adhered powder. Likewise, Mc Dermott et.al (2011) [52] attained a material-sparing protocol for sticking analysis while Stephens et.al (2012)[53] suggested a real-time monitoring compaction process. Akseli et.al (2012) [41] proposed a model by using ultrasonic measurement for predicting tablet capping. These five studies that applied different approaches have successfully obtained a relationship that described the compression process better. The instrumentation-based models are not as robust in term of the applicability as mainly the development is to cater a particular problem, i.e., capping, sticking or quantity of powder used.

3.3.5.3 Interparticle-based model

Finally, the interparticle-based model is focusing on understanding the primary compaction factor (as defined earlier in subsection 3.3.2) that are interaction created as well as the surface area involved during particles coalition [23]. In assessing the surface area involved in interparticle bonding, Hiestand et.al (1985) [54] assumed that the surface involves the bonding is spherical curvature. From here, some contact

points per unit area are taken as the number deduced from the multiplication of particle size, hardness values and the solid fraction. Based on the same approach, bonding index is identified. Additionally, observation of interparticle interaction also can be achieved by tablet indices namely brittle-fracture index and multi-compression cycle [24]. An investigation by Gharabeh and Iba'a (2011) [55], reported the detection of forces exerted on the punch surface during decompression of APIs. The forces are believed to originate from the high elastic energy trapped in the APIs from the earlier compaction of the tablet. Indirectly, the high elastic energy showed the interparticle interaction involves during tabletting.

Correspondingly, it was shown that plastic materials are improving the compaction behaviour of tablet effectively up to a certain amount of composition in the formulation. Composition beyond the limit will weaken the tablet strength [56]. It is interesting to understand the underlying factors behind the observation by correlating the powder to single particle properties.

Collectively all available models outline a critical role of powder properties to the tablet compaction performance, particularly elastic-plastic behaviour. However, the nature of each theoretical model, which is developed through powder study, therefore make it directly dependent on powder properties for instance shape and size. This dependency stimulates variation between powder batches of same APIs or blends tested. This then pinpoint needs to have model that is tailored to the APIs or excipients itself and eliminate the variation of powder shape and size. The crystal engineering can assist the development of the fit to purpose model.

3.4 Particle mechanical properties impact on deformation

In recent years, crystal engineering has become the interest of many for designing better APIs mechanical properties by having polymorphs, co-crystals, salts and hydrates [57–60]. Crystal engineering is looking into intermolecular interaction from the crystal packing perspective to fit specific processing purposes. The process involves the relationship between chemistry and crystallography of solid forms [61-62]. The crystal engineering exploits the mechanical behaviour of the formulation and integrates it during the tailoring of the formulation to fit certain processing route, such as direct compression.

The understanding of individual components behaviour is necessary for the rational development of new formulations. Characterisation of particulates can be used to guide development towards an optimum formulation, but the process relies extensively on trial and error. One obvious reason is that prior understanding of individual formulation property's contribution towards the observed behaviour is limited [35]. By studying crystallographic and molecular properties of structure the relationship between powders to single particle mechanical properties can be achieved. Effectively, modelling the crystallographic and molecular properties of APIs and excipients will fill in the gap posed by the available theoretical model.

3.4.1   Solid forms for direct compression

Many APIs are identified as brittle because of their obvious anisotropic properties and the complicated micro-molecular structure, for instance, paracetamol [63] and aspirin[64]. There have been quite some studies at the molecular level emphasizing on the structure-property relationship. The tests focus on several attributes which are crystal geometry[65], slip system availability and molecules arrangement within the structure crystal [27,66-67]. These tests are carried out by micro/nano-indentation compaction and also by qualitative analysis of the crystallographic structure.

3.4.1.1   Crystallographic packing evaluation

By studying the crystal packing pattern, the mechanical properties of the crystal are namely bending, shearing and brittle can be anticipated. This correlation is presented in Figure 3-9 showing the three polymorphs of 6-Chloro-2,4-dinitroaniline that have three distinct mechanical properties that are depending on the pattern of crystal packing. A flat layered packing pattern with strong in-plane interaction tends to shear while herringbone pattern with directed interactions between structures will bend. Finally, a structure with interlock positions with interactions formed between the layers will be brittle. The case of 6-Chloro-2,4-dinitroaniline polymorphs makes up part of the many studies that looks into crystal packing pattern [68,69,70,71]. However, much of the research looking into crystallographic pattern up to now has been qualitative in nature which creates needs to have a quantitative model to interpret the relation between crystallographic patterns to the observed mechanical properties.
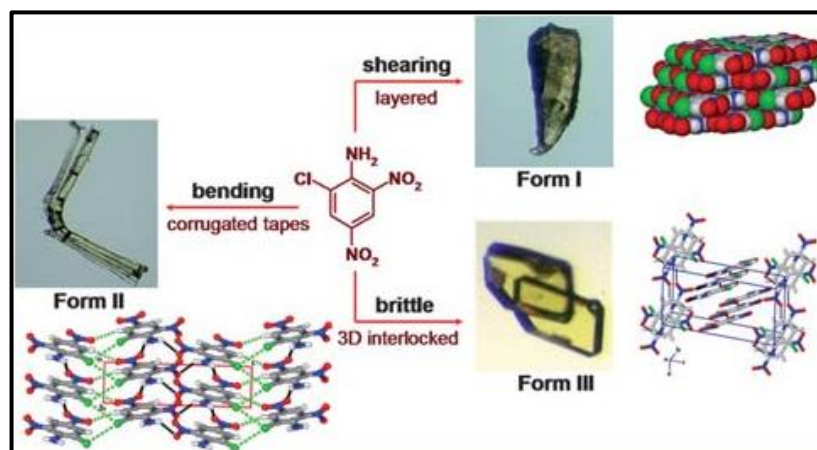
Figure 3-9 Crystal packing of three polymorphs of 6-Chloro-2, 4-dinitroaniline. All three polymorphs are having different crystal packing pattern that correspond to the observed mechanical properties, namely brittle, bending and shearing (Figures from [76] adapted from [97][98])

In one study done by Andre et.al [72], on the discoveries of the new crystal, changes of pharmacokinetics and physical properties were observed between different crystal forms. The assessment was conducted based on the crystallographic packing of each crystal by analysing the synthons created, pH contributions and supramolecular arrangements of the crystal. The crystal packing was highlighted to contribute to the better behaviour of the newly discovered crystal (Figure 3-10). Synthons are the intermolecular interactions which can be conventional molecular synthons and supramolecular synthons [73]. The newly formed crystal was also seen to show better stability.
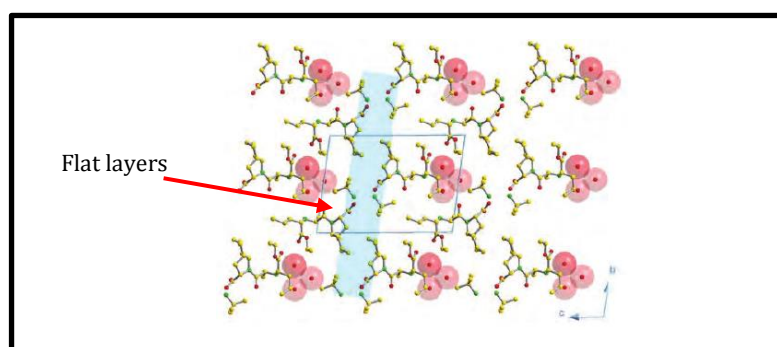
Figure 3-10 Hydrated form of novel perindopril erbumine (1:1:1.25). The crystal packing was shown to be flat layers (Figure taken from [72])

3.4.1.2 Different solid forms

In another study of Andre et.al (2012) paracetamol, a well-known crystal structure, has been used as the case study to understand further the capping and laminating issues during compression. The investigation involves the creation of prospective paracetamol co-crystal in tackling the capping, laminating and other mechanical

weaknesses found in paracetamol. The results from both studies highlight the newly formed crystal, behaving differently from the original form either with improved properties or resulting in an entirely different functionality of the crystal. Figure 3-11 shows the synthons interactions that contribute to the stability and better mechanical behaviour of the newly formed crystal.
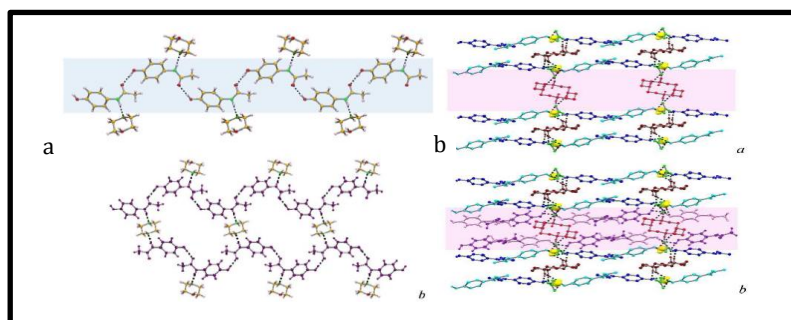
Figure 3-11 (a) Paracetamol morpholine co-crystal with the packing arrangement resembles paracetamol Form II, paracetamol is in blue (b) Paracetamol cyclam co-crystal with a supramolecular synthons interaction (Figure taken from [99])

An additional example is the p-hydrobenzoic acid monohydrate (HM) /anhydrate (HA) that have different tabletting properties (Figure 3-12) [74]. The HM demonstrates better compression properties compared to the HA form because of the availability of water molecules in between the corrugated molecular structures. By spacing the layers, the water molecule can prevent interlocking of the molecule and hence create a smooth surface for a slip to occur. It shows a 'spring-like' behaviour, in between the layer creating space to promote displacement during compression. Likewise, having a bigger interplanar d-spacing has been shown to result in easier slip deformation [75].
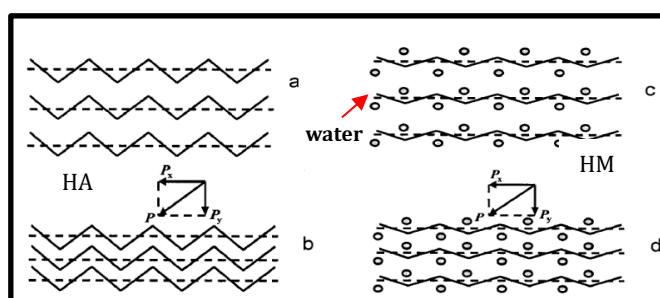
Figure 3-12 P-hydroxybenzoic acid anhydrate (HA) monohydrate (HM) showing with similar crystallographic packing pattern i.e herring-bone. The availability of water molecule cushioned ('spring-like') the molecules from interlock between layers when under pressure (Figure taken from [74])

Similarly, polymorphic forms of paracetamol, carbamazepine, sulfamerazine and paraben demonstrate different mechanical behaviour through either fragmentation or plasticity when undergoing compaction tests. These outcomes were related to the distinct molecular arrangements of materials also the intrinsic properties such as hydrogen bonding. The diverse macro-properties exhibited by materials too can be described through an analysis of intermolecular interactions in materials. The diverse type of intermolecular interactions including weak π-π bond or stronger hydrogen bond revealed to be acting like a buffer range to give flexibility for a molecule to shift when under pressure [67-68,76].

3.4.1.3 Slip systems availability

A molecular model for materials undergoing plastic deformation suggest that deformation occurred as layered-like, where the atoms slide over each other. The sliding between atoms involves breaking and creating of van der Waals and hydrogen bonds between molecules of materials which require enough energy to drive the movement, breaking and creating bonds. The crystal structure information of the materials provides the computation of energy for the displacement. The information includes the number, strength and type of bonds constructing the crystals.

Slip systems availability causes the slipping movement. The theoretical definition for slip systems is in subsection 2.3.2. Shariare et.al (2011) suggests the relationship between interplanar spacing (d_{hkl}), slip system energies to be the first order indicator to elucidate the mechanical properties of crystal [75]. In the study, three different approaches were tested for slip plane identification. The three approaches were, BFDH, attachment and surface energies. The largest interplanar d-spacing is plotted against the Brittleness Index 1[77] and brittle-ductile transition size. It was observed that, as the d-spacing gets larger, the weaker the interaction between adjacent planes will be, therefore promoting slip to occur. Nevertheless, he pointed out that the model is not applicable for predicting corrugated crystallographic pattern, because of the direction used by the model in perpendicular as represented in Figure 3-13.
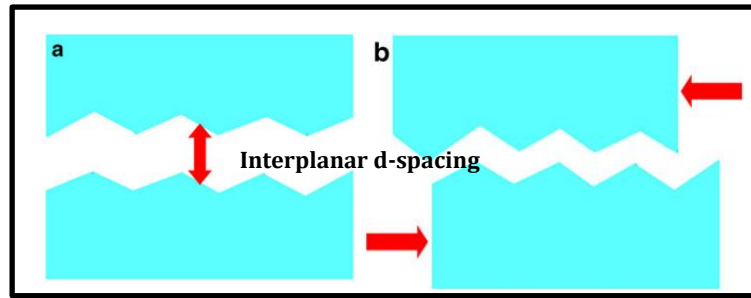
Figure 3-13 The representations of a) detachment energy b) energy barrier to lateral displacement showing the different direction between the two. The energy barrier displacement is representing corrugated structure, whereby the interplanar d-spacing prediction is slightly inexact (Figure from [75])

Similarly, Wildfong et.al (2006) [46] has conducted another prominent study for modelling the slip behaviour in seven pharmaceuticals compounds. In the study, the critical dislocation model (Equation 3-1) which considers deviations in fine-energy necessary for incorporating a critical dislocation density was adapted. The basis for his study is a complete disorder state is achieved after undergoing high shear milling.

$$\Delta G_d \approx \rho_d M_v \frac{b^2 \mu_s}{4\pi} \ln \left| \frac{2(\rho_d)^{-1/2}}{b} \right|$$ (*Equation 3-1*)

where ρ_d is dislocation density, M_v is molar volume, ΔG_d is free energy with incorporated specific density of dislocations, b is Burgers vector and μ_s is elastic shear modulus. The equation is altered to cater for the anisotropic properties of molecular crystal.

Instead of plainly having Burgers vector as it is, it will consider the steric hindrance of molecular structure. Additionally, the identification of preferred Burgers vector is based on probable slip plane. The likely slip plane was identified based on attachment energy calculations. The study that was done by Wildfong et.al (2006) is much molecular specific structure by considering the dislocation occurrence for its Burgers vector identification. Even so, for both proposed model (Shariare et.al and Wildfong et.al) the characterisation of the potential slip planes require a further inspection to quantify its surface roughness also an intermolecular interactions influence.

The reason is by selecting slip plane based on attachment energy solely will discriminate the influence of the crystallographic packing pattern that potentially may be corrugated. Corrugated crystallographic packing may interlock under force and halt slip displacements. Besides that, the models were partly incorporating compaction

measurements. The available studies are yet to have a best practice for identifying slip systems with regards to crystallographic structure. A study by Olusanmi et.al [64], a set of features for predicting the mechanical properties of the anisotropic crystal, was put forward. These features are summarised as follow:

i. Highly anisotropic molecular structure leads to the complex shape with low symmetry

ii. Intermolecular forces relate to the hardness of materials

iii. Potential slip planes are one with low surface energy and rugosity

iv. Low availability of slip system restricts the plastic deformation

v. Fracture behaviour, brittle, semi-brittle or cleavage is resulting from activation energies, rugosity and surface energy

The study qualitatively evaluates the crystal packing to identify potential slip planes and taken the shortest unit cell parameter to be the direction of preferred Burger's vector. By linking all desirable features for characterising mechanical deformation of crystal, a prediction table is acquired (Table 3-2). The observed slip systems were agreeing well with the quasi-static indentation analysis of Aspirin.

Table 3-2 Plastic deformation prediction table outlining the important parameters in the study (Table from [5])

$(h\,k\,l)$	Surface[a] Energy (mJ/mm^2)	Slip plane rugosity	Interlocking of slip planes?	Slip system with $b=[0\,1\,0]$	Slip involving hydrogen bond breaking	Surface cleavage likely?	Plastic deformation likely?
$(1\,0\,0)$	$(0.0829$	Very low	N	Y	N	Y	Y
$(0\,0\,1)$	$(0.0904$	Low	N	Y	N	Y	Y
$(0\,1\,1)$	$(0.1550$	High	Y	N	Y	N	N
$(1\,1\,0)$	$(0.1430$	High	Y	N	Y	N	N
$(1\,0\,1)$	N/A	Low	N	Y	Y	N	Possible

[a] Data obtained from Hammond et al. (2006).

The favourable features that have been put forward frame the crystallographic dimensions for predicting mechanical properties of solid forms. Besides that, the list of features may provide standard practice to test slip planes crystallographically. However, currently, many of these features are obtained qualitatively namely slip plane rugosity and interlocking, thus, triggers a need for work to interpret it as tangible quantitative values. Arising from the needs for quantifications of slip plane, the approach to measure the features have to be addressed. The selected approach needs to keep aligned with the aim to have quick but reliable prediction tools.

The overview of available models described throughout this chapter proved there is a necessity to assess the reliability of having the molecular and crystallographic

modelling to understand the mechanical properties of solid form further. Hence, this study set to explore the probability of having crystallographic and molecular modelling to predict the mechanical behaviour of pharmaceutical particulates.

3.5 Case study systems

The selected solid forms for used as case studies were presented in the introduction chapter earlier. Now, the existing prediction study for each of the selected solid forms is elaborated. The elaboration then provides the basic mechanical properties knowledge about the case study systems. The evaluation of known studies indicates the significance of having seven different solid forms to be explored. The crystal cell properties and codes were also given as in Table 3-3. These crystal structures are taken from the Cambridge Structural Database (CSD) [32].

3.5.1 Pentaerythritol (PET)
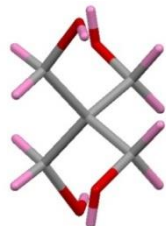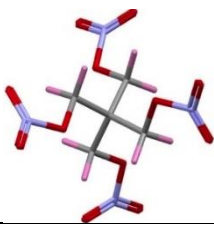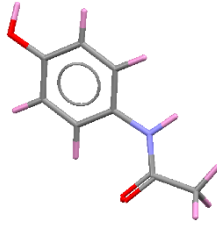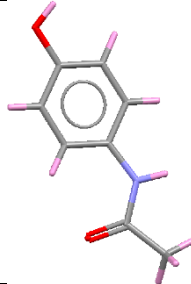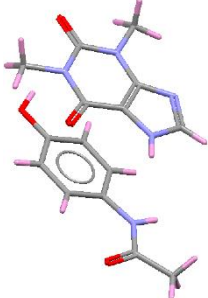
PET is a white, odourless crystalline polyol with the molecular formula of $C_5H_{12}O_4$. PET is also sugar. It is a body-centered crystal with four hydroxyl terminal. The first structure was crystallised by Llewyn et.al (1937) [82]. This structure was further refined with a considerable alteration to the z-coordinates [83]. Typically, the morphology of PET, when crystallised in aqueous solution, is tetragonal bipyramid with the face (101) at almost equilateral [84]. It is said that it is challenging to produce a high yield, and purity PET [84] adapted from [85] that was suspected to be caused by secondary reactions. The PET system is determined as soft materials based on calculated and measured elastic components[86,87,88].
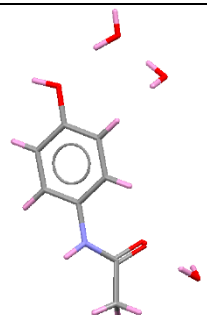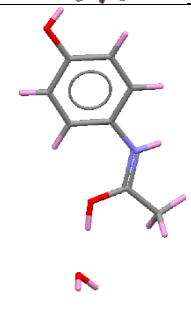
3.5.2 Pentaerythritol tetranitrate (PETN)

PETN is a non-hygroscopic crystalline system. PETN is also a known explosive compound that is sensitive to shock, and mechanical impact. Nonetheless, PETN is insensitive to friction and difficult to ignite. Besides being explosive materials, PETN is also used as pharmaceutical drugs for relieving the acute attacked of angina pectoris [89]. PETN is reported to reduce the frequency and severity of the attack. PETN's symmetrical components consist of two four-fold roto-inversions and three 2-fold screw axis those results in two molecules in a unit cell. The symmetry operator contributed to PETN crystal stability [33]. The molecular position in PETN is similar to PET with slight different for terminals connected to the central carbon, where PETN have nitrate group instead of the hydroxyl group. It has a molecular formula of

$C_5H_8N_4O_{12}$. It is crystallised as tetragonal ($P\bar{4}2_1c$) with only difference is in the type of lattice system, whereby PETN is a primitive crystal.

Table 3-3 Crystallographic information for the diverse solid forms used. The information includes the name used for this study and reference code in the Cambridge Structural Database (CSD)

Term	CSD ref.code	Crystal structure (Ă,degree,SG)	Molecular structure
PET	PERYTO04	a: 6.09 c: 8.49 $\alpha=\beta=\gamma=90^0$ Z: 2 Space group: I-4	
PETN	PERYTN12	a: 9.28 c: 6.61 $\alpha=\beta=\gamma=90^0$ Z: 2 Space group: P-42$_1$c	
P1	HXACAN30	a: 7.09 b: 9.21 c: 11.59 $\alpha=\gamma=90^0$ $\beta=97.84^0$ Z: 4 Space group: P2$_1$/n	
P2	HXACAN32	a: 7.20 b: 11.78 c: 17.17 $\alpha=\beta=\gamma=90^0$ Z: 8 Space group: Pcab	
PTHEO	KIGLUI01	a: 8.75 b: 15.39 c: 11.62 $\alpha=\gamma=90^0$ $\beta=99.02°$ Z: 4 Space group: P2$_1$/n	

Term	CSD ref.code	Crystal structure (Ă,degree,SG)	Molecular structure
PTRI	XOMWOL	a: 7.33 b: 12.59 c: 22.64 $\alpha=\gamma=\beta=90^0$ Z: 8 Space group: Pbca	
PHM	LATBUF	a: 6.28 b: 22.34 c: 6.88 $\alpha=\gamma=90^0$ $\beta=97.26^0$ Z: 4 Space group: $P2_1/n$	

3.5.3 Paracetamol polymorphs

Five diverse solid forms paracetamol were chosen to provide a variation of prediction. Paracetamol is a well-studied and usually is used as the basis system with regards to direct compression process development. Paracetamol too is a simple system with mechanical properties difference from one type to another. For example, paracetamol polymorphs, F1 is behaving poorly during direct compression while F2 an orthorhombic, behave well but it is a metastable form. By analysing the crystal, molecular packing shows completely different arrangements and probably the reason for the exact opposite of the mechanical behaviour for both polymorphs. Therefore, based on the mechanical behaviour and availability of many types of paracetamol, it is selected as the case study system for the current research.

Paracetamol is also known as Acetaminophen ($HO\text{-}C_6H_4\text{-}NH\text{-}C(=O)\text{-}CH_3$) with chemical name N-(4-hydroxyphenyl) acetamide a renown analgesic and antipyretic. It is used as a fast solution for fever and pain reliever since 1956. Paracetamol has three known polymorphs, stable monoclinic of F1, metastable orthorhombic of F2 and elusive F3, that is obtained from the melt and yet to be characterised. Because of F3 elusiveness, this current research focuses on F1 and F2. Both forms have similar molecular configurations with only a disparity in the positioning of atoms in the crystal packing.

The F1 structure consists of four identical molecules related by symmetry centres arranged in pairs and perpendicular between each other. The centre of symmetry occurs at positions (1/2, 1/2, 1/2) with translating symmetry along normal in the ac-plane, perpendicular to the b axis respectively. F1 is the stable form at room temperature. F2 is an orthorhombic crystal system with space group Pcab. F2 have eight molecules in a unit cell with a centre of symmetry at the point (1/2, 1/2, 1/2) the same as in F1. The arrangement of molecules in the packing are about three glide planes along a, b, and c that is perpendicular to plane ab, ac, and cb respectively. Both polymorphs of paracetamol have three obvious terminals functional groups that are hydroxyl, amide and methyl. These terminal groups give the stability and compressibility function for the polymorphs.

The extensive study has been conducted to either improve the mechanical properties of F1 or stabilise the crystallisation of F2 to isolate enough materials for compaction study [20,63,91-93]. Likewise, crystallisation of different size and shape of paracetamol was also shown to be successful to provide better behaving F1.

3.5.4 Paracetamol theophylline (PTHEO)

PTHEO is a co-crystal of paracetamol. Paracetamol is lacking acidity and basicity, which prevent the formation of salt and stable form for its metastable polymorph [94]. Therefore, co-crystal is targeted to be the solution for the poor tabletability of F1. PTHEO is categorised in the monoclinic space group of $P2_1/n$. PTHEO consists of one molecule of theophylline and a molecule of paracetamol in an asymmetric unit (Figure 3-14). Theophylline is reported to be amphiprotic and performs well when co-crystallise with a broad range of guest molecules [58]. A unit cell of PTHEO is built from four asymmetric units that resulting from the combination of glide plane and screw axis that translate and reflect the molecules with an additional half (1/2) lattice distance shifted. Theophylline has carbonyl and amine group at its terminal. The dominating functional groups affect the way PTHEO grows and its morphology. Theophylline by itself is an excellent source of the proton for ionisation to occur [58].

The co-crystal creates a layer between paracetamol molecule and theophylline. Theophylline by its own is used as the respiratory drugs. The selection of theophylline as co-crystal former for paracetamol is to discover the impact of having theophylline in improving the mechanical properties namely compactibility and better dissolution. The calculated tensile strength is 2.79MPa [94].
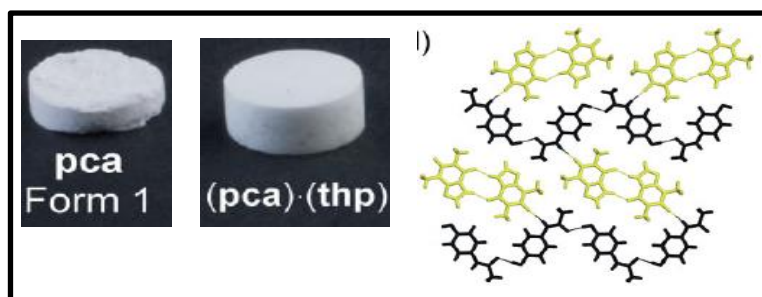
Figure 3-14 PTHEO crystal packing showing stacking of paracetamol (black) and theophylline (yellow). PTHEO was shown to be better at tabletting by staying intact after ejection (Figure from [94])

3.5.5 Paracetamol trihydrates

Paracetamol trihydrates is one of the paracetamol hydrates. The paracetamol trihydrates crystallises in the orthorhombic crystal system, space group Pbca. Paracetamol trihydrates (PTRI) have four molecules in an asymmetric unit. Each unit will have a molecule of paracetamol and three molecules of water. It is a lath-like form (Figure 3-15) and is highly metastable [95]. A unit cell of PTRI is built from eight asymmetric unit that resulting from the combination of glide plane and screw axis that translate and reflect the molecules with an additional half (1/2) lattice distance shifted.
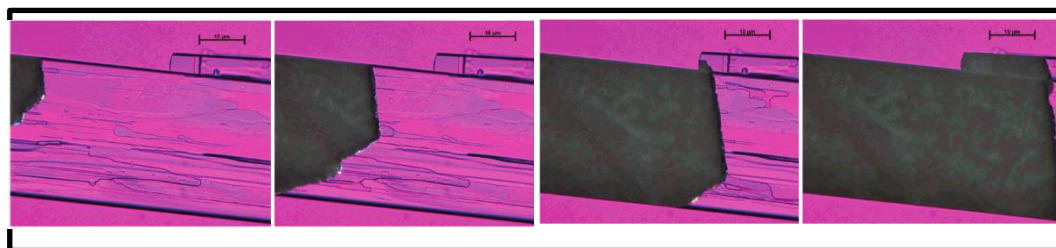
Figure 3-15 Solvation of PTRI into F1 by time showing the lath finally turns opaque (Figure from [95])

The availability of three water molecules makes PTRI a heavily hydrogen bonded. Each water molecule will create three hydrogen bonds with the amino (-NH), hydroxyl (-OH) and carbonyl (=O) group from the paracetamol molecule. The molecule contains three water molecules interacting with the paracetamol structure forming hydrogen bonds. It can be observed that two hydrogen atoms from the water molecules forming bonding with the carbonyl oxygen (=O) created a dimer bond. The functional groups dominating PTRI are methyl (-CH$_3$), carbonyl oxygen (=O) and the amino group (-NH).

3.5.6   Paracetamol hydrochloride monohydrate

Paracetamol hydrochloride monohydrate is the first identified ionisable paracetamol discovered by Perumalla et.al (2012) [96]. The discoveries of an ionisable paracetamol provide an alternative for the production of paracetamol besides the formation of co-crystal approach. Moreover, the discoveries of the structure improve significantly tablettability of paracetamol and propose that structure with carboxamide that's hard to protonate. Paracetamol Hydrochloride Monohydrate (PHM) consists of one molecule paracetamol, a water molecule and a chloride ion in an asymmetric unit. PHM provides the acidic and basic functionalities for ionisation to take place.
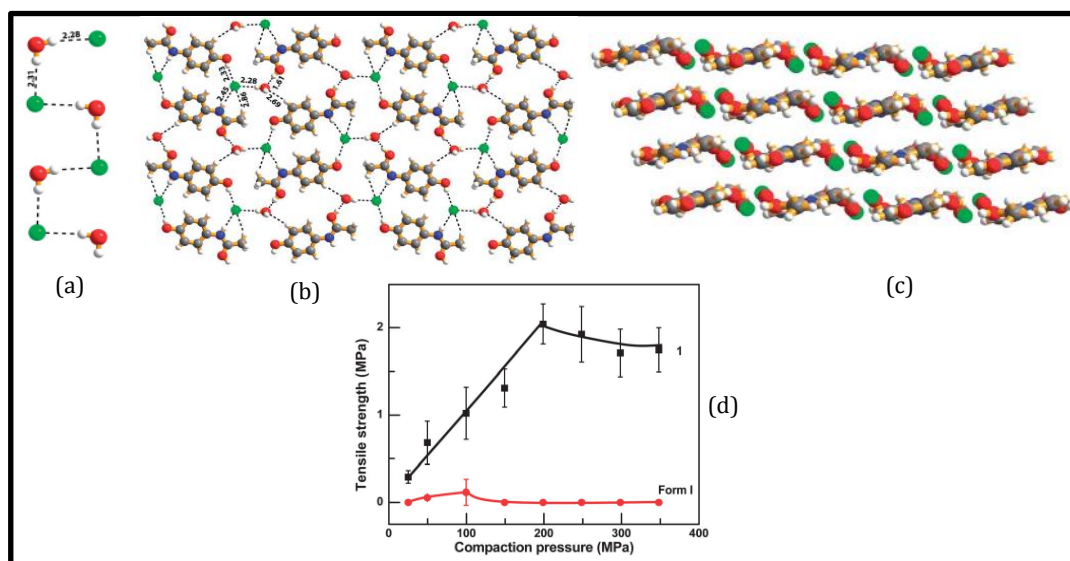
Figure 3-16 PHM crystal packing with a) hydrogen bond interaction between water molecule and chloride ion b) hydrogen bond network created c) the layering of molecular structure d)Tabletability plot of F1 and PHM. PHM has better tensile strength (Figure from [96])

The reason for the poor ionisable ability is due to the amide group that is having an impact on the paracetamol mechanical properties. A unit cell of PHM is built from four asymmetric units that resulting from the combination of glide plane and screw axis that translate and reflect the molecules with an additional half (1/2) lattice distance shifted. Observation of the molecular packing from [100] direction shows perfectly distanced sheets of planes with a molecule of water and chloride ion separating each plane (Figure 3-16) [96]. It is interesting to note the alternating direction of hydrogen created between the water molecules to chloride ions. PHM is dominated by hydroxyl (-OH), amine (-NH) and partial of the benzene ring.

3.6 Conclusions

The three core themes presented in this chapter are tablet's performance, powder characteristics and single particle functionality. Tablet performance can be assessed through the BCS, MCS and also the MST concept. From the studies discussed, the interplay between structure-property relationships showed a clear impact towards devising APIs suitable for DC. Collectively, the available prediction models are devising similar aspect for predicting the tablet deformation properties. Simplified list of essential behaviours for predicting deformation are surface characteristics, bonding interactions, and strength of the system. Consequently, numerous studies begin to shift from the qualitative molecular evaluation to a real quantitative method, for instance, the experimental-based model in evaluating the effectiveness and suitability of APIs for use in direct compression.

Overall, this chapter highlights the missing pieces to link between macroproperties to the microproperties. The microproperties include intermolecular interactions, crystallographic structure, and dislocations. The tests focal points are crystal geometry, slip system availability and crystal packing arrangements within the crystal. The summary of microproperties was based on studied carried out by micro/nano-indentation, compaction and also by qualitative analysis of the crystallographic structure. A comprehensive understanding of the microproperties of materials help in explaining different macroproperties exhibited during tabletting and milling.

Though there are possible slip deformation theoretical models, the approach to characterise the slip systems based on crystallographic structure quantitatively is yet to be explored. Therefore, the current study is set to fill in the gap for developing a quantitative model to predict mechanical properties of pharmaceutical particulates through molecular and crystallographic modelling by exploiting the selected seven solid forms.

References:

[1]   K.J. Bittorf, T. Sanghvi, J.P. Katstra, Design of Solid Dosage Formulations, Chemical Engineering in the Pharmaceutical Industry: R&D to Manufacturing. (2011) 673–702.

[2]   S.M. Tozer, Implementation of the new FDA quality by design guidance in pharmaceutical production, 2008.

[3]   P.I. Report, Drug Discovery and Development, 2007.

[4]   R. Creekmore, E. Dokou, A. Eylath, D. Joiner, M. Lovdahl, J. Pellett, et al., Early Development GMPs for Drug-Product Manufacturing of Small Molecules: An Industry Perspective (Part III), Pharmaceutical Technology. 36 (2012) 56–61.

[5]   E. Bharath, S. Manjula, A. Vijaychand, In silico drug design-tool for overcoming the innovation deficit in the drug discovery process, International Journal of Pahrmacy and Pharmaceutical Sciences. 3 (2011) 8-12.

[6]   A.D. Bond, Pharmaceutical crystallography: is there a devil in the details?, CrystEngComm. (2012).

[7]   S.L. Price, The computational prediction of pharmaceutical crystal structures and polymorphism, Adv. Drug Deliv. Rev. 56 (2004) 301–319.

[8]   S.P. Chamarthy, R. Pinal, M.T. Carvajal, Elucidating raw material variability—importance of surface properties and functionality in pharmaceutical powders, AAPS PharmSciTech. 10 (2009) 780–788.

[9]   Y. Feng, D.J.W. Grant, C.C. Sun, Influence of crystal structure on the tabletting properties of n-alkyl 4-hydroxybenzoate esters (parabens), Journal of Pharmaceutical Sciences. 96 (2007) 3324–3333.

[10]   Conclusions of FDA-EMA Parallel Assessment of Quality-By-Design Elements of Marketing Applications, (n.d.).

[11]   K.J. Roberts, Private Communication

[12]   M.E. Aulton, T. Wells, Pharmaceutics: The science of dosage form design, Churchill Livingstone London:, 2002.

[13]   Food, D. Administration, others, Guidance for Industry: Waiver of in vivo bioavailability and bioequivalence studies for immediate-release solid oral dosage forms based on a Biopharmaceutics Classification system, Food and Drug Administration, Rockville, MD. (2000).

[14]   M. Leane, K. Pitt, G. Reynolds, A proposal for a drug product Manufacturing Classification System (MCS) for oral solid dosage forms, Pharmaceutical Development and Technology. (2014) 1–10.

[15] B.B.K. Reddy, A. Karunakar, Biopharmaceutics classification system: a regulatory approach, Dissolution Technologies. 18 (2011) 31–37.

[16] G. Clydesdale, R.B. Hammond, K.J. Roberts, Molecular modeling of bulk impurity segregation and impurity-mediated crystal habit modification of naphthalene and phenanthrene in the presence of heteroimpurity species, The Journal of Physical Chemistry B. 107 (2003) 4826–4833.

[17] D. McCormick, Evolutions in direct compression, Pharmaceutical Technology. 17 (2005) 52–62.

[18] J.K. Prescott, R.J. Hossfeld, Maintaining product uniformity and uninterrupted flow to direct-compression tabletting presses, Pharmaceutical Technology. 18 (1994) 98–115.

[19] S. Byrn, R. Pfeiffer, M. Ganey, C. Hoiberg, G. Poochikian, Pharmaceutical solids: a strategic approach to regulatory considerations, Pharmaceutical Research. 12 (1995) 945–954.

[20] E. Joiris, P. Di Martino, C. Berneron, A.-M. Guyot-Hermann, J.-C. Guyot, Compression behavior of orthorhombic paracetamol, Pharmaceutical Research. 15 (1998) 1122–1130.

[21] L. Salbu, A. Bauer-Brandl, I. Tho, Direct compression behavior of low-and high-methoxylated pectins, AAPS PharmSciTech. 11 (2010) 18–26.

[22] J.M. Fachaux, A.M. Guyot-Hermann, J.C. Guyot, P. Conflant, M. Drache, S. Veesler, et al., Pure Paracetamol for direct compression Part II. Study of the physicochemical and mechanical properties of sintered-like crystals of Paracetamol, Powder Technology. 82 (1995) 129–133.

[23] C. Nyström, Gör. Alderborn, M. Duberg, P.-G. Karehill, Bonding Surface area and Bonding Mechanism-Two Important Factors fir the Understanding of Powder Comparability, Drug Development and Industrial Pharmacy. 19 (1993) 2143–2196.

[24] S. Patel, A.M. Kaushal, A.K. Bansal, Compression physics in the formulation development of tablets, Critical Reviews™ in Therapeutic Drug Carrier Systems. 23 (2006).

[25] K. Seppälä, J. Heinämäki, J. Hatara, L. Seppälä, J. Yliruusi, Development of a new method to get a reliable powder flow characteristics using only 1 to 2 g of powder, AAPS Pharmscitech. 11 (2010) 402–408.

[26] H. Kristensen, P. Holm, T. Schaefer, Mechanical properties of moist agglomerates in relation to granulation mechanisms part I. Deformability of moist, densified agglomerates, Powder Technology. 44 (1985) 227–237.

[27] P. Narayan, B.C. Hancock, The relationship between the particle properties, mechanical behavior, and surface roughness of some pharmaceutical excipient compacts, Materials Science and Engineering: A. 355 (2003) 24–36.

[28] D. Schulze, Powders and bulk solids: behavior, characterization, storage and flow, Springer Science & Business Media, 2007.

[29] K.-H.L. Kimio Kawakita, Some Considerations on Powder Compression Equations, Powder Technology-Elsevier Sequoia. (1969).

[30] H. Hou, C.C. Sun, Quantifying effects of particulate properties on powder flow properties using a ring shear tester, Journal of Pharmaceutical Sciences. 97 (2008) 4030–4039.

[31] J. Tomas, Fundamentals of cohesive powder consolidation and flow, Granular Matter. 6 (2004) 75–86.

[32] D. Schulze, Flow properties of powders and bulk solids, Braunschweig/Wolfenbu Ttel, Germany: University of Applied Sciences. (2006).

[33] A. Jenike, Steady gravity flow of frictional-cohesive solids in converging channels, Journal of Applied Mechanics. 31 (1964) 5–11.

[34] A.W. Jenike, Storage and flow of solids, bulletin no. 123, Bulletin of the University of Utah. 53 (1964).

[35] R. Roopwani, I.S. Buckner, Understanding deformation mechanisms during powder compaction using principal component analysis of compression data, International Journal of Pharmaceutics. 418 (2011) 227–234.

[36] C.C. Sun, Materials Science tetrahedron—A useful tool for pharmaceutical research and development, Journal of Pharmaceutical Sciences. 98 (2009) 1671–1687.

[37] R. Roberts, R. Rowe, Brittle/ductile behaviour in pharmaceutical materials used in tabletting, International Journal of Pharmaceutics. 36 (1987) 205–209.

[38] M.P. Mullarney, B.C. Hancock, G.T. Carlson, D.D. Ladipo, B.A. Langdon, The powder flow and compact mechanical properties of sucrose and three high-intensity sweeteners used in chewable tablets, International Journal of Pharmaceutics. 257 (2003) 227–236.

[39] A. Nokhodchi, O. Amire, M. Jelvehgari, Physico-mechanical and dissolution behaviours of ibuprofen crystals crystallized in the presence of various additives, Daru: Journal of Faculty of Pharmacy, Tehran University of Medical Sciences. 18 (2010) 74.

[40] J. Garr, M. Rubinstein, An investigation into the capping of paracetamol at increasing speeds of compression, International Journal of Pharmaceutics. 72 (1991) 117–122.

[41] I. Akseli, N. Ladyzhynsky, J. Katz, X. He, Development of predictive tools to assess capping tendency of tablet formulations, Powder Technology. 236 (2013) 139–148.

[42] O. Akande, M. Rubinstein, P. Rowe, J. Ford, Effect of compression speeds on the compaction properties of a 1: 1 paracetamol-microcrystalline cellulose mixture prepared by single compression and by combinations of pre-compression and main-compression, International Journal of Pharmaceutics. 157 (1997) 127–136.

[43] S.F. Yap, M.J. Adams, J.P.K. Seville, Z. Zhang, Single and bulk compression of pharmaceutical excipients: Evaluation of mechanical properties, Powder Technology. 185 (2008) 1–10.

[44] R. Heckel, An analysis of powder compaction phenomena, Transactions of the Metallurgical Society of AIME. 221 (1961) 1001–1008.

[45] E. Walker, The properties of powders. Part VI. The compressibility of powders, Transactions of the Faraday Society. 19 (1923) 73–82.

[46] P.L.D. Wildfong, B.C. Hancock, M.D. Moore, K.R. Morris, Towards an understanding of the structurally based potential for mechanically activated disordering of small molecule organic crystals, Journal of Pharmaceutical Sciences. 95 (2006) 2645–2656.

[47] R.A.V.S. M.Rehula, Stress Relaxation Study of Fillers for Directly Compressed Tablets, Powder Technology, Elsevier. (2012) 510–515.

[48] R. Moreno-Atanasio, M. Ghadiri, Mechanistic analysis and computer simulation of impact breakage of agglomerates: Effect of surface energy, Chemical Engineering Science. 61 (2006) 2476–2481.

[49] M. Landin, R.C. Rowe, P. York, Establishing and Analysing The Design Space In The Development Of Direct Compression Formulations By Gene Expression Programming, International Journal of Pharmaceutics. (2012).

[50] H. Nakamura, Y. Sugino, T. Iwasaki, S. Watano, Development of a Novel Tablet Machine for a Tiny Amount of Powder and Evaluation of Capping Tendency, Chemical and Pharmaceutical Bulletin. 59 (2011) 1518–1522.

[51] M.P. Mullarney, B.C. MacDonald, A. Hutchins, Peer-reviewed research-formulation development-Assessing Tablet-Sticking Propensity-The authors designed an upper punch with a removable punch tip to determine a tablet formulation's propensity to stick by weighing the mass of powder adhered to the punch tip., Pharmaceutical Technology. 36 (2012) 57.

[52] T.S. McDermott, J. Farrenkopf, A. Hlinak, J.P. Neilly, D. Sauer, A material sparing method for quantitatively measuring tablet sticking, Powder Technology. (2011).

[53] J.D. Stephens, B.R. Kowalczyk, B.C. Hancock, G. Kaul, C. Cetinkaya, Ultrasonic real-time in-die monitoring of the tablet compaction process—A proof of concept study, International Journal of Pharmaceutics. 442 (2013) 20–26.

[54] E.N. Hiestand, Dispersion forces and plastic deformation in tablet bond. J Pharm Sci. 74 (1985) 768–70.

[55] S.F. Gharaibeh, I.N.C. Al-Ard, Mechanical energies associated with compaction of form I and form II paracetamol powder, Powder Technology. 214 (2011) 161–168.

[56] M. Roberts, J.L. Ford, P.H. Rowe, A.M. Dyas, G.S. MacLeod, J.T. Fell, et al., Effect of lubricant type and concentration on the punch tip adherence of model ibuprofen formulations, Journal of Pharmacy and Pharmacology. 56 (2004) 299–305.

[57] M.A. Lovette, A.R. Browning, D.W. Griffin, J.P. Sizemore, R.C. Snyder, M.F. Doherty, Crystal shape engineering, Industrial \& Engineering Chemistry Research. 47 (2008) 9812–9833.

[58] S.L. Childs, G.P. Stahly, A. Park, The salt-cocrystal continuum: the influence of crystal structure on ionization state, Molecular Pharmaceutics. 4 (2007) 323–338.

[59] T. Frivsvci'c, W. Jones, Benefits of cocrystallisation in pharmaceutical materials science: an update, Journal of Pharmacy and Pharmacology. 62 (2010) 1547–1559.

[60] L. Orola, M.V. Veidis, I. Sarcevica, A. Actins, S. Belyakov, A. Platonenko, The effect of pH on polymorph formation of the pharmaceutically active compound tianeptine, International Journal of Pharmaceutics. (2012).

[61] G.R. Desiraju, G.W. Parshall, Crystal engineering: the design of organic solids, Materials Science Monographs. 54 (1989).

[62] G.R. Desiraju, Crystal engineering: from molecule to crystal, Journal of the American Chemical Society. 135 (2013) 9952–9967.

[63] G. Nichols, C.S. Frampton, Physicochemical characterization of the orthorhombic polymorph of paracetamol crystallized from solution, Journal of Pharmaceutical Sciences. 87 (1998) 684–693.

[64] D. Olusanmi, K. Roberts, M. Ghadiri, Y. Ding, The breakage behaviour of Aspirin under quasi-static indentation and single particle impact loading: Effect of crystallographic anisotropy, International Journal of Pharmaceutics. (2011).

[65] S. Mirza, I. Miroshnyk, J. Heinämäki, O. Antikainen, J. Rantanen, P. Vuorela, et al., Crystal morphology engineering of pharmaceutical solids: tabletting performance enhancement, AAPS PharmSciTech. 10 (2009) 113–119.

[66] G.R. Desiraju, Designer crystals: intermolecular interactions, network structures and supramolecular synthons, Chemical Communications. (1997) 1475–1482.

[67] C.M. Reddy, K.A. Padmanabhan, G.R. Desiraju, Structure-property correlations in bending and brittle organic crystals, Crystal Growth & Design. 6 (2006) 2720–2731.

[68] S. Ghosh, C.M. Reddy, Elastic and Bendable Caffeine Cocrystals: Implications for the Design of Flexible Organic Materials, Angewandte Chemie. 124 (2012)

10465–10469.

[69] C. Sun, D.J.W. Grant, Influence of crystal structure on the tabletting properties of sulfamerazine polymorphs, Pharmaceutical Research. 18 (2001) 274–280.

[70] C. Sun, D.J. Grant, Influence of crystal shape on the tabletting performance of L-lysine monohydrochloride dihydrate, Journal of Pharmaceutical Sciences. 90 (2001) 569–579.

[71] P.P. Bag, M. Chen, C.C. Sun, C.M. Reddy, Direct correlation among crystal structure, mechanical behaviour and tabletability in a trimorphic molecular compound, CrystEngComm. 14 (2012) 3865–3867.

[72] V. André, M.T. Duarte, Novel challenges in crystal engineering: polymorphs and new crystal forms of active pharmaceutical ingredients, INTECH Open Access Publisher, 2011.

[73] G.R. Desiraju, Supramolecular synthons in crystal engineering—a new organic synthesis, Angewandte Chemie International Edition in English. 34 (2003) 2311–2327.

[74] C. Sun, D.J.W. Grant, Improved tabletting properties of p-hydroxybenzoic acid by water of crystallization: A molecular insight, Pharmaceutical Research. 21 (2004) 382–386.

[75] M.H. Shariare, F.J.J. Leusen, M. de Matas, P. York, J. Anwar, Prediction of the Mechanical Behaviour of Crystalline Solids, Pharmaceutical Research. (2011) 1–13.

[76] C.M. Reddy, G.R. Krishna, S. Ghosh, Mechanical properties of molecular crystals—applications to crystal engineering, CrystEngComm. 12 (2010) 2296–2314.

[77] R. Roberts, The elasticity, ductility and fracture toughness of pharmaceutical powders., 1991.

[78] R.V. Rao, J. Davim, A decision-making framework model for material selection using a combined multiple attribute decision-making method, The International Journal of Advanced Manufacturing Technology. 35 (2008) 751–760.

[79] T.L. Saaty, Basic theory of the analytic hierarchy process: how to make a decision, Revista de La Real Academia de Ciencias Exactas, F'isicas Y Naturales. 93 (1999) 395–423.

[80] T.L. Saaty, L.G. Vargas, The seven pillars of the analytic hierarchy process, in: Models, Methods, Concepts & Applications of the Analytic Hierarchy Process, Springer, 2001: pp. 27–46.

[81] T.L. Saaty, A scaling method for priorities in hierarchical structures, Journal of Mathematical Psychology. 15 (1977) 234–281.

[82] F. Llewellyn, E. Cox, Goodwin, TH, J. Chem. Soc. 1937 (1937) 883.

[83] R. Shiono, D. Cruickshank, E. Cox, A refinement of the crystal structure of pentaerythritol, Acta Crystallographica. 11 (1958) 389–391.

[84] J.F. Rogers, D.E. Creasy, Crystallisation of pentaerythritol, Journal of Applied Chemistry and Biotechnology. 24 (1974) 171–180.

[85] P. Sherwood, Here's the Complete Story on This Petrochemical, Pentaerythritol, Petroleum Refiner. 35 (1956) 171–179.

[86] R. Srivastava, A note on the elastic properties of pentaerythritol, Acta Crystallographica. 15 (1962) 1306–1306.

[87] R. C. Srivastava, S. C. Chakraborty, Determination of the Elastic Constants of Pentaerythritol by X-Ray Diffraction Method, Journal of the Physical Society of Japan. 17 (1962) 1767–1770.

[88] G.M. Day, S.L. Price, M. Leslie, Elastic constant calculations for molecular organic crystals, Crystal Growth & Design. 1 (2001) 13–27.

[89] M. Ebadi, CRC Desk Reference of Clinical Pharmacology, Taylor & Francis, 1997.

[90] S. Finnie, K.V.R. Prasad, D.B. Sheen, J.N. Sherwood, Microhardness and dislocation identification studies on paracetamol single crystals, Pharmaceutical Research. 18 (2001) 674–681.

[91] Y.V. Nelyubina, I.V. Glukhov, M.Y. Antipin, K.A. Lyssenko, "Higher density does not mean higher stability" mystery of paracetamol finally unraveled, Chemical Communications. 46 (2010) 3469–3471.

[92] A.G. Ogienko, E.V. Boldyreva, A. Yu Manakov, V.V. Boldyrev, A.S. Yunoshev, A.A. Ogienko, et al., A New Method of Producing Monoclinic Paracetamol Suitable for Direct Compression, Pharmaceutical Research. (2011) 1–12.

[93] K.V.R. Prasad, R.I. Ristic, D.B. Sheen, J.N. Sherwood, Dissolution kinetics of paracetamol single crystals, International Journal of Pharmaceutics. 238 (2002) 29–41.

[94] S. Karki, T. Frivsvci'c, L. Fábián, P.R. Laity, G.M. Day, W. Jones, Improving mechanical properties of crystalline solids by cocrystal formation: new compressible forms of paracetamol, Advanced Materials. 21 (2009) 3905–3909.

[95] M.L. Peterson, D. McIlroy, P. Shaw, J.P. Mustonen, M. Oliveira, Ö. Almarsson, Crystallization and transformation of acetaminophen trihydrate, Crystal Growth & Design. 3 (2003) 761–765.

[96] S.R. Perumalla, L. Shi, C.C. Sun, Ionized form of acetaminophen with improved compaction properties, CrystEngComm. (2012).

[97] C.M. Reddy, S. Basavoju, G.R. Desiraju, Sorting of polymorphs based on mechanical properties. Trimorphs of 6-chloro-2, 4-dinitroaniline, Chemical Communications. (2005) 2439–2441.

[98] J.A. Sarma, A. Nagaraju, Solid state nuclear bromination with N-bromosuccinimide. Part 1. Experimental and theoretical studies on some substituted , Journal of the Chemical Society, Perkin Transactions 2. (2000) 1113–1118.

[99] V. André, M.T. Duarte, Revisiting paracetamol in a quest for new co-crystals, CrystEngComm. (2012).

Chapter Four

_____

Materials and Methods

This chapter defines the diverse solid forms used for this study and the reasons behind the selection. Details for methodology adopted for achieving this study's objective are described. The selected method includes molecular and synthonic modelling.

Chapter 4 Materials and methods

4.1 Introduction

This chapter starts by describing the materials used for this study and their usage using various computational and experimental approaches. The method section is divided into computational techniques and experimental methods. Basic theories related to the selected computational techniques and experimental methods were defined in Chapter 2 and are referred to, where appropriate. Figure 4-1 shows the content of this chapter, starts with the description of materials up to the validation steps.
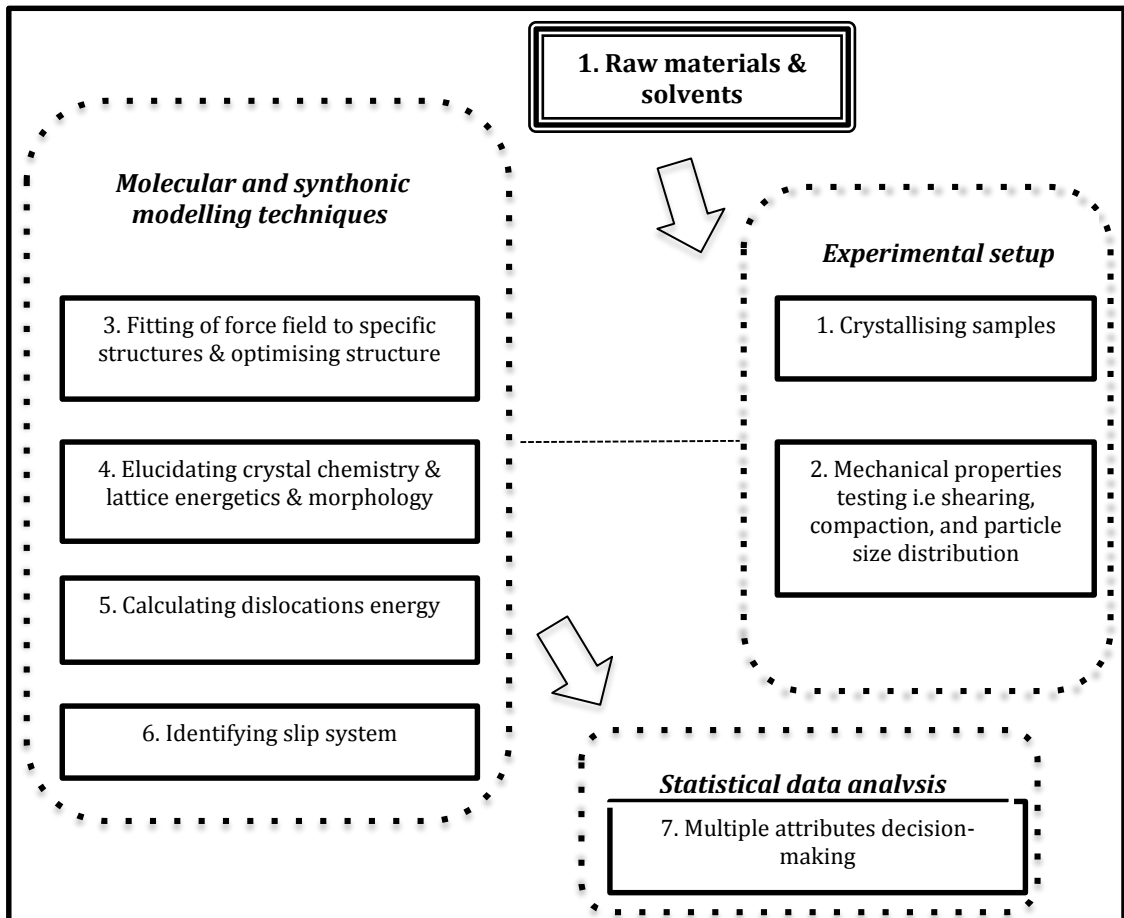
Figure 4-1 Summary representing sequence of this method chapter. Firstly, the raw materials and solvents used for experiments are described. Secondly the experimental setup for crystallisation and characterisation. Thirdly the molecular and synthonic modelling techniques and finally the statistical data analysis are defined

4.2 Materials

This subsection provides the list of materials and solvents used for the crystallisation process. The list includes the purity of the materials also the source of the chemicals.

4.2.1 Chemical powders

The raw materials used for the crystallisation process are shown in Table 4-1 below. These materials were used as supplied.

Table 4-1 Raw material information for use in crystallisation experiments indicating the percent of purity, source and other comments relating to the materials

Compound	% Purity	Source	Comment
Pentaerythritol	90	Merek milipore	
Paracetamol	98	Acros organics	Recrystallized for metastable crystallisation
Theophylline anhydrous	>=99	Sigma	Co-former

4.2.2 Solvents

The physical properties of solvents used for the crystallisation process are presented in Table 4-2 showing together the grade of the solvent and the source.

Table 4-2 Solvents used in the crystallisation process showing the grade and source of the solvent

Solvent	% Purity	Source	Comment
Ethanol	99.8	Fisher chemical	Absolute for HPLC
Methanol	99.8	Fisher chemical	Absolute for HPLC
Acetone	99.8	Fisher chemical	
Chloroform		VWR brand	Co-crystallisation

This chapter continues with the method for carrying out the computational and conducting the experiments. The experimental section will consist of two major sections that are crystallisation and characterisation approach.

4.3 Experimental setup for crystallisation

This section described the reactor configuration and the procedure adopted for crystallising different forms of paracetamol and pentaerythritol samples. The layout of this section follows that crystallisation of paracetamol Form I (FI), paracetamol Form II (FII), paracetamol theophylline (PTHEO) and lastly pentaerythritol.

4.3.1 Crystallisation of monoclinic paracetamol Form I

The FI that is stable at room temperature was crystallised using cooling crystallisation method. By varying few crystallisation parameters namely, solvent and cooling rate, eight batches of paracetamol samples were prepared. The crystallisation batches represent the small and large-scale experiments. Crystallisation of small-scale experiment was carried out using Easymax (Mettler Toledo) with 100ml round bottom reactors. The jacket temperature of the reactor system was ranging from -40°C to 180°C. The large-scale experiments were carried out using 500ml reactors, which are having similar reactor system conditions to the 100ml. Two binary solutions were used that are methanol-water and acetone-water. The small-scale experiments were treated as method testing. Thus, in Chapter 7, only the large-scale experiment results were described.

The solution contains 30% acetone and 70% water. The solubility of paracetamol for the acetone-water was taken from the previous study of Granberg et.al [1999] [1]. For the methanol-water, the solubility was estimated from the solubility of pure methanol [2]. The experiment for both methanol-water and acetone-water were carried out at 50°C and setting out to crystallise about 100 grams of the sample for mechanical properties characterisation. The solution was cooled at slowly at 0.1°C/min with seeds added in between the cooling period. Both of the sample batches were extracted at -5°C. After isolation, the samples were left to dry in the oven at 45°C for 30 minutes. The solubility of acetone-water at 50°C was 261.28g/kg, and crystallisation was carried out using the same steps of crystallisation as with methanol.

4.3.2 Antisolvent crystallisation of paracetamol Form II

Reactor vessel with size 100ml that is suitable for atmospheric pressure was used. The successful run was adopting the anti-solvent approach. The experiment was conducted using auto-MATE with 100ml flat-bottom reactor. The reactor is equipped with glass impeller to ensure homogeneous mixing. For precise measurement of temperature and

turbidity changes, the auto-MATE reactor is set with Hastelloy-C type K thermocouples and turbidity probe with computerised operational control. Heat transfer was taking place efficiently by having internal and external heating system.

WinISO program provides the temperature control and data acquisition for the crystallisation experiment. The crystallisation temperature profile for this study is as in Figure 4-2. Initially, the reactor was held at 25°C for 5 minutes before being increased to 40°C with a heating rate of 1°C/min under constant agitation. At 40°C the saturated solution was held for 30 minutes to ensure all paracetamol has dissolved completely. The saturated solution was then cooled to -5°C with a cooling rate of 1°C/min. After 15 minutes of cooling, chilled water was added as an anti-solvent. By adding the chilled water, the temperature was reduced to about 15°C instantaneously. The cooling was continued until the solution reaches -5°C before crystals being harvested using a vacuum pump and filter paper (Whatman no.4). Finally, the harvested crystal was placed in the oven at 50°C for an hour to dry.
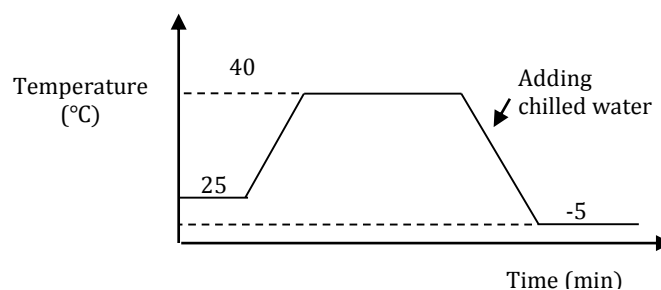
Figure 4-2 Temperature profile for crystallisation process set using WinISO software

4.3.3   Crystallisation of co-crystal- paracetamol theophylline

Paracetamol theophylline was obtained using non-stoichiometric approach. The ratio of paracetamol-theophylline was determined by trial and error. The trial and error were conducted by crystallising samples in 20ml vials. 1:1 volume ratio of methanol: water was used. Trial and error started with increasing the amount of paracetamol.

Initially, paracetamol and theophylline were ground gently using mortar and pestle. Then, paracetamol and theophylline were dissolved using ultrasonic analogue SRH baths from Fisherbrand. The paracetamol theophylline was formed from 3:1 molar ratio of paracetamol: theophylline. Harvested crystals from the vials were tested using DSC for initial identification.

By replicating the 3:1 molar ratio paracetamol: theophylline roughly 100 grams of samples were crystallised following the same method, only it was carried out in a beaker covered with parafilm. Isolated samples were then dried in the oven at 50℃.

4.3.4 Crystallisation of pentaerythritol

The synthesis of the crystal was done according to its solubility at 15℃ in water. 5.6 grams of pentaerythritol powder was poured into 250 ml beaker and dissolved in 100 ml of water using a hot plate. The beaker was covered with parafilm to avoid evaporation and contamination. After 10 minutes of heating, the temperature was increased from 15 to 25℃ to ensure that all complete dissolution of pentaerythritol. The clear saturated solution was then removed from the heat with holes were punched at the parafilm and beaker was placed on the bench top to undergo slow evaporation. Harvested crystals were dried in the oven to remove any solvent residue. The pentaerythritol crystals were not being characterised and used only for morphology reference.

4.4 Characterisation of samples

This section is describing the techniques used for characterisation of crystal samples. It is divided into three main characterisation techniques, thermal analysis, structure determination and lastly morphology identification.

4.4.1 Thermal analysis

Determination of samples' melting temperature and latent heat changes, were carried out using differential scanning calorimetry (DSC 1) by Mettler Toledo (Figure 4-3). DSC measures the heat flow difference between sample as a function of temperature or time. The setup of the DSC is given in Figure 4-3. Measurements were analysed using STAR^e software by taking onset temperature (T_{onset}) or peak temperature (T_{peak}) and the integration of the endothermic and exothermic peaks. Similarly, the experiments' temperature profiles were controlled using STAR^e software [3]. 5-7miligrams of samples were cautiously placed into standard 40μl aluminium pans. Samples were then heated to 190℃ for paracetamol, 290℃ for paracetamol theophylline and pentaerythritol with the rate of 10℃/min and purged by nitrogen gas at 60cm^3/min. Samples were held at respective heating temperature for 10 minutes before cooled to 25℃ to ensure all samples had already melted.
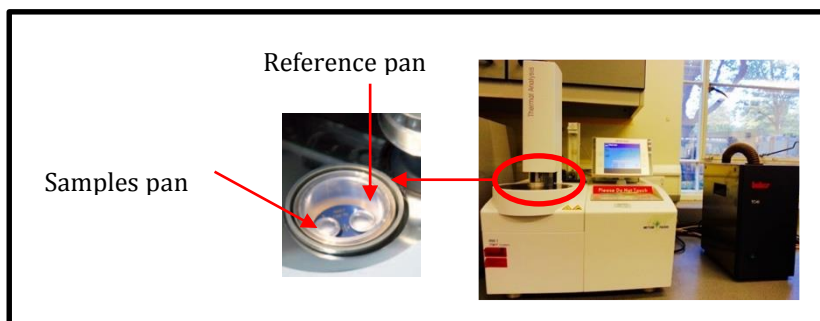
Figure 4-3 Differential scanning calorimetry (DSC1 Star^e system) by Mettler toledo unit

4.4.2 Structure determination

Structures of harvested crystals from all experiments were confirmed using the D8 ADVANCE-BRUKER AXS model X-Ray Powder Diffraction (PXRD) shown in Figure 4-4. The diffraction angles were measured simultaneously using the Lynx-eye sensitive detector following Braggs law (Figure 4-4). As the radiation beam hit the samples, atoms caused incident x-rays to diffract into multiple directions.

Samples were ground gently and spread evenly on specimen holder rings. Samples were scanned from 5.0 to 50.0° of 2θ range with a step size of 0.01. The diffraction patterns were analysed using PanAnalytical HighScore Plus software [4].
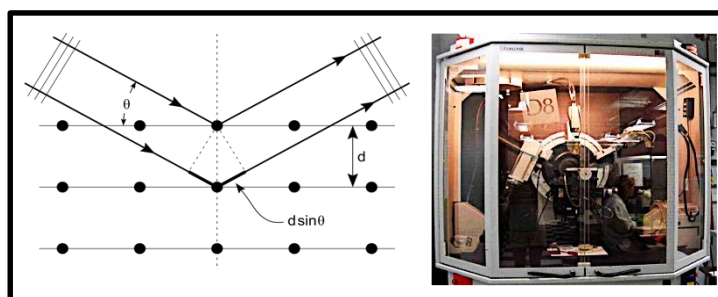
Figure 4-4 X-Ray powder diffraction showing the instrumental setup of D8 Advance Bruker

4.4.3 Morphology identification

The morphology of crystals was perceived using optical microscopy and scanning electron microscopy (SEM). SEM was used for detailed appreciation of crystals surface topography.

4.4.3.1 Indexing crystal- interfacial angle estimation

Crystal indexing was carried out based on the law of constancy of interfacial angles. Lines were drawn in the middle of each face of crystal micrographs as shown in Figure 4-5. Angles between the faces were calculated. SHAPE [37] software was used to measure the interfacial angle and predict the BFDH morphology of crystal structure taken from the database (CSD). Comparing between the two measured interfacial angles, crystal faces can be indexed.
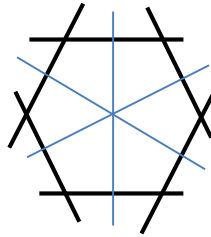
Figure 4-5 Example of constancy of interfacial angles. Lines were drawn in the middle of each faces to measure the angle and compared with values obtained through SHAPE software

4.4.3.2 Olympus microscope

The images of crystals were observed under the upright Olympus BX15 microscope (Figure 4-6). The system is equipped with transmitted light imaging with 5× to 25× objective lenses. Snapshots of crystal were taken using a QImaging colour camera that is linked to Image Pro Plus software [5]. Samples were placed with care on microscope slides before observing under a microscope.

Figure 4-6 Upright Olympus BX15 microscopy equipped with transmitted light with capabilities to measure length and observe morphology of crystal

4.4.3.3 Scanning electron microscopy (SEM)

Detailed observations of crystals surface topography were attained using Hitachi High-Tech Tabletop Scanning Electron Microscopy (SEM) TM3030 (Figure 4-7). This instrument is set with a magnification of 15-60,000× with digital zoom of 2× and 4× and a high-sensitive semiconductor 4-segment back-scattered electrons (BSE) signal detector. Samples were evenly mounted on the sample holder. The holder with samples was then placed into the analysis chamber, and adjusted, so it was at the centre of the chamber. The adjustment was crucial to ensure that samples were aligned with the electron gun beam. A comprehensive auto function program came together with the instrument. Charge reduction mode was selected to reduce charge building up at the surface.
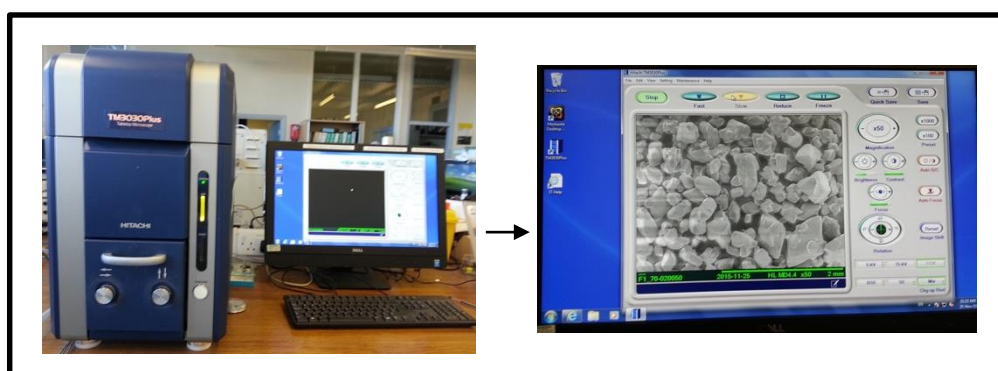
Figure 4-7 Table top SEM model- TM3030 Hitachi High Tech for higher resolution images

4.4.4 Particle size distribution – Laser diffraction

The particle size distribution was measured by laser diffraction. Laser diffraction assumed that particle shape is a sphere. The laser diffraction operated by using light intensity and angle changes.

To give a three-dimensional assessment of particle size and shape, the Sympatec QICPIC/R with Gradis disperser and Vibri feeder were used. The system comprises of modular high-speed image analysis sensor for quasi-static imaging. The measuring range was set to 5-1075 μm with 30% feed rate and initial pressure of 1.0 bar. 1 gram of samples was used for every QICPIC measurement. Instrument parameters, including sample feed rate, dispersing air pressure, and frame rate, were evaluated with each sample during the experiments to get the optimum conditions. The optical concentration was kept below 0.5% to minimise overlapping of particles.

A bottle containing the primary sample was repeatedly rolled and inverted to ensure thorough mixing. The thorough mixing will provide the best representation of particles for

sampling and will give precise particle shape and size distributions (PSD). A scoopful (1 gram) of the sample was taken from the bottle and transferred into the hopper funnel placed at the top of the QICPIC instrument. A little tap against the sides of the hopper will maximise the transfers of sample hence minimise the mass of residues left in the scoop.

The gap width between the hopper and chute was set at 5mm, which is optimized with regards to the sample feeding rate. The vibration of chute helps to segregate the particles to provide well-separated particles for the image analysis. The said optimum combinations of feed rate and gap width are crucial to ensure that the sample is well separated and not overlapping which will not give a good image during measurements.

The VIBRI chute was coated with the sample by passing the sample through the chute once and collected in a separate container. The image analysis measurements were then performed. In between of measurements of different batches of the sample, approximately 0.5 grams of sand were passed through the dispersing line to ensure dispersion properties of the instrument. Both the VIBRI chute and hopper funnel too were cleaned with methanol and left to dry.

4.4.5   Mechanical properties measurement

This section consists of powder mechanical property measurements specifically compaction and shear test. These tests are providing data for powder strength and flowability.

4.4.5.1   Compaction test

The compaction test was carried out using Manesty, F.Press Kilian RX51 simulator. Punch displacement profile was set using virtual control panel (VCP). The simulator is driven by a hydraulic pack and pumped at high flow rates for actuators to move. The actuators were set to oscillate for 15 minutes with a compression force of 5kN (low compression force). 'F' type punch tooling was used to produce tablets. The compaction speed was 0.3m/s using "V" profile. After each tablet had been produced, it will be crushed to measure and enabled the hardness against compression force graph to be plotted.

4.4.5.2 Shear analysis using Schulze RST shear cell

The flowability of samples was measured using ring shear cell, Schulze RST-XS (Figure 4-7). Preparation of samples was done in a glove box to avoid moisture that changes the relative humidity of samples. Roughly 30 grams of samples were placed into the small size shear ring. Samples were left to equilibrate with the environment condition for 24 hours in the glove box. Experiments were controlled using RST control software. Load pressure was set to be 4kPa. Typically, cohesive samples will take longer time for measurement.

4.5 Molecular modelling methods

This section contains the molecular modelling step taken in this study comprising steps for force field fitting, calculation of lattice energetics and crystal chemistry and computation of dislocation energy.

4.5.1 Fitting of force field

The fitting of force field was carried out using general utility lattice program (GULP) [6], a symmetry-adapted software package. GULP too was used to calculate the matrix of elastic constants. GULP increased the calculation efficiency of dispersion energy convergence by applying symmetry also by least squares fitting.

Input for GULP is crystal structure and known properties of the crystal in particular elastic constants. Dreiding force field [7] is used in this study, and the default parameters were computed following Equation 4-1 to 4-6. The fitting was carried out by varying the Lennard-Jones (Equation 4-7) and torsional parameters (Equation 4-5) and compares the observable values obtained from the literature. The fitted parameters were used for optimisation of structure using GULP. Fitting was carried out to get the closest predicted values compared to the observables. GULP computes twenty-one independent entries of the elastic tensor in six by six symmetric matrix format while calculating lattice properties of the crystal. The computed elastic or stiffness tensors were tested for mechanical stability using Born criteria [8][9].

The force field computes total lattice energy (E_{sum}) by considering two parts of interactions, energy from valence interaction (E_{val}) and energy from non-bonded interaction (E_{nb}) as shown in Equation 8.

$$E_{sum} = E_{val} + E_{nb} \hspace{4cm} \textit{(Equation 4-1)}$$

E_{val} comprising of two (E_{bon}), three (E_{ang}) and four (E_{tor}) body interactions is shown in Equation 4-1 and the following Equations 4-2 to 4-3 represent the component for valence energy.

$$E_{val} = E_{bon} + E_{ang} + E_{tor} \qquad \text{(Equation 4-2)}$$

$$E_{bon} = {}^1\!/_2 \, k_n (r - r_e)^2 \qquad \text{(Equation 4-3)}$$

k_n is adjustable constant and r_e is the radius at equilibrium. For three-body interaction,

$$E_{ang} = {}^1\!/_2 \, k_{ang} (\theta_{ang} - \theta_0)^2 \qquad \text{(Equation 4-4)}$$

k_{ang} and θ_{ang} are adjustable constant and angle between two bonds involved in the interactions. For torsion interaction,

$$E_{tor} = {}^1\!/_2 \, V_c [1 - \cos[n_c(\varphi - \varphi_e^0)]] \qquad \text{(Equation 4-5)}$$

V_c and n_c are adjustable barrier and periodicity of the common bond involved in the torsion interaction. φ and φ_e^0 are dihedral angle change and at point of equilibrium. The non-bonded interactions consist of hydrogen bond (E_{hb}), electrostatic (E_q), and Van der Waals (E_{vdw}) as shown in Equation 13.

$$E_{nb} = E_{hb} + E_q + E_{vdw} \qquad \text{(Equation 4-6)}$$

The hydrogen-bonded interaction has been designed as the interaction between donor, hydrogen and acceptor. While for the non-bonded term, Lennard-Jones 12-6 function is used to compute the van der Waals interactions as given in Equation 4-7. The Lennard-Jones consists of two adjustable parameters, collision diameter, σ and well depth, ε. When fitting the force field, all parameters consist in each potential within the force field were varied to satisfy the experimental values.

$$v(r) = 4\varepsilon \left[\frac{\sigma}{r} \right]^{12} - \left[\frac{\sigma}{r} \right]^6 \qquad \text{(Equation 4-7)}$$

4.5.2 Structure conformation analysis

BIOVIA Materials Studio 6.0 [10] is used to carry out the conformation analysis of solid forms. The conformational analysis involves the identification of torsional terminal within a molecular structure. All the paracetamol molecular structures are compared to the FI, which is set as the basis structure.

Conformational analysis is done using the Conformers module within Materials Studio 6.0 using the crystallographic information obtained from the Cambridge Structural Database (CSD). The conformation of a paracetamol molecule was varied by adjusting the torsion angle describing the orientation of all structures in 10° steps noting, that a conformation indistinguishable from the starting position is obtained after a 180° rotation. The torsion angle is expressed on the positions of the nitrogen atom and an oxygen atom of the benzene ring. The torsion energies calculated were mapped to show the torsion energy differences of all the paracetamol solid forms.

4.5.3 Lattice energetics and crystal chemistry computation

Lattice energetics calculation and intermolecular interactions analysis were completed using VisualHabit module embedded in Cambridge Crystallographic Database software, Mercury 3.5.1 [11]. The VisualHabit program is the extended version of HABIT98 [12] with graphical user interface (GUI). However, preliminary calculations were carried using HABIT98.

The lattice energy(E_{latt}), was evaluated separately for all asymmetric units within a single unit cell in crystal host. This evaluation includes together the slice energies (E_{sl}) and attachment energies (E_{att}) for the growth surfaces that are under consideration. The calculation is done with having limiting radii in the range of 10-60Å to limit the area of calculation. All of the atom-atom interaction energy that are within the range were summed to give the lowest lattice energy. The calculation of interactions was carried out along specific crystallographic directions that allows the slice and attachment energy to be calculated.

4.5.4 Dislocation energy calculation

Dislocation energy is computed with the aid of computer program, DISLOC [13] to assist the numerical derivation of the preferred line dislocation. The program calculates the dislocation energy per unit line length constant according to the anisotropic elasticity

theory of straight dislocations. The dislocation energy as shown in Equation 2-13 (Chapter 2), consisted of two components, core dislocation energy and line dislocation energy whereby the latter is related to the strain field around dislocation line represented by the elasticity. The core energy is highly distorted beyond the limit of elasticity. Computation of the core energy may well be computationally expensive hence, approximation following Huntington et.al (1955) [14] is adapted, giving 0.1 of dislocation line energy. Because of the small magnitude, the core dislocation energy is neglected.

The calculation is done in the Cartesian coordinates system to which the elastic constants C_{ij} (Equation 2-19) are referred. The program works by having the elastic constants, lattice parameters and Burgers vector as the input properties. Figure 4-8 shows the calculation step for the program. The angles of θ and $\emptyset$ are varied in integer steps of degrees. The program can calculate up to 20 angle scans with each direction calculate the K and W with a maximum 20 Burgers vectors. Computed K values are then applied to Equation 2 to get preferred dislocation energy.
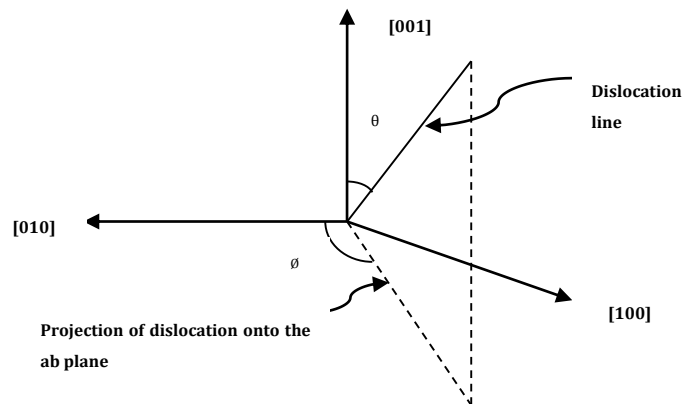
Figure 4-8 Dislocation scanning grid showing the dislocation line and projection of the line on the ab axes

Edge type dislocation is when dislocation line and Burgers vector are perpendicular to each other. For screw-type dislocation, Burgers vector will be parallel to the dislocation line. Hence, identification of angle $\emptyset$ and θ was carried out. K is depending on the line dislocation, Burgers vector and elastic tensors of properties. Using linear anisotropic K values generated was used to compute the energy of line dislocation.

4.5.5 Stereographic projection

The stereographic projection was used to identify the angle for $\emptyset$ and θ of the dislocation line direction. A commercial stereographic plotter WinWulff [15]was used to plot the stereograms for all test systems with regards to its Burgers vector. From the stereograms, all vector that is $\approx 90°$ are taken as the dislocation line direction for edge dislocations.

4.6 Statistical data analysis

Statistical analysis was needed to provide a fair selection of the most probable slip plane. As the results from all test were normative and prescriptive, an approach to transform the results into the same dimension seems obligatory. The multiple attribute decision-making (MDAM) approaches was adopted. MDAM combined several statistical methods, for example, weighting method, fuzzy logic and analytic hierarchy process (AHP). MDAM is commonly used in the materials selection with specific requirement to meet.

This study adopts MDAM approach as found in Jahan and Rao (2008)[16]. The combination of two MDAM approaches namely analytic hierarchy approach (AHP), and technique for order preference by similarity to ideal solution (TOPSIS) was used to get the optimum rank of slip plane. Firstly, the AHP is carried out followed by the TOPSIS. One part of the AHP analysis will involve judgment based on previous knowledge to assign relative importance (weighting factor) of one attribute against the other. To test the consistency of the judgements made, the Eigen factors calculation was used. Eigen factors here relate to the constant variation during matrix transformation. In this analysis, attributes represented the mechanical properties and alternative is the slip plane candidates.

The AHP help to set out the priorities for slip plane characteristic. AHP too provides a rationale for judgements of each slip plane selection process. In this section, the equations behind the AHP are presented. Firstly, results (d_{ij}) from each test were transferred into decision matrix and normalised. Normalisation transforms the d_{ij} values into range of 0-1, therefore can be compared equally. Normalisation equation is as shown.

$$R_{ij} = \frac{d_{ij}}{\left\{\sum_{j=1}^{M} d_{ij}^2\right\}^{0.5}} \hspace{4cm} \textit{(Equation 4-8)}$$

Next, the weighted normalised matrix V_{ij} was obtained by multiplying the normalised values (R_{ij}) and the respective weighting factors (W_{ij}). After obtaining the matrix, the ideal best solution was determined using technique for order preference by TOPSIS.

Theoretically optimum selection will have the shortest Euclidean distance to the ideal solution. The analyses are represented by Equation 4-9 and 4-10.

$$V^+ = \left\{ \left(\frac{\Sigma_i^{max} V_{ij}}{j} \in J \right), \left(\frac{\Sigma_i^{min} V_{ij}}{j} \in J \right) \right\}$$ *(Equation 4-9)*

$$V^- = \left\{ \left(\frac{\Sigma_i^{min} V_{ij}}{j} \in J \right), \left(\frac{\Sigma_i^{max} V_{ij}}{j} \in J \right) \right\}$$ *(Equation 4-10)*

The positive (S_i^+) and negative separations (S_i^-) of results to the ideal solution are calculated using Equation 4-11 and 4-12.

$$S_i^+ = \left\{ \Sigma_{j=1}^N (V_{ij} - V_j^+)^2 \right\}^{0.5}$$ *(Equation 4-11)*

$$S_i^- = \left\{ \Sigma_{j=1}^N (V_{ij} - V_j^-)^2 \right\}^{0.5}$$ *(Equation 4-12)*

The relative closeness (C_i) to the ideal solution is calculated using Equation 4-13.

$$C_i = S_i^- / (S_i^+ + S_i^-)$$ *(Equation 4-13)*

4.7 Conclusions

This chapter has demonstrated the experimental steps and computational techniques used throughout this study. The experimental sections are representing the validation of the modelling findings. This chapter represents the direction of tests to develop the mechanical properties prediction model. Next, result from the case study that represents the two main prediction route is presented.

Reference:

[1]   R.A. Granberg, D.G. Bloch, Å.C. Rasmuson, Crystallization of paracetamol in acetone-water mixtures, J. Cryst. Growth. 198 (1999) 1287–1293.

[2]   R.A. Granberg, Å.C. Rasmuson, Solubility of paracetamol in pure solvents, Journal of Chemical \& Engineering Data. 44 (1999) 1391–1395.

[3]   STARe Excellence Software. Available at: http://us.mt.com/us/en/home/products/Laboratory_Analytics_Browse/TA_Family_Browse/TA_software_browse.html

[4]   HighScore Plus software. Available at: http://us.mt.com/us/en/home/products/Laboratory_Analytics_Browse/TA_Family_Browse/TA_software_browse.html

[5]   Image-Pro Plus software. Available at: http://www.mediacy.com/index.aspx?page=IPP

[6]   J.D. Gale, A.L. Rohl, The general utility lattice program (GULP), Molecular Simulation. 29 (2003) 291–341.

[7]   S.L. Mayo, B.D. Olafson, W.A. Goddard, DREIDING: a generic force field for molecular simulations, The Journal of Physical Chemistry. 94 (1990) 8897–8909. doi:10.1021/j100389a010.

[8]   M. Born, K. Huang, Dynamical Theory of Crystal Lattices, P Clarendon, 1954.

[9]   F. Mouhat, F.-X. Coudert, Necessary and sufficient elastic stability conditions in various crystal systems, Physical Review B. 90 (2014) 224104.

[10]   BIOVIA Materials Studio. Available at: http://accelrys.com/products/collaborative-science/biovia-materials-studio/

[11]   C.F. Macrae, P.R. Edgington, P. McCabe, E. Pidcock, G.P. Shields, R. Taylor, et al., Mercury: visualization and analysis of crystal structures, Journal of Applied Crystallography. 39 (2006) 453–457.

[12]   G. Clydesdale, K. Roberts, R. Docherty, HABIT95-a program for predicting the morphology of molecular crystals as a function of the growth environment, J. Cryst. Growth. 166 (1996) 78–83.

[13]   H.Klapper, Compueter Program to Aid Dislocation Energy Calculation, (1976).

[14]   H. Huntington, Modification of the Peierls-Nabarro model for edge dislocation core, Proceedings of the Physical Society. Section B. 68 (1955) 1043.

[15]   WinWulff-Stereographic projection plotter. Available at: http://www.jcrystal.com/products/winwulff/index.htm

[16]   R.V. Rao, J. Davim, A decision-making framework model for material selection using a combined multiple attribute decision-making method, The International Journal of Advanced Manufacturing Technology. 35 (2008) 751–760.

[17] D. Schulze, Flow properties of powders and bulk solids, Braunschweig/Wolfenbu Ttel, Germany: University of Applied Sciences. (2006).

[18] SHAPE software. Available at: http://www.shapesoftware.com/00_Website_Homepage/

Chapter Five

Prediction of Pentaerythritol & Pentaerythritol Tetranitrate Mechanical Properties

Development of the mechanical properties prediction model based on qualitative and quantitative analysis. This chapter shows the essential tabletting properties being correlated to give relationship between macro and micro behaviour of organic solids

Chapter 5 Mechanical Properties Prediction of Pentaerythritol and Pentaerythritol Tetranitrate

5.1 Introduction

As reviewed in the precedent chapters, the production of drugs tablet from powder involves the clever interplay between the material's deformation behaviour, particularly elasticity and plasticity, to the processing environment condition. It was highlighted in chapter three, that the powder mechanical characteristics observed during compression have a direct relationship to its properties at the molecular level. The few number of crystallographic structure based mechanical properties prediction model of APIs is related to the complexity of molecular crystal structure that is usually having low symmetry.

Now, this chapter will propose a molecular and crystallographic-based mechanical properties prediction to understand the solid forms for direct compression (DC). Here, the Pentaerythritol (PET) and Pentaerythritol Tetranitrate (PETN) were used as case study systems to design the prediction model because of known mechanical behaviour. The prediction revolves around identifying slip systems, entailing the slip plane and direction. This study prediction model leads to two routes, firstly with an active primary slip system and secondly without slip system. Results for PETN were verified against the microhardness indenter study by Halfpenny (1982) [1]. The outcome of the analysis is the identification of ductile or brittle materials. The results obtained in this chapter will serve as the basis structure for predicting the mechanical properties of the five solid forms of paracetamol.

The chapter will comprise of mostly pictorial diagrams to depict clearly the prediction analysis besides the statistical decision matrix to rank the characterised slip plane. Hence, it is useful to note the common representations and annotations. Similar representations will be used for the following chapter.

1. The elements colour code for the molecular structure is carbon (grey), oxygen (red), hydrogen (pink) and nitrogen (blue).
2. The interlock plane is represented by projection of molecules (M_x) in a unit cell onto normal plane. The brackets used will represent (hkl) a specific plane and [uvw] for specific direction.

3. All stereographic projection centre pole will be the specific Burgers vector for calculation.

The general schemes of this chapter are that crystallographic analysis of structures, the test system's mechanical property results, discussions and finally the conclusion. The overall flow of the chapter is as in Figure 5-1. This chapter will present the PET study first follows by the PETN, which both represent the two prediction route of the developed model. The next section will describe the theoretical development of the prediction model.
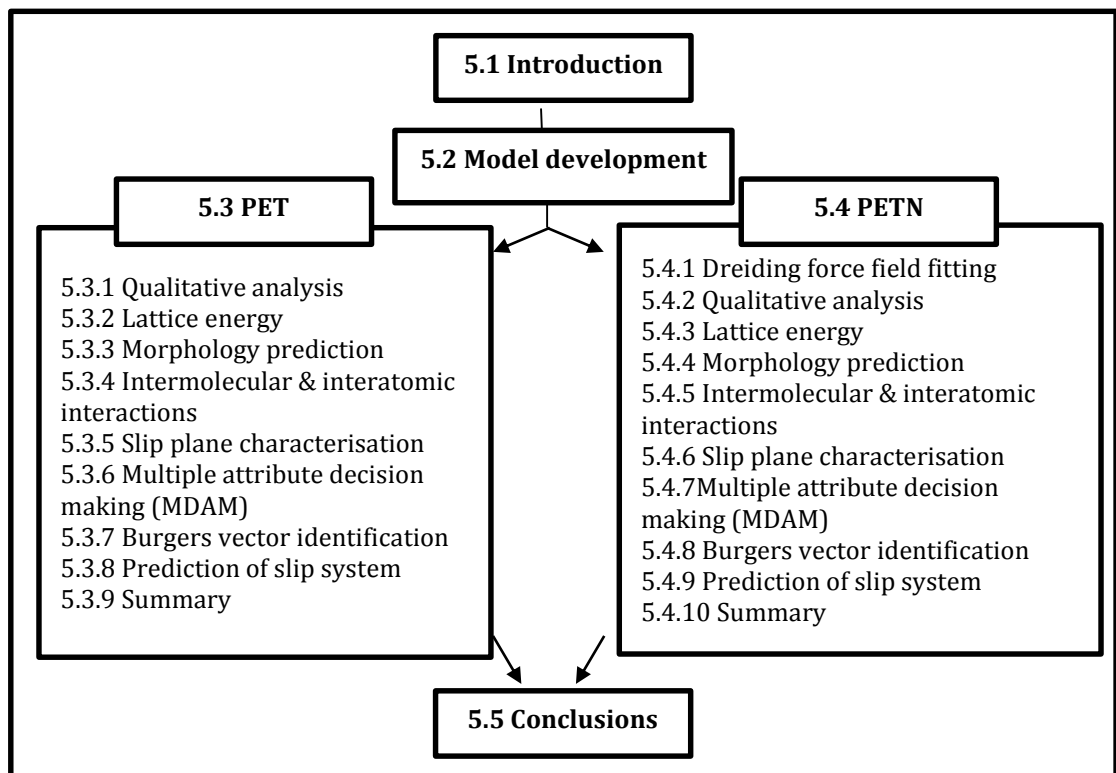
Figure 5-1 Layout for this chapter follow that introduction, PET case study, PETN case study, discussions and finally conclusion. Case study will include tests following the proposed mechanical properties prediction attributes

5.2 Designing the mechanical property prediction model

The general features that are highlighted by Olusanmi et.al (2011) [2] has been adapted as the basis hypotheses for this current research. It is anticipated that the outcome of the prediction model can facilitate in solid forms selection for DC. The dominant features favoured by the mechanical deformation can be categorised into two, surface behaviour and crystal structure. These essential features were divided into four themes namely crystal geometry, crystal chemistry, lattice energetic and elastic energy as illustrated in Figure 5-2. The core themes coloured as green, blue, red, and orange corresponding to the essential features.

Development is done by taking together the quantitative and qualitative work done aforementioned, as a conceptual relationship. Each of these themes will be calculated using several molecular modelling (MM) software. The outputs from these MM calculations were correlated, and most likely slip plane are predicted via multiple attribute decision-making methods (MADM) [3]. The model prediction criteria are related to the displacement plane and direction. The development of prediction model is centered on the concept of an active slip system. Active slip systems occur when the Burgers vector lies within the slip planes. Normally, the crystal has defects that affect the Burgers vector. Hence, the influence of Burgers vector can be emphasised further by working out the dislocations energies for the organic crystals.

Slip planes in the crystallographic structure are commonly recognised by having the densest plane. Besides, having the most atoms, slip planes can also be characterised by knowing its surface energy and rugosity, interlock or intermolecular bond breaking considerations. Properties of the most likely slip planes are having low surface energy and rugosity also the plane does not break any strong intermolecular bond and do not have an interlocking pattern. The summaries of these are seen in Figure 5-2. The identified planes that meet all the attributes for potential slip planes are then tested further to determine if cleavage fracture will take place. The most prominent intermolecular interaction is used for the testing. If the intermolecular interaction direction lies within the plane, then cleavage may take place. This current study is aimed to develop a foundational quantitative model with a less computational cost for predicting mechanical properties based on crystallographic structures.
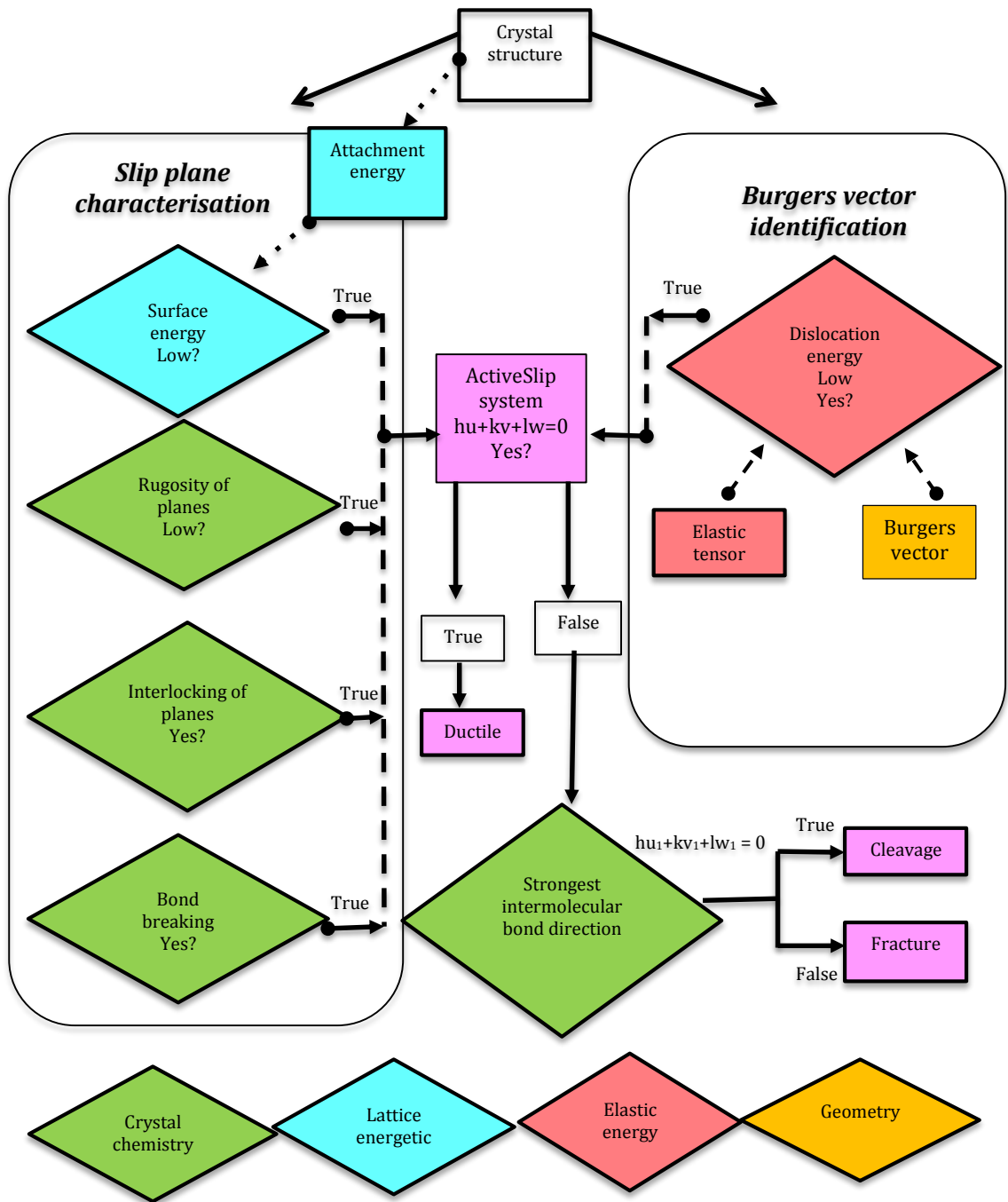
Figure 5-2 Summary for development of the prediction model method. The prediction model is depending on four crystal molecular themes represented by different colours. Green: crystal chemistry, blue: lattice energetic, red: elastic energy, orange: crystal geometry, purple: outcome. All of the themes are interrelated in order to predict mechanical properties of materials. If all of the attributes are true, the slip plane and Burgers vector candidate are tested if there are active. If the result is false, hence the system will not have an active slip system at the primary slip system and potentially will have fracture of cleavage

5.3 Prediction of mechanical properties for the Pentaerythritol

Results from the analysis of pentaerythritol (PET) mechanical properties study was presented according to the way the tests carried out as shown in Figure 5-2. The PET mechanical properties study represents the non-slip system route specifically cleavage.

5.3.1 Qualitative analysis of crystallographic structure of Pentaerythritol

The qualitative analysis of crystal packing pattern and probable slip plane is shown in Figure 5-3. Moreover, identified potential hydrogen bond donor and acceptor are given together. The asymmetric unit of PET molecule consists of a quarter molecule of PET. The type crystal lattice makes the central carbon for molecule one is at (0, 0, 0) and the other is at $(^1/_2, ^1/_2, ^1/_2)$. Molecules in a unit cell of PET are positioned as flat layers within the crystal packing. From a qualitative appreciation of PET molecular packing in Figure 5-3, there are three obvious slip plane candidates, which are (001), (011) and (101). These planes are indicated by the broken lines across the crystal packing. The most likely slip plane is the one having most clearance, which is planes without interlocking or breaking of intermolecular bonds. In PET this is shown to be (001) plane. It can be observed that (011) and (101) planes were cutting hydrogen bond. Hydrogen bonds were created between hydroxyl terminals and represented by the light green dotted lines.

5.3.2 Pentaerythritol lattice energy calculation

Lattice energy calculations were carried out using optimised crystal structures until the energy converged as it reaches the optimum condition. PET lattice energy starts to converge at the radius of 30Å as seen in Figure 5-3 with a value of -136.69 kJ/mol. This lattice energy is comparable to the sublimation enthalpy by [4] that is -131.26 kJ/mol. The lattice energy is related to the sublimation enthalpy by having the correction of -2RT at which R is the gas constant, and T is the temperature.

The PET optimised unit cell parameters shown to be 0.9% to 3.28% difference in comparison to the experimental sublimation enthalpy. The higher calculated unit cell parameters are caused by the empirical force field used to carry out calculation also the electrostatic contributions.

5.3.3 Pentaerythritol morphology prediction

As been described in chapter four, the purpose of the morphology prediction is to assist in linking the bulk crystal properties to the interfacial interactions occurring when crystallisation is taking place. The morphology predicted based on BFDH were refined by using attachment energy model. PET showed to have a pyramidal morphology. Figure 5-3 illustrated observed striations in PET. The attachment energy is computed during calculation of the lattice energy and represented in Table 5-1. Data include values for attachment and slice energies, interplanar spacing according to the morphological importance faces and anisotropy factor. The anisotropy factor describes the satisfaction of each face towards intermolecular interactions [5]

Table 5-1 Predicted morphological importance faces for PET using the attachment energy model. Included together were the interplanar d-spacing, attachment and slice energy and the anisotropy factor

			PET	
Face (hkl)	d_{hkl} (Å)	Slice energy (kJ/mol)	Attachment energy (kJ/mol)	% Saturation of surface molecule (anisotropy factor)
101	5.12	-54.70	-81.99	47.00
110	4.44	-42.52	-94.18	11.76

The most unsatisfied face for PET was (110), with anisotropy values of 11.76% and was reflected by its' highest attachment energy of -94.18 kJ/mol. The high anisotropy factor for (101) face with (47.00%) showed that the plane satisfaction, hence reduce desires to form interactions with incoming molecules. The exposed faces properties are vital for driving the growth rate during the crystallisation process. Likewise, the exposed faces purportedly effect the final shape of the crystal. It can be seen that for (110) and (101) faces, the hydroxyl group was exposed. Exposed hydroxyl group promotes the formation of hydrogen bond. The summary for the early stage of the crystallisation properties of PET structure can be appreciated based on the morphology prediction as seen in Figure 5-3.
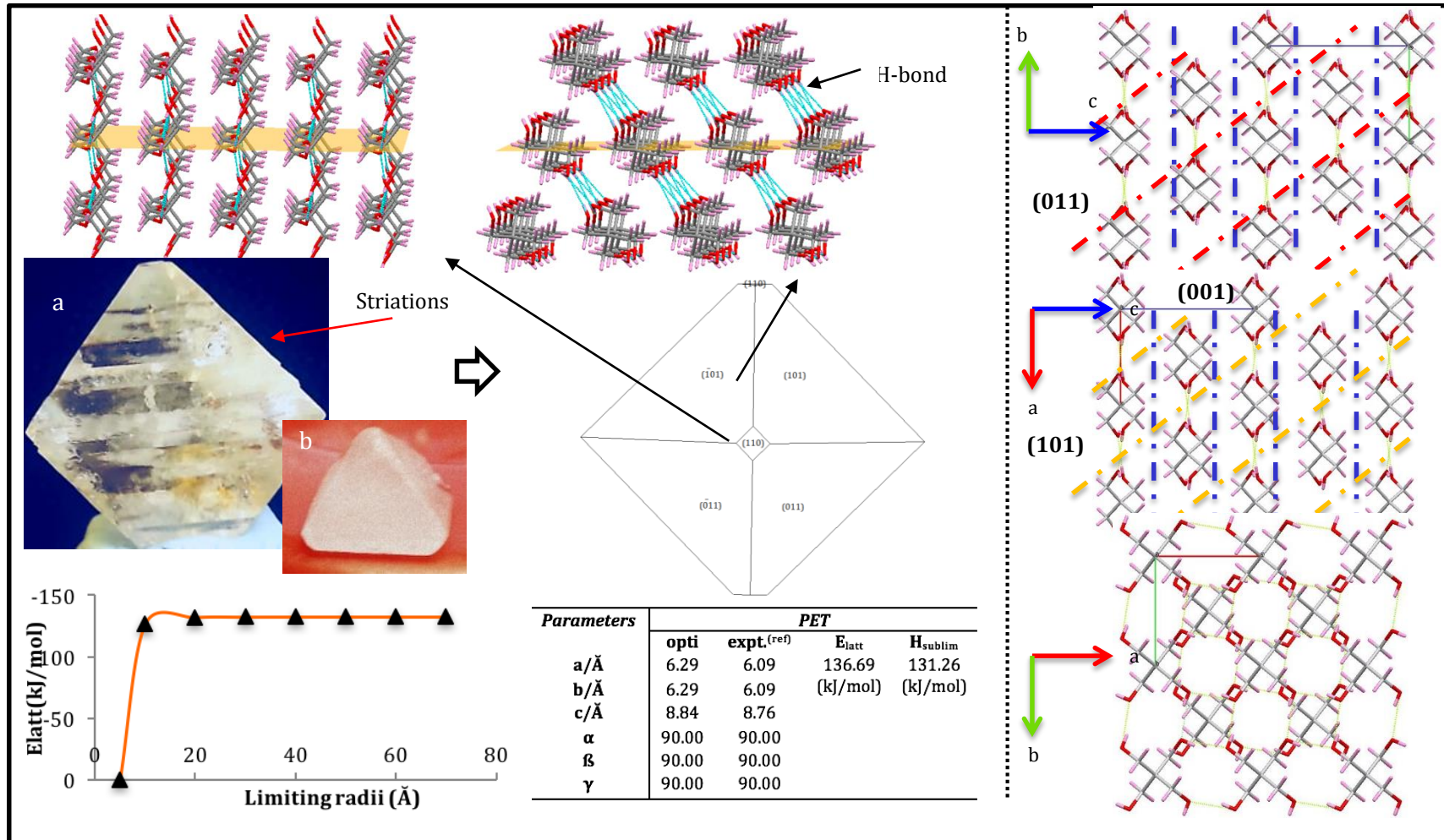
Figure 5-3 PET predicted morphology using attachment energy model in comparison to the experimental grown crystal with striations/ trace of cleavage [12] pointed in red. The plot for lattice energy convergence plot and the optimised structure unit cell parameters were given. The 2 × 2 × 2 crystal packing viewing from [100], [010] and [001] were shown with potential slip plane highlighted in broken lines. Potential slip planes are (011), (001) and (101)

Figure 5-3 PET predicted morphology using attachment energy model in comparison to the experimental grown crystal with striations/ trace of cleavage [12] pointed in red. The plot for lattice energy convergence plot and the optimised structure unit cell parameters were given. The 2 × 2 × 2 crystal packing viewing from [100], [010] and [001] were shown with potential slip plane highlighted in broken lines. Potential slip planes are (011), (001) and (101)

5.3.4 Pentaerythritol intermolecular and interatomic interactions elucidation

The intramolecular is associated towards the lattice energy and stability of the molecular structure, and intermolecular interaction is indirectly related to the formation of the final morphology of crystal. This section provides the findings of intermolecular and interatomic interactions of PET.

The interatomic analysis of PET showed that the major contributor towards PET lattice energy is the hydrogen atom involves in hydrogen bonding with -94.81kJ/mol. The full calculated results are shown in Table 5-2. Second in rank is oxygen with -56.44kJ/mol followed by carbon atoms with -23.93kJ/mol. The individual atomistic contributions can be seen in Figure 5-4.

Table 5-2 Atom type contribution towards the total lattice energy of PET with the highest contributor is hydrogen in H-bond

Atom type	Attractive (kJ/mol)	Repulsive (kJ/mol)	Coulombic (kJ/mol)	Total (kJ/mol)
Hydrogen (H-bond)	-87.65	75.19	-82.29	-94.81
Hydrogen	-32.34	20.92	86.85	75.19
Carbon	-35.77	10.25	1.59	-23.93
Oxygen	-116.64	86.02	-25.82	-56.44

Taking from the individual atom analysis, the energy contributions of the main functional groups exist in the structure can be determined (Table 5-3). It was shown that the hydroxyl terminal of PET was contributing the most towards the lattice energy with 79% compared to the aliphatic chain with only 21%.

Table 5-3 Main functional group contributions towards the lattice energy of PET. The hydroxyl was giving 79% while aliphatic only 21%

Main functional group	Attractive (kJ/mol)	Repulsive (kJ/mol)	Coulombic (kJ/mol)	Total (kJ/mol)	%
Hydroxyl	-126.52	89.70	-17.57	-54.39	79
Aliphatic	-110.12	92.22	-3.85	-21.76	21
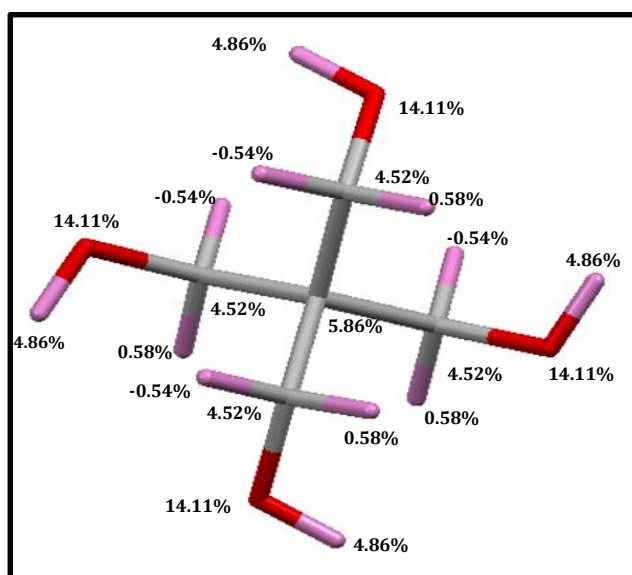
Figure 5-4 PET molecular structure highlighting the specific atomistic contributions to the computations of lattice energies

List of the strong intermolecular interactions was presented in Figure 5-5 and Table 5-4. Because of the nature of PET that has four terminals exposing the hydroxyl group, mostly the intermolecular interactions created were a hydrogen bond. Therefore, in this section, only the top three strongest interactions were described. Results from the crystallographic calculations with the limit for zero bond strength is 0.418 kJ/mol revealed three significant intermolecular bonds ranging from -20.17 to -1.34 kJ/mol created within the range of 30Å limiting radius.

Table 5-4 Intermolecular interactions strength analysis for PET. There are eight strongest bonds in PET, identified as the hydrogen bond with the strength of -20.17 kJ/mol. The other two van der Waals bonds is much weaker with the strength of -5.06 and -1.34 kJ/mol

Bond	Multiplicity	Distance (Å)	Intermolecular energy (kJ/mol)	Dominating interatomic interaction type
A	8	6.28	-20.17	H-bond
B1	16	6.27	-5.06	VdW
B2	8	8.89	-1.34	VdW

By looking into the molecular structure of PET, the intermolecular interactions were identified as hydrogen bond (A) as seen in Figure 5-5. It was also apparent from Table 5-4 there are eight of the A bonds in a unit cell of PET. These interactions took place in the directions of [010] with a distance of 6.28 Å. Interestingly, there was a striking difference in the intermolecular energy strength of PET. The strength of the strongest bond (A) was four times higher in comparison to the next strong bond (B1). The substantial strength drop supports the inference that PET micro properties are governed by hydrogen bonds. The huge difference between the hydrogen bonds and the van der Waals intermolecular interactions was related to the domination of coulombic energy.
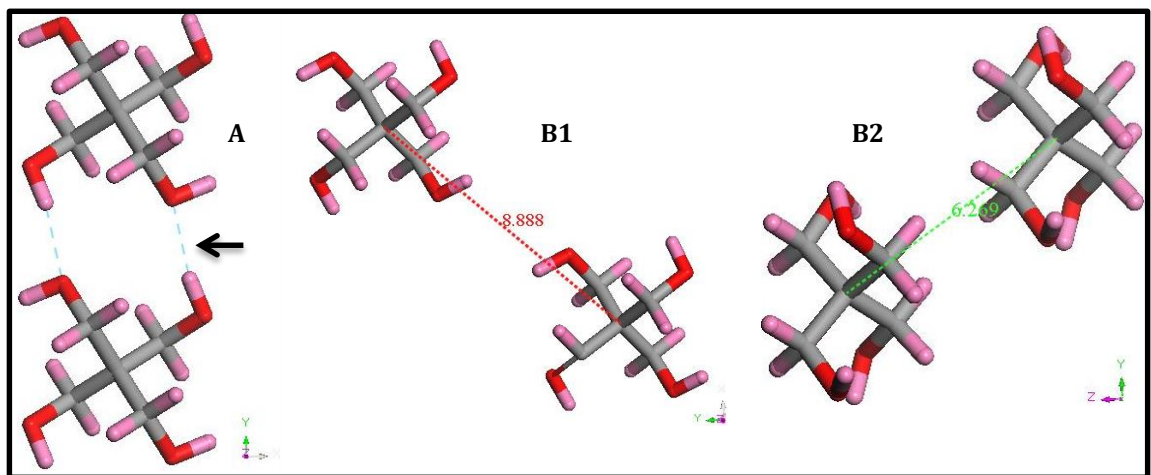
Figure 5-5 Dominating intermolecular interactions created between molecules in a unit cell of PET. The strongest intermolecular interaction in PET is between oxygen of hydroxyl group in the direction of [010] towards hydrogen in neighbouring molecule

The hydrogen bond domination and direction of the bond created are representing the directionality of the PET crystallographic structure. The hydrogen bond was created parallel to (001) plane, hence creating strong in-plane interactions. Moreover, this directionality plays a vital part in deciding the type of fracture as suggested in this study prediction model. A significant amount of hydrogen bond supposedly will increase the strength of PET. Having to interpret the PET interatomic and intermolecular interaction, the next section will present the results for the characterisation of slip plane following attributes listed in Figure 5-2.

5.3.5 Pentaerythritol slip plane characterisation

Previous qualitative appreciation of crystal packing, as shown in Figure 5-3 showed that PET had three candidates slip plane that were (101), (011) and (001). These observed slip planes were compared with a set of planes that were quantitatively tested. Slip plane analysis is crucial in proving the extent of deformation that is happening in anisotropic materials. Though PET exhibited certain morphological importance planes, this study considers combinations of Miller indices set to be maximum at 1. Therefore, seven combinations were identified from (100) to (111). The reason is to test the applicability of the parameters tested used in the model development and not to overlook potential slip plane that is not morphological importance.

5.3.5.1 Approach proposed for rugosity calculation

Rugosity is representing surface roughness. The analysis for surface rugosity reflects the ease of plane to slip. A computational relationship using geometry plane equation was derived to tackle the slip plane rugosity quantitatively. In this study, the surface rugosity was described based on distance deviation of atoms positioned within the molecular packing towards the potential slip plane as seen in Figure 5-6. This is the first time that the surface rugosity is represented using crystallographic structure by applying numerical relationship specifically the plane equation. Rugosity of the surface has been studied previously for bulk powder using empirical and numerical model, namely, atomic force microscopy [6] and non-contact optical profilometry [7] but there was no study found to represent rugosity based on the crystallographic analysis.

The calculation involves finding the projected distance parallel to the plane normal of each atom in molecules of one unit cell and computing the distance root mean square (RMS) (Figure 5-6). The RMS values are optimised by allowing the plane to be adjusted to scale up to one d-spacing. The ideal condition is at a minimum RMS with respect to the rugosity between the slip plane and atoms of the molecule. Low RMS values with regards to distance separating between the candidate of slip plane and atoms in a unit cell, define a minimum deviation. Minimum deviation correlates to flat layers of crystal packing. Moreover, this minimum deviation is being used as a measure to reflect the crystal-packing pattern that is useful for interlocking analysis. The Cartesian coordinates are used for the RMS calculation.

Besides being able to represent rugosity of surface, the proposed relationship can also elucidate the interlock of slip planes. The interlock of slip planes has been emphasised as one crucial crystallographic behaviour in the molecular crystal that posed affect to the mechanical property of materials. Before the quantitative analysis, the interlock of planes is analysed qualitatively. Based on this proposed mathematical relationship, the interlock within crystal packing can be represented quantitatively. The plane is interlocked when the range of one molecule intercept another molecule in the unit cell. The range is the farthest and closest atom distance for one molecule with respect to the plane. The interlock of planes will halt slip deformation to take place when under force.
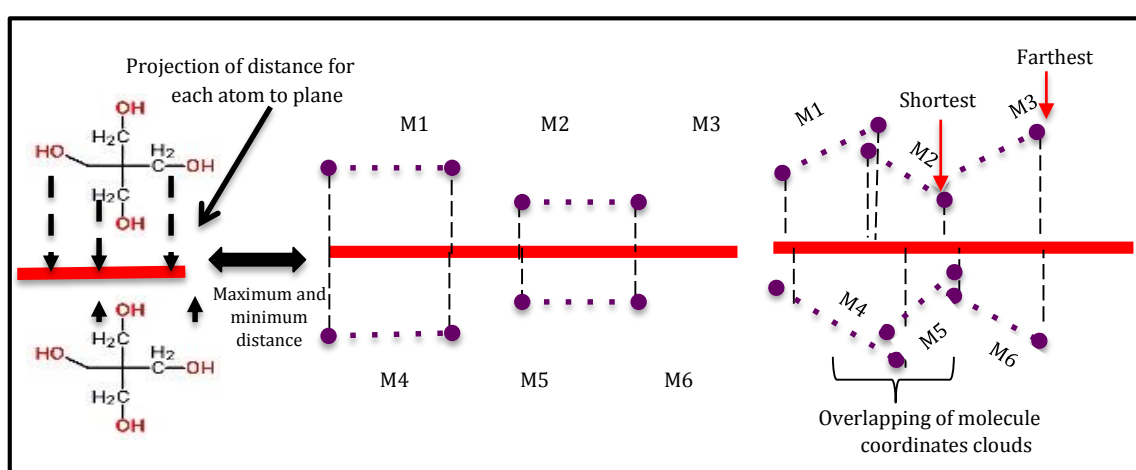
Figure 5-6 Example of one unit cell of crystal consisting two molecules. Rugosity is work out by calculating each distance projection to the plane normal for each atom in molecules in the unit cell. The shortest and farthest distance for each atom in unit cell was taken for interlocking of slip planes analysis. Illustrations represent the projection of each atom to scaled candidate slip plane. Overlapping of the range between shortest and farthest atom is representing corrugated molecules position within crystallographic structure

Apart from the rugosity, another attribute to describe plane's ease to slip is the specific surface energy. Surface energy is calculated using the attachment energy of specific surface as given in Equation 2-11 in section 2.2.2 (Chapter 2). A high surface energy is associated with a strong attachment energy that in turn makes it difficult for the surface to slip. The ability of the plane to slip too may well be related to the amount of energy needed to break the hydrogen bonds. For PET, the hydrogen bond breaking is represented by binary numbers to define yes or no. Table 5-5 listed the rugosity, surface energy and hydrogen breaking results.

From Table 5-5, PET is shown to have highest RMS value of 4.94 for (010) and (100) planes, and the lowest RMS was 3.03 for (110) plane. The lowest surface energy for PET is 136.00 mJ/m^2 with the highest is 215.00 mJ/m^2 for (111) and (010) plane respectively. The main

observation is that the surface energy did not have a direct relation to the rugosity values. Though theoretically rugosity and surface energy is describing plane ease to slip, the manner of calculation separates the two. The rugosity list of slip plane candidates with increasing values is (110) < (101) = (011) = (111) < (001) < (100) = (010). From Table 5-5 PET hydrogen bond interactions are evident whereby most planes need to break hydrogen bonds except for (001).

The abovementioned approach for calculating rugosity, provide a new and quick tool to characterise mechanical properties of materials with regards to crystallographic structure. The next subsection describes quantitative representation for interlocking of slip planes.

5.3.5.2   Interlocking representation

Potential slip planes arrangement in the crystallographic packing was evaluated by examining the overlapping of molecules on its farthest and shortest atomic distance towards candidate slip plane. Schematic representation relating to the interlocking of slip planes was studied and shown in Figure 5-6. This test correlate to the degree of the interlocking between slip planes with regards to its crystallographic structure position.

Crystals with corrugated molecules are suspected to have less freedom to move when a force is imposed. The interlock analysis of planes in PET showed that (001) range was not overlapping however other planes did. Figure 5-7 showed the differences between candidate planes interlocking properties clearly. The overlapping was assessed based on projection normal to the plane.
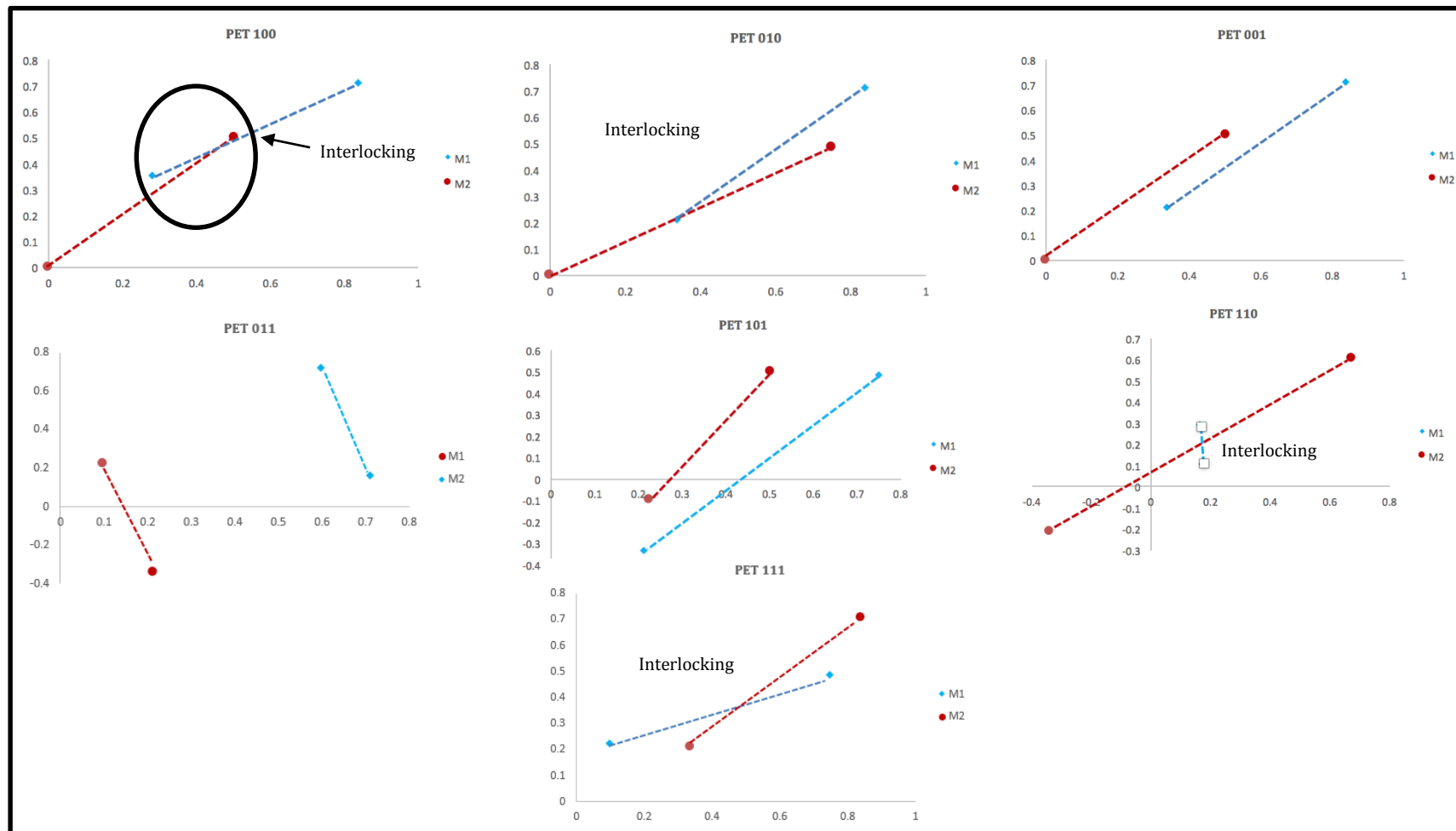
Figure 5-7 Representation of interlocking analysis showing two molecules in a unit cell of PET, molecule 1 (M1-red) and molecule 2 (M2-cyan). Two data points of M1 and M2 were representing atomic coordinates. The two atoms were the shortest and farthest distance for each molecule projected onto lattice plane. If the molecules overlapped i.e. line intercepting, it is assumed that it will interlock

5.3.6 Multiple attribute decision-making calculations

So far this chapter has described the quantitative steps taken for examining slip plane candidates through rugosity, surface energy, hydrogen bond breaking and interlock of planes. Noticed that all attributes were in different dimensions. Thus a statistical approach mentioned in Section 4.6 was adopted to compare all planes equitably. This subsection will demonstrates the selection of the best slip plane using multiple attribute decision-making (MADM) concepts.

As highlighted in Section 4.6, MDAM will involve judgements and prior knowledge to decide the weighting factor corresponding to each attribute. The weighting involves vital input from materials scientist experience dealing with the attributes tested. Because of there is less information to show relative importance between attributes, all were weighted equally. The importance of each attribute is decided using pairwise matrix. The pairwise matrix represents the importance of one attribute in comparison to the other to meet preferred slip plane characteristic. At the moment, the weighting assigned is sufficient to describe the process for characterising the ideal slip plane.

5.3.6.1 Construction of decision matrix

The values obtained from the molecular modelling calculations were transferred into decision matrix as shown in Table 5-5. All qualitative evaluations were converted into quantitative values. The normalisation was carried out to make the values in the same physical dimension for comparison which was 0-1. The normalisation values are denoted in Table 5-6. The normalisation values of each attribute of PET are ranging between 0 and 0.49.

Table 5-5 Data obtained from molecular modelling were transferred into decision matrix. The qualitative analysis, i.e., the interlocking of slip plane and hydrogen bond breaking were transformed into quantitative values using binary numbers, yes (1) and no (0)

PET				
Attributes / Alternatives	Surface energy (mJ/m^2)	Rugosity	Interlock of planes	H-bond breaking
(100)	215.00	4.94	1.00	1.00
(010)	215.00	4.94	1.00	1.00
(001)	151.00	3.36	0.00	0.00
(110)	152.00	3.03	0.00	1.00
(101)	175.00	3.29	1.00	1.00
(011)	175.00	3.29	0.00	1.00
(111)	136.00	3.29	1.00	1.00

Table 5-6 Normalised values of each attribute with regards to the alternatives (potential slip planes) for PET were in the range between 0.00 and 0.49

Attributes Alternatives	PET Surface energy	Rugosity	Interlock of planes	H-bond breaking
(100)	0.46	0.49	0.40	0.41
(010)	0.46	0.49	0.40	0.41
(001)	0.32	0.33	0.00	0.00
(110)	0.33	0.30	0.40	0.41
(101)	0.37	0.33	0.00	0.41
(011)	0.37	0.33	0.40	0.41
(111)	0.29	0.33	0.40	0.41

Table 5-7 Weighted normalised values for all attributes about slip plane candidates. The best value for rugosity was 0.08, and the least is 0.12. For surface energy, the best was 0.07 and the least was 0.12. The interlock of planes and hydrogen bond breaking, the best was 0.00 and the least was 0.10

Attributes/ Alternatives	PET Surface energy	Rugosity	Interlock of planes	H-bond breaking
(100)	0.12	0.12	0.10	0.10
(010)	0.12	0.12	0.10	0.10
(001)	0.08	0.08	0.00	0.10
(110)	0.08	0.08	0.10	0.10
(101)	0.09	0.08	0.10	0.10
(011)	0.09	0.08	0.10	0.00
(111)	0.07	0.08	0.10	0.10

Working with the values of the weighted normalised attribute as given in Table 5-7, the best and least condition for each attribute with regards to ideal behaviour can be determined. From this values, the separation from the ideal condition can be obtained and presented in the next subsection.

5.3.6.2   Separation measures for alternatives

Turning now to the analysis of alternatives that have attributes fit to be the ideal slip plane. The positive and negative limit or separations to the optimum condition are calculated and shown in Table 5-8. PET has positive separation values ranging between 0.103 and 0.157 while the negative separation is between 0.070 and 0.148. The (001) and (011) planes had the least separation from the ideal conditions.

Table 5-8 Separation analysis (TOPSIS) of alternative (potential slip planes) with regards to specific attributes. The smallest different showed an alternative that is closer to the optimum condition

Attributes Alternatives	Surface energy	Rugosity	Interlock of planes	H-bond breaking	Squared of sum	Positive Separation
PET (positive separation)						
(100)	2.03E-03	1.80E-03	1.04E-02	1.04E-02	2.47E-02	1.57E-01
(010)	2.03E-03	1.80E-03	1.04E-02	1.04E-02	2.47E-02	1.57E-01
(001)	1.17E-04	1.06E-05	0.00E+00	1.04E-02	1.05E-02	1.03E-01
(110)	1.29E-04	2.43E-05	1.04E-02	1.04E-02	2.10E-02	1.45E-01
(101)	5.61E-04	2.30E-06	1.04E-02	1.04E-02	2.14E-02	1.46E-01
(011)	5.61E-04	2.30E-06	1.04E-02	0.00E+00	1.10E-02	1.05E-01
(111)	7.86E-06	2.30E-06	1.04E-02	1.04E-02	2.08E-02	1.44E-01
PET (negative separation)						
(100)	2.41E-05	5.75E-06	4.16E-06	1.44E-03	1.47E-03	3.84E-02
(010)	2.41E-05	5.75E-06	4.16E-06	1.44E-03	1.47E-03	3.84E-02
(001)	1.53E-03	1.35E-03	1.00E-02	1.44E-03	1.43E-02	1.20E-01
(110)	1.49E-03	2.02E-03	4.16E-06	1.44E-03	4.96E-03	7.04E-02
(101)	6.93E-04	1.48E-03	4.16E-06	1.44E-03	3.62E-03	6.02E-02
(011)	6.93E-04	1.48E-03	4.16E-06	1.96E-02	2.18E-02	1.48E-01
(111)	2.23E-03	1.48E-03	4.16E-06	1.44E-03	5.15E-03	7.18E-02

Table 5-7 to Table 5-9 which was consisting the normalised weighted normalised and separation values were shown to demonstrate the ways to process results that lead to the final ranking system. It is important to note that, the values in Table 5-7 to Table 5-9 does not carry real meaning on its own. However, these values were needed to get to the final ranking percentage.

Table 5-9 Ranking of candidates slip plane according to MDAM analysis. The most preferred slip plane based on the analysis is (001) with 94% fit the optimum condition

	PET	
Rank	*Alternatives*	*%optimum*
1	**(001)**	94
2	**(011)**	58
3	**(101)**	54
4	**(110)**	33
5	**(111)**	33
6	**(100)**	25
7	**(010)**	21

The full rank of the calculated values of deviation to optimum attributes for all alternatives tested is in Table 5-9. As can be seen, the smallest deviation from the optimum condition was 94% that was for (001) plane. The striking difference of (001) to the other planes was that it did not break hydrogen bond. For this particular reason, there was a huge gap between (001) to the next (011) with 36% difference. Consequently, in characterising the slip plane, it will involve the clever interplay between all tested attributes and satisfaction of each. The preferred Burgers vector results are presented in the next subsection.

5.3.7 Pentaerythritol vector calculations

Potential Burgers vectors were analysed by crystal structure geometry so intermolecular bonds relationship were ignored. The calculation computed 31 probable Burgers vector each for PET. Because of the symmetrically equivalent properties of the crystal system, the only vector with lowest Miller indices was considered. In this study, only seven Burgers vector were used for calculations with limiting vector being double the longest unit cell parameters. Given that the Bravais lattice of PET is a body-centered, the shortest Burgers vector was halved.

The shortest Burgers vector was expected to be the preferred direction for line dislocations to occur to give minimum dislocation energy for PET. The dislocation energy is related to work done in displacing atoms during a slip, and the Burgers vector represents the displacement. Within this section, the calculated values for elastic tensor constant are presented first followed by the dislocation energy calculation and finally the identification of active slip systems.

5.3.7.1 Elastic constants calculations

Elastic constants are signifying the strength and toughness of compounds under pressure. The elastic components used for computing the dislocations energies were presented in Table 5-10. The result from the calculation was compared to the literature values [30-31] for validation. The calculated elastic tensors showed a good fit to the tensors calculated using ultrasonic (US) with about 15% difference for each component. For PET, the elastic tensor revealed that the uniaxial stress constant is demonstrating that PET stiffness is anisotropic to compression because C_{11} and C_{22} (45.73 GPa) is not equal to C_{33} (11.31 Gpa). The low stiffness value in the C_{33} direction shows the potential for deforming in the [001] direction. The computed diagonal shear constants for PET, $C_{44}=C_{55} \approx C_{66}$ were low with only ≈ 1 GPa difference between the two values. The diagonal elastic constants values showed

lower values compared to the other uniaxial stiffness constants. The calculated elastic tensor was used for computing the dislocations energy. The following subsection, list the dislocation energy and possible type of dislocation taking place in PET.

Table 5-10 Comparisons between calculated elastic tensors using GULP and the literature values for PET. Calculated elastic constants value ranging from 2.03 to 45.73 GPa. The literature values are measurement from DRX (dynamic recrystallisation microstructure), Brillouin, ultrasonic (US), wave velocities (WV)

Crystal system	Elastic constants (GPa)	This study	(US) [∝]	(DRX) [∝]	(WV) [∝]
PET	$C_{11}=C_{22}$	45.73	40.50	6.10	39.95
	C_{12}	22.10	26.60	-2.50	24.82
	$C_{13}=C_{23}$	8.97	10.50	0.50	9.13
	C_{33}	11.31	13.90	8.00	13.67
	$C_{44}=C_{55}$	5.85	2.74	3.50	2.58
	C_{66}	6.62	2.52	4.60	2.49
	C_{16}	2.03	3.10	-0.39	1.97

∝[8]

5.3.7.2 Dislocation energy calculations

To compute the dislocation energy, the Burgers vector of the PET was calculated beforehand. List of Burgers vector without considering the dislocation energy is presented in Table 5-12 The shortest Burgers vector for PET was half of translational vector [111] giving 3.14Å in length. This followed by [010] and [100], which are the unit cell parameters. The dislocation energy was given by the dislocation energy constant K and the square value of Burgers vector length b^2 using Equation 2-15 or Equation 2-16 section 2.3.2.3 (Chapter 2). The list of preferred Burgers vector slightly changes when sorted following the dislocations energy analysis. The K values for PET are in the range of 5.85 to 14.17GPa as shown in Table 5-12.

Table 5-11 Summary of Burgers vector and dislocation energy constant (K). The line dislocation energy with respect to each Burgers vector were given in eVnm^{-1}. The halving of [111] significantly reduced the line dislocation energy compared to the other magnitude of Burgers vector

BV	Magnitude BV(Å)	Magnitude BV²(Å)²	K(GPa)			$K(BV)^2$
			[100]	[010]	[001]	($evnm^{-1}$)
$^1/_2$[111]	3.14	9.86	8.11	8.19	10.01	0.50-0.62
[010]	6.29	39.501	12.84	6.19	13.83	1.53-3.41
[100]	6.29	39.501	7.92	8.19	10.01	1.95-2.02
[001]	8.84	78.181	6.39	6.38	5.85	2.86-3.12
[110]	8.89	79.002	9.53	9.99	14.17	4.70-6.99
[011]	10.85	117.682	8.56	6.32	8.53	4.65-6.29
[101]	10.85	117.682	9.31	8.55	8.49	6.24-6.84

The values of K in three axial directions indicated the anisotropy behaviour of PET. The continuum analysis for K values in a different angle about the three axial directions were presented by the polar plot (Figure 5-8). The polar plot will then describe the dislocation energy variation about the K factors. From Table 5-11, the shortest Burgers vector, $^1/_2$[111] gave the smallest dislocation energy with 0.50evnm^{-1}. The largest dislocation energy was 6.99evnm^{-1}. The polar plot showed that the generally the K values in the [100] and [010] were slightly similar. The most uniform distribution was given for [111] Burgers vector across all angle (0-360°).

Burgers vector [100]
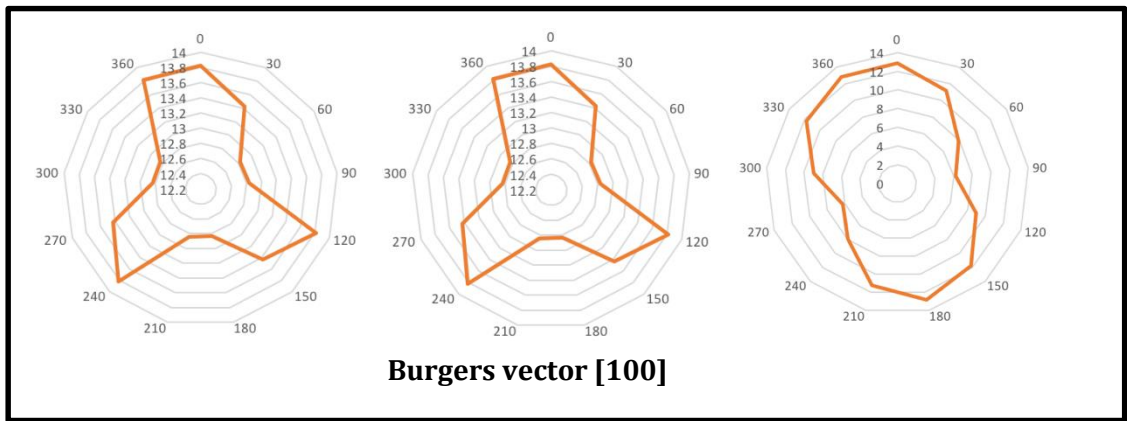
Figure 5-8 The dislocation factor (K) continuum representation showing the anisotropy effects. It was plotted in the three axial directions [100], [010] and [001] of polar plot. The scanning angle related to the dislocation program is $\emptyset = 0 - 360°$ $\theta = 0 - 360°$. Determination of specific axial K values: [100] $\emptyset = 90$ $\theta = 90$ [010] $\emptyset = 0$ $\theta = 90$ and [001] $\emptyset = 90$ $\theta = 0$
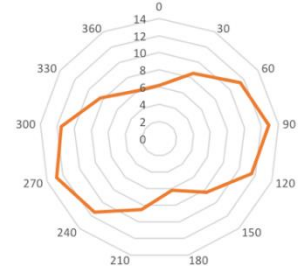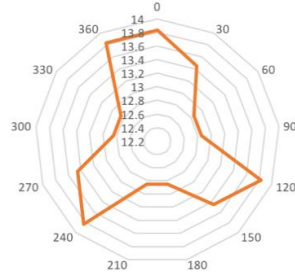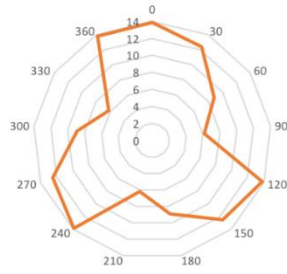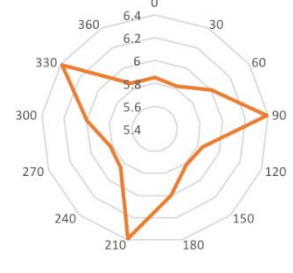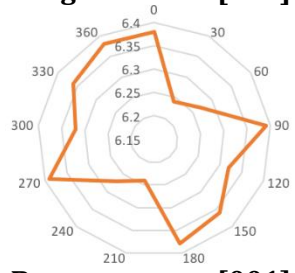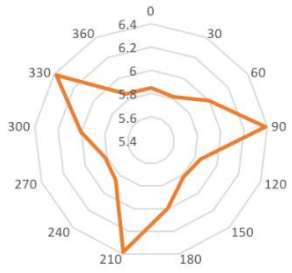
Burgers vector [010]
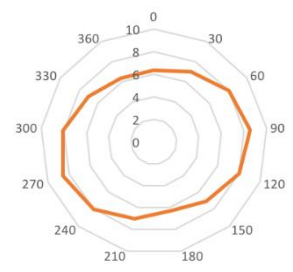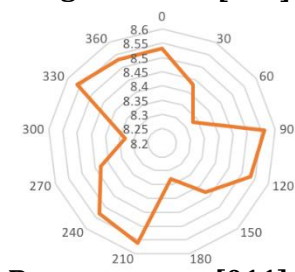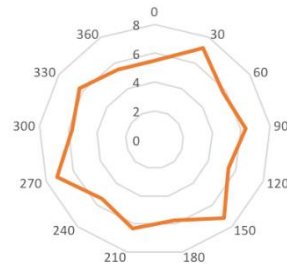
Burgers vector [001]
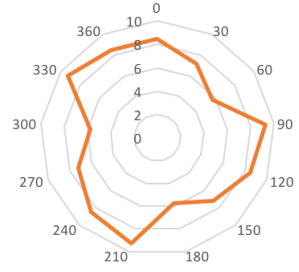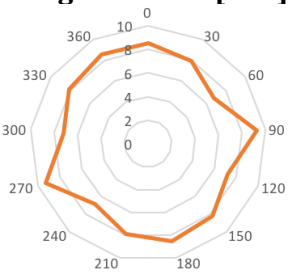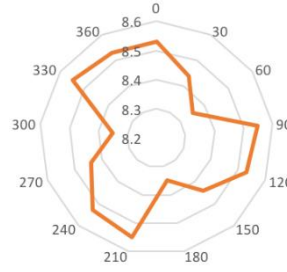
Burgers vector [011]
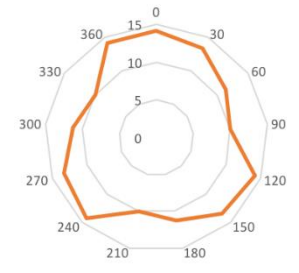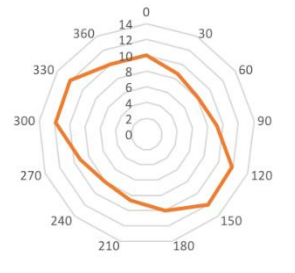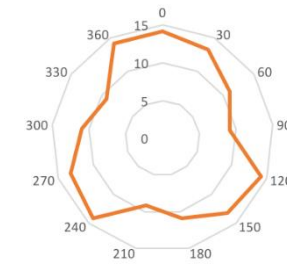
Burgers vector [101]
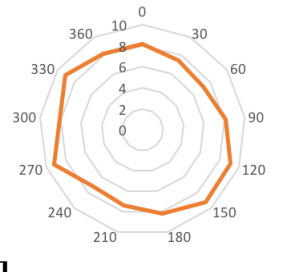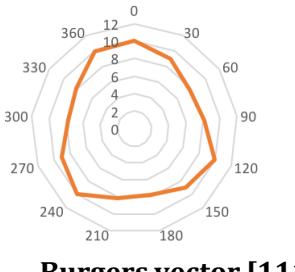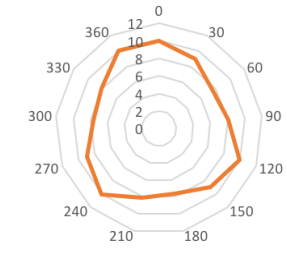
Burgers vector [110]

Burgers vector [111]

From the continuum, the potential edge and screw dislocations for PET were identified. Table 5-12 lists the possible type of dislocations in PET together with the K and the corresponding energy. The stereographic projection in Figure 5-9 depicted the line dislocation at 90° to the respective Burgers vector for edge dislocations. The stereographic projection in this subsection demonstrated the standard approach for determining line direction positions of the PETN and the five solid forms of paracetamol case studies. This was because of the space limitation, but the projections for the other system will be provided in Appendix A. Because PET is a tetragonal system, therefore, the perpendicular dislocation line identification is straightforward. However, this will not be the case for a non-orthogonal system such as monoclinic as the transformation angle need to be considered.
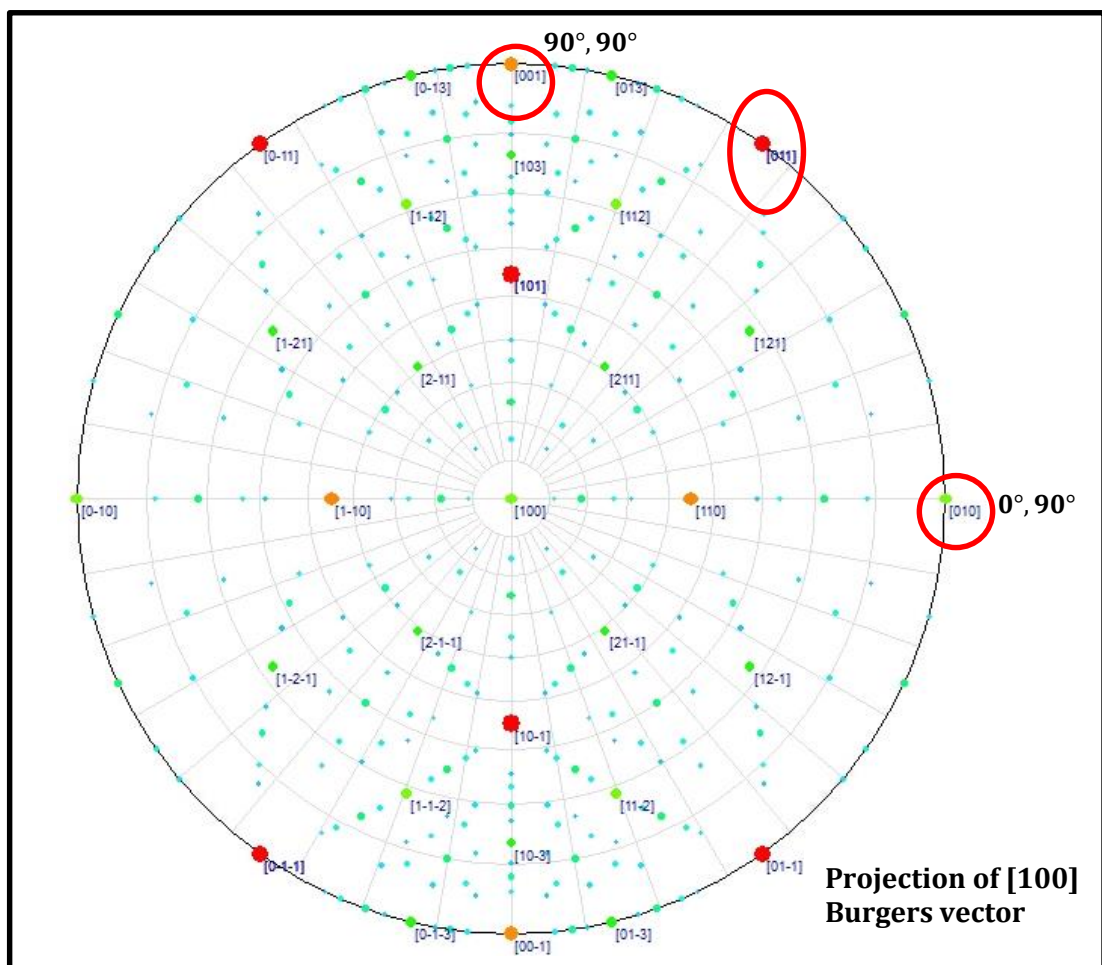
Figure 5-9 Stereographic projection for all Burgers vector with the perpendicular dislocation line directions will potentially have be edge (vector circled in red). The pole is the specific Burgers vector tested. The angle between the Burgers vector and the dislocation line was taken as the scanning parameters to calculate dislocation factor (K)

Projection of [010] Burgers vector

Projection of [001] Burgers vector

Projection of [011] Burgers vector

Projection of [101] Burgers vector
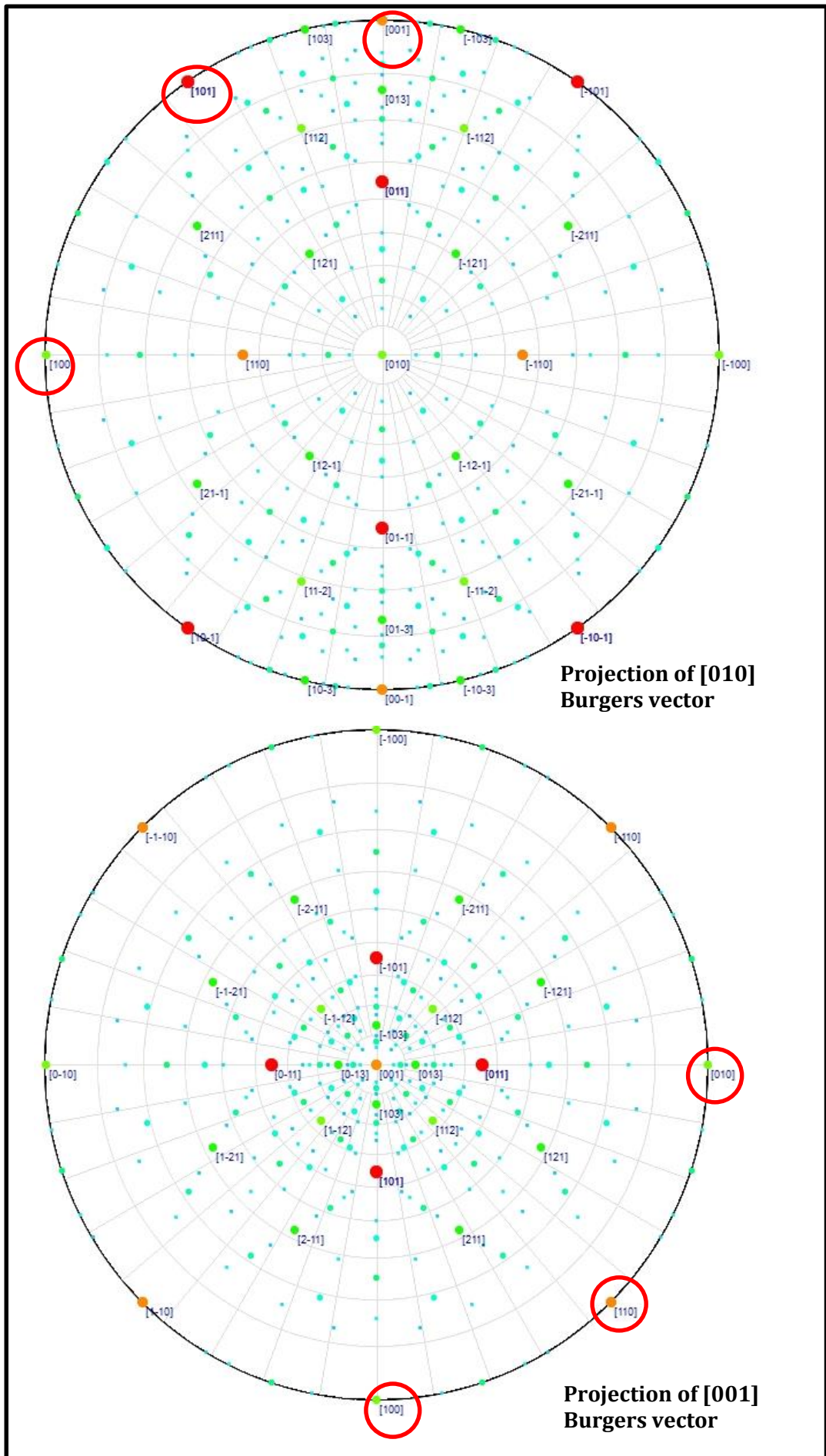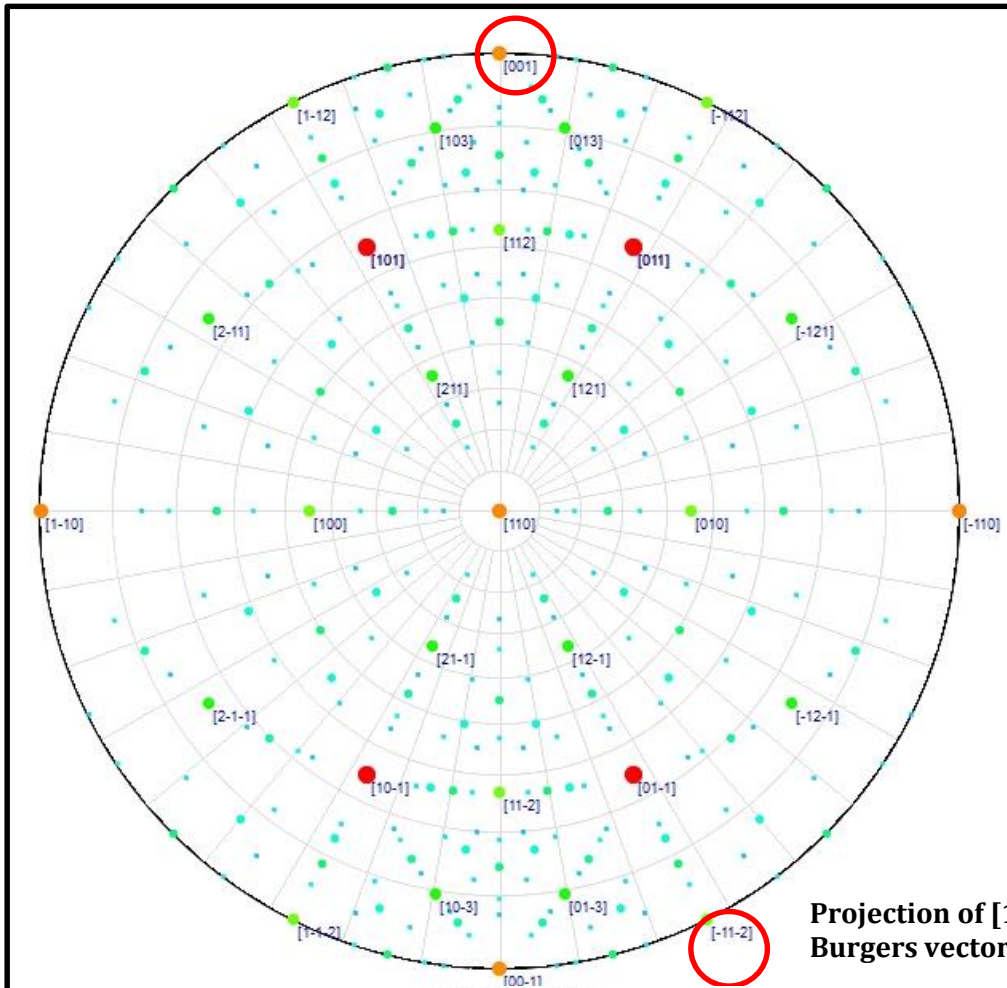
Projection of [110]
Burgers vector
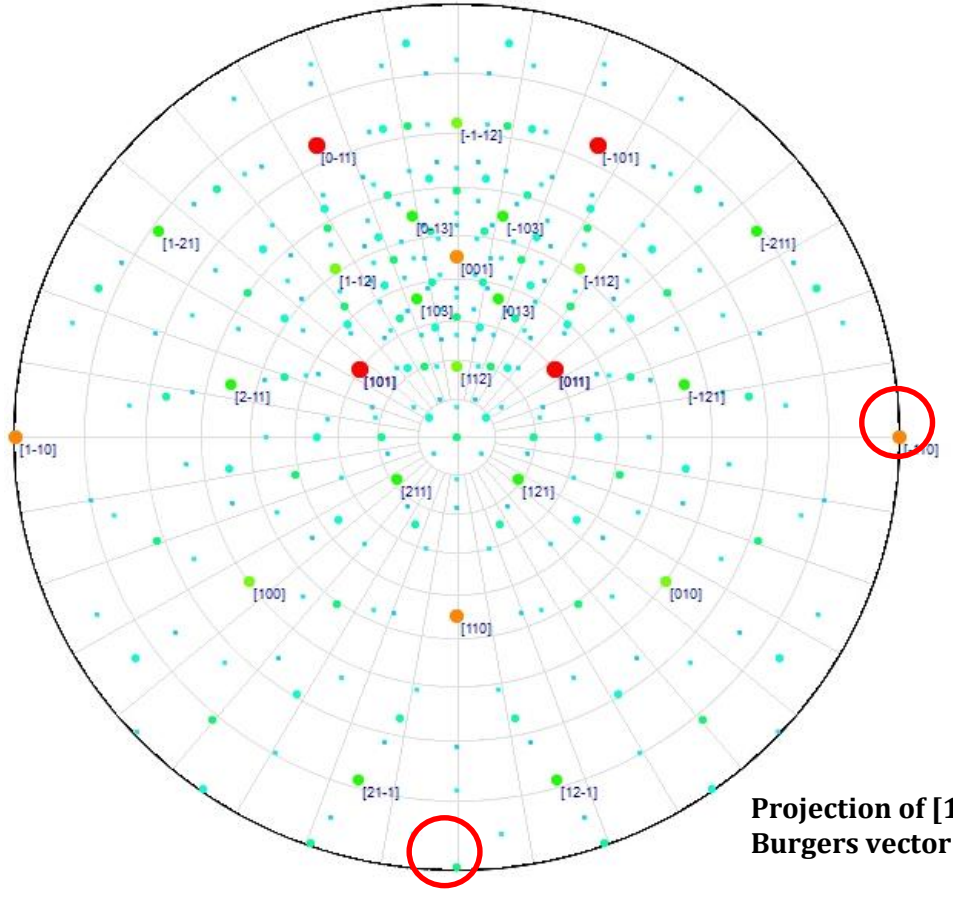
Projection of [111]
Burgers vector

Vectors identified through the stereographic projection were taken as the vector involved in edge dislocations and presented in Table 5-12. Besides the edge dislocations, vectors that were parallel to the projected Burgers vector were the screw dislocations. Table 5-12 showed that 20 edge and seven screw dislocations were identified with regards to the Burgers vector tested. Burgers vector with the lowest dislocation energy was $\frac{1}{2}$[111] with all energies below 1eVnm^{-1}. Therefore, the primary Burgers vector for PET is the $\frac{1}{2}$[111] and the least likely was [110]. The difference of classifying Burgers vector with regards to the dislocation energy is presented in Table 5-13. Slight changes of preferential for most likely to slip Burgers vector was seen. Nonetheless, the primary Burgers vector was the same.

Table 5-12 List of potential edge and screw dislocations in PET. There are 20 edge and seven screw dislocations. The largest dislocation energy is 6.99 in the [110] direction

				PET		
BV	**LV**	**Angle $\emptyset°$**	**Angle $\theta°$**	**K (GPa)**	**Kb^2(eVm^{-1})**	**Type**
[100]	[100]	90	0	7.92	1.95	Screw
	[010]	0	90	8.19	2.02	Edge
	[011]	54	90	8.61	2.12	Edge
	[001]	90	90	10.01	2.47	Edge
[010]	[010]	0	90	6.19	1.53	Screw
	[100]	180	90	12.84	3.17	Edge
	[101]	125	90	11.06	2.73	Edge
	[001]	90	90	13.83	3.41	Edge
[001]	[001]	90	0	5.85	2.86	Screw
	[010]	0	90	6.38	3.12	Edge
	[110]	315	90	6.32	3.09	Edge
	[100]	270	90	6.39	3.12	Edge
[011]	[011]	0	45	6.39	4.70	Screw
	[100]	180	90	8.56	6.29	Edge
	[02-1]	270	89	8.55	6.29	Edge
	[121]	247	89	8.24	6.06	Edge
[101]	[101]	90	45	6.37	4.68	Screw
	[010]	0	90	8.55	6.29	Edge
	[20-1]	270	89	6.4	4.70	Edge
	[21-1]	292	89	6.97	5.12	Edge
[110]	[110]	45	90	8.31	4.10	Screw
	[001]	90	90	14.17	6.99	Edge
	[-112]	63	90	8.14	4.02	Edge
	[-111]	44	90	8.33	4.11	Edge
$\frac{1}{2}$[111]	[111]	45	45	7.79	0.48	Screw
	[-110]	0	90	8.19	0.50	Edge
	[20-1]	234	89	7.27	0.45	Edge

Table 5-13 Comparison of preferred Burgers vector for PET using geometrical and dislocation calculations. Lists are in descending order with the most preferred at the top

	PET	
Rank	Burgers vector (Geometrical)	Burgers vector (Dislocation Energy)
1	½[111]	½[111]
2	[010]	[001]
3	[100]	[100]
4	[001]	[010]
5	[110]	[011]
6	[011]	[110]
7	[101]	[101]

5.3.8 Prediction of pentaerythritol slips system

The dot product analysis shows that the shortest Burgers vector of PET, ½ [111] did not lie in the most likely slip plane (001), and therefore it is not active. From Figure 5-2, the final step for route two (inactive primary Burgers vector) is to test either cleavage, or brittle fracture will take place. Taking the likely slip plane, Weiss zone law (dot product) test was carried out. Probing the intermolecular interactions in PET, the strongest bond direction that was [010] was taken for the dot product test. Therefore, the direction was on the plane, making strong in-plane bonds that propagate the cleaving to take place at (001) plane in the direction of [010]. The scanning electron microscopy micrograph of PET (Figure 5-10) showed the detachment of top exposing the cleavage face. Hence cleaving may happen with relation to the dominating intermolecular interaction directionality instead of preferred Burgers vector

(a) (b)
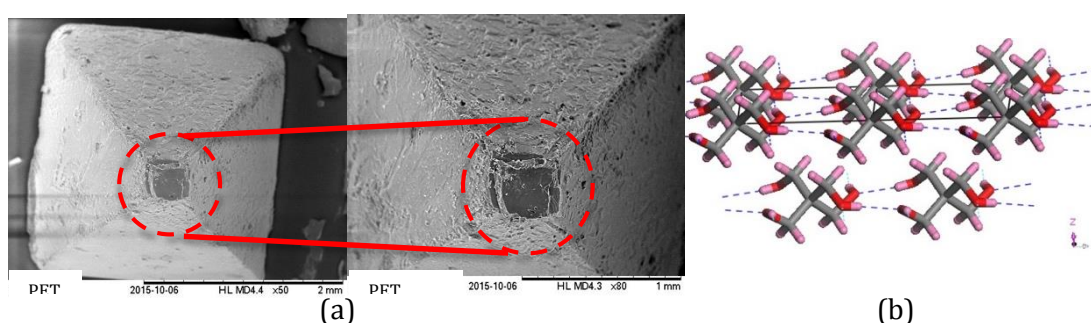
Figure 5-10 a) SEM images of PET crystal showing the probable cleavage plane when small force were applied. b) Surface of (001) for PET with hydrogen bonding created in the direction of [010] that explains the cleaving of the surface besides differentiating of having strong intermolecular bond to give the direction for displacement

5.3.9 Summary

At this point, the standard approach for the proposed mechanical properties prediction model has been acquired. To recap important findings so far,

1. PET crystal structure have four hydroxyl terminals that lead to domination of hydrogen bond interactions. The strongest intermolecular interaction was created in the [010] direction.

2. The four attributes of slip plane namely rugosity, surface energy, hydrogen bond breaking and interlocking are interrelated and more industrial input needed for the relative weighting factor.

3. The (001) plane was characterised to have 94% of the ideal behaviour of a slip plane.

4. The calculated line dislocation energies were increasing as the preferability of Burgers vector decreasing (Table 5-13). As shown in Table 5-11, the anisotropy behaviour in molecular structure affects the slip property.

The presence of defects, particularly, dislocations result in a variance of energy needed for a slip to take place also the direction of slip. Better slip system analysis is expected by considering dislocation energy as shown in the vicinity of this case study. PET showed the applicability of the first route of the prediction model developed. Next subsection will describe the results for the second prediction route that is having active slip system. The test is done using PETN.

5.4 Prediction of the mechanical properties for the Pentaerythritol Tetranitrate

This section is presenting results from the analysis of pentaerythritol tetranitrate (PETN) mechanical properties study. The layout of this section is following that of PET case study. While PET showed the non-active route, PETN case study represents the active slip system route precisely plastic deformation.

5.4.1 Dreiding force field fitted to pentaerythritol tetranitrate

Initially, PETN was fitted against Dreiding force field in an attempt to have tailored to structure parameters and better elastic components result. In this study, the force field parametisation involved only the soft degree's parameters, that is the Lennard-Jones and

four body bond (torsional contributions). Because of the large numbers of parameters involved, the parametisation were carried in stages by trial and error. Tests were carried out for both Lennard-Jones A and B parameters, and results showed that only B changes when manipulated. Hence, only the B parameter that represents the attractive interactions was further parametised. From computed results, when varying bonds that are involved in hydrogen bonding, the attractive energy values changes significantly. Furthermore, the computed percentages of error were higher compared to the atoms that were not participating in a hydrogen bonding interaction, making the fitting further from the target values.
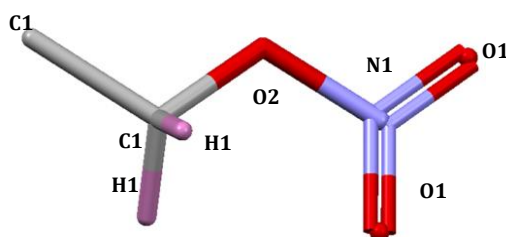
Figure 5-11 Asymmetric unit of PETN molecular structure labelled with atom type for force field fitting

Fitted Dreiding force field parameters can be obtained in Table 5-14, while Figure 5-11 illustrates the asymmetric structure for PETN showing the atomic position. The newly fitted force field parameters values were significantly varying when compared to the original parameters values specifically the N1-O1 interaction with values of 30.04 kcal/mol (125.78kJ/mol). The large differences between the initial and final parameters values reflect the amount of fitting needed for PETN. The substantial changes of N1-O1 interaction parameter were caused by the electrons resonance interaction between the two atoms.

By applying the newly fitted Lennard-Jones parameters to Dreiding force field, the optimised PETN structure was generated. In contrast, for PET, the structure optimisation was carried out using the generic Dreiding force field as it produces a good fit between calculated and observables values. The results reflect the suitability of the force field and the semi-empirical charges to PET and PETN for the cohesive and electrostatics energies contribution. Nonetheless, the parametised Dreiding force field in this study need to be tested for transferability for use in a different molecular system as the fitted force field was meant specifically for PETN.

Table 5-14 The Lennard-Jones B parameters, which represents the attractive part for Dreiding force field fitted to the PETN structure. The percent of difference showed the substantial different between initial B parameter to the final calculated values for N1-O1 interaction

Atom 1	Atom 2	Potential form	B (kcal/mol)-Fitted	B (kcal/mol)- Original
C1	C1	Lennard-Jones	3.48	3.90
C1	N1	Lennard-Jones	0.04	3.78
N1	N1	Lennard-Jones	1.56	3.66
C1	O2	Lennard-Jones	4.95	3.65
N1	O2	Lennard-Jones	0.04	3.53
O2	O2	Lennard-Jones	2.47	3.40
N1	O1	Lennard-Jones	30.04	3.53
O1	O2	Lennard-Jones	0.01	3.40
O1	O1	Lennard-Jones	1.89	3.40

Computed values of elastic constants for PETN are presented in Table 5-15. From the table, the elastic tensors of PETN agree well with experimental values measured using resonant ultrasound microscopy. PETN stiffness values showed that the diagonal constants were showing the lowest values with $C_{44}=C_{55}$, 2.29 GPa and C_{66} are 7.79 GPa. The diagonal constants represent the resulting shearing components. The low stiffness values for the diagonal components make potential shearing takes place in the C_{44}, C_{55} or C_{66} directions taking through ab, bc, or ac-plane. The calculated result matched the literature with most components have 10% difference. The largest difference was for $C_{44} = C_{55}$ that may be due to the resonance terminal of the nitrate esters.

Compared to PET, PETN calculated stiffness constants were much lower with values ranging from 2.29-15.33 GPa. The PETN stiffness components satisfied the Born mechanical stability criteria exhibiting positive free energy hence no spontaneous reaction can take place. The PET stiffness values were 60% higher from the PETN for C_{11}, C_{22}, C_{44} and C_{66} while 11% for C_{33}. The higher stiffness values reflect the hydrogen bonding networks within the PET molecular structure contrasted to PETN that has no hydrogen-bonding network observed. Instead, PETN was dominated by close contacts interaction particularly van der Waals.

Table 5-15 Comparisons between calculated elastic tensors using GULP and literature values for PETN. The literature measurements shown are Brillouin, resonant ultrasound spectroscopy (RUS), and pulse-echo ultrasound (P-E)

Crystal system	Elastic constants (GPa)	This study	RUS$^{\propto}$	Brillouin$^{\propto}$	$P - E^{\propto}$
PETN	$C_{11}=C_{22}$	15.33	16.77	16.92	17.18
	C_{12}	9.36	5.75	5.14	5.43
	$C_{13} =C_{23}$	6.42	5.57	7.80	7.48
	C_{33}	10.07	10.33	11.62	12.44
	$C_{44} =C_{55}$	2.29	5.04	4.45	5.03
	C_{66}	7.79	3.04	3.80	3.93

$\propto$: [8]

The elastic components of PETN have maximum strength of 15.33GPa in the $C_{11} = C_{22}$. The next subsection will characterise the crystallographic structure, lattice energetics and morphology prediction.

5.4.2 Qualitative analysis of crystallographic structure of Pentaerythritol Tetranitrate

The pentaerythritol tetranitrate (PETN) molecule is comparable to pentaerythritol (PET) with only slight different for the terminals connected to the central carbon, whereby, PETN have the nitrate group (O=N=O), while PET the hydroxyl group (-OH). The unit cell of PETN was seen to have a similar molecular arrangement as PET, with one molecule, was positioned at the centre and another molecule at the corner of the unit cell. It is useful to reiterate that PET is a body-centered while PETN is a primitive crystal. The reason for taking the PETN molecule positioned in the centre was to simplify the subsequent calculations.

From a qualitative overview of Figure 5-12, there were no obvious hydrogen bonds' forming between PETN molecules in the unit cell. Nonetheless, the analysis of close contacts, particularly the van der Waals showed that several bonds were forming between the double-bonded oxygen atoms towards the hydrogen atoms connected to the carbon atoms. As seen in Figure 5-12 PETN molecules arrangement within the molecular packing follows the screw axis resulting in capping pattern when viewed through a and b-axis. Viewing from c-directions displayed a flat layer crystallographic pattern. It was apparent from Figure 5-12 the potential slip planes for PETN were of the family (110) on the basis of it did not interlock with molecules and did not cut any strong intermolecular interactions.

Hypothetically, the intermolecular interactions created in PETN were not imposing much towards the mechanical properties based on the qualitative analysis done. However, concentrated van der Waals may poses same strength as hydrogen bond as describe by [9] earlier in their study. Next, result for the lattice energy calculation of PETN is presented and followed by the morphology prediction.

5.4.3 Pentaerythritol tetranitrate lattice energy calculations

The equilibrium conditions were achieved by observing the lattice energies convergence. From the calculation, PETN converged at 30Å with -161.54 kJ/mol, approximately 10kJ/mol higher than the sublimation enthalpy [4] as represented in Figure 5-12. The difference was associated with the temperature at which the sublimation enthalpy was measured. Larger lattice energy was expected for PETN compared to PET because of the four nitrate terminals. The optimised structure of PETN was shown to have the a and b unit cell components to be 3.13% and to be 7.72% differences compared to the experimental structure. It shows that the predicted values were slightly higher than the experimental.

5.4.4 Pentaerythritol tetranitrate morphology prediction

The PETN was predicted to have a tabular habit as seen in Figure 5-12. For PETN, the most unsatisfied face given in Table 5-16 was (101), with anisotropy value of 39.3% and attachment energy of -98.17 kJ/mol. For face (110) the percentage of saturation of surface molecule was 52.90%, that is 13.6% higher than (101) face. The attachment energy for (110) was -75.91kJ/mol showing fewer interactions at the surface.

Table 5-16 Predicted morphological importance faces for PETN using the attachment energy model. Included together are the interplanar d-spacing, attachment and slice energy and the anisotropy factor

			PETN	
Face (hkl)	d_{hkl} (Å)	Slice energy (kJ/mol)	Attachment energy (kJ/mol)	% Saturation of surface molecule (anisotropy factor)
(110)	6.77	-85.41	-75.91	52.90
(101)	5.71	-63.40	-98.17	39.3

Comprehensive evaluations of intermolecular interactions were elaborated in the following subsection. This will include the quantitative calculations of the intermolecular and interatomic interactions energies contribution.
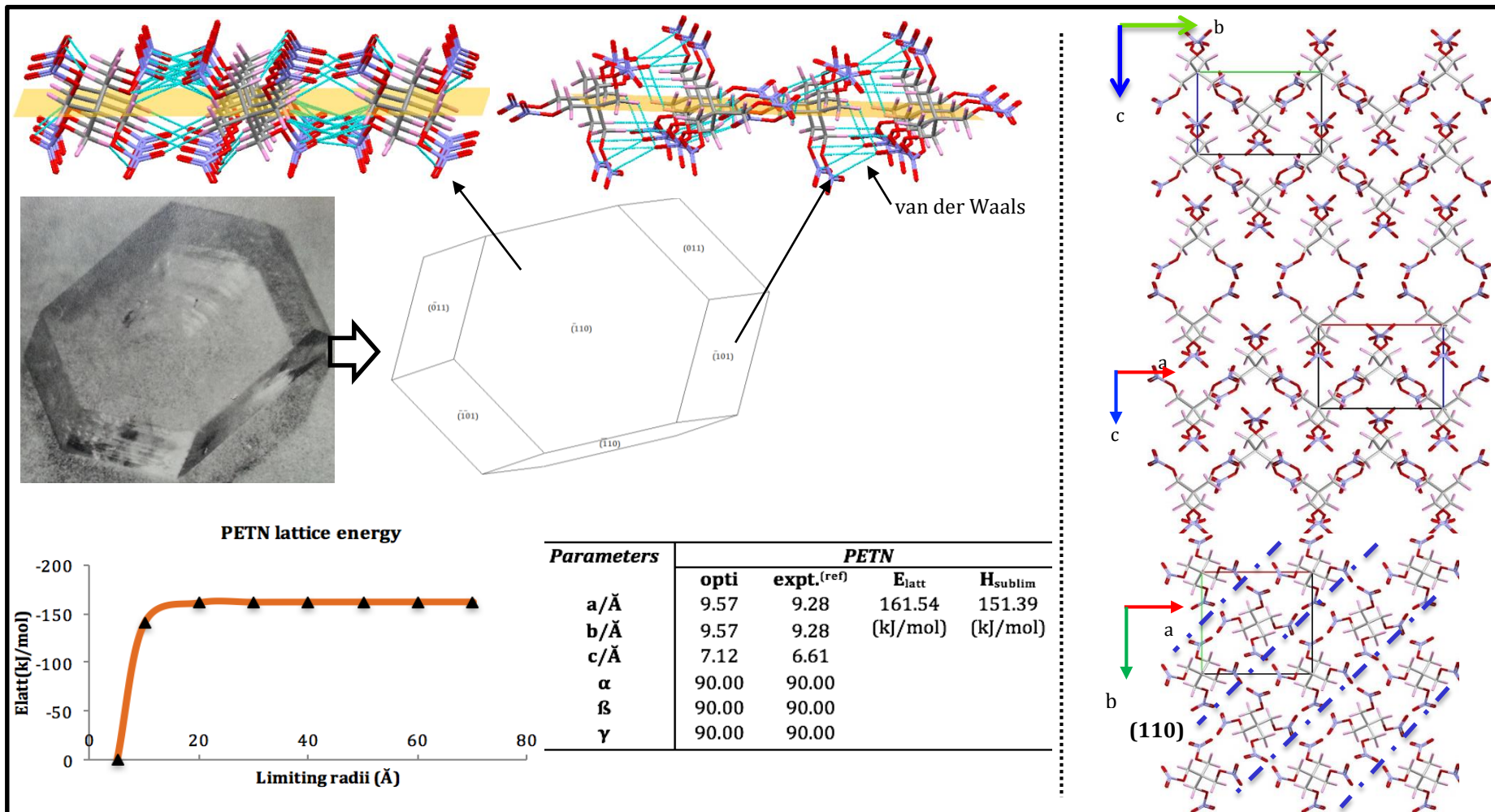
Figure 5-12 Predicted morphology for PETN compared to the experimental crystal [1]. Dominant faces are (110) and (101). The Lattice energy converged at -161.54 kJ/mol. The 2 × 2 × 2 crystal packing viewed from [100]. [010] and [001] with potential slip plane shown as broken line. The identified plane is (110). Cleaved surfaces of (110) and (101) showed close contacts interaction created parallel to the plane

5.4.5 Pentaerythritol tetranitrate intermolecular and interatomic interactions elucidation

The interatomic analysis of PETN showed that oxygen contributes the most atomic interactions with -405.47kJ/mol. The high energy values were compensated by the nitrogen atoms with 269.70kJ/mol. The energy of nitrogen was caused by the electrostatic contribution represented by coulombic energy as shown in Table 5-17. The coulombic energy showed to dominate the PETN structure. Compared to the nitrogen atom, the oxygen atom has higher attractive energy with -84.10kJ/mol while nitrogen was -23.64kJ/mol. Figure 5-13 showed clearly the total distribution of specific atom types for PETN.

Table 5-17 Interatomic contributions of PETN structure with the highest contributor is oxygen. Dominant energy is coulombic reflecting the electron shifting to fill in the valence

Atom type	Attractive (kJ/mol)	Repulsive (kJ/mol)	Coulombic (kJ/mol)	Total (kJ/mol)
Nitrogen	-23.64	6.15	287.15	269.70
Hydrogen	-19.62	19.66	6.19	6.23
Carbon	-26.86	8.70	7.78	-10.38
Oxygen	-84.10	45.56	-366.94	-405.47
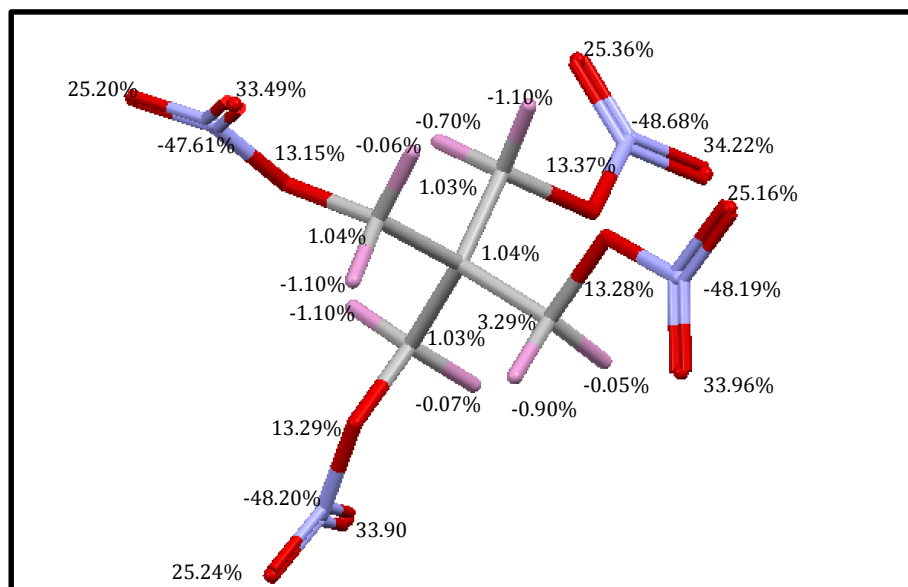
Figure 5-13 The PETN molecular structure highlighting the specific atomistic contributions towards the computations of lattice energies. The highest contributor for PETN is oxygen with 34.22%. The oxygen involved in the nitrate terminals

The main functional group influence towards the lattice energy was determined and given in Table 5-18. The nitrate group contributed the most energies with 97%. This showed the domination of the groups situated at the terminal.

Table 5-18 Main functional group contributions towards the lattice energy of PETN. The nitrate is contributing 97% while neopentane (penta-carbon) only 3%

Main functional group	Attractive (kJ/mol)	Repulsive (kJ/mol)	Coulombic (kJ/mol)	Total (kJ/mol)	%
Nitrate	-107.61	51.71	-79.79	-135.69	97
Neopentane	-46.61	28.37	13.97	-4.27	3

For further analysis of PETN intermolecular bonds, only the top three strong energies were chosen. It was evident in Table 5-19 the intermolecular bonding analysis of PETN had uniform energy distributions. The strongest bond in PETN was formed between two central carbon atoms reflecting the stacking position of PETN crystallographic structure.

Table 5-19 Intermolecular interactions strength analysis for PETN. PETN strongest interaction was determined as van der Waals. PETN intermolecular bonds were distributed uniformly with four multiplications of each of the top three strong bonds

Bond	Multiplicity	Distance (Ă)	Intermolecular energy (kJ/mol)	Dominating intermolecular interaction type
C1	4	7.65	-15.15	vdW
C2	4	7.65	-14.98	vdW
C3	4	7.12	-10.25	vdW

The strength of intermolecular energy of PETN was distributed evenly in comparison to PET. There was only small difference approximately 1% to 4% between the top three strong bonds. Interestingly, the intermolecular bonds were distributed evenly throughout the unit cell, creating three bonds. The strongest interactions exhibited the bonds in the directions of [101], [100] and their opposites. It is acknowledged that the strength of the intermolecular interactions become weaker as the distance goes further. Contrasting from PET, the PETN was dominated by van der Waals interactions. The nitrate terminal connected to the carbonyl oxygen contributes 84.29% to its total interatomic interactions (Figure 5-14).
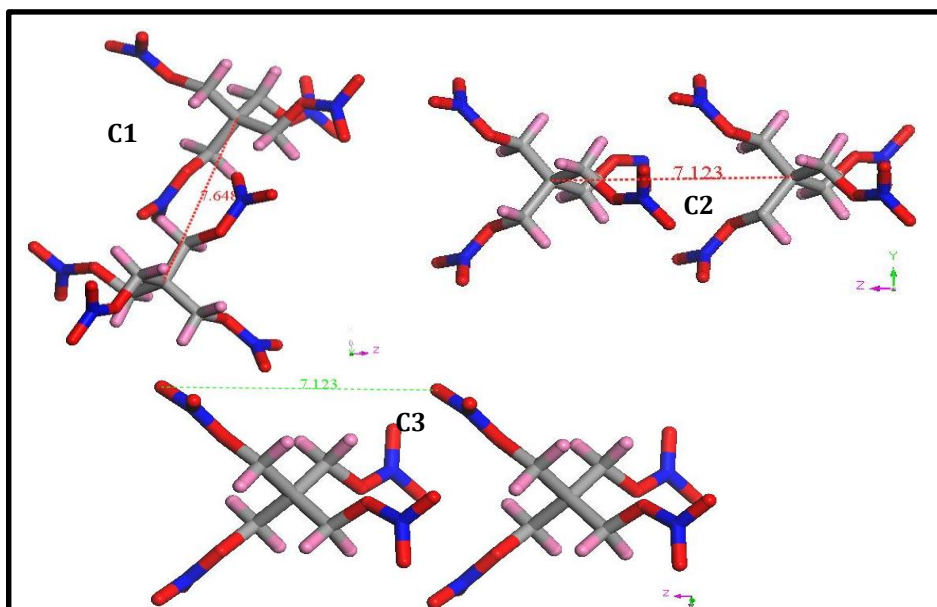
Figure 5-14 Dominating intermolecular interactions created between molecules in a unit cell of PETN. PETN has no obvious hydrogen bond; the strongest bond was created between central carbons of neighbouring PETN molecule

The nitrate terminal that consists of three oxygen atoms with a trigonal planar position with a nitrogen atom in the centre carries a polyatomic charge. Each of the oxygen atoms is having -2/3 charge while the nitrogen carries +1 charge. This polyatomic charge system resulted in the resonance occurrence when calculations were carried out. Resonance amplifies the oscillation of atom-atom interactions reflecting in the resulting inter and intramolecular energy. Working with the knowledge acquired from the intermolecular and interatomic interactions studies, give a simple prediction of crystal system strength and directionality of slip.

Having to assess the intermolecular and interatomic interactions of PETN, it was clear that PETN was governed by weak van der Waals bonds. This subsection correlates to the second objective of this study that was to relate the effects of crystal chemistry towards the mechanical properties of the organic crystal. The following section defines the work undertaken to predict the slip system for PETN.

5.4.6 Pentaerythritol tetranitrate slip planes characterisation

Similar to the previous test carried out for PET, candidates slip plane of PETN were characterised. The next subsection described calculated rugosity, surface energy, interlocking analysis and hydrogen bond breaking for all slip plane candidates.

5.4.6.1 Rugosity calculation

The lowest surface energy was 41.00 and highest 81.00 mJ/m^2 for (111) and (010) face accordingly. From Table 5-20 it can be seen that face (111), though having the lowest surface energy, but it did not have the lowest rugosity values. The rugosity was low for faces (011) and (101) with 4.01. The (111) have rugosity of 4.18. The third in increasing order was the face (110) with 4.32. The highest rugosity values for PETN were for two faces, (010) and (100), with surface energies of 7.39 respectively. A possible explanation for the indirect relationship between surface energy and rugosity might be that rugosity was depending on the individual atomic coordinates of each molecular structure whereas the surface energy was calculated based on atomic interactions within a coordination sphere bound by radii set during calculation. An additional test is needed to decide the most probable slip plane for PETN because the lowest surface energy and rugosity face are not the same. Therefore, the following result from the interlocking test is crucial to show if (111), (011), (101) and (110) will be the preferred slip plane.

5.4.6.2 Interlocking representation

Interlocking representations given in Figure 5-15 showed that three planes were identified as not interlock, (011), (110) and (111). If we recall from the qualitative observation of crystallographic packing, face (110) has the most clearance that was not corrugating and not breaking any hydrogen bonds. Hence this test was in agreement with the qualitative observation.
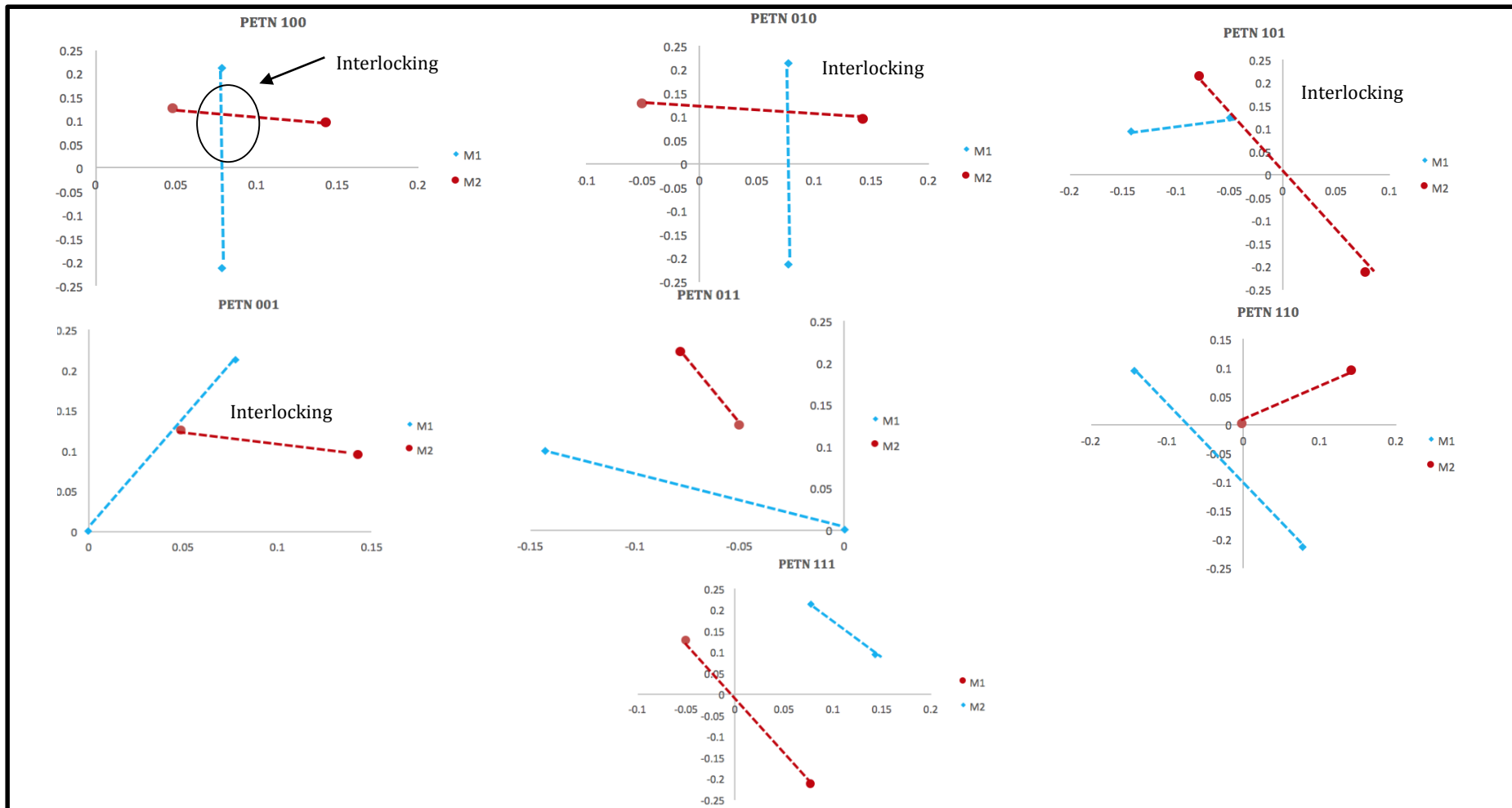
Figure 5-15 Representation of interlocking analysis showing two molecules in a unit cell of PETN, molecule 1 (M1-red) and molecule 2 (M2-cyan). Two data points of M1 and M2 were representing atomic coordinates. The two atoms were the shortest and farthest distance for each molecule projected onto lattice plane. If the molecules overlapped i.e. line intercepting, it is assumed that it will interlock

Also, in the rugosity ranking for preferred slip planes, (110) face was the third lowest with a value of 4.32, which were 0.31 differences from the lowest rugosity. The interlocking of faces will halt the dislocations slip to takes place. Results from the candidates of slip plane analysis were ranked using MDAM, and the results were presented next.

5.4.7 Multiple attribute decision-making calculations

Similar as in PET the MDAM analysis was carried out to rank PETN candidates slip plane. As shown in Table 5-20 the interlock analysis is translated from qualitative to quantitative binary numbers, 1.00 is representing interlock while 0.00 is not interlocked. Similar to hydrogen breaking test, it can be seen that no hydrogen breaking can be observed. Normalised values of each test data are given in Table 5-21, and all values now were converted into the range of 0.00 to 1.00. Hence comparison between the attributes can be made fairly. The surface energy was in the range of 0.25 to 0.49. The rugosity was in the range of 0.28 and 0.51.

Table 5-20 The multiple dimensions result from PETN slip plane tests were transferred into decision matrix. The qualitative analysis, i.e., interlock of slip plane and hydrogen bond breaking were transformed into quantitative values using binary numbers

	PETN			
Attributes	*Surface energy (mJ/m²)*	*Rugosity*	*Interlock of planes*	*H-bond breaking*
Alternatives				
(100)	81.00	7.39	1.00	0.00
(010)	81.00	7.39	1.00	0.00
(001)	68.00	5.79	1.00	0.00
(110)	57.00	4.32	0.00	0.00
(101)	48.00	4.01	1.00	0.00
(011)	48.00	4.01	1.00	0.00
(111)	41.00	4.18	1.00	0.00

Table 5-21 Normalised values for PETN slip plane candidates (alternatives) analysis with all data in the limit of 0.00 to 1.00. Surface energy is ranging between 0.25 to 0.49; rugosity was 0.29 to 0.51 and interlock of planes 0.41

	PETN			
Attributes	*Surface energy*	*Rugosity*	*Interlock of planes*	*H-bond breaking*
Alternatives				
(100)	0.49	0.51	0.41	0.00
(010)	0.49	0.51	0.41	0.00
(001)	0.41	0.40	0.41	0.00
(110)	0.35	0.30	0.00	0.00
(101)	0.29	0.28	0.41	0.00
(011)	0.29	0.28	0.41	0.00
(111)	0.25	0.29	0.41	0.00

The importance of each attribute was assigned as 25%. The Eigenvalues for the pairwise analysis were calculated to be 0.25. The consistency ratio was -0.055 that is far lower than 0.1. Based on the AHP approach consistency ratio below 0.1 was showing consistent judgments.

The weighted normalised value given in Table 5-22 showed the smallest value for surface energy and rugosity was 0.07 while for interlock of planes and hydrogen bond breaking was 0.00. For PETN the positive separation (Table 5-23) the lowest value was for face (110) that was 0.13. The highest were for (100) and (010) faces. These large values reflect deviation of faces from the optimised condition expected for preferred slip plane. The negative separation value (Table 5-23) for (110) face showed the largest as expected because most of its attributes were meeting the requirement of preferred slip plane. Based on the positive and negative separation values, the ratio of closeness to optimum conditions was calculated for all candidate slip planes. The closest to optimum conditions was the (110) with 82%. The list of rank following decreasing preferability to be slip plane was (110)> (111) > (101)=(011) > (001) > (100)=(010). Calculated values can be obtained from Table 5-24. Next subsection will present the Burgers vector calculations.

Table 5-22 Weighted normalised values of ideal attributes corresponding to a different set of slip plane candidates

| Attributes/ Alternatives | PETN | | | |
	Surface energy	*Rugosity*	*Interlock of planes*	*H-bond breaking*
(100)	0.12	0.13	0.10	0.00
(010)	0.12	0.12	0.10	0.10
(001)	0.10	0.10	0.10	0.00
(110)	0.09	0.07	0.00	0.00
(101)	0.07	0.07	0.10	0.00
(011)	0.07	0.07	0.10	0.00
(111)	0.06	0.07	0.10	0.00

Table 5-23 Classification of alternatives according to the TOPSIS analysis. The closest value for PETN was 0.98. The values reflect the closeness to ideal conditions

Attributes	Surface	Rugosity	Interlock	H-bond	Squared	Positive
PETN (positive separation)						
Alternatives	energy		of planes	breaking	of sum	Separation
(100)	3.92E-03	3.27E-03	1.04E-02	0.00E+00	1.76E-02	1.33E-01
(010)	3.92E-03	3.27E-03	1.04E-02	0.00E+00	1.76E-02	1.33E-01
(001)	1.84E-03	8.77E-04	1.04E-02	0.00E+00	1.31E-02	1.15E-01
(110)	6.90E-04	1.87E-05	0.00E+00	0.00E+00	7.09E-04	2.66E-02
(101)	1.60E-04	1.01E-06	1.04E-02	0.00E+00	1.06E-02	1.03E-01
(011)	1.60E-04	1.01E-06	1.04E-02	0.00E+00	1.06E-02	1.03E-01
(111)	4.22E-06	3.69E-06	1.04E-02	0.00E+00	1.04E-02	1.02E-01
PETN (negative separation)						
Attributes	Surface	Rugosity	Interlock	H-bond	Squared	Positive
Alternatives	energy		of planes	breaking	of sum	Separation
(100)	6.73E-06	8.12E-06	4.16E-06	0.00E+00	1.90E-05	4.36E-03
(010)	6.73E-06	8.12E-06	4.16E-06	0.00E+00	1.90E-05	4.36E-03
(001)	2.92E-04	9.23E-04	4.16E-06	0.00E+00	1.22E-03	3.49E-02
(110)	1.14E-03	3.10E-03	1.00E-02	0.00E+00	1.42E-02	1.19E-01
(101)	2.24E-03	3.72E-03	4.16E-06	0.00E+00	5.97E-03	7.73E-02
(011)	2.24E-03	3.72E-03	4.16E-06	0.00E+00	5.97E-03	7.73E-02
(111)	3.36E-03	3.37E-03	4.16E-06	0.00E+00	6.74E-03	8.21E-02

The final rank of ideal slip plane for PETN was given in Table 5-24. An ideal plane is (110) with 82% behaviour of optimum attributes. In the case of PETN, (110) was a clear choice because the other candidates were below 50%. The least to be selected as slip plane was (100) and (010).

Table 5-24 List of potential slip planes (alternatives) ranked according to MDAM analysis. The lowest deviation was the most preferred slip plane

	PETN	
Rank	Alternatives	% Optimum
1	(110)	82
2	(111)	45
3	(101)	43
4	(011)	43
5	(001)	23
6	(100)	3
7	(010)	3

5.4.8 Pentaerythritol tetranitrate Burgers vector calculations

PETN shortest Burgers vector was in the lattice translational vector of [001], with the length of 7.12 Å as shown in Table 5-25. Observation from the table, the magnitudes of the Burgers vector were increasing as the Burgers vector moving away from the densest plane in PETN. The largest magnitude was 15.30Å in the direction of [111].

5.4.8.1 Dislocation energy calculation

Results for dislocations analysis was listed in Table 5-25. The K values showed to be in the range of 2.29 to 6.78GPa. The anisotropy behaviour of PETN was characterised by looking into energy constant values (K). Results were shown in Table 5-25 with the dislocation energy increasing as the Burgers vector magnitude increases. The lowest calculated dislocations energy was in the direction [001] with $1eVnm^{-1}$. PETN was observed to have low dislocation energy with values below $10eVnm^{-1}$.

Table 5-25 The dislocation energy factors varying in the [100], [010] and [001] directions representing the anisotropy behaviour of PETN. The dislocation energy was in the range of 0.72 to 7.77$evnm^{-1}$

BV	Magnitude BV(Å)	Magnitude BV²(Å)²	K(GPa)			$K(BV)^2$ $(eVnm^{-1})$
			[100]	[010]	[001]	
[001]	7.12	50.65	3.69	3.69	2.29	0.72-1.17
[100]	9.58	91.74	4.22	4.55	6.78	2.42-3.89
[010]	9.58	91.74	4.55	4.22	6.78	2.42-3.89
[011]	11.93	142.39	4.24	4.07	4.2	3.62-3.77
[101]	11.93	142.39	4.06	4.24	5.7	3.61-7.77
[110]	13.55	183.48	4.42	4.39	6.78	5.03-7.77
[111]	15.30	234.13	4.28	4.26	5.53	6.23-8.09

The low dislocation energy in the [001] direction relate to it was the shortest Burgers vector magnitude. The polar plot of the K factors continuum in Figure 5-16 showed that it varies most in the [001] direction. The variation in [001] was because the elastic component was different in this direction.
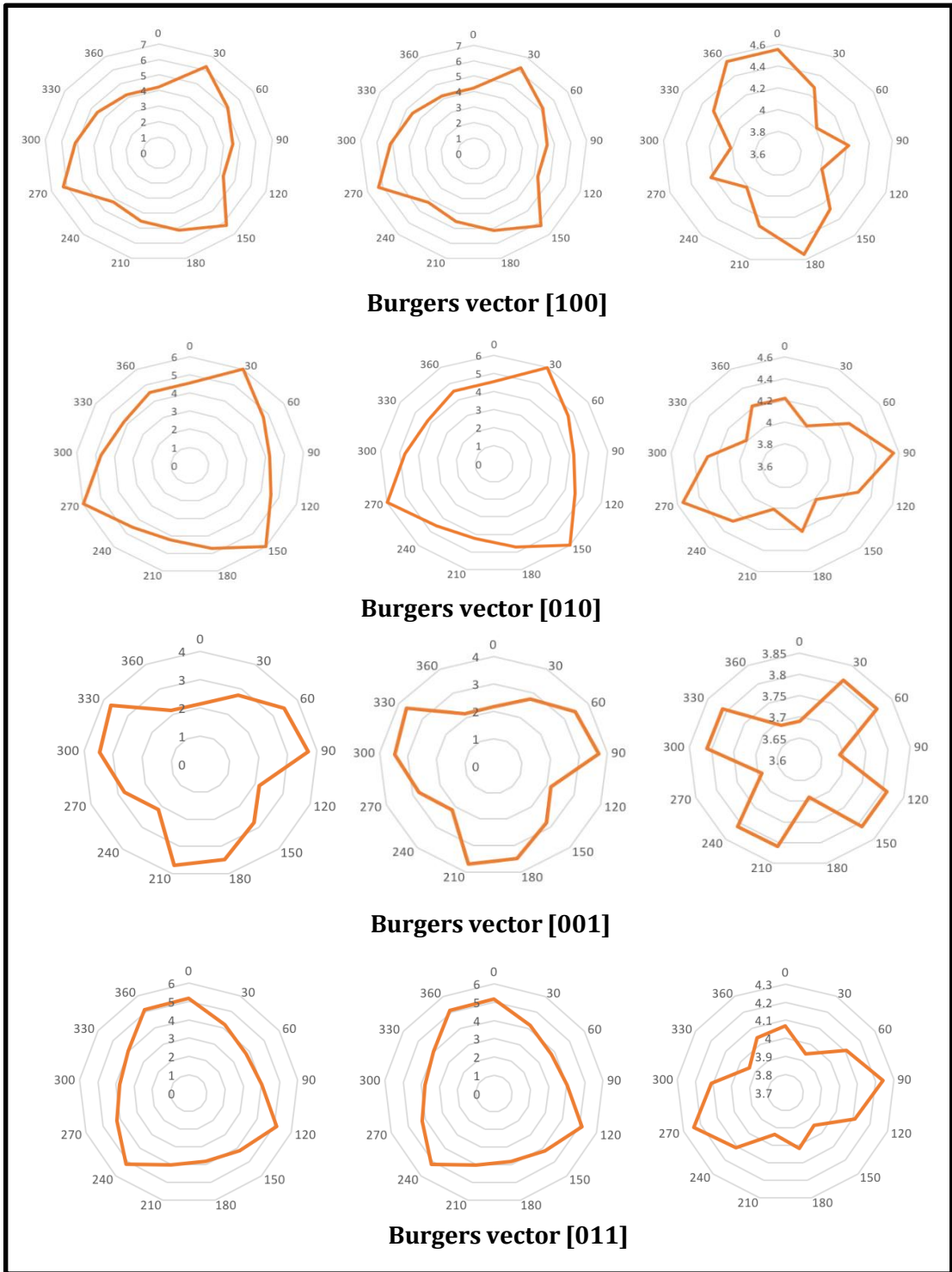
Figure 5-16 Dislocation energy factor continuum analysis with respect to Burgers vector represented as polar plot. The polar plot is given in the three axial directions [100], [010] and [001]. The scanning angle related to the dislocation program was $\emptyset = 0 - 360° \; \theta = 0 - 360°$. Determination of specific axial K values: [100] $\emptyset = 90 \; \theta = 90$ [010] $\emptyset = 0 \; \theta = 90$ and [001] $\emptyset = 90 \; \theta = 0$

Burgers vector [111]

Burgers vector [101]

Burgers vector [110]
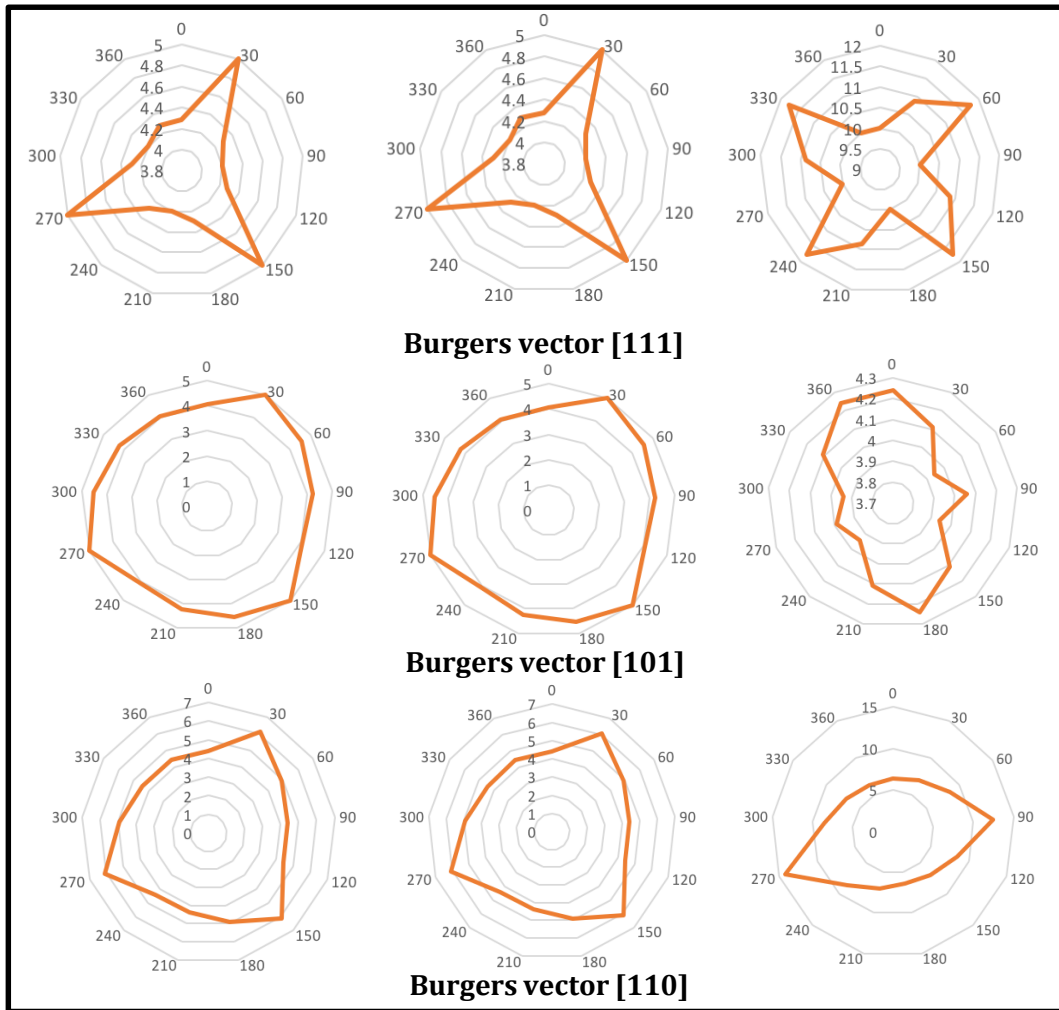
5.4.8.2 Type of dislocations identification

The probable type of dislocations taking place in PETN was presented in Table 5-26. There were 18 possible edge and seven screw dislocations taking place in PETN. The line directions were identified from the stereographic projection given in the Appendix A. The [001] Burgers vector with line direction of [110] was characterised to undergo edge dislocation and agrees with the findings of Halfpenny (1982)[1]. Halfpenny(1982) observed dislocations with the same Burgers vector in the (110) growth sector from the microhardness indentation. Similar observations were obtained for Burgers vector [100] with line direction of [011] that shows it will undergo edge dislocation.

The geometrical-based Burgers vectors were further ranked according to dislocations energy values. Table 5-27 compares the Burgers vector values showing the slight difference for some of the vector. The shortest Burgers vector is [001]. The [001] was the primary direction for a slip to takes place as the dislocations energy was the lowest compared to other Burgers vector.

Table 5-26 List of potential edge and screw dislocations in PETN. There are 18 edge and seven screw dislocations. The largest dislocation energy is 7.77 in the [110] direction. The smallest dislocation energy is 0.72 in the [001] direction

				PETN		
BV	LV	Angle $\emptyset°$	Angle $\theta°$	K (GPa)	$Kb^2(eVm^{-1})$	Type
[100]	[100]	90	0	4.22	2.42	Screw
	[010]	0	90	4.55	2.61	Edge
	[001]	90	90	6.78	3.89	Edge
	[011]	36	90	4.18	2.40	Edge
[010]	[010]	0	90	4.22	2.42	Screw
	[100]	180	90	4.55	2.61	Edge
	[001]	90	90	6.78	3.89	Edge
	[101]	143	90	3.99	2.29	Edge
[001]	[001]	90	0	2.29	0.72	Screw
	[010]	0	90	3.69	1.17	Edge
	[100]	270	90	3.69	1.17	Edge
	[110]	315	90	3.88	1.23	Edge
[011]	[011]	0	45	3.89	3.46	Screw
	[100]	180	90	4.24	3.77	Edge
	[012]	90	87	4.25	3.78	Edge
[101]	[101]	90	45	3.89	3.46	Screw
	[010]	0	90	4.24	3.77	Edge
	[-102]	90	87	3.99	3.55	Edge
	[-112]	60	87	3.88	3.45	Edge
[110]	[110]	45	90	2.61	2.99	Screw
	[001]	90	90	6.78	7.77	Edge
	[-112]	46	90	2.62	3.00	Edge
	[-111]	27	90	3.08	3.53	Edge
[111]	[111]	45	45	3.93	5.75	Screw
	[-110]	0	90	4.26	6.23	Edge

Table 5-27 Comparison of Burgers vector calculated using geometry and dislocations energy. The list showed slight difference with the [100], [011], and [101] Burgers vector were alternating

	PETN	
Rank	Burgers vector (Geometrical)	Burgers vector (Dislocation Energy)
1	[001]	[001]
2	[010]	[010]
3	[100]	[011]
4	[011]	[101]
5	[101]	[100]
6	[110]	[110]
7	[111]	[111]

5.4.9 Prediction of pentaerythritol tetranitrate mechanical slip system

Now, having to identify the most preferred Burgers vector as [001], determination of active slip system was carried out by taking the most likely slip plane, (110). The dot product calculation showed that PETN has an active slip system. So, PETN satisfies the first route of prediction, therefore was predicted to undergo plastic deformation. This outcome is agreeing with the microhardness indentation results by Halfpenny et.al [1,10] that showed PETN slipped on the (110) growth sector in the direction of [001]. The etching pit propagated in the [001] direction as illustrated in Figure 5-17. From the etching diagrams, no other traces of direction were seen, and slippage was following only one direction.
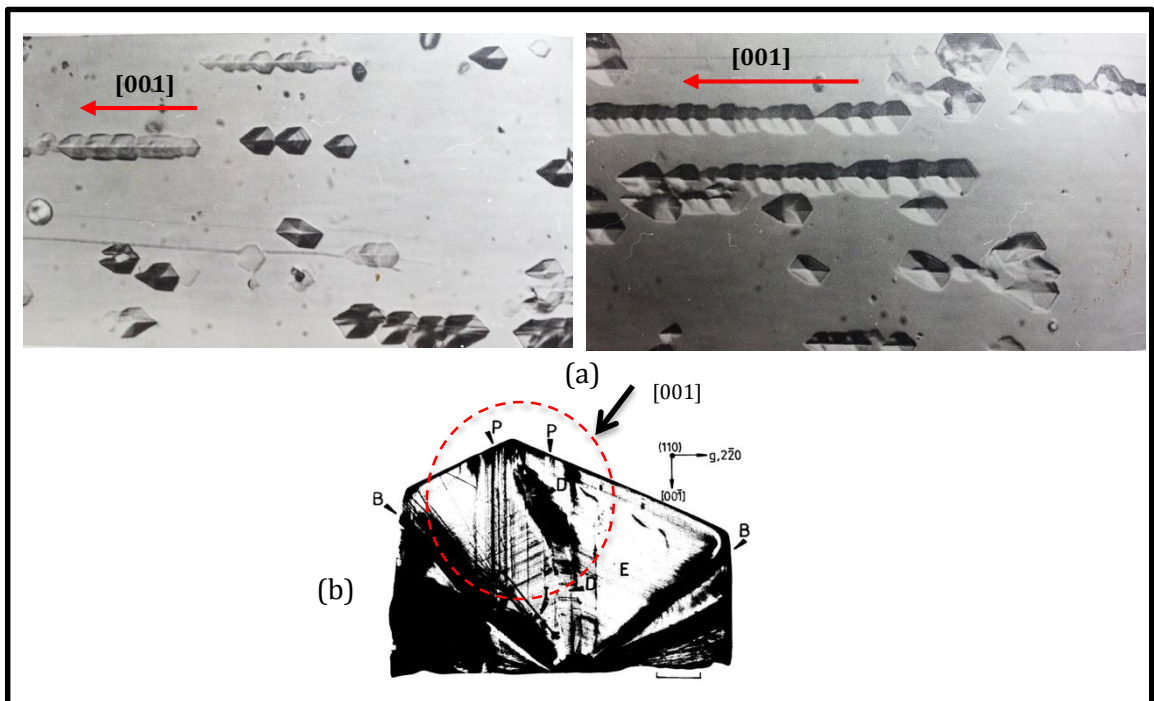
Figure 5-17 a) Etching at (110) face exhibit propagation in the [001] direction b) PETN (110) surface showing the slip bands in the direction of [001] (Figure from [1])

Revisiting the crystallographic structure of PETN Figure 5-12, the (110) showed clearance without hydrogen bond created perpendicular to the plane. The strength which holds the interplanar was weaker compared to the intraplanar. This weak interaction, therefore, promotes the ease for slippage in the [001] direction.

5.4.10 Summary

Based on the PETN case study, the application of the first route of prediction has been described. The plastic deformation of PETN has been successfully being characterised. To sum up important findings of PETN:

1. Fitted Dreiding parameters result in sensible elastic components. Nonetheless, the force field still in need of further refinement.
2. PETN crystal structure has four nitrate terminals that gave the resonance effect. There was no obvious hydrogen bond observed.
3. The (110) plane was identified as the ideal slip plane with 82% of the ideal behaviour.
4. The anisotropy influence was evidence through the dislocation energy factor (K) continuum. The shortest Burgers vector according to the dislocation energy was [001].

5.5   Conclusions

PET showed obvious striations trace that was identified to be the cleavage plane which was (001). It was predicted that PET would cleaved as its primary slip system was inactive. Though the slip was not active, the optimal surface properties of the slip plane make it possible for the strong intraplanar hydrogen bond to supply the force for cleavage to occur. Meanwhile for PETN, it was observed that it would undergo slip deformation at its primary slip system of (110) plane and [001] direction. These two extreme cases become the basis to test the proposed applicability of the proposed prediction model.

The proposed rugosity qualitative evaluation was giving a good prediction of PET crystallographic stacking pattern. Similarly, for PETN, the layered positions of molecules were represented. Despite the promising results based on PET and PETN, there is still needs to explore further on the rugosity of surface by considering the atomic orbitals that pose a potential steric hindrance. The anisotropic properties of the molecular system increase the complexity for prediction to be carried out using theoretical model. In contrast, the elemental materials that are isotropic usually have better prediction using theoretical model. For this instance, the rugosity mathematical relationship provides a satisfactory prediction of molecular deformation using crystallographic structure and supports the aim of this study to develop foundational mechanical properties prediction model. Moreover, by having the rugosity predicted, the estimation of solid form deformation advances.

The molecular interlocking was the first time represented based on quantitative analysis. Elucidating the lattice and crystal chemistry of both systems showed the impact of the crystallographic structure towards the geometrical and deformation behaviour of PET and PETN. By probing the strength of interactions taking place within the crystal bulk, the observed mechanical behaviour can be studied. Besides that, from the observation in this chapter, it can be said that the surface energy and rugosity of materials are closely related to represent the surface behaviour.

The MDAM approach that combined the AHP and TOPSIS provide ways to process data comprises qualitative and quantitative for final rationale comparison. By using the MDAM, a more objective and straightforward selection approach was obtained. Nonetheless, the need of having more information for the relative weighting for one to one comparison is vital. By having data available for comparison will provide better weighting factor. The availability of data provides better slip plane comparison.

By knowing the type of materials, ductile or brittle, the API-excipients formulation suitable for direct compression can be determined easily. For example, if the API is brittle, and dominating the dosage formulation, slightly ductile excipients is needed to compensate the elastic recovery of the APIs'. The results in this chapter corroborate the findings of the previous work in predicting the mechanical properties by relating it to slip system activity [11] that emphasised the vital influence of the molecular to the bulk powder tabletting.

Together the PET and PETN results become the basis for the application of the mechanical properties prediction model. The results presented in earlier sections showed evidence of the reliability of using the molecular and crystallographic modelling to predict the mechanical properties of PET and PETN.

References

[1] P. J.Halfpenny, A Study of Crystal Defects in Pentaerythritol Tetranitrate and Cryslotrimethylene Trinitramine, 1982.

[2] D. Olusanmi, K. Roberts, M. Ghadiri, Y. Ding, The breakage behaviour of Aspirin under quasi-static indentation and single particle impact loading: Effect of crystallographic anisotropy, International Journal of Pharmaceutics. (2011).

[3] R.V. Rao, J. Davim, A decision-making framework model for material selection using a combined multiple attribute decision-making method, The International Journal of Advanced Manufacturing Technology. 35 (2008) 751–760.

[4] R.H.Ba. Evelyn Berlow, JohnE.Snow, The Pentaerythritols, New York:Reinhold Pub.Corp, 1958.

[5] I. Rosbottom, K. Roberts, R. Docherty, The solid state, surface and morphological properties of p-aminobenzoic acid in terms of the strength and directionality of its intermolecular synthons, CrystEngComm. 17 (2015) 5768–5788.

[6] T.-H. Fang, W.-J. Chang, Effects of AFM-based nanomachining process on aluminum surface, Journal of Physics and Chemistry of Solids. 64 (2003) 913–918.

[7] P. Narayan, B.C. Hancock, The relationship between the particle properties, mechanical behavior, and surface roughness of some pharmaceutical excipient compacts, Materials Science and Engineering: A. 355 (2003) 24–36.

[8] L.L. Stevens, D.E. Hooks, A. Migliori, A comparative evaluation of elasticity in pentaerythritol tetranitrate using Brillouin scattering and resonant ultrasound spectroscopy, Journal of Applied Physics. 108 (2010) 053512.

[9] G.R. Desiraju, Designer crystals: intermolecular interactions, network structures and supramolecular synthons, Chemical Communications. (1997) 1475–1482.

[10] P. Halfpenny, K. Roberts, J. Sherwood, Dislocations in energetic materials. 2. Characterization of the growth-induced dislocation structure of pentaerythritol tetranitrate (PETN), Journal of Applied Crystallography. 17 (1984) 320–327.

[11] P. York, Solid-state properties of powders in the formulation and processing of solid dosage forms, International Journal of Pharmaceutics. 14 (1983) 1–28.

[12] K.J. Roberts, Private Communication.

Chapter Six

Crystal Chemistry Study of Five Diverse Solid Forms of Paracetamol Using Molecular Modelling

This chapter presents the characterisation of crystal lattice, chemistry and elastic energy of five diverse paracetamol systems. The molecular and crystallographic modelling were applied for computation

Chapter 6. Crystal Chemistry Study of Five Diverse Solid Forms of Paracetamol using Molecular Modelling

6.1   Introduction

The molecular crystal physicochemical behaviour that was described in Chapter 2, showed a direct dependency to its molecular chemistry and crystallographic structure. This indirectly support the reliability of using the crystal chemistry and crystallographic structure as the first degree prediction. This chapter present the intermolecular interactions, lattice energetics and elasticity results of five diverse paracetamol solid forms. The elastic tensors computed using the density functional theory(DFT) that were taken as reference values were part of the collaboration with the Hartree Centre, Warrington. Figure 6-1 illustrates the content for this chapter. This chapter starts with the molecular conformational analysis exhibiting the flexibility of paracetamol molecular structure. Next, the newly fitted Dreiding force field parameters onto paracetamol were presented and lastly the chapter conclusions.
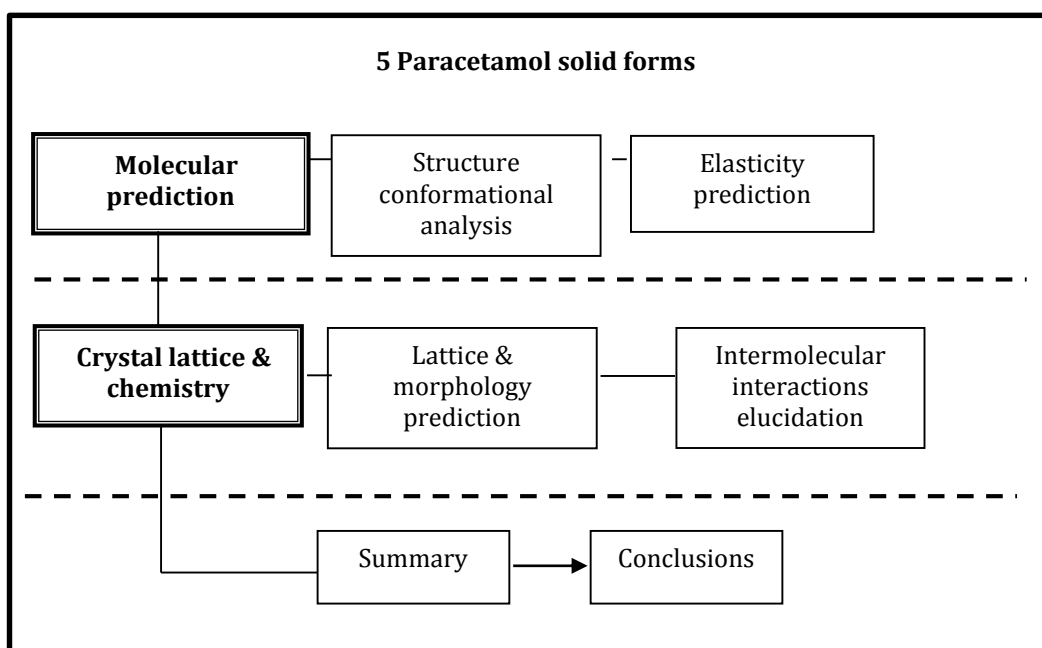
Figure 6-1 Summary of content for this chapter

6.2 Structure conformational analysis

The objective of the analysis was to examine the flexibility and stability of paracetamol (FI) molecular structure through potential torsional changes. Only the molecular structure of paracetamol was taken for analysis with regards to PTHEO (co-crystal), PTRI (trihydrate) and PHM (salt). The influence of the introduction of new molecules for instance water towards paracetamol molecular structure were observed.

6.2.1 Comparison of the paracetamol conformation in five solid forms

The molecular conformation analysis had identified four possible torsion angles for the paracetamol structure. Identified torsions were related to the paracetamol main functional groups that were hydroxyl, amide and carbonyl. The identified torsion angles are T1 (C_2-C_1-O_1-H_1), T2 (C_3-C_4-N_1-H_7), T3 (O_2-C_7-N_1-C_4) and T4 (H_9-C_8-C_7-O_2) given in Figure 6-2(a).

It was obvious in Figure 6-2(b-e) that all paracetamol structures were the exact match with only small different seen for the FII. Furthermore, analysis of benzene ring angles for FI andFII, disclose the planar movement was resulted from the active functional group attached to its aromatic ring that were amide and hydroxyl groups.

TORSION TYPE	ATOMS INVOLVE
T1	C_2-C_1-O_1-H_1
T2	C_3-C_4-N_1-H_7
T3	O_2-C_7-N_1-C_4
T4	H_9-C_8-C_7-O_2
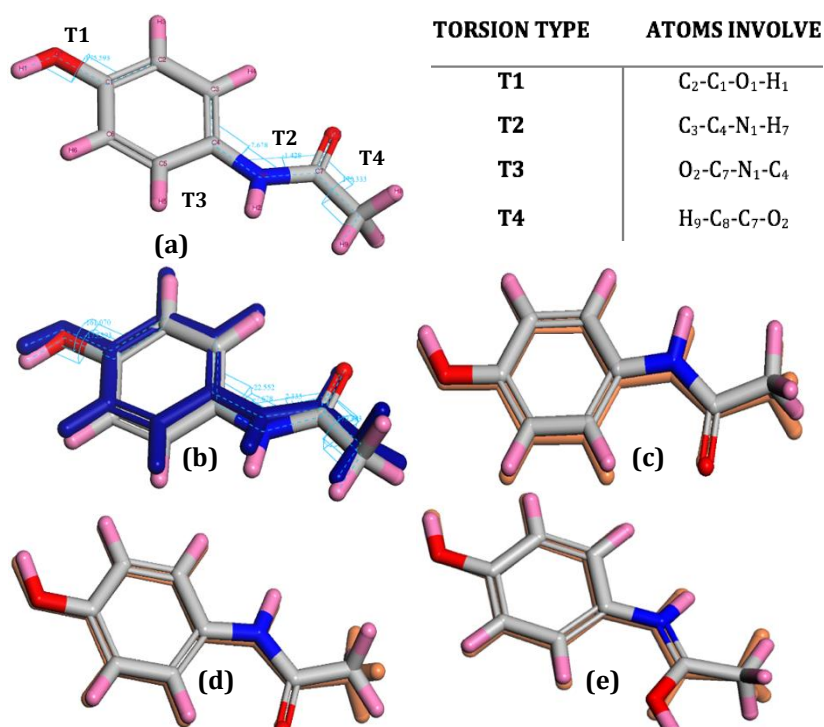
Figure 6-2 a) The potential torsion changes that were identified in the paracetamol molecular structure. b) Overlay of the metastable (F2-blue) over the stable (F1) paracetamol structures showing the torsion angles changes between -8.32 to 52.86° for F2. c-e) Overlay of paracetamol structure isolated from PTHEO, PTRI and PHM over F1 (orange) showing very small differences. It was shown that paracetamol structure does not affected much with the introduction of theophylline and water molecules in PTHEO, PTRI and PHM

Likewise, the observed hydroxyl alteration agrees with the observation by Haisa et.al (1976) [1,3] that reported elongations of 2.21Å for FII corresponding to the terminal which was slightly higher than FI, 2.05 Å. The elongation was described to be related to the hydrogen interactions in the direction of hydrogen bond created between the carbonyl (C=O) and amide (N-H) to the hydroxyl (O-H) groups. Besides that, the benzene ring was laid flat for all structures shown in Figure 6-2 (b-e) conforming to the FI structure. The flat configurations partly contribute towards the stability of the paracetamol structure. A relax aromatic ring will have 120° angles between each hexagon edge. In a relaxed structure of FI, an equal distribution of 118.190° was observed for five edges with an exception for one edge with 120.84° while in FII, the angles alternate between 118.31° to 120°.

Results of the torsion angle shown in Table 6-1 showed that the potential rotations were related to the intermolecular networks formed within each solid forms. PHM, salt was having strong polar bonds created between the chloride (Cl-) ions with the hydrogen atom either in water molecules or amide group. The strong intermolecular interactions were reflected through the large rotations of T1 to T4 (-4.49 to -179.44°). Correspondingly, PTRI that is heavily hydrogen bonded was showing much resistance towards torsion with rotations between 2.38 to -169.80°. PTHEO had the smallest resistance to torsion with the T1 to T4 between 0.12 to 175.58°. In the subsequent sections, further elucidation of the intermolecular interactions of all solid forms will be discussed. A relative torsion energies map will depict further the flexibility and stability of paracetamol structure in different solid forms.

Table 6-1 Paracetamol torsion angles for FI, FII, PTHEO, PTRI and PHM for all possible rotations in paracetamol molecular structure. The rotations were shown to be related to the intermolecular bond networks within each system

Torsion type	FI	FII	PTHEO	PTRI	PHM
T1	-161.07	-19.79	175.58	-169.80	-179.09
T2	-22.55	17.12	3.79	-48.70	-179.44
T3	2.34	0.73	0.12	2.38	-16.25
T4	-169.29	94.31	120.67	-4.95	-4.49

6.2.2   Relative torsion energy map

The relative energy resulting from the calculation was represented in the energy map shown in Figure 6-3 by plotting the T1 to T4 angles against corresponding torsion energy resulted. It is evident from the relative energy map that three systems were distributed mostly in the blue region(stable) compared to the FII that can sometimes be seen in the red and orange(unstable) and PTHEO in the green area (mild). FII was in the unstable regions particularly in three relative torsion energy plots, T2-T4, T1-T4 and T3-T4. Additionally, FII was seen to be dependent most on T4 that deviates the energy from the stable to the unstable region. This phenomenon was also observed by Boldyreva et.al (2004) [2-4] from their X-ray and IR-spectroscopy measurements. In their observation, the angles between molecules were flattened, extending the hydrogen bond of FII related to the carbonyl (C=O) by 0.6Å compared to the original position with increasing pressure. Hence, the flexibility of FII is predominantly contributed by the T4 torsions.

For PTHEO it can be seen that it was in the green region for one plot, T1-T4.. Similar to the FII, this was largely influenced by the T4. For FI, PTRI and PHM, all were in the stable region for in all plot. Hence showing the stability of the molecule. This outcome leads to an inference that the relative torsion energy analysis alongside the individual torsion contributions was essential to have a better understanding of the molecular flexibility and stability from the molecular conformation analysis.

Briefly, the addition of the co-former, water molecules and chloride ion effects the paracetamol structure through the strength of intermolecular interactions. FI, PTRI and PHM resisted potential torsion hence explain the stability of the systems. Thus, the paracetamol structure was considerably rigid based on the angle distortions and torsion energies evaluation except for PTHEO that shown to be somewhat flexible. Now, that the molecular conformation has been described, its role in mechanical properties for example elasticity can be explored next.
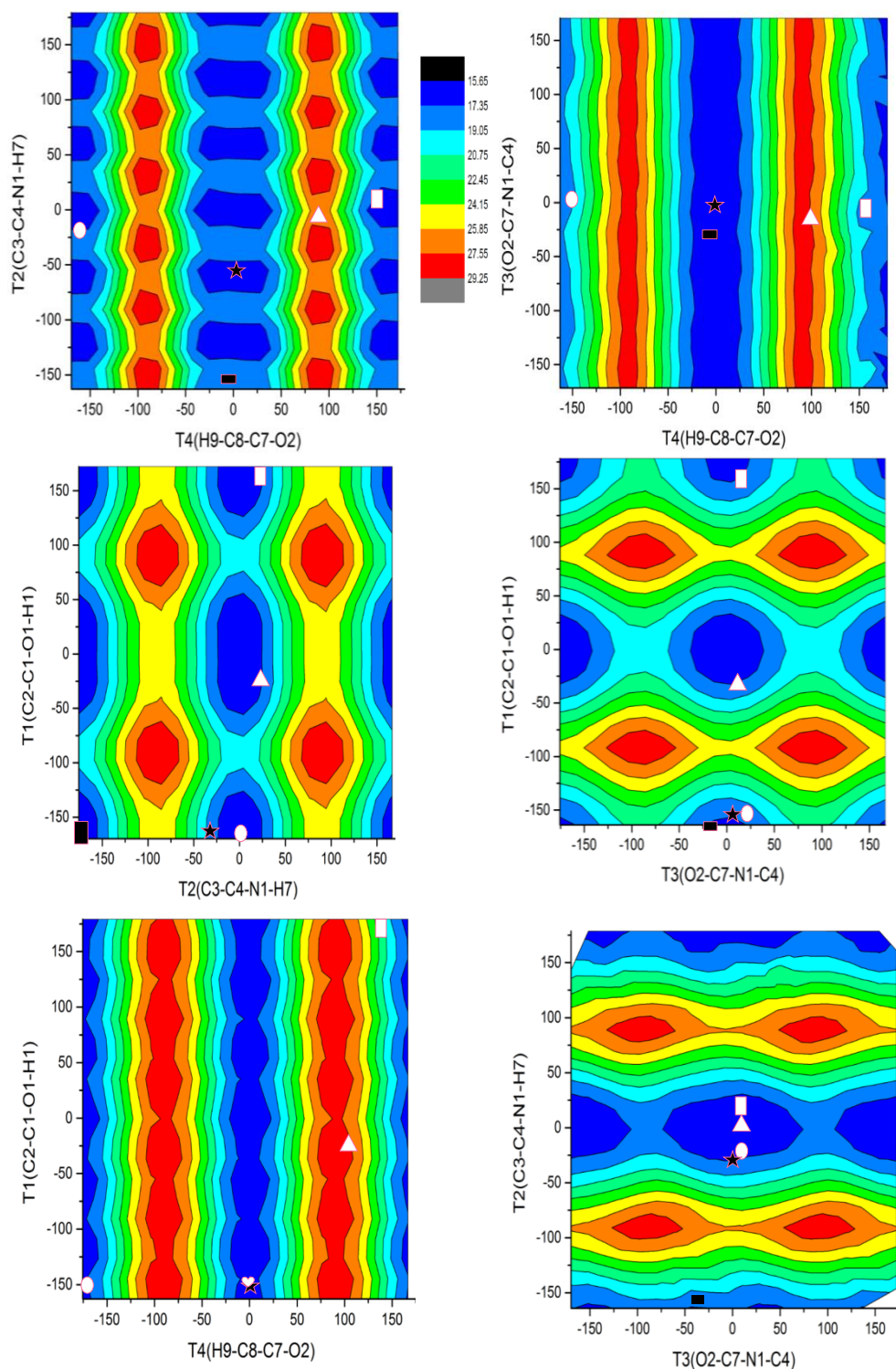
Figure 6-3 Torsional energy map of F1 in F2, PTHEO, PTRI and PHM. The F1 was recognised to be the most stable form (O). The F2 (Δ) exhibited the most torsion energy variations. For PTHEO (•), PTRI (*) and PHM (■) the torsion energy did not varied much with respect to the F1

6.3   Fitting of force field

After having some knowledge regarding the conformation of paracetamol and its influence towards stability and flexibility of molecular structure, the study was then extended by exploring the structure impact on physical properties specifically the elastic tensor. The elastic tensor is used as means to further reflect and characterises the rigidity of paracetamol.

6.3.1   Fitting of Dreiding parameters against the paracetamol

It was perceived when fitting only FI structure against the generic Dreiding parameters, the calculated output particularly the elastic tensors were seemed to be less accurate to match the literature. The addition of FII structure for simultaneous calculations increased the accuracy of the calculated elastic constants compared to the literature and the density functional theory (DFT) as given in Table 6-5. Further addition of PTHEO structure, resulted in better elastic constant compared to prior computation values when fitting only using FI and FII. This study only managed to fit FI, FII and PTHEO against Dreiding parameters because of the time constraint. The computation was expensive as this study considers the full unit cell, therefore, increase the time for inversion of Hessian-matrix. Nonetheless, the influence of different structure onto the elastic tensors exhibited during fitting of FI, FII and PTHEO. It is interesting to explore the impact of adding PTRI and PHM which is trihydrates and salt to the elastic tensors for all solid forms.

The force field fitting carried out by varying particularly bonded, and non-bonded terms showed that only those repulsive terms of Lennard-Jones varied to give the smallest error between the observables and the calculated values. The final parameter gradients were ranging between 0 and 1.0×10^{-2} making the new parameter values near to convergence. It can be recognised that only the repulsive parameters vary most. The obvious respond given by the repulsive terms were related to its power term (r^{-12}) that is sensitive to change in atomic distance giving a steep well of Lennard-Jones curve similar to the representation in Figure2-3 (Chapter 2). The deeper the well the stronger the interactions between two atoms. In this study, the repulsive interactions relate well with the flexibility of the FII and PTHEO as determined in the conformational analysis. Therefore, when including the FII and PTHEO the torsions flexibility gave better minimisations of energy giving improved elastic tensors.

Table 6-2 Fitted Lennard-Jones parameters compared to the initial values

Atom 1	Atom 2	Potential form	A(kcal)-Original	A(kcal)-Fitted
H2	H2	Lennard-Jones	$0.66E^{-3}$	3.81
H1	H2	Lennard-Jones	$0.54E^{-4}$	$0.19E^{-3}$
H1	H1	Lennard-Jones	$0.43E^{-5}$	$0.40E^{-5}$
H2	C2	Lennard-Jones	$017E^{-2}$	3.08
H1	C2	Lennard-Jones	$0.13E^{-3}$	$0.18E^{-3}$
C2	C2	Lennard-Jones	$0.41E^{-2}$	$0.41E^{-2}$
H2	C1	Lennard-Jones	$0.17E^{-2}$	2.00
H1	C1	Lennard-Jones	$0.13E^{-3}$	$0.84E^{-3}$
C1	C2	Lennard-Jones	$0.41E^{-2}$	26.42
C1	C1	Lennard-Jones	$0.41E^{-2}$	16.63
H2	N1	Lennard-Jones	$0.15E^{-2}$	$0.25E^{-2}$
H1	N1	Lennard-Jones	$0.12E^{-3}$	1.41
C2	N1	Lennard-Jones	$0.37E^{-2}$	0.04
C1	N1	Lennard-Jones	$0.37E^{-2}$	13.06
N1	N1	Lennard-Jones	$0.34E^{-2}$	$0.34E^{-2}$
H2	O1	Lennard-Jones	$0.17E^{-2}$	0.01
H1	O1	Lennard-Jones	$0.13E^{-3}$	1.46
C2	O1	Lennard-Jones	$0.41E^{-2}$	$0.44E^{-2}$
C1	O1	Lennard-Jones	$0.41E^{-2}$	11.92
N1	O1	Lennard-Jones	$0.37E^{-2}$	$0.47E^{-2}$
O1	O1	Lennard-Jones	$0.42E^{-2}$	$0.42E^{-2}$
H2	O2	Lennard-Jones	$0.17E^{-2}$	$0.33E^{-2}$
H1	O2	Lennard-Jones	$0.13E^{-3}$	$0.13E^{-3}$
C2	O2	Lennard-Jones	$0.41E^{-2}$	$0.53E^{-1}$
C1	O2	Lennard-Jones	$0.41E^{-2}$	7.16
N1	O2	Lennard-Jones	$0.37E^{-2}$	$0.39E^{-2}$
O1	O2	Lennard-Jones	$0.42E^{-2}$	$0.43E^{-2}$
O2	O2	Lennard-Jones	$0.42E^{-2}$	$0.42E^{-2}$

Table 6-3 The original and fitted Cartesian atomic coordinates for FI and FII structures

	FI							FII					
Atom name	**Fitted**			**Original**			**Atom name**	**Fitted**			**Original**		
	x	*y*	*z*	*x*	*y*	*z*		*x*	*y*	*z*	*x*	*y*	*z*
O1	-2.23	1.25	0.44	0.02	3.90	8.30	**O1**	0.67	-1.38	2.25	5.35	2.96	6.34
O2	-1.08	0.06	-0.72	2.02	-0.05	3.54	**O2**	0.08	-1.28	0.17	5.37	1.22	-0.05
N1	-1.52	-0.50	-1.64	-0.17	0.47	3.90	**N1**	0.18	-2.10	-0.46	5.55	-0.16	1.77
C1	-0.14	-0.92	-1.53	-0.05	3.05	7.23	**C1**	-0.03	0.90	1.33	5.51	0.69	2.82
C2	0.64	0.17	0.47	1.02	2.18	7.01	**C2**	0.16	-1.17	-1.58	5.43	2.25	5.19
C3	0.75	-0.27	-0.01	1.02	1.32	5.92	**C3**	-0.37	0.50	-0.60	5.01	2.01	2.80
C4	0.07	1.02	1.22	-0.07	1.31	5.03	**C4**	0.12	-2.09	-1.22	5.47	0.07	0.44
C5	-0.75	0.26	-0.45	-1.15	2.16	5.28	**C5**	0.33	-0.76	0.17	6.00	0.18	4.04
C6	-0.63	0.66	0.26	-1.15	3.03	6.37	**C6**	0.22	-0.33	0.72	5.95	0.95	5.22
C7	-1.11	-1.01	-2.01	0.82	-0.13	3.22	**C7**	-0.25	0.76	-0.14	4.97	2.79	3.98
C8	-0.02	0.24	0.01	0.37	-0.93	2.02	**C8**	-0.02	0.09	0.10	5.54	-1.06	-0.50
H1	-3.66	2.29	1.01	-0.88	4.23	8.55	**H1**	-0.57	-0.22	0.28	6.34	-0.90	-1.22
H2	-3.40	-0.07	-1.88	-1.12	0.38	3.56	**H2**	-0.10	0.54	-0.29	5.73	-2.00	0.03
H3	0.32	0.04	0.09	1.85	2.16	7.70	**H3**	0.61	-0.03	0.13	4.60	-1.15	-1.03
H4	0.53	-0.07	0.23	1.82	0.61	5.76	**H4**	0.17	-0.36	0.27	6.39	-0.76	4.09
H5	-0.50	0.29	-0.13	-1.99	2.14	4.60	**H5**	-0.10	0.45	-0.39	4.60	3.73	3.95
H6	-0.46	0.31	-0.03	-2.00	3.66	6.53	**H6**	-0.34	0.57	-0.16	4.64	2.42	1.95
H7	-0.36	0.012	0.25	1.07	-0.79	1.20	**H7**	0.03	-0.40	0.29	6.31	0.56	6.09
H8	-0.21	0.71	-0.17	0.44	-1.99	2.22	**H8**	0.49	-3.76	0.56	5.64	-1.10	2.01
H9	0.64	-0.05	-0.10	-0.65	-0.76	1.76	**H9**	1.07	-1.97	3.98	5.56	2.52	7.19

Table 6-4 The original and fitted Cartesian atomic coordinates for PTHEO

Atom name		Fitted			Original		Atom name		Fitted			Original	
	x	y	z	x	y	z		x	y	z	x	y	z
O1	1.31	-1.22	-0.39	0.28	5.18	12.34	H7	0.16	0.62	-0.30	2.48	6.79	12.28
O2	0.23	1.99	-0.25	1.83	0.88	11.95	C7	-1.59	-0.63	0.68	-0.33	2.54	12.64
O3	0.30	2.68	-0.32	-0.97	3.44	9.24	H8	-0.33	-0.43	-0.18	-0.52	2.94	13.64
H1	-0.02	4.51	-0.44	-0.94	4.42	9.16	H9	-0.53	0.22	0.28	-0.41	1.45	12.70
O4	1.14	0.64	-0.42	3.25	-1.53	7.93	H10	-0.26	-0.36	0.56	-1.12	2.88	11.97
N1	-0.50	-0.51	0.20	4.56	4.17	10.65	C8	1.60	-0.88	-0.57	0.12	2.74	8.85
N2	-0.11	-1.24	0.18	4.29	2.00	10.91	C9	-0.71	-0.46	0.26	0.17	1.35	9.04
H2	0.78	-3.76	0.02	4.46	1.05	10.89	H11	-0.37	-0.57	0.11	-0.62	0.86	9.45
N3	1.36	0.50	-0.47	0.96	3.01	12.16	C10	-0.31	-0.76	0.08	1.32	0.63	8.66
N4	-0.63	-1.18	0.28	2.36	4.86	11.50	H12	-0.61	-0.42	0.13	1.34	-0.38	8.84
N5	2.04	0.60	-0.95	3.61	0.72	7.69	C11	-1.35	0.83	0.29	2.43	1.29	8.08
H3	2.99	2.35	-1.33	4.28	1.35	7.40	C12	0.62	0.57	-0.37	2.35	2.68	7.89
C1	2.77	-0.04	-1.08	5.13	2.96	10.50	H13	0.29	0.50	-0.21	3.12	3.19	7.46
H4	-0.58	0.06	0.34	6.07	2.80	10.12	C1	-0.04	0.82	-0.05	0.23	0.21	0.73
C2	-0.64	-2.02	0.36	3.34	3.97	11.17	H2	0.21	0.33	-0.13	0.23	0.28	0.72
C3	-2.78	1.22	1.02	3.17	2.61	11.33	C1	2.38	-0.11	-0.88	0.52	-0.04	0.67
C4	1.82	1.76	-0.81	1.96	2.13	11.83	C2	-0.02	0.14	0.04	0.66	-0.05	0.64
C5	0.49	-0.72	-0.14	1.18	4.37	12.01	H2	0.06	0.62	0.05	0.68	-0.12	0.63
C6	0.35	2.05	-0.24	2.57	6.28	11.32	H2	-0.10	-0.25	-0.43	0.74	-0.02	0.70
H5	0.55	0.49	0.18	1.82	6.68	10.64	H2	0.07	-0.18	0.67	0.66	-0.03	0.55
H6	-0.17	0.66	-0.01	3.55	6.53	10.91							

List of the new parameters for intermolecular Lennard-Jones was shown in Table 6-2 while the two, three and four-body parameters were taken from the generic Dreiding force field [3,5]. This observation suggests that simultaneous calculation with a second structure that is behaving well with Dreiding was helping to give better fitting. Table 6-5 presented FI elastic tensors generated during force field parametisation with three different ways, only FI, FI and FII and FI, FII and F3 simultaneous fitting. The newly fitted FI, FII and PTHEO unit cell atomic coordinates were presented in Table 6-3 and Table 6-4.

6.3.2 Elastic tensors for five solid forms of paracetamol

These study results were compared to the DFT and literature (ab-initio) computed tensors as there is lacking of experimental elasticity for PTHEO, PTRI and PHM. The goal is to show the reliability of calculating the fourth-rank elastic tensor using second derivatives approach that is not computationally expensive. It is also of interest to explore the effects of simultaneous fitting for the five paracetamol solid forms relative to the elastic tensor.

It was apparent that the FI elastic tensors were showing huge variation between the components with the largest was C_{33}, 93.62GPa and smallest C_{25}, -53.52GPa as seen in Table 6-5. Other components that were showing huge different of approximately four times the values with regards to the DFT and literature are C_{22} (78.7GPa), C_{55} (66.8GPa) and C_{35} (33.5GPa). The C_{55} was the shearing and the C_{35} was the transverse component corresponding to the C_{22}, therefore, explains the relation between them. The 2-fold screw axis in the [010] direction may be the cause for the sensitivity of the C_{22}, which then relate to its associated components (C_{55} and C_{35}). However, when the FII structure was included (Fit 2) for simultaneous fitting, the huge variation reduces resulting in better distribution of each component. It was seen clearly from Fit 2; the elastic components were much stable with highest C_{11}, 24.1GPa and smallest, C_{46} -2.3GPa. The addition of PTHEO (Fit 3) for simultaneous fitting further refined the elastic components make it closer to the DFT and literature values. The calculated tensor from Fit 3 was taken for used in subsequent sections.

Table 6-5 Elastic tensors comparison between calculated and literature values for FI, FII, PTHEO, PTRI and PHM. Elastic tensors computed from three approaches were given and shown as Fit 1 (FI only), Fit 2(FI+FII) and Fit 3(FI+FII+PTHEO). The literature values were computed using ab-initio. DFT values were given to compare the reliability of using GULP to compute elastic tensors. For PTRI and PHM, elastic tensors were calculated using fitted force field combine with generic values for unavailable fitted parameters

Elastic (GPa)	FI					FII				PTHEO		PTRI		PHM	
	Fit 1	Fit 2	Fit 3	DFT	Lit.[α]	Fit2	Fit 3	DFT	Lit.[α]	Fit3	DFT	This study	DFT	This study	DFT
C_{11}	35.0	24.1	23.9	21.9	21.2	10.47	10.42	9.14	30.0	7.27	13.02	9.29	2.03	19.96	-72.71
C_{22}	78.7	8.0	7.9	8.9	14.4	25.21	25.21	11.06	22.7	21.71	37.42	8.27	2.3	21.21	50.94
C_{33}	93.6	11.3	11.3	11.8	21.6	37.60	37.42	24.32	12.5	9.83	6.44	14.64	22.52	17.15	2.08
C_{44}	10.4	4.3	4.2	8.1	5.5	9.34	9.29	3.98	3.0	-1.58	3.38	3.78	4.39	2.34	5.39
C_{55}	66.8	6.1	6.1	8.2	5.9	1.59	1.60	-1.93	0.8	2.91	3.58	0.35	4.57	1.64	-4.46
C_{66}	-5.5	6.5	6.3	8.5	8.9	2.64	2.62	4.95	7.6	6.02	9.38	1.02	2.38	5.74	-3.49
C_{12}	-0.6	8.0	7.8	3.9	12.3	4.27	5.42	2.57	14.5	5.63	9.12	5.42	-4.6	7.68	15.2
C_{13}	10.5	7.3	7.1	5.7	10.5	0.78	0.88	-2.27	4.4	2.53	4.64	3.10	2.01	10.52	1.66
C_{15}	3.1	1.1	1.2	-7.3	-0.4	-	-	-	-	-2.25	-6.81	-	-	0.85	-27.81
C_{23}	-8.7	5.5	7.9	6.0	11.0	12.23	12.08	0.46	8.7	1.68	0.78	3.89	2.97	13.70	31.91
C_{25}	-53.5	-1.6	-1.5	-3.6	1.4	-	-	-	-	-2.11	-3.9	-	-	-0.65	5.84
C_{35}	33.5	1.8	1.8	2.2	2.8	-	-	-	-	3.18	3.04	-	-	-2.19	-21.03
C_{46}	9.3	-2.3	-2.5	-1.4	2.3	-	-	-	-	-5.27	-4.14	-	-	0.54	0.83

α: [4]

The addition of FII and PTHEO improves the fitting values might be the results of the flexibility of both structures as identified earlier in the conformational analysis. The ease for torsional of main functional terminals in the FII result in swift calculations to compute the relative orientations at which all structures was at energy minima. That was contributing towards the huge differences between elastic components calculated in Fit 1 and Fit 2. In Fit 3, the values did not change much, this was because the FI and FII were already at the minimum and the presence of PTHEO only refined the components further. In this instance, the FII impact was clearly demonstrated. It would be interesting to see the influence of PTHEO if it was included before FII for future study. The rigid-flexible behaviour of FI, FII and PTHEO compensate each other functional term so that at the best orientations

The C_{11} component with 23.9GPa was the stiffest for FI as given in Table 6-5. The formation of $C = O \cdots H - O$ hydrogen bonds along a direction contributes to the stiffness of C_{11}. Conversely, the $N - H \cdots O - H$ hydrogen bonds along c direction as depicted in Figure 6-4 contributes to the C_{33} stiffness of 11.3GPa. The axial (C_{11}, C_{22}, C_{33}) large values compared to other components, reflected the strength created from having the hydrogen-bond networks created following these directions. The shearing components, C_{55} (6.1GPa) and C_{66} (6.3GPa) were large for molecular crystals that were more than 5GPa [5-6] and indicate resistance to shear. The elastic tensors computed confirmed the rigidity obeserved previously from the molecular conformation torsion energies analysis. FI molecules crystal paking were alternating, head to tail as seen in Figure 6-4 (a) and packed along the b axis. The alternating molecules arrangement creates a corrugated molecular packing therefore promotes resistance to shear through b-direction.
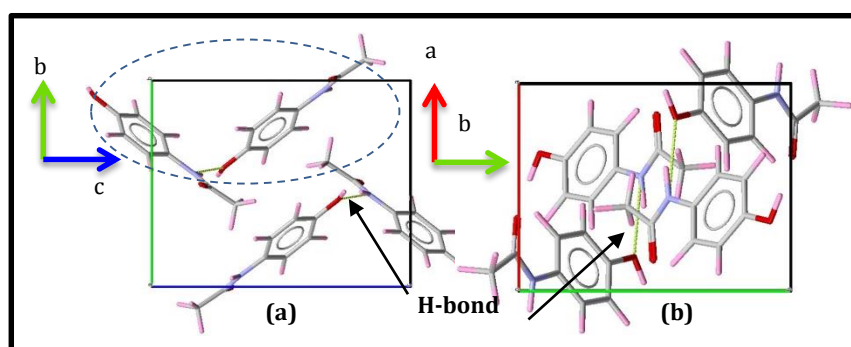
Figure 6-4 The unit cell of F1 viewing from [100] and [001] directions. The hydrogen bonds formed approximately along the [100] and [001] axis

Nevertheless, the huge variations of elastic components were not significant for FII as in FI shown in Table 6-5. The elastic components computed from Fit 2 and Fit 3 were marginally difference. The stiffest component was C_{33}, 37.42GPa and the softest was C_{13}, 0.8GPa. Similar to FI, the high C_{33} value was associated to the $C = O \cdots H - O$ hydrogen bond created in the c-direction. Moreover, the $N - H \cdots O - H$ hydrogen bonding was created in the b-direction as shown in Figure 6-5. The hydrogen bond networks were pulling the FII molecules in two directions (b and c) that creates a flat pleated sheets of a-b plane, stacking along a-axis. The smallest shearing component was C_{55} with 1.60GPa that relate to the potential deformation behaviour of FII. This shearing direction relate to the pleated sheets stacked along the a-axis with strong in-plane hydrogen bonds. The stacking of the flat planes with inter-planar distances approximately 4Å with no evident intermolecular interactions created in-between, this then justifies the lower C_{11} component of 10.42GPa compared to the other axial components (C_{22} and C_{33}). This flat pleated sheets were the most apparent slippage plane for FII. FII was identified as stable with regards to the Born stability with C_{44}, C_{55}, C_{66} components were all positive.
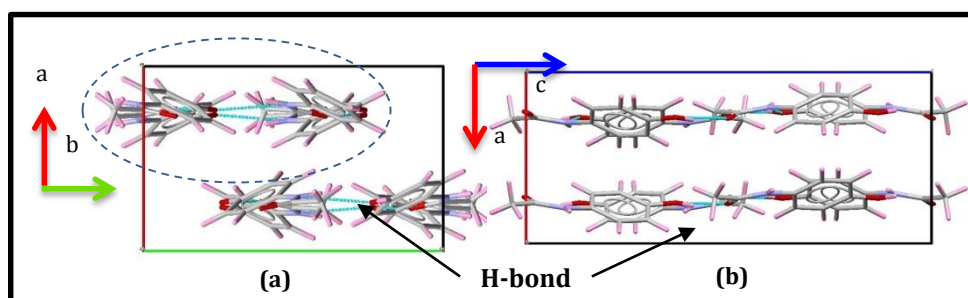
Figure 6-5 F2 unit cell viewing from [001] and [010] directions. The hydrogen bonds formed approximately along the [010] and [001] axis

Comparably, the PTHEO showed anisotropy behaviour with differing axial and shearing components, C_{11}, C_{22} and C_{33} with 7.27:21.71:9.83GPa and C_{44}, C_{55} and C_{66} with -1.58:2.91:6.02GPa respectively (Table 6-5). The C_{22} was the stiffest which interrelated to the $C = O \cdots H - N$ hydrogen bond created in the b direction between theophylline and paracetamol. Identical to the FII, the hydrogen bond network creates a flat pleated sheets, just about 45° diagonally along the c axis (Figure 6-5). The distance between the pleated sheets was roughly 3.7Å. There were no intermolecular interactions created in between the flat sheets and confirmed by the low off-diagonal component values (C_{15}, C_{25} and C_{46}) of -2.25: -2.11: -5.27GPa. These flat sheets seem to be the prominent slippage plane for PTHEO.

Accordingly, analysis of PTRI showed that the stiffest component was C_{33} with 14.64GPa. The other two axial components, C_{11} and C_{22}, exhibited similar strength with 9.20GPa and 8.27GPa respectively as presented in Table 6-5. The presence of three water molecules within PTRI gave a heavily hydrogen bonded system. The hydrogen bonds network created, $H - O - H \cdots O = C$ and $H - O \cdots H - N$ influences were obvious in the three axial components, C_{11}, C_{22} and C_{33} that were having large values compared to the diagonal and off-diagonal components. PTRI shearing components of 3.78GPa, 0.35GPa and 1.02GPa were well below 5GPa, manifesting less resistance to deformation. The smallest component is in the C_{55} direction relate to the stacking of molecules lying flat along the b axis (Figure 6-6(b)). The distance between the flat sheets were observed to be approximately 2Å. It was observed too that the diagonal components were positive therefore meeting the Born criteria for stable systems.

For the PHM, the axial had larger components compared to the diagonal with C_{11} (19.96GPa), C_{22} (21.21GPa) and C_{33} (17.15GPa). The diagonal components were C_{44} (2.34GPa), C_{55} (1.64GPa), and C_{66} (5.74GPa) which were about four times smaller to the axial. The low shearing component of C_{55} corresponds to the stacking of flat layer molecules along the b-axis. Furthermore, the formation of hydrogen bonds going in the three axial directions corroborates to the formation of flat layers of the b-c plane as seen in Figure 6-6 (c). The distance in-between the flat layers was about 2Å. The close positions between layers increase the strength of interactions, therefore, explains the rigidity observed in the conformation analysis.
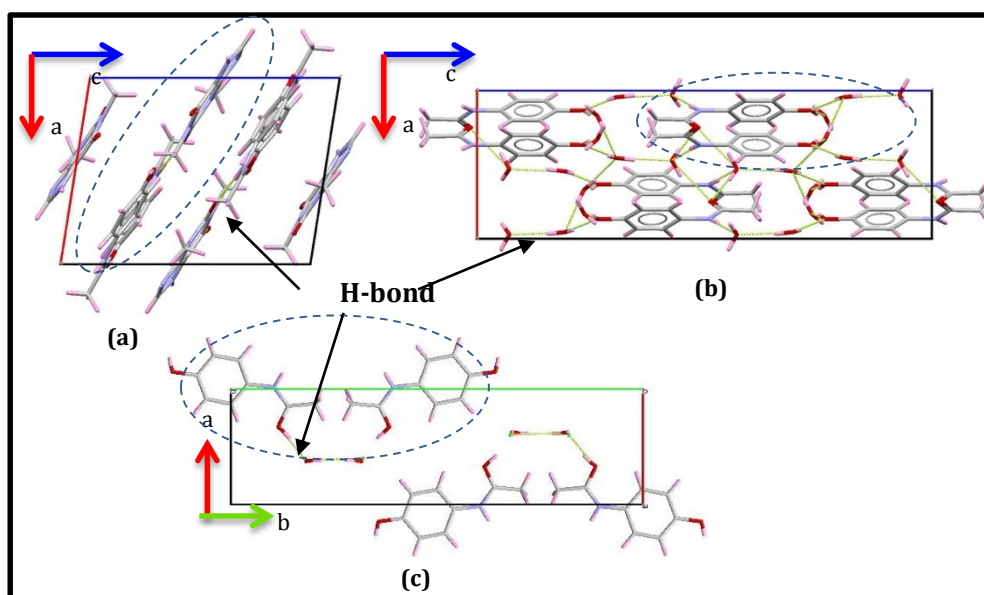
Figure 6-6 Unit cell of a) PTHEO b) PTRI c) PHM viewing from [010] and [001] respectively. The hydrogen bond created within each system were shown. The flat molecule arrangement was circled in blue

6.3.3 Elasticity as a factor to describe the mechanical properties

The computed tensors of the selected five solid forms of paracetamol were comparable to the DFT and literature except for the PHM. In PHM, DFT values showed quite a variation with the maximum component being 50.94GPa and minimum -72.71GPa. This variation relates to the probability that PHM is a salt, with strong contributions of interelectronic interactions between the chloride ions and hydrogen from water that bring about high kinetic energy of the electrons. The computed elastic components within this study, for selected paracetamol structures were seemly with the DFT and ab-initio. This demonstrate that it is feasible to get sensible tensors that can be done quickly and computationally cheaper. The simultaneous fitting is an approach which is useful to improve the computation of the elastic components.

Contrasting the elasticity for FI, FII, PTHEO, PTRI and PHM in Table 6-5, a stiffness rank amongst the compounds can be obtained by taking the axial components. The axial components were recognised as the Young's modulus while the diagonal components were the shear modulus [6-7]. In order of increasing stiffness, the rank was PTRI<PTHEO≈PHM<FI<FII. Unpredictably the FII was stiffer than the FI though the shearing components were smaller than the FI. The same trend was observed with the DFT and literature. The contradiction of the elastic components with regards to the deformability behaviour of FI and FII, suggested to be related to how molecules were packed within crystallographic packing. In FII, the flat layers create shorter distances between these planes which gave a denser condition that need more energy to deform. Moreover, the shorter distance hence increases the strength in the axial directions.

Though, through prior knowledge, FII was renowned to be softer than FI, this was not well represented if the axial components were to be used. For this case, the shearing components were best to represent the deformability of FII. This then create an issue of the best practice to use the elastic components to represent the stiffness of materials between the axial and shearing components for compounds which are not familiar for example new drugs candidate. From this observation, prior knowledge or more accompanying analysis was needed to assist the understanding of compounds deformability specifically the molecular systems. In this study, it was shown that the shearing components were best to describe the stiffness of the compounds. PTHEO was identified to be the softest and the stiffest was FI.

Comparing the elasticity properties of this study five paracetamol forms with the comprehensive lists of Young's modulus of Roberts, Rowe and York [5-6] indicated that FI was comparable to ibuprofen that was having Young's modulus of 5.02GPa measured by the three-point beam bending. The FII, PTHEO, PTRI and PHM can be classed together with long carbon chain molecules which are plastic behaving for instance testosterone propionate (3.16GPa), steric acid (3.84GPa) and polytetrafluoroethylene (PTFE) (0.71GPa). Moreover, the compounds were also comparable to the phenylbutazone with (3.33GPa). Thus, the derivation of paracetamol into co-crystals, hydrates and salts saw improvements in it mechanical strength based on the current elastic analysis. Consequently, the elasticity can be the first rank attributes to define the mechanical properties of molecular systems. Nonetheless, the calculated results of elastic components need to be treated with cautious as the mechanical properties of the molecular systems were more complicated that need further analysis to elucidate the reasons behind the behaviour shown.

At this point, the molecular structure of the five selected paracetamol systems had been grouped into their mechanical properties based on the conformational analysis and elastic calculations. Now, the mechanical properties characterisation is taken further by exploring the ins and outs of the solid forms behaviour by using this study proposed prediction tools. The predictions will offer more evidence of the crystal chemistry and lattice energetics that contributes to the mechanical deformation particularly plastic or fracture behaviour observed in solid forms. The following section will postulate the presence of potential slip systems within the five solid forms of paracetamol.

6.4 Molecular crystallographic computation for paracetamol Form I

Molecular and crystallographic modelling of paracetamol Form I (FI) were presented within this subsection. This include the lattice energetics and crystal chemistry analysis.

6.4.1 Crystallographic structure qualitative analysis of paracetamol Form I

FI molecules in a unit cell were seen to have a herring-bone (corrugated) position causing interlock if the system tries to slip under pressure. The molecule layers are linked by a glide plane (Figure 6-7). FI gained its stability from the formation of hydrogen bond [7-8]. Looking into the FI crystallographic structure in three-unit cell directions showed that FI was heavily corrugated as mentioned in the previous section. The nature of FI crystallographic structure makes identifying candidate slip plane not possible. The closest to slip plane was (011) shown in blue dotted line. Notice that (011) plane was cutting

through molecules creating a rough surface. Figure 6-7 illustrates the crystal packing ($2 \times 2 \times 2$) for FI inspecting from [100], [010], and [001]. FI crystal consists of four molecules in a unit cell with a complete structure in an asymmetric unit. From previous section two hydrogen bonds can be observed in FI that are $C = O \cdots H - O$ and $N - H \cdots O - H$ seen in green dotted line in Figure 6-7. Hence, from the qualitative crystallographic analysis, with minimal availability of potential slip plane, FI was anticipated to be rigid [8-9] consistent with elasticity calculation.

6.4.2   Lattice and morphology prediction of paracetamol Form I

Lattice energy of FI crystal was -81.22kJ/mol. The lattice energy has $\simeq$20kJ/mol difference in comparison to the sublimation enthalpy of -117.9kJ/mol [9-10]. This relatively big difference related to the use of gasteiger as partial charge. Gasteiger considers only the connectivity of the atoms during calculation hence slightly reduce the accuracy. The optimised unit cell parameters had differences of 2 to 8% compared to the experimental structure. Gasteiger was chosen because it was showing sensible lattice energy when used with the other four paracetamol structure when compared to the MOPAC charges. Therefore, to maintain consistency, gasteiger was used.

Plot of lattice energy convergence showed that point of convergence starts at lattice energy of -73.84kJ/mol and stabilises at -81.22kJ/mol as seen in Figure 6-7. The van der Waals (vdW), electrostatic and hydrogen bond contributions towards the lattice energy was given in Table 6-6. The lattice energy of FI was mainly contributed by the van der Waals attractive force with -124.34kJ/mol at 30Å. Moreover, it can be seen that the repulsive part of the van der Waals forces was consistent at 57.60kJ/mol starting at 9Å. The domination of the attractive part maybe caused by increase of the total hydrogen bond interactions as the limiting radii moves outwards to reach the limiting radii of 30Å.

Table 6-6 Contributions of van der Waals (vdW), electrostatic (coul) and hydrogen bond (h-bond) interactions towards the lattice energy of FI. Each of the components was divided into attractive (att), repulsive (rep) and a total of energy. All energies were given in kJ/mol

Range (Å)	VdW Att	VdW Rep	Total VdW	Coul	H-bond Att	H-bond Rep	Total H-bond	Total Energy
3	0.00	0.00	0.00	0.00	0.00	0.00	0.00	0.00
6	-48.38	20.33	-28.05	-2.77	-0.49	0.22	-0.28	-31.10
9	-116.52	57.55	-58.97	-14.49	-0.63	0.25	-0.38	-73.84
12	-121.24	57.60	-63.64	-13.21	-0.65	0.25	-0.40	-77.26
15	-122.89	57.60	-65.29	-14.24	-0.65	0.25	-0.40	-79.93
18	-123.69	57.60	-66.09	-13.52	-0.65	0.25	-0.40	-80.01
21	-124.01	57.60	-66.40	-14.15	-0.65	0.25	-0.40	-80.96
24	-124.19	57.60	-66.59	-13.93	-0.65	0.25	-0.40	-80.92
27	-124.28	57.60	-66.68	-13.96	-0.65	0.25	-0.40	-81.04
30	-124.34	57.60	-66.73	-14.08	-0.65	0.25	-0.40	-81.22

Predicted morphology using the attachment energy approach was illustrated in Figure 6-7 with FI shown to have a bulky hexagonal habit. There was four morphological importance faces namely (011), (110), (101) and (002). The biggest area coverage was (011). In Figure 6-7, it is apparent that the predicted morphology was comparable to the shape of the experimentally grown crystal. The (011) plane that was identified quantitatively as candidate slip plane for FI was marked clearly with the red broken line at the filled morphology. These list of morphological importance made part of the candidate slip planes to be tested next. The cleaved morphological importance faces demonstrated molecules at each face also the hydrogen bond created between molecules. As anticipated, each cleaved face cuts through corrugated FI molecules exposing carbonyl, amide and hydroxyl group for interaction. Moreover, the hydrogen bond was created in the direction normal and parallel to each importance plane.

Table 6-7 Morphological importance faces breakdown showing the slice and attachment energy for each. It was obvious that all four faces were fairly satisfied with values well above 30%

			FI	
Face (hkl)	d_{hkl} (Å)	Slice energy (kJ/mol)	Attachment energy (kJ/mol)	% Saturation of surface molecule (anisotropy factor)
(011)	7.19	-41.97	-39.25	51.7
(110)	5.59	-37.28	-43.93	45.9
(10-1)	6.39	-37.27	-43.94	45.9
(101)	5.66	-39.92	-41.30	49.2
(002)	5.74	-24.77	-56.44	30.5
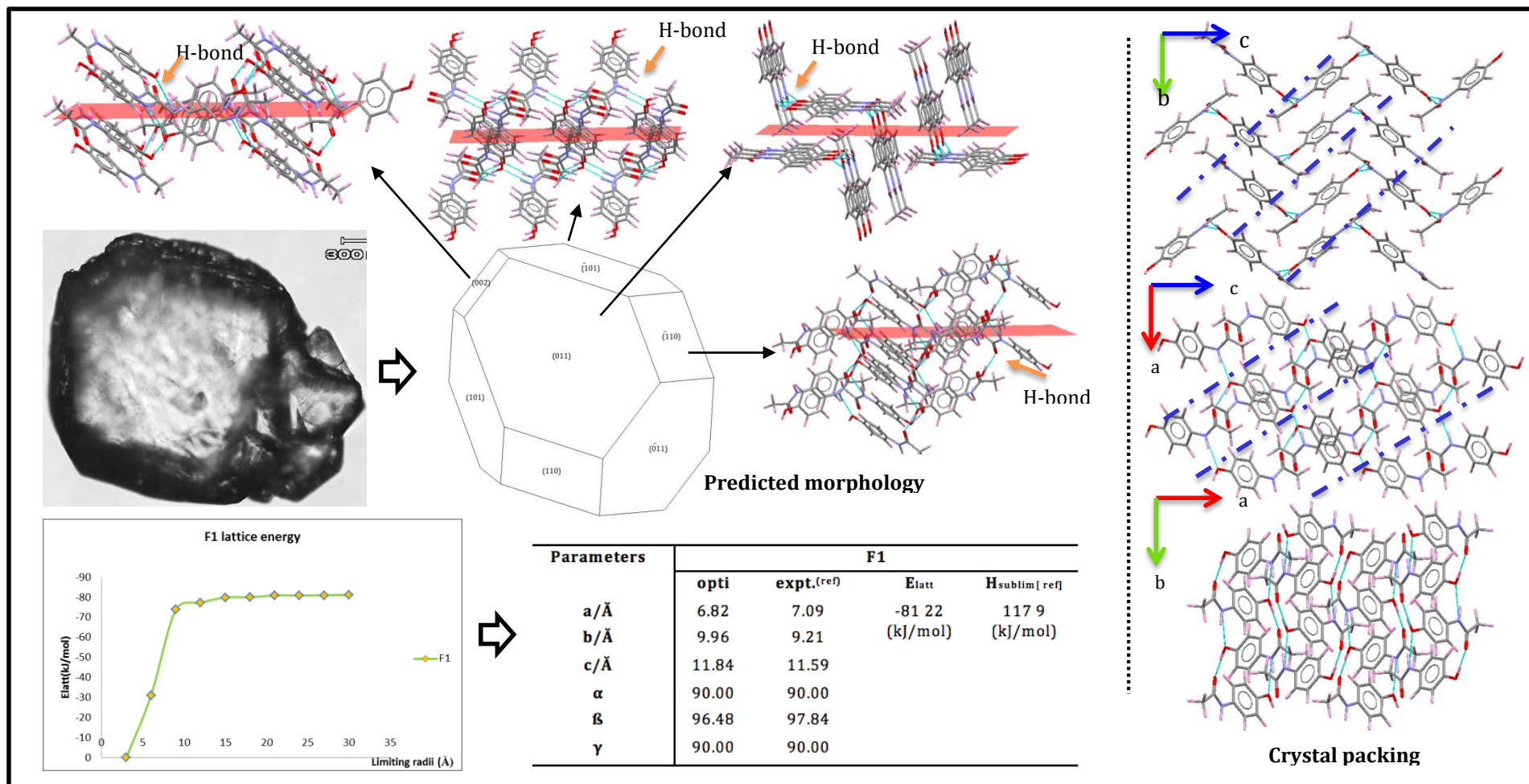
Figure 6-7 F1 predicted morphology using attachment energy model in comparison to the experimental grown crystal. The bottom left is the lattice energy convergence plots together with the optimised unit cell parameters. (011) as the potential slip plane (broken lines) showed through the crystal packing viewed from [100], [010], and [001]. Top four are cleaved faces that represent the general surface chemistry of the morphological importance faces namely (002), (101), (110) and (011). Hydrogen bond was clearly highlighted from the exposed faces showing the direction of the interaction

The anisotropy factor reflects best the face saturation correlating to the crystal growth rate of the specific face [10-11]. One interesting outcome was that all of the FI morphological planes were having reasonably high anisotropy factor that was well above 30% as given in Table 6-7. The most satisfied habit plane was (011) with 51.7%, and the least is (002) with 30.5%. The rest of the important habit planes specifically (110) and (101) were 45.9 and 49.2% satisfied at the surface. The (011) which was the biggest face was exposing the hydroxyl and carbonyl groups that were ready to make interactions with incoming new layers. The knowledge of surface chemistry for the dominant face offers an initial understanding of the behaviour of FI during crystallisation and milling process. Inspection on (002) showed that available hydroxyl terminals free to form bonds (Figure 6-7). Moreover, the high attachment energy demonstrates the activity of bond formation at (002). The predicted morphology of FI is depicted in Figure 6-7 showing the labile (002) having the smallest surface area, agreeing with the attachment activity observed.

6.4.3 Paracetamol Form I interatomic and intermolecular contacts elucidation

Table 6-8 provide types of atomic contributions to the lattice energy for FI. FI interatomic stability was given by carbon atom with -43.01kJ/mol contribution towards the total lattice energy. This result was somewhat expected because the aromatic ring in FI. Besides carbon atom, another major contributor was a hydrogen atom that was involved in a hydrogen bond with -36.19kJ/mol. Specific percent for atom's contributions towards the stability of the FI molecular structure was depicted in Figure 6-8.

Table 6-8 Atom type contribution towards the total lattice energy of FI with the highest contributor was carbon

Atom type	Attractive (kJ/mol)	Repulsive (kJ/mol)	Coulombic (kJ/mol)	Total (kJ/mol)
Hydrogen (H-bond)	-7.95	11.46	-39.71	-36.19
Hydrogen	-27.57	18.49	21.34	12.26
Carbon	-70.04	27.74	-0.71	-43.01
Nitrogen	-14.18	8.66	7.49	2.01
Oxygen	-17.66	16.53	-6.32	-7.41

Turning now to the main functional group contributions to the lattice energy given in Table 6-9. It is apparent from Table 6-9; the phenyl ring was the highest with 53%.
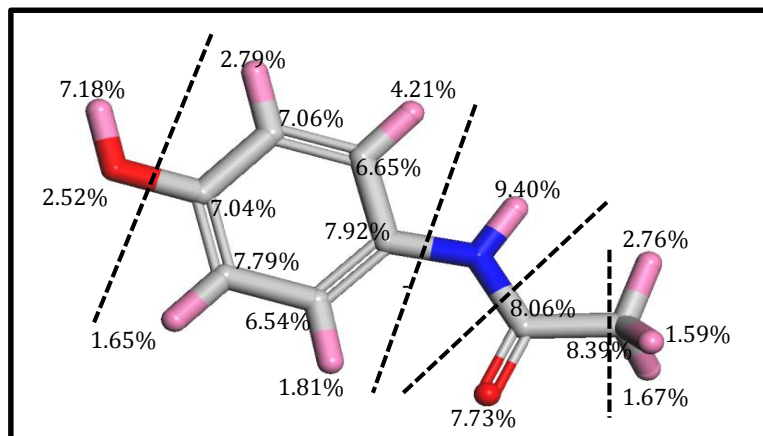
Figure-6-8 Specific atoms contribution towards the stability of F1 molecular structure. The distributions were dominated by carbon with the presence of aromatic carbon

Table 6-10 provides the dominating intermolecular interaction of FI. The strongest interaction was hydrogen bond with the strength of -19.29kJ/mol in [100] direction. Both bonds were represented in Figure 6-9. This striking strength difference suggested that FI was held together by hydrogen interaction hence provide its stability at room temperature [7-8]. Furthermore, the domination of hydrogen bond confirms the earlier conformational analysis of FI that has close distance and strong hydrogen bond network. The formation of this hydrogen bond network further strengthened the herring-bone formation within the FI crystal. Besides the two dominant bonds, another three types of bond that contributed to the lattice energy were also given with one was the $\pi - \pi$ stacking in [011] direction.

Table 6-9 Main functional group contributions to the lattice energy. The highest contributor was phenyl with 53%

Main functional group	Attractive (kJ/mol)	Repulsive (kJ/mol)	Coulombic (kJ/mol)	Total (kJ/mol)	%
Phenyl	-62.43	26.02	-2.22	-38.62	53
Hydroxyl	-20.21	20.21	-7.07	-7.07	10
Amide	-17.20	13.39	-1.05	-4.85	7
Methyl	-20.33	11.59	-1.72	-10.46	14
Carbonyl	-17.24	11.67	-5.86	-11.42	16

Table 6-10 The dominating intermolecular bond in FI. The strongest bond was hydrogen bond with a distance of 3.64 Å. Another obvious bond was the van der Waals with a distance of 6.80 Å. Other bonds that were contributing towards the lattice energy also given

Bond	Multiplicity	Distance (Å)	Intermolecular energy (kJ/mol)	Dominating intermolecular interaction type
A	4	3.64	-19.29	hydrogen bond
B	8	6.80	-7.03	van der Waals
C	8	7.21	-5.94	van der Waals
D	4	7.34	-5.27	van der Waals
E	4	5.96	-4.35	$\pi - \pi$ bond
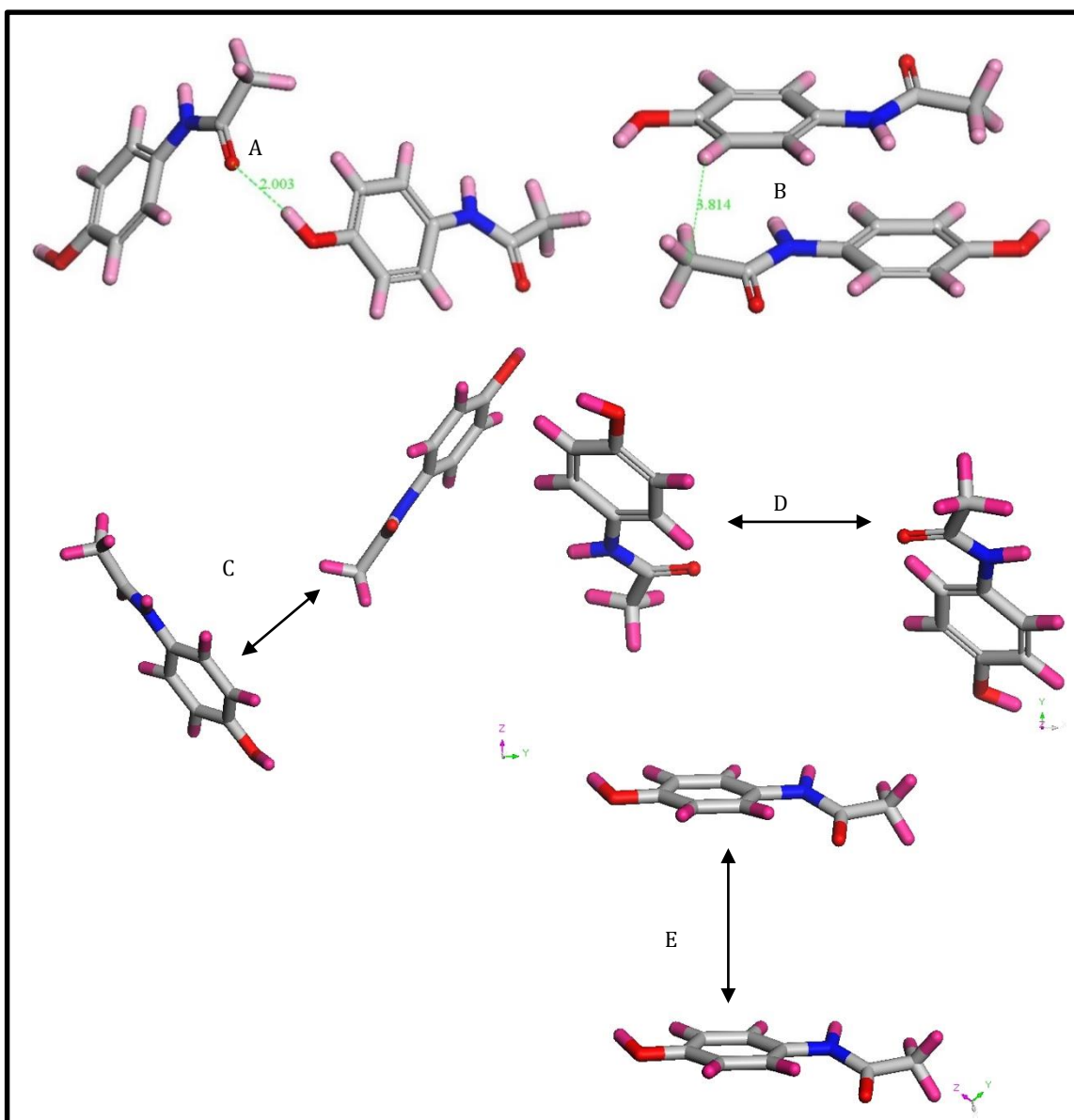
Figure 6-9 The dominant intermolecular bonds that are a) hydrogen bond ($C = O \cdots H - O$) b) van der Waals ($C - H \cdots C - H$) and c) $\pi - \pi$ bond. The hydrogen bond was 3.64 Å separated between two molecules while the van der Waals was 6.80 Å

Overall, this subsection concludes that FI crystal chemistry was driven by hydrogen bond. This interaction was supported with the 50.03% of interatomic contribution was from the hydrogen atom in a hydrogen bond. The crystal chemistry that governs the directionality of interactions was essential for some molecular systems. Now that the crystal chemistry has been investigated, the following subsection will integrate the lattice energetics and crystal chemistry findings to quantitatively analyse the potential slip plane.

6.5   Molecular crystallographic computation for paracetamol Form II

Paracetamol Form II (FII) was reported to show better tabletability compared to the stable form [11,15]. The objective of this section is to compute the lattice and crystallographic behaviour of FII that contributes to its deformation.

6.5.1   Qualitative analysis of crystallographic structure of paracetamol Form II

An asymmetric unit of FII contains a complete molecule and in total, there were eight molecules in a unit cell placed as flat layers as seen in Figure 6-10. The apparent intermolecular interaction was a hydrogen bond. By looking into the crystallographic packing of FII through [100], [010] and [001], two probable slip planes were identified that are (100) and (110). The (100) and (110) planes were shown as blue and purple broken line in Figure 6-10. Notice that the layer did not intercept, and this makes the slip easy to occur and increase the compressibility of FII compared to FI. Hydrogen bond were observed in the direction of [010] and [001] identified as $C = O \cdots H - O$ and $N - H \cdots O - H$ as mentioned in the elasticity analysis. Moreover, the pattern of hydrogen bond formation between molecules created a close ring that was supporting the stability of FII. Slip may take place in the direction parallel to [010]. Compares to FI, hydrogen bond formation in FII did not create dimers, hence giving FII its flexibility.

6.5.2   Lattice and morphology prediction paracetamol Form II

Lattice energy of FII calculated in this study was -80.01kJ/mol. It was $\simeq$25kJ/mol difference with the experimentally measured sublimation enthalpy, -115.9kJ/mol (Figure 6-10). There was less than 4% difference between the calculated and experimental unit cell parameters. From the plot of lattice energy (kJ/mol) against the limiting radii (Å) in Figure 6-10, FII starts to converge at lattice energy of -72.13kJ/mol and stabilises at -80.10kJ/mol. The plot of lattice energy convergence showed that point of convergence starts at -

72.13kJ/mol and stabilises at -80.01kJ/mol as seen in Figure 6-10. The van der Waals (vdW), electrostatic and hydrogen bond contributions towards the lattice energy were given in Table 6-11. The lattice energy of FII was mainly contributed by the van der Waals attractive force with -124.34kJ/mol at 30Å. Moreover, it can be seen that the repulsive part of the van der Waals forces was consistent at 85.40kJ/mol starting at 15Å. For FII, the coulombic interaction was seen to contribute approximately half of the van der Waals interactions. As the distance between two atoms become smaller, the coulombic contributions increases.

The predicted morphology of FII has a columnar shape as depicted in Figure 6-10. There is four morphological importance faces namely (111), (012), (002) and (020) as given in Table 6-12. Face (111) has the biggest fractional surface area with 61.96%. The smallest surface area was (020) face with less than 10% area.

Table 6-11 Contributions of van der Waals (vdW), electrostatic (coul) and hydrogen bond (h-bond) interactions towards the lattice energy of FII. Each of the components was divided into attractive (att), repulsive (rep) and a total of energy. All energies were given in kJ/mol

Range (Å)	VdW Att	VdW Rep	Total VdW	Coul	H-bond Att	H-bond Rep	Total H-bond	Total Energy
3	0.00	0.00	0.00	0.00	0.00	0.00	0.00	0.00
6	-31.24	16.71	-14.54	-1.67	0.00	0.00	0.00	-16.20
9	-132.05	85.17	-46.88	-24.33	-1.23	0.32	-0.92	-72.13
12	-138.71	85.39	-53.32	-22.49	-1.24	0.32	-0.92	-76.73
15	-140.38	85.40	-54.98	-22.35	-1.24	0.32	-0.92	-78.26
18	-141.16	85.40	-55.76	-23.02	-1.24	0.32	-0.92	-79.70
21	-141.43	85.40	-56.03	-22.89	-1.24	0.32	-0.92	-79.84
24	-141.61	85.40	-56.21	-22.37	-1.24	0.32	-0.92	-79.50
27	-141.70	85.40	-56.31	-22.67	-1.24	0.32	-0.92	-79.90
30	-141.77	85.40	-56.38	-22.79	-1.24	0.32	-0.92	-80.09

The predicted morphology of FII resembled the experimentally grown crystal. Only that, the predicted morphology, was slightly bulkier than the experimentally grown crystal. The minor mismatch was due to solvent effects during crystallisation was not considered during the morphology prediction. Seemingly, (100) plane was marked in blue dotted line the predicted morphology. The four cleaved faces shown in Figure 6-10, demonstrated molecules exposed at each dominant face also the hydrogen bond created between molecules. Each cleaved face cuts through FII molecules exposing carbonyl and hydroxyl groups.

Table 6-12 FII Attachment energy distributions showing the attachment and slice energy contributions. The surface satisfactions were also included to describe the surface interactions of each dominant face

			FII		
Face (hkl)	**d_{hkl} (Å)**	**Slice energy (kJ/mol)**	**Attachment energy (kJ/mol)**	**% surface area**	**% Saturation of surface molecule (anisotropy factor)**
(111)	5.9	-35.91	-44.10	61.96	44.9
(012)	7.17	-27.00	-53.01	14.30	33.8
(002)	8.90	-30.72	-49.29	13.68	38.5
(020)	6.06	-55.63	-55.76	7.88	30.4

Table 6-12 morphological importance faces breakdown showing the slice and attachment energy for each. The (111) face shown to have the biggest surface area while (020) the smallest and prone to interact during crystallisation. The high rate makes (020) face smaller. There was an insignificant difference of anisotropy factor between the morphological importance faces. The most satisfied face is (111) while the lowest was the (020) with 44.9% and 30.4% satisfactions respectively as presented in Table 6-12. The cleaved face of (111) showed that molecules were slanting clockwise following the hydrogen bond directions. The high values of anisotropy factor, makes (111) face did not prone to interaction as it was near to its saturation point.

The less interaction makes the crystals grow in (002) and (111), resulting in a columnar habit as shown in the micrograph. Moreover, it can be observed that (020) face slowly disappear. The orders of anisotropy factor for FII is (020)>(012)>(002)>(111). This outcome relates to hydrophilicity tendency of specific face studied by Heng et.al.[12] [16] In their study, they found out that (010) face was the most hydrophilic with available hydroxyl group ready for binding. Hence the anisotropy factor was shown to be a good indicator for analysing growth of crystal also for understanding the morphology of crystal.

6.5.3 Paracetamol Form II interatomic and intermolecular contacts analysis

Interatomic interaction in FII showed that the major contributor towards the lattice energy was carbon with -42.24kJ/mol. 78% of total carbon energy contributions originate from an aromatic ring. The total contributions of each atom type of FII were presented in Table 6-13. For another atom type beside hydrogen, specific atom type contributions were represented in Figure 6-11. The hydrogen atom in hydrogen bonding contributions was -28.60kJ/mol.
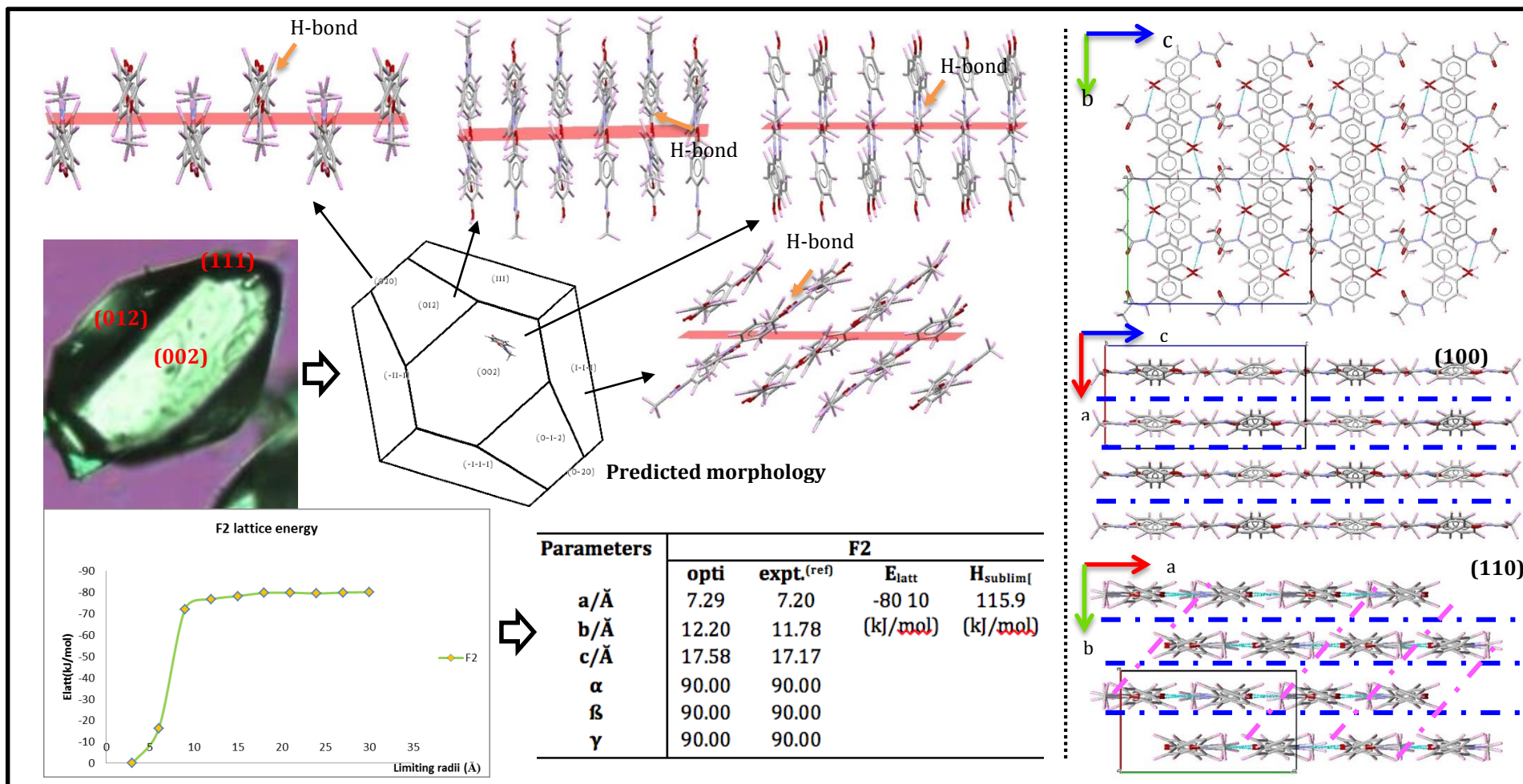
Figure 6-10 F2 predicted morphology using attachment energy model in comparison to the experimental grown crystal. The bottom left is the lattice energy convergence plots together with the optimised unit cell parameters. (100) and (110) as the potential slip planes (broken lines) showed through the crystal packing viewed from [100], [010], and [001]. Top four are cleaved faces that represent the general surface chemistry of the morphological importance faces namely (002), (101), (110) and (011). Hydrogen bond was clearly highlighted from the exposed faces showing the direction of the interaction

Table 6-13 Atom type contribution towards the total lattice energy of FII with the highest contributor was carbon with 70.37% of total lattice energy

Atom type	Attractive (kJ/mol)	Repulsive (kJ/mol)	Coulombic (kJ/mol)	Total (kJ/mol)
Hydrogen (H-bond)	-51.79	42.62	-19.47	-28.60
Hydrogen	-34.04	46.77	13.40	26.17
Carbon	-73.73	29.60	1.84	-42.24
Nitrogen	-6.57	2.93	0.67	-2.97
Oxygen	-69.50	70.55	-13.44	-12.39

Phenyl group contributed 58% towards the total lattice energy of FII. The second highest contributor was carbonyl group with 42%. The main functional group contributions are given in Table 6-14.

Table 6-14 Lattice energy contribution of the main functional group in FII. Major contributor was phenyl with 58% follows by carbonyl with 42%

Main functional group	Attractive (kJ/mol)	Repulsive (kJ/mol)	Coulombic (kJ/mol)	Total (kJ/mol)	%
Phenyl	-69.20	34.14	1.13	-33.93	58
Hydroxyl	-14.14	29.33	-6.11	9.08	-15
Amide	-62.68	65.81	-4.60	-1.46	2
Methyl	-21.97	14.43	-0.59	-8.12	14
Carbonyl	-67.45	49.62	-6.74	-24.56	42
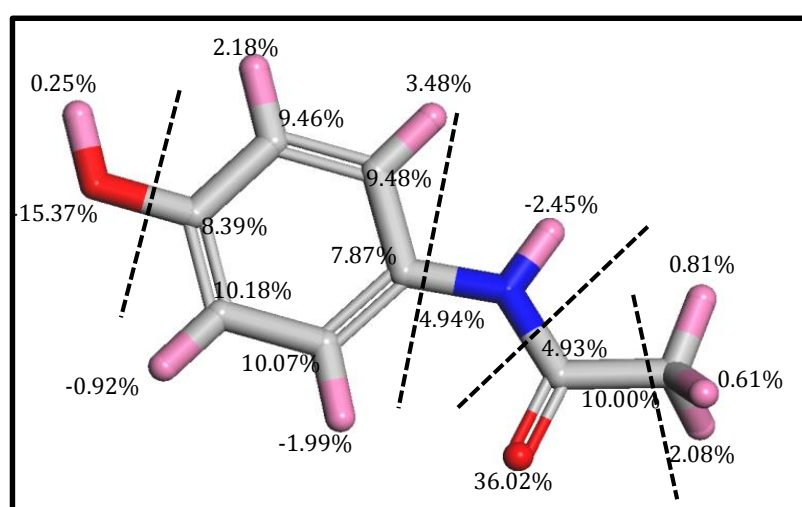
Figure 6-11 Represent the specific atom types contributions toward the lattice energy of F2. The phenyl makes 58% of the F2 lattice energy

Turning now to the intermolecular interaction in FII, the strongest bond was between carbonyl oxygen and hydroxyl hydrogen (A) as shown in Figure 6-12. The strength of the interaction was 13.52kJ/mol with a distance of 8.79Å. The strength of the bond was contributed most by the attractive force between carbonyl atom and hydrogen. Table 6-15 provides a list of significant intermolecular interaction for FII. Besides hydrogen bond, FII also was governed by the van der Waals interaction between nitrogen and hydrogen (G). The strength of C is -9.80kJ/mol with a distance of 7.09Å.
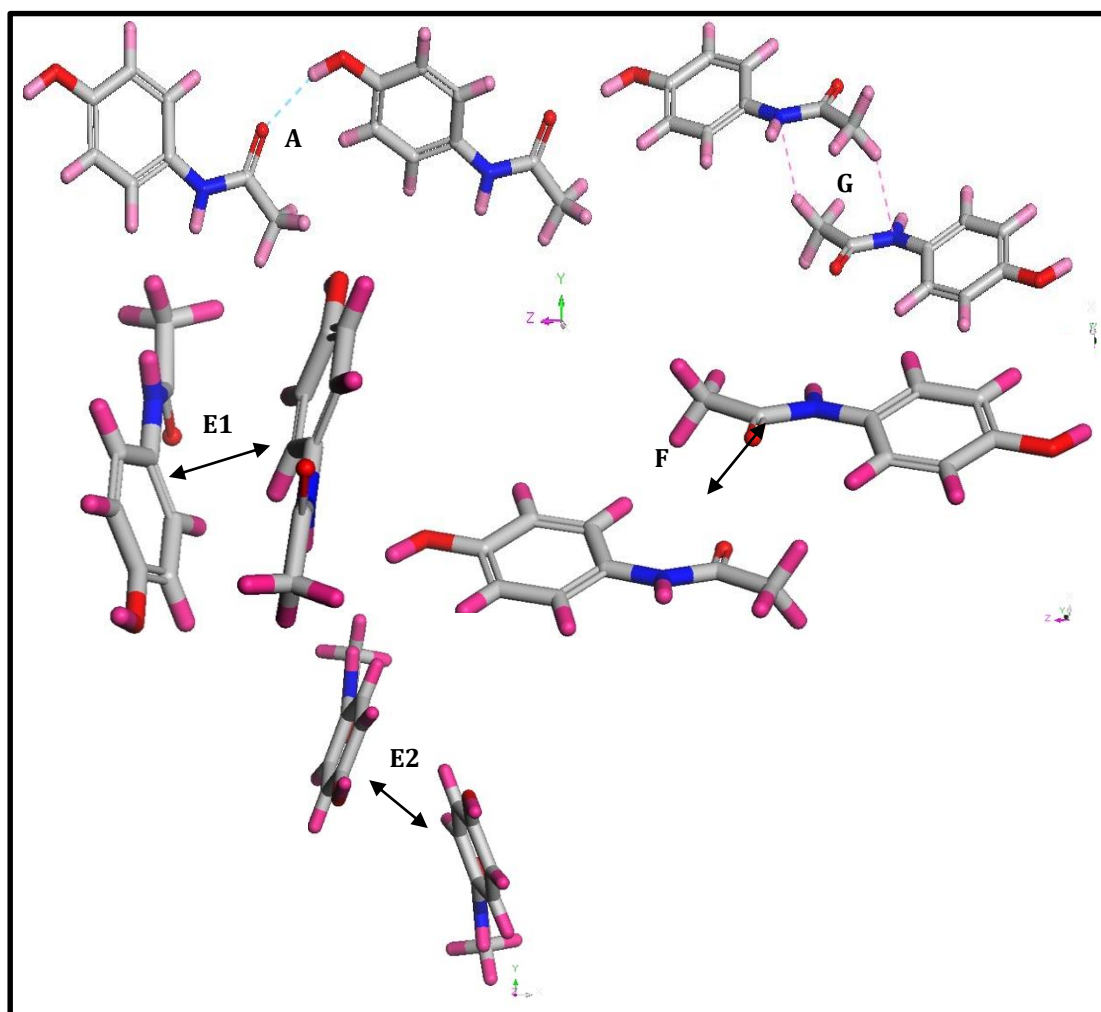
Figure 6-12 Five most dominant intermolecular bonds consisting a) hydrogen bond b) van der Waals. The hydrogen bond (A) was 2.00 Å separated between molecule while the van der Waals (G) is 3.81 Å

From Figure 6-12, the hydrogen bond was created in the direction of [010]. The short contacts formed by the van der Waals interaction were forming a dimer in the direction of [100]. The hydrogen bonding formation was stacked along the [010] direction with no inter-plane hydrogen bond form. This condition strengthened the in-plane strength, therefore, easier for the plane to slip. The sheets of plane that were placed in flat layers were reinforced by the availability of in-plane hydrogen bond network. The directionality of the hydrogen bond explains the elongation of the crystal forming the columnar habit.

The significant strong in-plane hydrogen network bonding makes the inter-planar interaction became weak hence easier to slip between planes when under pressure. The ability to easily slip in the direction parallel to the ab-plane, provide the plasticity properties of FII. Dimer formation between the van der Waals bonds contributes to the stability of FII. Though the van der Waals short contact was slightly weaker from the hydrogen bond by -4kJ/mol, the repetition of the bonding gave reasonable strong force towards the FII stability.

Table 6-15 The dominating intermolecular bond in FII. The strongest bond was hydrogen bond with a distance of 8.79 Å. Another obvious bond is the van der Waals with distance of 7.09 Å

Bond	Multiplicity	Distance (Å)	Intermolecular energy (kJ/mol)	Dominating intermolecular interaction type
A	16	8.79	-13.51	hydrogen bond
G	8	7.09	-9.80	van der Waals
E1	16	5.36	-9.41	$\pi - \pi$ bond
F	8	7.06	-8.20	van der Waals
E2	16	5.27	-6.78	$\pi - \pi$ bond

6.6 Molecular crystallographic computation for paracetamol theophylline co-crystal

Paracetamol theophylline (PTHEO) co-crystal was reported to create a layered-like crystallographic pattern. The nature of the crystallographic pattern created in the PTHEO was investigated. This section will present the results of the crystallographic packing analysis of PTHEO.

6.6.1 Crystallographic structure qualitative analysis of paracetamol theophylline

Observation of the PTHEO molecular packing from [100] direction showed wavy sheets of planes. When viewed from [010] distinct diagonal layers were seen with both paracetamol and theophylline molecules were laid flat. This diagonal plane was recognised as (101) and served as the most probable plane to slip. Furthermore, no intermolecular networks were observed created in between the flat layers which make the inter-planar interactions as weak, compared to the intra-planar interactions. In the [001] direction, the theophylline and paracetamol molecules were seen stacked in an alternating manner.

6.6.2 Lattice and morphology prediction paracetamol theophylline

Lattice energy of PTHEO crystal was calculated to be -145.06kJ/mol. The lattice energy starts to converge at 15Å as seen in Figure 6-13. The attractive and repulsive components were contributing significantly to the lattice energy with approximately -350.37 and -223.47kJ/mol respectively as given in Table 6-16. The optimised unit cell parameters had differences of 2 to 9% compared to the experimental structure. given in Figure 6-13.

Table 6-16 Contributions of attractive (Att), repulsive (Rep) and electrostatic (Coul) towards the lattice energy of PTHEO

Range(Å)	Att	Rep	Coul	Total Energy
3	-32.51	15.02	-0.33	-17.82
6	-107.40	89.04	-1.84	-20.21
9	-236.44	173.68	-10.29	-73.05
12	-329.20	218.53	-15.94	-126.61
15	-343.76	222.13	-16.36	-137.99
18	-348.53	223.47	-18.07	-143.13
21	-348.95	223.47	-18.87	-144.35
24	-349.99	223.47	-17.95	-144.47
27	-350.20	223.47	-18.03	-144.77
30	-350.37	223.47	-18.16	-145.06

Predicted morphology using the attachment energy approach was illustrated in Figure 6-13 giving octagonal shape crystal and matched the experimentally grown crystal. There was four morphological importance faces namely (011), (020), (101) and (10-1). The biggest area coverage was (101). The (101) plane that was identified qualitatively as candidate slip plane for PTHEO was marked clearly with blue broken line at crystal packing viewing from [010]. The cleaved morphological importance faces demonstrated molecules at each face also the hydrogen bond created between a molecule of paracetamol and theophylline. Cleaving of the surfaces exposed the hydroxyl and amide terminal. The (101) plane showed molecules arranged parallel to the plane. Moreover, it was obvious that the hydrogen bond was forming in-plane suggesting a strong in-plane intermolecular interactions. For (10-1) and (011), the hydrogen interactions were normal to the plane.

Table 6-17 Morphological importance faces breakdown showing the slice and attachment energy for each. It is obvious that three out of the four faces were very satisfied with values well above 60%. The only unsatisfied face was (020) with 49%

Face (hkl)	d_{hkl} (Å)	Slice energy (kJ/mol)	Attachment energy (kJ/mol)	% Saturation of surface molecule (anisotropy factor)
(011)	9.17	-101.34	-47.95	67.89
(10-1)	7.66	-125.65	-23.64	84.17
(101)	6.99	-94.14	-55.19	63.06
(020)	7.86	-73.18	-76.11	49.00

One interesting outcome was that all of the PTHEO morphological planes were having reasonably high anisotropy factor that was between 49% and 84% as given in Table 6-17. The most satisfied habit plane was (10-1) with 84.17%, and the least is (020) with 49%. The rest of the important habit planes specifically (101) and (011) were 63.06 and 67.89% satisfied at the surface. The satisfaction correlates well with the predicted morphology which showed the smallest face of (020). Moreover, the low satisfaction, promote the high attachment energy on the (020) face to achieve stability. The plate-like morphology can also be explained by the huge gap between the smallest to the largest dominating face of PTHEO with ratio approximately 0.58 based on the anisotropy factor.
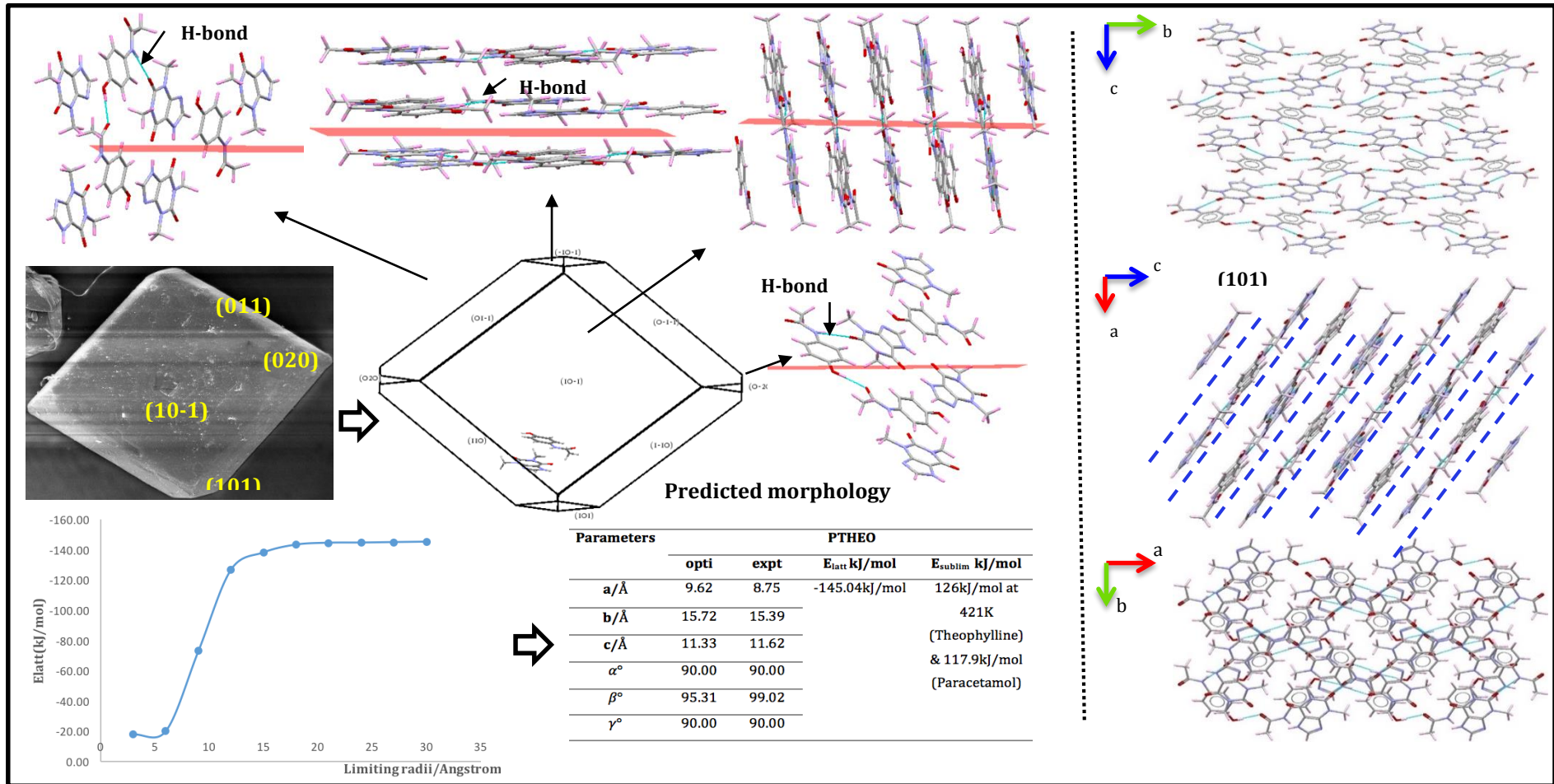
Figure 6-13 PTHEO predicted morphology using attachment energy model in comparison to the experimental grown crystal. The bottom left was the lattice energy convergence plots together with the optimised unit cell parameters. (101) as the potential slip plane (broken lines) showed through the $2 \times 2 \times 2$ crystal packing viewed from [100], [010], and [001]. Top four were cleaved faces that represent the general surface chemistry of the morphological importance faces namely (10-1), (101), (020) and (011). Hydrogen bond was clearly highlighted from the exposed faces

6.6.3 Paracetamol theophylline interatomic and intermolecular contacts elucidation

Each of the dominant morphology faces was seen to either have a high slice energy that was related to satisfied face or high attachment energy which represents the less satisfy hence prone to interact with the incoming new slice. The demarcation of the intermolecular interactions that lead to the different slice and attachment for PTHEO will be presented in this subsection.

The interatomic interactions showed that the highest atoms contributing towards the lattice energy were carbon with 83.47% as presented in Table 6-18. The carbon atom was shown to dominate with other atoms were contributing between 27.76% to -9.80%. The attractive component was the reason for this obvious domination with contributions of -129.66kJ/mol. There were 15 carbon atoms in a PTHEO structure, whereby 10 of these atoms were in a phenyl and purine ring. It was suspected because of the resonance within the phenyl and purine rings promote the attractive interactions of PTHEO. Specific atoms contribution was shown in Figure 6-14. Though paracetamol (FI) and theophylline (THEO) have similar molecular size with THEO consists an extra atom, the interatomic analysis indicated that the paracetamol molecule was contributing a total of 63.79% towards the lattice energy.

Table 6-18 Atom type contribution towards the total lattice energy of PTHEO with the highest contributor was carbon with 83.47%

Atom type	Attractive (kJ/mol)	Repulsive (kJ/mol)	Coulombic (kJ/mol)	Total (kJ/mol)	%
Hydrogen (H-bond)	-0.63	4.94	-32.72	-36.19	26.76
Hydrogen	-48.91	47.49	10.42	12.26	-9.80
Carbon	-129.66	51.59	-0.71	-88.74	83.47
Nitrogen	-31.63	12.64	7.49	-4.27	4.01
Oxygen	-35.61	42.76	-6.32	4.73	-4.44
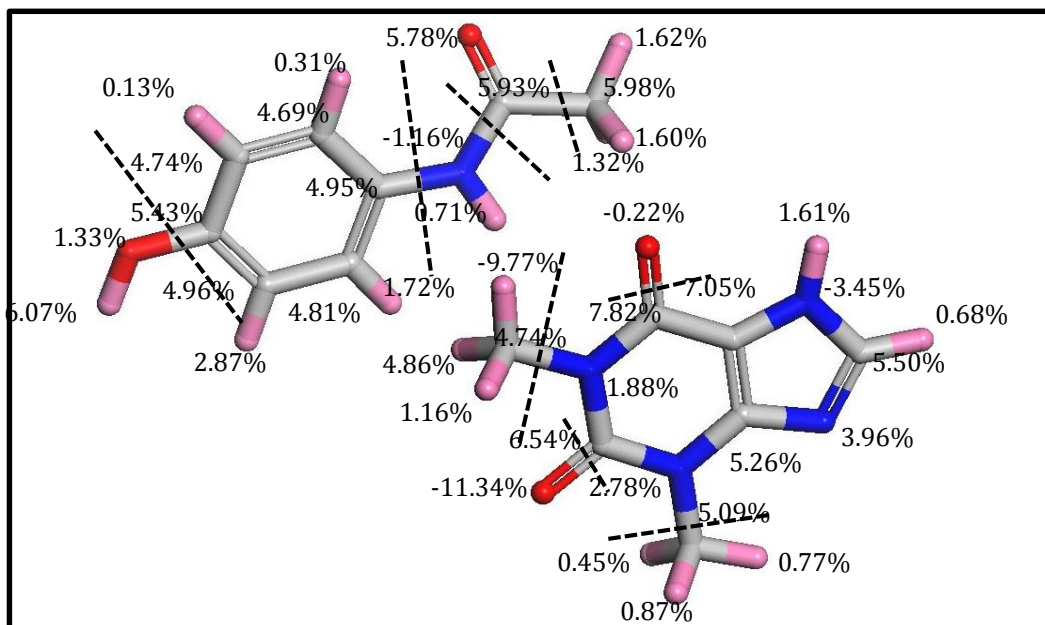
Figure 6-14 Specific atoms contribution towards the stability of PTHEO molecular structure. The distributions were dominated by carbon with the presence of aromatic carbon

The distribution of lattice energy was fairly equal when analysing it based on the main functional group. The major contributor was phenyl with 35% follows by purine with 25%. Both were aromatic structures.

Table 6-19 Functional group contributions toward the lattice energy of PTHEO. The major contributor was phenyl with 35% while the least is amide

Main functional group	Attractive (kJ/mol)	Repulsive (kJ/mol)	Coulombic (kJ/mol)	Total (kJ/mol)	%
Phenyl	-63.60	27.99	-1.13	-36.74	35
Hydroxyl	-10.71	6.86	-4.06	-7.91	7
Amide	-9.96	5.40	5.06	0.50	0
Methyl	-55.27	48.91	-13.43	-19.79	19
Carbonyl	-53.85	50.29	-11.88	-15.44	15
Purine	-53.18	20.00	6.32	-26.86	25

The intermolecular interactions were given in Table 6-20 presented the top five strong bonds created between FI-FI, FI-THEO and THEO-THEO molecules. The strongest intermolecular interaction was the hydrogen bond (H) created between FI-THEO with -16.61kJ/mol at a distance of 4.08Å. Besides hydrogen bond, the $\pi - \pi$ bond (I) formed between FI-THEO exhibited quite significant strength with -10.54kJ/mol. Other type of bond was van der Waals interactions (J) formed between FI-THEO. All five strong intermolecular interactions were depicted in Figure 6-15.

Table 6-20 The dominating intermolecular bond in PTHEO. The strongest bond was hydrogen bond with a distance of 4.08 Å. Another obvious bond is the $\pi - \pi$ bond with distance of 5.78 Å

Bond	Multiplicity	Distance (Å)	Intermolecular energy (kJ/mol)	Dominating intermolecular interaction type
H	8	4.08	-16.61	hydrogen bond
I	8	5.78	-10.54	$\pi - \pi$ bond
A	4	6.41	-8.66	hydrogen bond
J1	8	5.96	-7.95	van der Waals
J2	8	6.58	-5.15	van der Waals
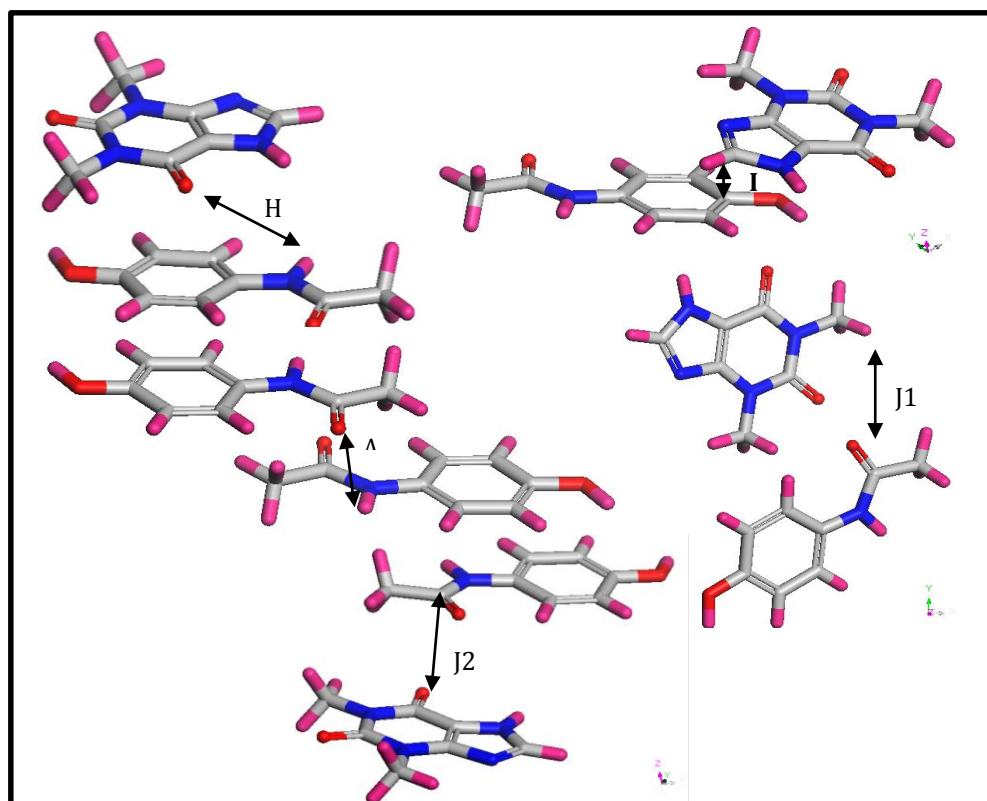
Figure 6-15 Five strong intermolecular interactions for PTHEO. The strongest was given by hydrogen bond (H) created between ($C = O \cdots H - N$) with -16.61kJ/mol. The bond was separated by 4.08Å. Other interactions were identified to be $\pi - \pi$ bond (I) between paracetamol-theophylline, van der Waals (J) between paracetamol-theophylline and hydrogen bond (A) between paracetamol-paracetamol molecules

The interatomic result showed that PTHEO lattice energy was contributed most by carbon atoms, and the most strongest intermolecular interaction was hydrogen bond created by FI-THEO. PTHEO was suggested to have directionality following the four hydrogen bonds created within a unit cell. The strong hydrogen bond was responsible for giving the flat layer for PTHEO, which was similar to the FII crystal packing. The intermolecular interactions identified, reflect the amount of energy needed to break bonds if a plane cuts through a unit cell.

6.7 Molecular crystallographic computation for paracetamol trihydrates

The influence of three water molecules towards the FI was studied. Paracetamol trihydrates (PTRI) was heavily hydrogen bonded and from the elastic calculations showed to be the softest amongst the other selected paracetamol solid forms. This section provides the result of lattice energetics and crystal chemistry of PTRI.

6.7.1 Crystallographic structure qualitative analysis of paracetamol trihydrate

Observation of the PTRI molecular packing from [100] and [001] directions showed layers of molecules arranged flat with one water molecule in the middle (Figure 6-22). The presence of three water molecules (H_2O) make the PTRI heavily hydrogen bonded. The directionality of the hydrogen bond, makes the crystal packing of PTRI dense therefore no obvious potential slip plane can be identified. Nevertheless, hypothetically the hydrogen bonds were not present, the (010) plane will be the probable plane to slip shown as blue broken line in Figure 6-16.

6.7.2 Lattice and morphology prediction paracetamol trihydrates

Lattice energy of PTRI crystal was calculated to be -198.87kJ/mol. The lattice energy starts to converge at 12Å as seen in Figure 6-16. The attractive and repulsive components were contributing significantly to the lattice energy with approximately -650.57 and 525.18kJ/mol respectively as given in Table 6-21. The optimised unit cell parameters had 0.5 to 6% difference compared to the experimental structure given in Figure 6-16.

Table 6-21 Contributions of attractive (Att), repulsive (Rep) and electrostatic (Coul) towards the lattice energy of PTRI given in kJ/mol

Range (Å)	Att	Rep	Coul	Total Energy (kJ/mol)
3	-126.27	111.96	-19.25	-33.56
6	-219.41	176.73	-24.89	-67.57
9	-363.67	276.81	-39.29	-126.15
12	-524.42	397.73	-54.73	-181.42
15	-575.55	445.60	-67.32	-197.28
18	-610.49	472.16	-71.34	-209.66
21	-612.33	472.58	-71.59	-211.33
24	-647.01	512.71	-74.64	-208.95
27	-650.24	525.18	-75.35	-200.41
30	-650.57	525.18	-73.47	-198.87

Predicted morphology using the attachment energy approach was illustrated in Figure 6-16 giving hexagonal plate shape crystal which fit the experimentally grown crystal. There was four morphological importance faces namely (002), (020), (102) and (021). The slowest growing face was (010) with -23.64kJ/mol. The (002), (020) and (102) faces exhibited low attachment energy (Table 6-22) showing the lack of interest to form a new intermolecular bond with the incoming new layers. One striking observation was that all four morphological importance face were very satisfied with the anisotropy factor between 77 and 91%. Face (020) attachment energy was approximately three times smaller than (021) making the latter face disappears from the predicted morphology. Cleaved face of (020) exposed the $N - H$ and $O - H$ terminals of FI were interacting with the H_2O leaving only the $C = O$ terminal unoccupied. Similarly, (002) cleaved face showed all terminals were occupied that explains the 91% anisotropy satisfaction.

Table 6-22 Morphological importance faces breakdown showing the slice and attachment energy for each. It was obvious that three out of the four faces were very satisfied with values between 77 and 91%. Slice energy was contributing most towards the lattice energy

|			PTRI	
Face (hkl)	d_{hkl} (Å)	Slice energy (kJ/mol)	Attachment energy (kJ/mol)	% Saturation of surface molecule (anisotropy factor)
(002)	9.17	-101.34	-47.95	90.55
(020)	7.66	-125.65	-23.64	84.35
(102)	6.99	-94.14	-55.19	81.46
(021)	7.86	-73.18	-76.11	77.34
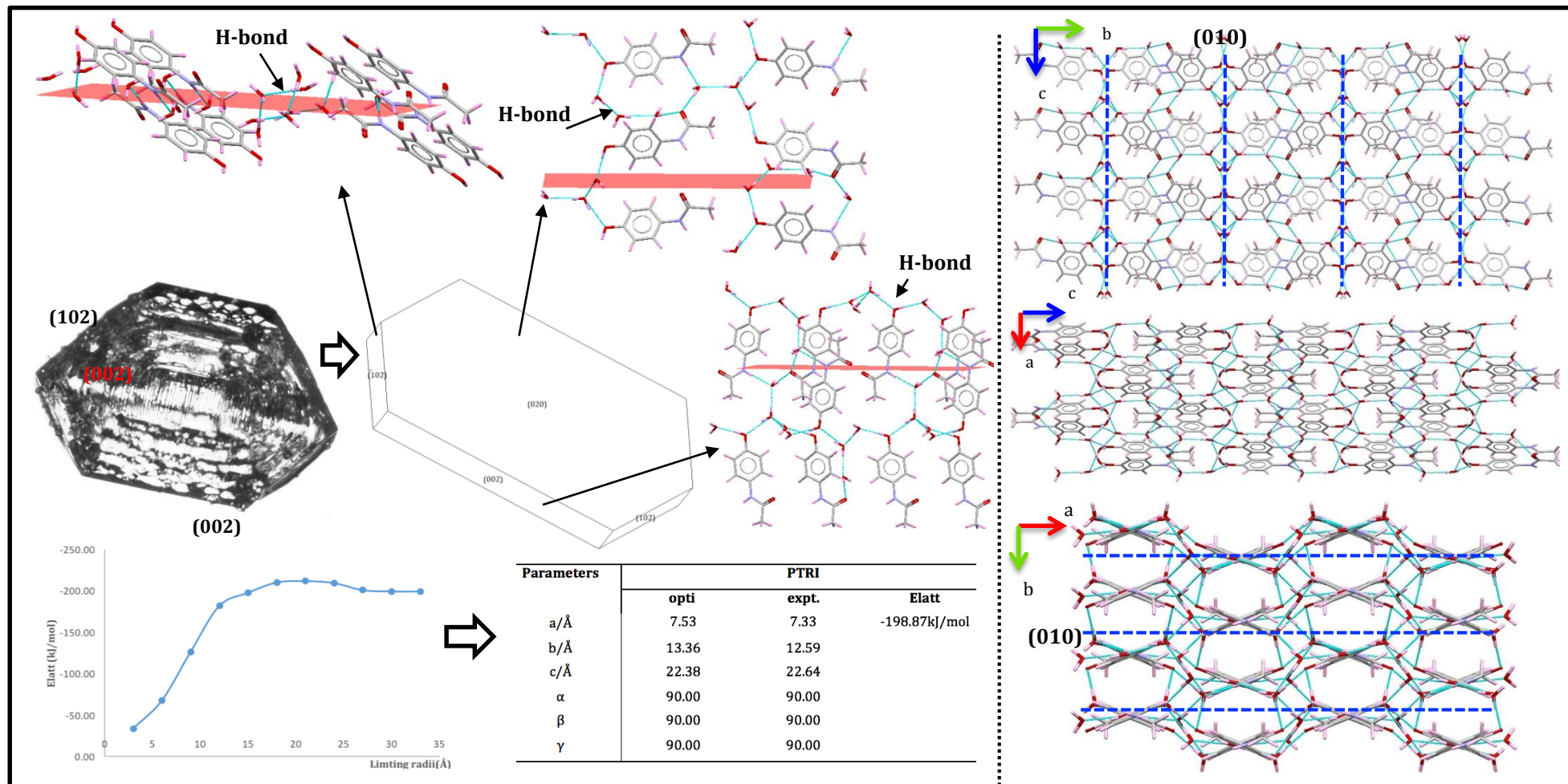
Figure 6-16 PTRI predicted morphology using attachment energy model in comparison to the experimental grown crystal. The morphology was drawn based on the centre to face distance. The bottom left was the lattice energy convergence plots together with the optimised unit cell parameters. (010) was the potential slip plane (broken lines) showed through the $2 \times 2 \times 2$ crystal packing viewed from [100], [010], and [001]. Top four were cleaved faces that represent the general surface chemistry of the morphological importance faces namely (002), (020) and (102)

The PTRI appeared as stable according to the attachment and lattice energy calculations. In the next subsection, the interatomic and intermolecular interactions that were contributing to the observed lattice energetics were presented.

6.7.3 Paracetamol trihydrates interatomic and intermolecular contacts elucidation

The interatomic interactions showed that the highest atoms contributing towards the lattice energy were hydrogen involves in hydrogen bonding (HB) with -490.57kJ/mol as presented in Table 6-23. The hydrogen energy was contributed majorly by the coulombic with -451.33kJ/mol as the attractive and repulsive components were fairly similar $\approx$ 200kJ/mol. The individual atomic contributions were presented in Figure 6-17. The three H_2O molecules were contributing up to 56.76% from the total interatomic interactions in PTRI. Likewise, the hydroxyl and amide terminals contributed 14.11% and 16.76% respectively that relate to the HB atom contributions towards the total interatomic interactions.

Table 6-23 Atom type contribution towards the total lattice energy of PTRI with the highest contributor was hydrogen involves in hydrogen bonding with 272.06%

Atom type	Attractive (kJ/mol)	Repulsive (kJ/mol)	Coulombic (kJ/mol)	Total (kJ/mol)
Hydrogen (H-bond)	-239.45	200.20	-451.33	-490.57
Hydrogen	-49.12	61.34	395.22	407.44
Carbon	-62.13	23.85	1.30	-36.99
Nitrogen	-8.45	4.23	-1.34	-5.56
Oxygen	-282.09	236.56	-9.12	-54.64
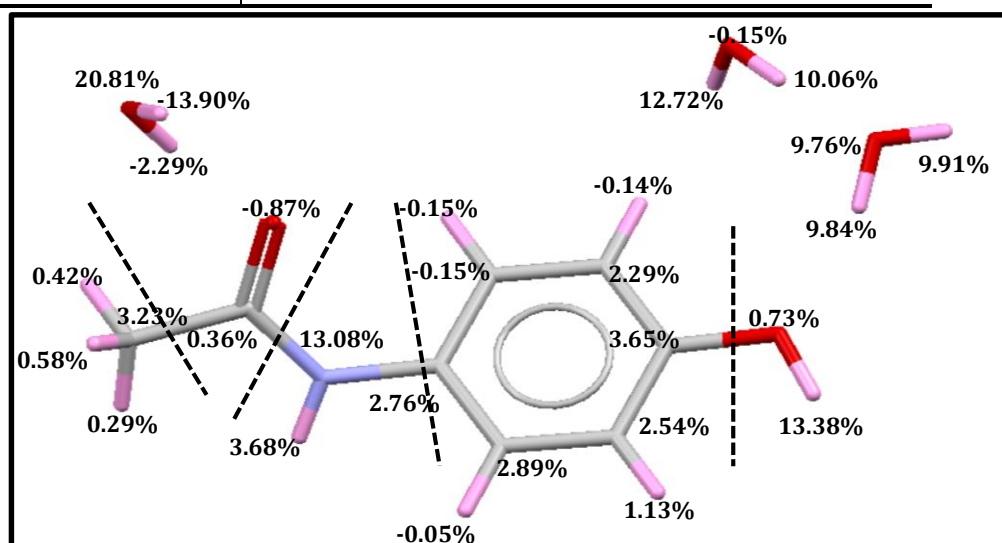
Figure-6-17 Specific atoms contribution towards the stability of PTRI molecular structure. The distributions were dominated by hydrogen involves in hydrogen bonding (HB). The water molecules contributed in total 56.76% while the hydroxyl terminal in paracetamol structure 14.11% and amide 16.76%. This in total showed the obvious HB domination in PTRI

The atomic pairing of the $O - H$ interatomic interactions demonstrates total domination as given in Table 6-24. The $O - H$ interactions correlate to the H_2O and hydroxyl terminal that contributed the most with 71%.

Table 6-24 Main functional group contributions to the lattice energy of PTRI. The $O - H$ interactions contributed the most towards the lattice energy of PTRI

Main functional group	Attractive (kJ/mol)	Repulsive (kJ/mol)	Coulombic (kJ/mol)	Total (kJ/mol)	%
Phenyl	-56.36	27.28	-4.10	-33.18	18
Hydroxyl	-489.57	412.71	-50.92	-127.78	71
Amide	-33.51	24.98	-3.68	-12.22	7
Methyl	-18.16	9.71	0.33	-8.12	5
Carbonyl	-43.60	51.51	-6.99	0.92	-1

The top seven intermolecular interactions were presented in Table 6-25 corroborates with the hydrogen bond network governing the PTRI structure. From the seven strong bonds, only one was identified as $\pi - \pi$ bond. The strongest interaction was created by $H_2O - H_2O$ molecules with -14.27kJ/mol known as K1. Similarly, the second strong was of the same type and represented as K2 in Figure 6-18. K1 and K2 was separated by $\approx$ 1Å. The third strong bond was between FI-H_2O noted as L1.

Table 6-25 The dominating intermolecular bond in PTRI. The strongest bond was hydrogen bond with a distance of 3Å with the strength of -14.27kJ/mol. The top four strong intermolecular interactions of PTRI was hydrogen bond

Bond	Multiplicity	Distance (Å)	Intermolecular energy (kJ/mol)	Dominating intermolecular interaction type
K1	16	3.00	-14.27	hydrogen bond
K2	16	2.96	-13.22	hydrogen bond
L1	16	5.84	-13.05	hydrogen bond
L2	16	5.59	-12.76	hydrogen bond
E	16	5.22	-11.76	$\pi - \pi$ bond
L3	16	3.63	-7.87	hydrogen bond
K3	16	2.95	-7.36	hydrogen bond
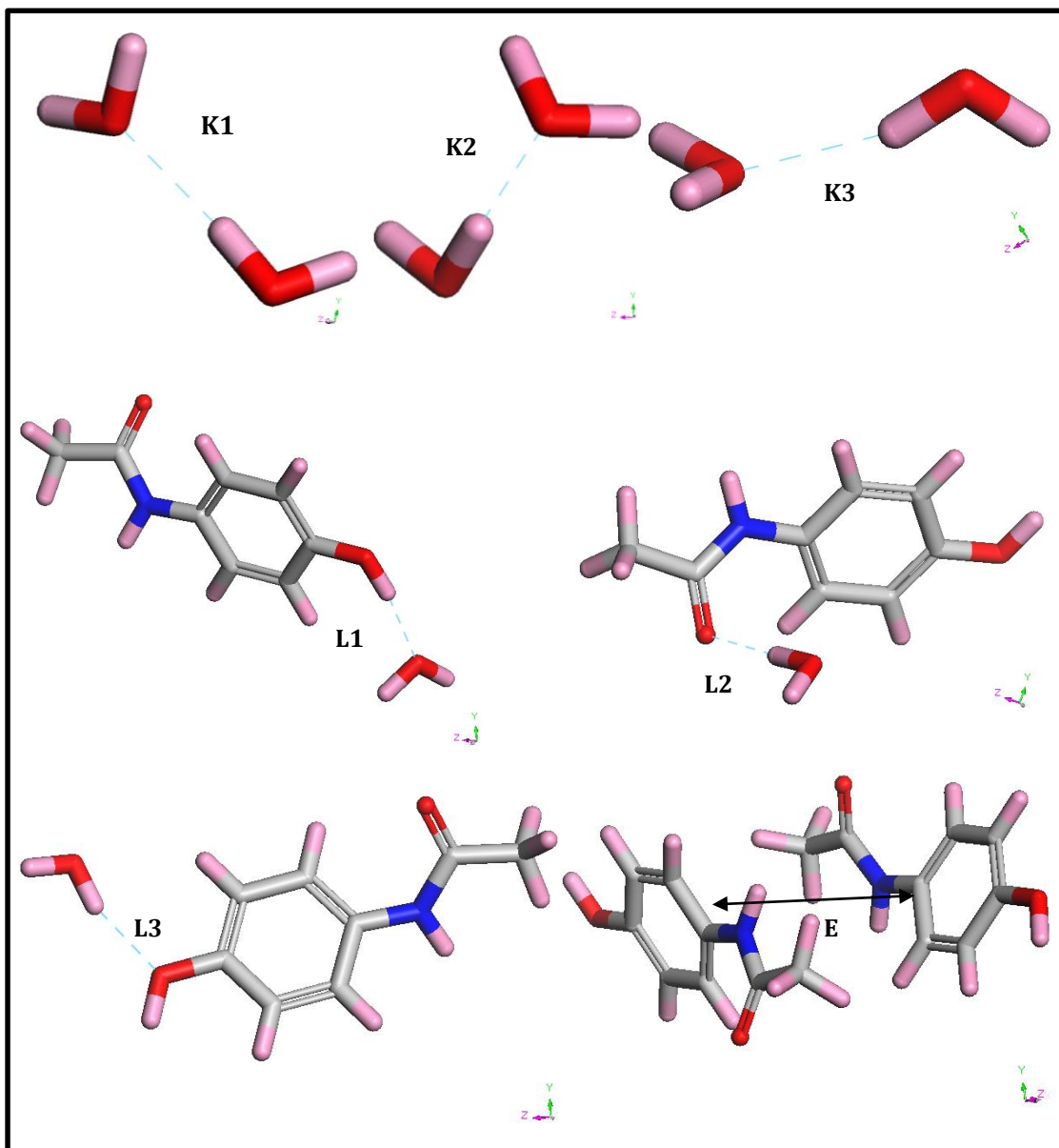
Figure 6-18 Top seven intermolecular interactions for PTRI. Clearly the hydrogen bond was dominating PTRI. Three types were seen that are $H_2O - H_2O$ (hydrogen bond), F1-F1($\pi - \pi$ bond) and F1-H_2O (hydrogen bond)

The PTRI was governed by the hydrogen bonds, therefore, making it highly directional. From the analysis, it was suspected that high energy would be needed for displacement to take place in PTRI.

6.8 Molecular crystallographic computation for paracetamol hydrochloride monohydrate

The paracetamol hydrochloride monohydrate (PHM) system was reported to have 2MPa yield strength, that is double the FI [13,18] resulting to better tabletability. This section attempted to predict the behaviour of the PHM through molecular and crystallographic modelling. This section results hope to add the knowledge of the paracetamol salts which was scarce with only six structures identified at the moment in the CCDC database [14,19].

6.8.1 Qualitative crystallographic structure analysis for paracetamol hydrochloride monohydrate

An asymmetric unit of PHM consists of a molecule of water, a chlorine atom and a molecule of paracetamol. In an asymmetric unit, the hydrogen of water and chlorine atoms were partially polar. The hydrogen positive charge (H^{δ^+}) and the chlorine negative charge (Cl^{δ^-}) will create dipole-dipole interactions. The dipole-dipole interactions tend to pull the atom involves aligned in order to have stronger bonds. The consequence of the dipole-dipole interactions was evident in Figure 6-19. The Cl^{δ^-} was seen to be positioned perpendicular to the H^{δ^+}. Besides the dipole-dipole, the oxygen of paracetamol interacts with another hydrogen atom of water forming hydrogen bond. The consequence of the rearrangement caused by the dipole-dipole interactions and hydrogen directionality onto the molecular packing of PHM was observed from the layered position of molecules in the crystal packing. The stack position promotes the $\pi - \pi$ interactions which expected to provide the structure stability. Looking into the crystal packing of PHM through [100], [010] and [001] directions, there were five potential slip planes that were (100), (010), (011), (001) and (101).

6.8.2 Lattice and morphology prediction paracetamol hydrochloride monohydrate

Lattice energy of PHM crystal was calculated to be -225.64kJ/mol. The lattice energy starts to converge at 20Å as seen in Figure 6-19 with values of -235.48kJ/mol. There was a huge drop of lattice energy from 89.16 at 10Å to -235.48kJ/mol at 20Å. This was related to the coulombic contributions that were 2.47kJ/mol at 10 Å then decreased to -136.86kJ/mol at 20Å. From Table 6-26 the repulsive and coulombic were seem to be of similar magnitude. The optimised unit cell parameters had 0.02% difference compared to the experimental structure given in Figure 6-19.

Table 6-26 Contributions of attractive (Att), repulsive (Rep) and electrostatic (Coul) towards the lattice energy of PHM given in kJ/mol

Range (Å)	Att	Rep	Coul	Total Energy (kJ/mol)
10	-56.09	74.93	2.47	89.16
20	-74.56	155.14	-136.86	-235.48
30	-74.72	155.14	-134.14	-224.76
40	-74.76	155.14	-134.04	-224.51
50	-74.76	155.14	-133.11	-220.62

Predicted morphology using the attachment energy approach was illustrated in Figure 6-19 giving thin needle shape crystal with a slight difference from the experimentally grown crystal that has flat ends [14,19]. There was four morphological importance faces namely (020), (100), (110) and (11-1) predicted. From the attachment energy (Table 6-27), the slowest growing face was (11-1) with -14.69kJ/mol. The fastest growing face was (020) with attachment energy of -151.84kJ/mol. The ratio between the slowest and fastest growing face was approximately $\approx$ 10 which resulted in the disappearance of the (020) and dominated by (11-1).

Table 6-27 Morphological importance faces breakdown showing the slice and attachment energy for each. It was obvious that two out of the four faces were very satisfied with values between 75 and 94%. Slice energy was contributing most towards the lattice energy

|		PHM		
Face (hkl)	d_{hkl} (Å)	Slice energy (kJ/mol)	Attachment energy (kJ/mol)	% Saturation of surface molecule (anisotropy factor)
(020)	10.98	-73.76	-151.84	33
(100)	6.25	-110.37	-115.27	49
(110)	6.01	-167.53	-58.12	75
(11-1)	4.58	-210.96	-14.69	94
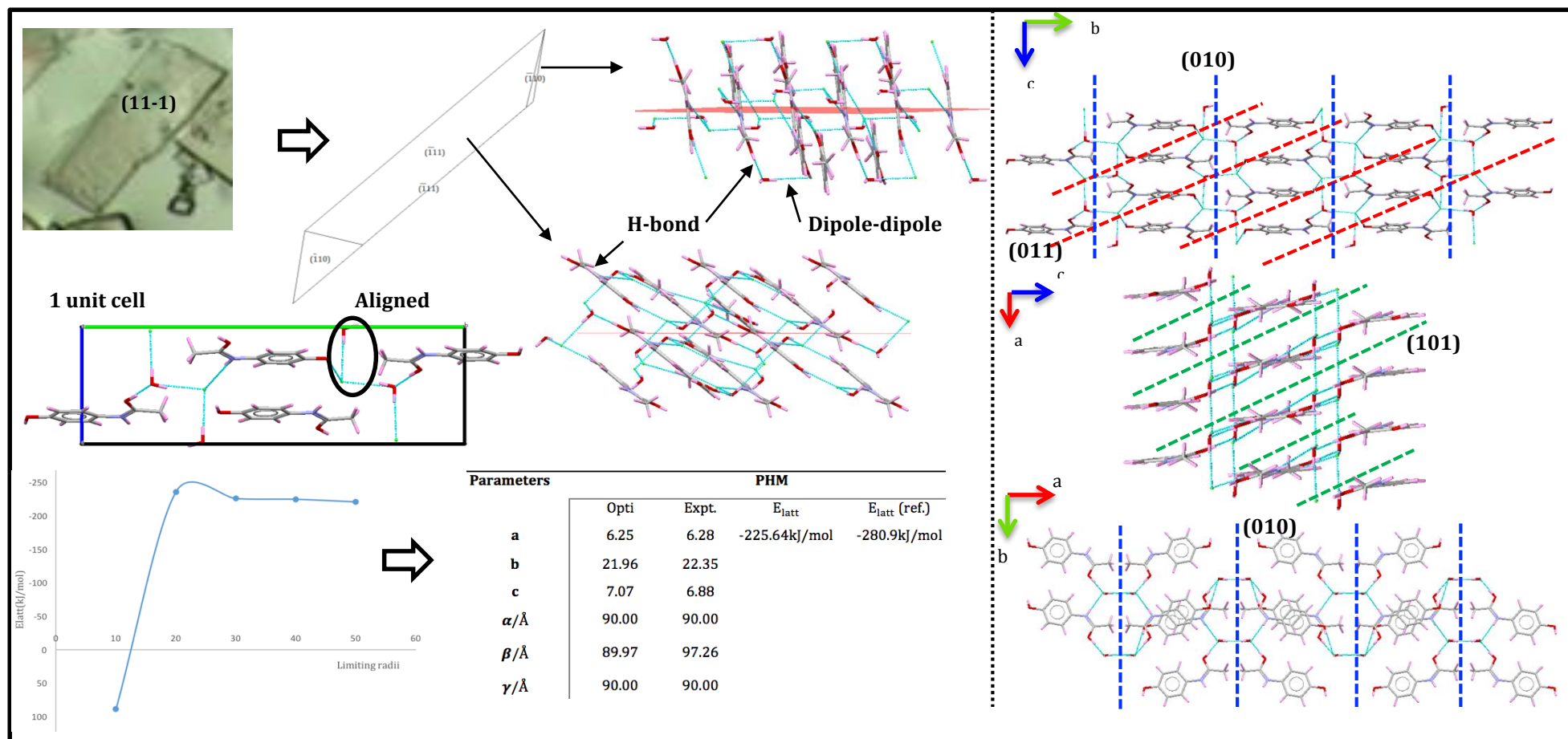
Figure 6-19 PHM predicted morphology using attachment energy model in comparison to the experimental grown crystal showed similarity. The morphology was drawn based on the centre to face distance. The bottom left was the lattice energy convergence plots together with the optimised unit cell parameters. The potential slip showed as broken lines through the 2 × 2 × 2 crystal packing viewed from [100], [010], and [001]. Top four were cleaved faces that represent the general surface chemistry of the morphological importance faces namely (-110), (-111), (020) and (100). Colour code: Pink: hydrogen Grey: Carbon Red: Oxygen Green: Chlorine Blue: Nitrogen

The least satisfied face was (020) with anisotropy factor of 33% followed by (100) with 49%. Another two faces that were (110) and (11-1) showed more satisfaction with 75% and 94% accordingly, therefore become the dominant faces. Cleaved faces of (110) and (11-1) depicted the exposed chlorine atom and hydroxyl group ready to bond with incoming new layers.

6.8.3 Paracetamol hydrochloride monohydrate interatomic and intermolecular contacts elucidation

The demarcation of the interatomic and intermolecular interactions that lead to the different slice and attachment for PHM will be presented in this subsection. The interatomic interactions showed that the highest type contributing towards the lattice energy was oxygen with -108.32kJ/mol as presented in Table 6-28. Domination of the hydrogen atom was related to the dipole-dipole interactions of Cl^{δ^-} to H^{δ^+}. Other types of atom the were contributing between -121.51 to 31.29%.

The distribution of specific atom contributions towards the lattice energy was presented in Figure 6-20. The distributions can be divided into six main functional groups which are, hydroxyl, amide, methyl, a phenyl ring, aliphatic carbon and chlorine. From the analysis, the hydroxyl group contributes the most with -123.85kJ/mol given in Table 6-29. The large energy amount described the energy compensation needed if the hydroxyl group were removed to create a new compound.

Table 6-28 Atom type contribution towards the total lattice energy of PHM with the highest contributor was oxygen with -108.32kJ/mol

Atom type	Attractive (kJ/mol)	Repulsive (kJ/mol)	Coulombic (kJ/mol)	Total (kJ/mol)
Hydrogen (H-bond)	-29.46	26.07	-42.05	-45.44
Hydrogen	-44.60	114.98	162.09	232.46
Carbon	-75.73	35.69	67.95	27.91
Nitrogen	-24.56	15.98	-8.54	-17.11
Oxygen	-37.87	28.66	-99.12	-108.32
Chlorine	-22.51	92.17	-69.96	-0.29
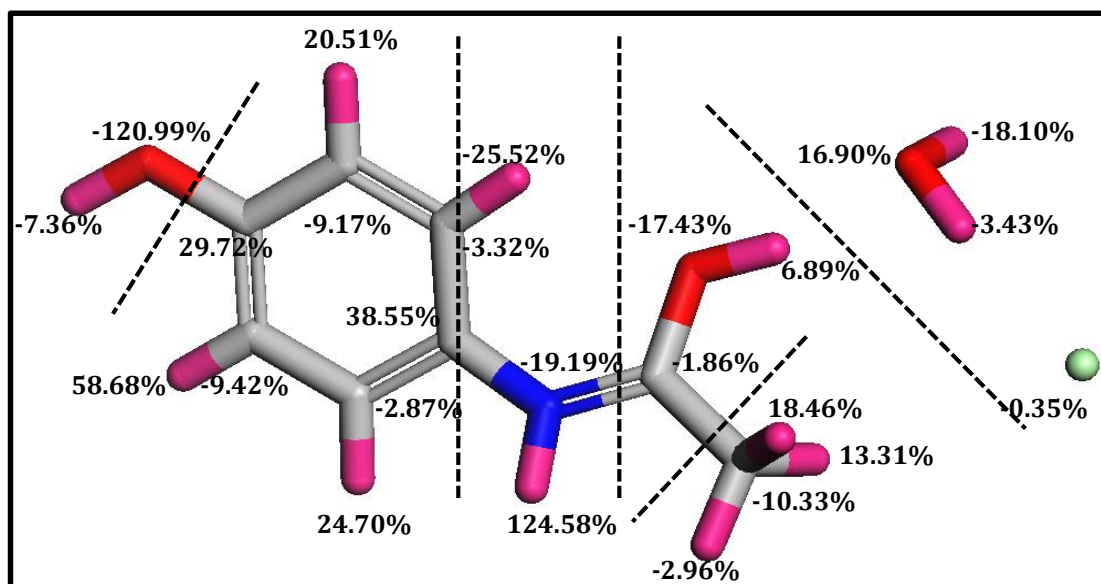
Figure 6-20 Specific atoms contribution towards the stability of PHM molecular structure. It was dominated by the hydrogen atom. Colour code: Pink: hydrogen Grey: Carbon Red: Oxygen Green: Chlorine Blue: Nitrogen

Table 6-29 Contributions of main functional groups in PHM molecule. The molecule was divided into five components shown by the broken lines

Main functional group	Attractive (kJ/mol)	Repulsive (kJ/mol)	Coulombic (kJ/mol)	Total (kJ/mol)	%
Phenyl	-71.67	41.00	139.24	108.57	-119.70
Hydroxyl	-33.18	18.41	-110.75	-125.52	138.38
Amide	-31.67	21.46	104.14	93.93	-103.55
Methyl	-40.08	74.73	-18.20	16.44	18.13
Chlorine	-22.51	92.17	-69.96	-0.29	4.51

Table 6-30 The dominating intermolecular bond in PHM. All five strong bonds were hydrogen bonds. The strongest was $C - O \cdots H - Cl^{-1}$ with distance of 7.12Å with strength of -102.51kJ/mol

Bond	Multiplicity	Distance (Å)	Intermolecular energy (kJ/mol)	Dominating intermolecular interaction type
M1	8	7.12	-102.51	Hydrogen bond
N1	8	8.26	-96.44	Hydrogen bond
M2	8	8.96	-93.18	Hydrogen bond
M3	8	6.03	-88.83	Hydrogen bond
O1	8	8.19	-82.51	Hydrogen bond

The intermolecular interactions were given in Table 6-30 presented the top five strong bonds created within the PHM. The strongest intermolecular interaction was the hydrogen bond of $C - O \cdots H - Cl^{-1}$ with -102.51kJ/mol at distance of 7.12Å. The other strong bonds were of the same type, with strength from -96.44 to -82.51kJ/mol. Figure 6-21 represents the five types of hydrogen bond within the PHM. The N1 was $C \cdots H - Cl^{-1}$ while O1 was $N \cdots H - Cl^{-1}$. Here, it was perceived that, the hydrogen bond was dominating the PHM as the dipole-dipole bonds were fairly weak when compared to the strength of the hydrogen bond.
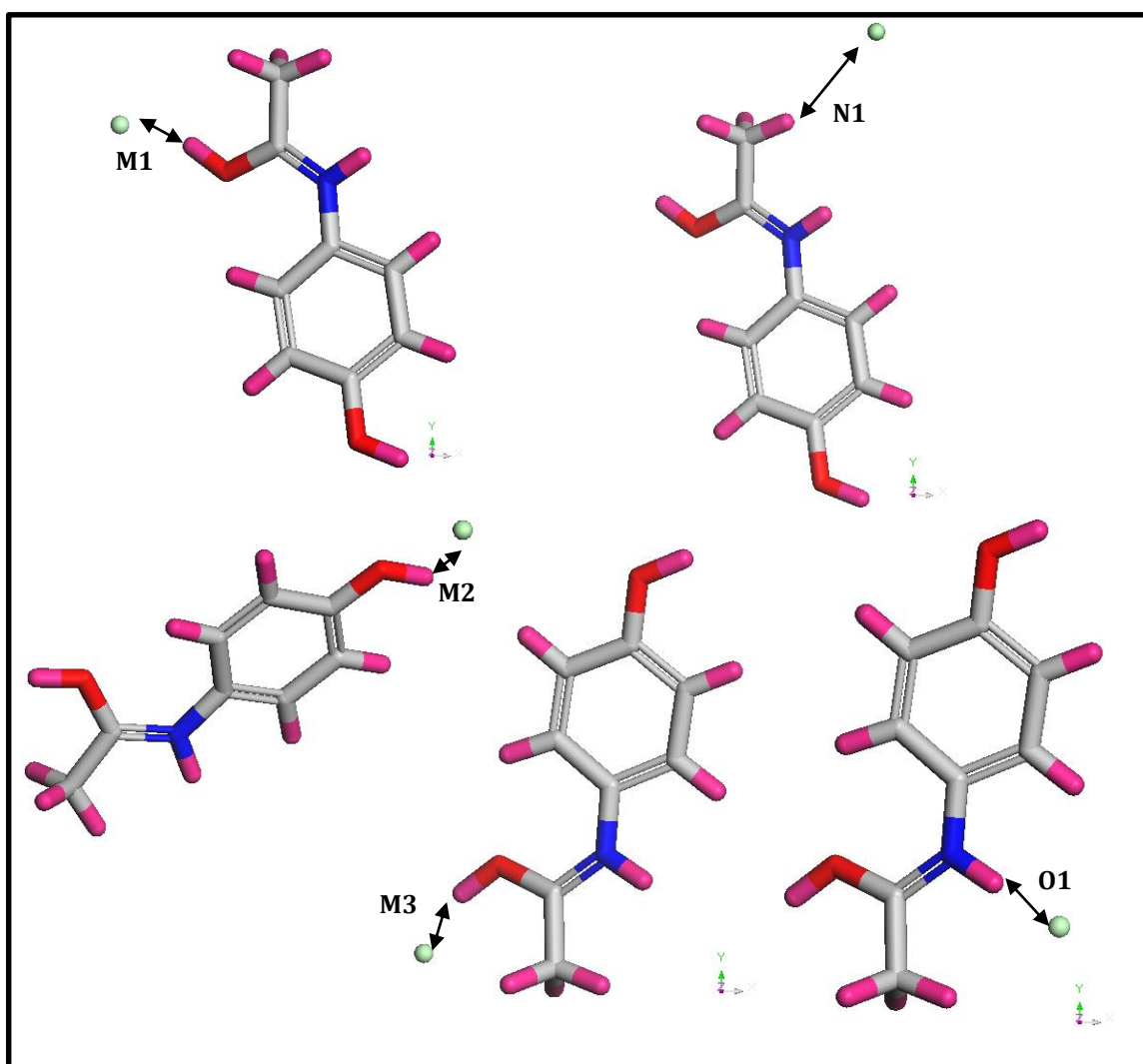
Figure 6-21 Five strong intermolecular interactions for PHM. The strongest was given by hydrogen bond (H) created between ($C - O \cdots H - Cl^{-1}$) with -102.51kJ/mol. The bond was separated by 7.12Å. All other bonds were of same type at different distance, strength and between ($N \cdots H - Cl^{-1}$) also ($C \cdots H - Cl^{-1}$)

6.9 Conclusions

Arriving from the lattice energetics and intermolecular interactions analysis, the diverse paracetamol systems were seen to be related directly to the type of intermolecular interactions. From Table 6-31 it can be seen that the lattice energy was increasing (-81.22 to -225.64kJ/mol) depending on the type of intermolecular interactions involve within the crystal system also the size of the solid forms. Moreover, the crystal packing of all systems was observed to follow the direction of the intermolecular interaction. The intermolecular interactions too were proposed to contribute to the elasticity with increasing stiffness following the direction of the interactions created. The aromatic groups were observed to have significant contributions toward four of the paracetamol solid forms except for paracetamol hydrochloride monohydrate (PHM). The intermolecular and interatomic interactions assist in understanding the molecular crystal mechanical behaviour. The next chapter will present the predicted deformation behaviour of the five solid forms of paracetamol.

Table 6-31 Summary for the prediction of mechanical properties of the five solid forms of paracetamol. For elastic tensor, the lowest of axial and diagonal components were given. Similarly, the dislocation energy, only the smallest was provided. The predicted mechanical behaviour showed probable fracture, plastic or cleaving

Solid forms	E_{latt} (kJ/mol)	Elastic components (GPa)	Dominant functional group	Strongest intermolecular bond direction
FI	-81.22	Axial: 7.9 Diagonal: 4.2	Phenyl	[100]
FII	-80.10	Axial: 10.42 Diagonal: 1.59	Phenyl	[010]
PTHEO	-145.04	Axial: 7.27 Diagonal: -1.58	Phenyl	[010]
PTRI	-198.87	Axial: 8.27 Diagonal: 0.35	Hydroxyl	[010]
PHM	-225.64	Axial: 17.15 Diagonal: 1.64	Hydroxyl	[010]

References

[1] M. Haisa, S. Kashino, H. Maeda, The orthorhombic form of p-hydroxyacetanilide, Acta Crystallographica Section B: Structural Crystallography and Crystal Chemistry. 30 (1974) 2510–2512.

[2] E. Boldyreva, High-pressure polymorphs of molecular solids: when are they formed, and when are they not? Some examples of the role of kinetic control, Crystal Growth & Design. 7 (2007) 1662–1668.

[3] S.L. Mayo, B.D. Olafson, W.A. Goddard, DREIDING: a generic force field for molecular simulations, The Journal of Physical Chemistry. 94 (1990) 8897–8909. doi:10.1021/j100389a010.

[4] T. Beyer, G.M. Day, S.L. Price, The prediction, morphology, and mechanical properties of the polymorphs of paracetamol, Journal of the American Chemical Society. 123 (2001) 5086–5094.

[5]   R.J.Rowe and R.C.Rowe, Brittle/ductile behaviour in pharmaceutical materials used in tabletting, International Journal of Pharmaceutics. 36 (1987) 205-209

[6] G.M. Day, S.L. Price, M. Leslie, Elastic constant calculations for molecular organic crystals, Crystal Growth & Design. 1 (2001) 13–27.

[7] Y.V. Nelyubina, I.V. Glukhov, M.Y. Antipin, K.A. Lyssenko, "Higher density does not mean higher stability" mystery of paracetamol finally unraveled, Chemical Communications. 46 (2010) 3469–3471.

[8] H.A. Garekani, J.L. Ford, M.H. Rubinstein, A.R. Rajabi-Siahboomi, Highly compressible paracetamol: I: crystallization and characterization, International Journal of Pharmaceutics. 208 (2000) 87–99.

[9] G. Perlovich, T.V. Volkova, A. Bauer-Brandl, Polymorphism of paracetamol, Journal of Thermal Analysis and Calorimetry. 89 (2007) 767–774.

[10] I. Rosbottom, K. Roberts, R. Docherty, The solid state, surface and morphological properties of p-aminobenzoic acid in terms of the strength and directionality of its intermolecular synthons, CrystEngComm. 17 (2015) 5768–5788.

[11] G. Nichols, C.S. Frampton, Physicochemical characterization of the orthorhombic polymorph of paracetamol crystallized from solution, Journal of Pharmaceutical Sciences. 87 (1998) 684–693.

[12] J.Y.Y. Heng, A. Bismarck, D.R. Williams, Anisotropic surface chemistry of crystalline pharmaceutical solids, AAPS PharmSciTech. 7 (2006) 12–20.

[13] S.R. Perumalla, L. Shi, C.C. Sun, Ionized form of acetaminophen with improved compaction properties, CrystEngComm. 14 (2012) 2389–2390.

[14] J.Krzysztof Paluch, .Lidia Tajber, I Owen Corrigan and A.Marie Healy, Impact of alternative solid state forms and specific surface area of high-dose. hydrophilic active pharmaceutical ingredients on tabletability, Molecular Pharmaceutics. 10 (2013),

Chapter Seven

Prediction of the Mechanical Properties for Five Diverse Solid Forms of Paracetamol

The influence of the five selected solid forms of paracetamol onto mechanical properties was explored. The diverse solid form case studies will indicate the sustainability of the mechanical properties prediction model developed in this study

Chapter 7. Prediction of the Mechanical Properties for Five Diverse Solid Forms of Paracetamol

7.1 Introduction

The large variations of APIs mechanical behaviour from brittle to plastic compounds motivate the increase of prediction models using molecular modelling to understand the deformation from the solid forms viewpoint [1]. Paracetamol is an API that has been routinely used to study solid forms suitable for direct compression [2]. A number of paracetamol co-crystals, solvates also polymorphs renders as the best system to show the variation in deformation behaviour and testing a newly developed prediction model.

This chapter extends the applications of the prediction model by applying it to the five selected solid forms of paracetamol. The physical properties of the selected paracetamol systems have been described in an earlier chapter, section 3.5. The predicted mechanical deformation of each paracetamol system was presented here. The goal of this chapter is to demonstrate the adaptability of the developed mechanical properties prediction model taking on polymorphs, co-crystals, hydrates and salts. Figure 7-1 illustrates the content of this chapter. This chapter starts with slip plane characterisation followed by burgers vector identification and mechanical prediction summary for each of the solid forms.
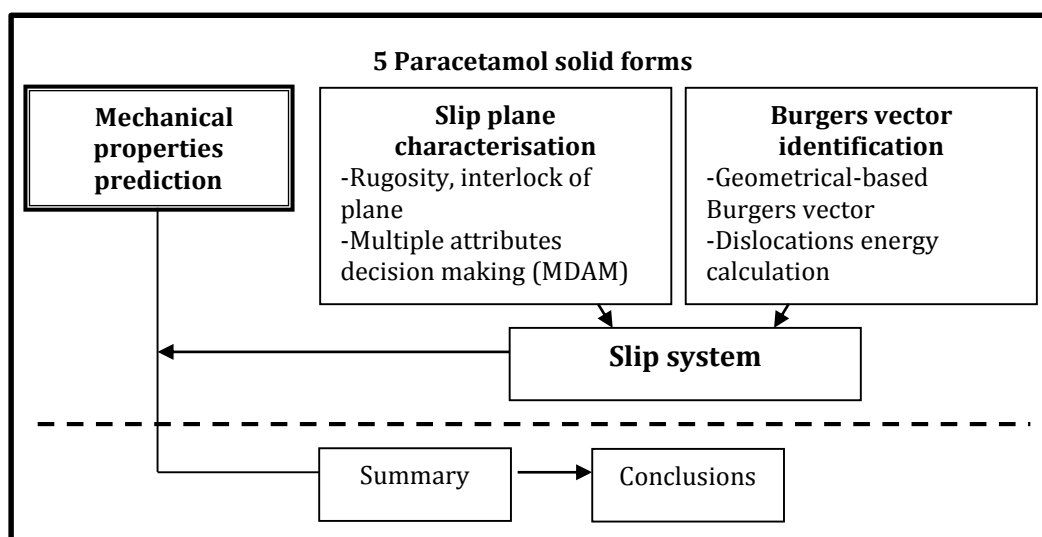
Figure 7-1 Summary of content for this chapter

7.2 Prediction of the mechanical properties for paracetamol Form I

The shearing behaviour is associated with the slip behaviour of compounds. This section will describe the stiff behaviour of paracetamol form I (FI) through its relation with slip systems. This section will provide an overview from the qualitative identification of slip plane up to a contribution of dislocations energy to promote slip movements.

7.2.1 Form I slip plane characterisations

In an earlier section, the qualitative analysis had identified only one candidate slip plane for FI that was (011). Now, quantitative analysis was carried out to second the candidate slip plane perceived qualitatively. The calculated surface characteristics of the plane were presented in Table 7-1. The lowest rugosity was 2.97, and highest was 6.39 corresponding to (110) and (001) planes. While for the surface energy, the lowest was 25.00mJ/m² for (111). The rugosity list for FI with increasing values was (110) < (011) < (101) < (111) < (100) < (002) < (010) < (001). The calculated surface energy approximately agrees with values measured through contact angle by Heng et.al (2006) [12] for face (011) with 33.9mJ/m².

There was no direct correlation observed between the surface energy, rugosity, and energy needed to break the hydrogen bond. The directionality of hydrogen bond was known to dictate mechanical properties of the crystal [13-14]. The (010) plane needs the least work for breaking hydrogen bond. Although the rugosity and surface energy has no obvious relation, both characteristics were crucial to have a surface that is smooth providing platform for a slip to take place. Another key characteristic for slip plane is interlock of planes.

Table 7-1 Slip plane rugosity, surface energy and hydrogen bond breaking analysis were presented. The lowest rugosity was 2.97 for (110) follows by 3.12 for (011). As seen in the table, all three attributes were not directly related in regards to slip plane characteristics

	FI		
Plane	Rugosity	Surface energy (mJ/m²)	% H-bond breaking
(100)	3.81	40.00	2.08
(010)	5.04	55.00	0.74
(001)	6.39	65.00	1.42
(110)	2.97	30.00	1.06
(101)	3.23	30.00	1.31
(011)	3.12	40.00	0.86
(111)	3.32	25.00	1.29
(002)	3.88	70.00	1.16

7.2.1.1 Interlocking representations

The graphical representation for interlock of slip plane was illustrated in Figure 7-2. It can be seen that from eight candidates slip planes only two obvious planes that were not interlocking which were (001) and (002). Surprisingly, this result did not echo the qualitative observation that only has one slip plane that was (011). The interlocking test was showing that the (011) was slightly interlocked. For (101), two molecules were slightly intercepting each other. The graphical misrepresentation was related to orientation for distant calculation that was affected by the complicated crystallographic structure. Taking together the slip plane analysis results of the rugosity, surface energy, hydrogen bond breaking and interlocking, there was a need for statistical measures to treat the outcomes so that it will be in the same dimension. The next subsection present result from the multidimensional attributes decision-making analysis to refine the list of candidates of slip plane.

7.2.1.2 Multiple attribute decision-making calculations (MADM)

The calculated values for describing slip plane were transferred into a decision matrix and normalised to transform values into the same dimension, in the range between 0-1.0 as shown in Table 7-2.

Table 7-2 Normalised values of calculated analysis for slip plane characterisation attributes. The dimension for the attributes was now is below 1.0

Attributes/ Alternatives	FI			
	Surface E	Rugosity	Interlock of slip planes	H-bond breaking
(100)	0.30	0.33	0.38	0.57
(010)	0.41	0.43	0.38	0.20
(001)	0.49	0.55	0.38	0.39
(110)	0.23	0.25	0.38	0.29
(101)	0.23	0.28	0.38	0.36
(011)	0.30	0.27	0.38	0.23
(111)	0.19	0.28	0.38	0.35
(002)	0.53	0.33	0.38	0.32

The interlocking reflections were represented as binary numbers, 1 for interlock and 0 for non-interlock. By doing so, the qualitative observation was transformed to quantitative analysis. The slip plane characteristics were now in the dimension of 1.0. It can be seen clearly after normalisation; each slip plane candidate will have one characteristic that was significance relative to the other.
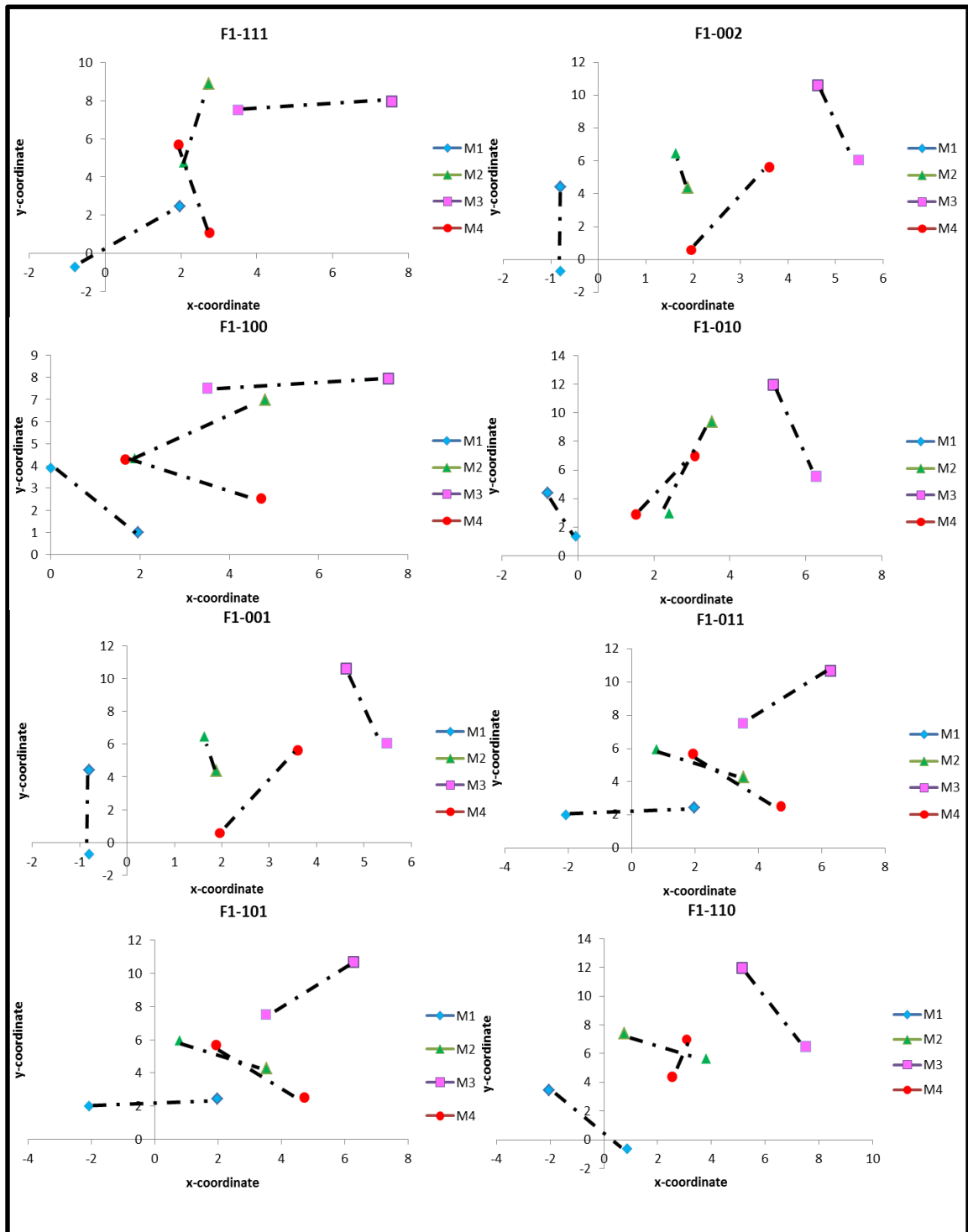
Figure 7-2 Projection of molecules in a unit cell onto respective candidates of slip plane. Each connected lines were representing distance between the maximum and minimum atom in every molecule considered. Two points plotted for each are the x and y coordinates for respective atoms that have the maximum and minimum distance. A candidate slip plane is interlocking when the projected lines are crossing each other. It can be seen that (001) and (002) were not interlocked

Table 7-3 The weighted-normalised values for attributes corresponding to different set of alternatives (slip planes)

	FI			
Attributes/ Alternatives	Surface E	Rugosity	Interlock of slip planes	H-bond breaking
(100)	0.08	0.08	0.09	0.14
(010)	0.10	0.11	0.09	0.05
(001)	0.12	0.14	0.09	0.10
(110)	0.06	0.06	0.09	0.07
(101)	0.06	0.07	0.00	0.09
(011)	0.08	0.07	0.09	0.06
(111)	0.05	0.07	0.09	0.10
(200)	0.13	0.08	0.00	0.10

From Table 7-3, if rugosity is the main attributes needed by the slip plane, the best slip plane will be (110). If surface energy is the important measure, plane (111) was the potential slip plane. Similarly, if the total of hydrogen bond breaking is the most important criteria, (010) was the slip plane. There was no obvious slip plane candidate that was better than the other. From this observation, it was obvious that all attributes did not have any direct relation. The normalised calculated values were tabulated to give an ideal and negative best values of each slip planes candidate.

Table 7-4 Positive and negative separation values of attributes with regards to achieving the optimum condition for slip plane. These separation analyses were carried out with respect to slip plane candidates

FI (positive separation)					
Attributes/ Alternatives	Surface E	Rugosity	Interlock of planes	H-bond breaking	Squared of sum	Positive separation
(100)	6.25E-04	4.73E-04	8.90E-03	8.41E-03	1.84E-02	1.36E-01
(010)	2.82E-03	2.32E-03	8.90E-03	1.67E-07	1.40E-02	1.18E-01
(001)	5.17E-03	5.95E-03	8.90E-03	2.18E-03	2.22E-02	1.49E-01
(110)	3.91E-05	1.39E-05	8.90E-03	4.93E-04	9.45E-03	9.72E-02
(101)	3.91E-05	8.67E-05	0.00E+00	1.54E-03	1.67E-03	4.08E-02
(011)	6.25E-04	4.83E-05	8.90E-03	7.37E-05	9.65E-03	9.82E-02
(111)	9.75E-06	1.26E-04	8.90E-03	1.43E-03	1.05E-02	1.02E-01
(002)	6.60E-03	5.41E-04	8.90E-03	8.42E-04	1.69E-02	1.30E-01
FI (negative separation)					
Attributes/ Alternatives	Surface energy	Rugosity	Interlock of planes	H-bond breaking	Squared of sum	Positive separation
(100)	3.02E-03	3.39E-03	1.88E-05	2.85E-06	6.44E-03	8.02E-02
(010)	7.22E-04	1.01E-03	1.88E-05	8.03E-03	9.78E-03	9.89E-02
(001)	6.59E-05	8.27E-06	1.88E-05	1.87E-03	1.97E-03	4.43E-02
(110)	5.44E-03	5.82E-03	1.88E-05	4.60E-03	1.59E-02	1.26E-01
(101)	5.44E-03	5.00E-03	8.10E-03	2.58E-03	2.11E-02	1.45E-01
(011)	3.02E-03	5.34E-03	1.88E-05	6.63E-03	1.50E-02	1.23E-01
(111)	6.91E-03	4.73E-03	1.88E-05	2.72E-03	1.44E-02	1.20E-01

The best scenario for surface energy, rugosity, and hydrogen bond breaking was when the values at a minimum while for interlocking when at 0.00. Table 7-4 represents the positive and negative separation values. These separations served as the Euclidean distances from the ideal conditions of a slip plane.

The final rank of slip plane candidate based on the MDAM analysis was given in Table 7-5. The least deviation from optimum was 42% for plane (110). The (110) was a plane that was 58% behaving as preferred slip plane. Also, can be seen that the (011) was exhibiting 57% behaviour of the slip plane, which was 1% less than (110). The least to be a slip plane was (001) with 77% deviation from the ideal attributes of preferred slip plane. Thus, the analysis can be said successfully to identify the potential slip plane observed qualitatively with only 1% difference in comparison to the ideal plane. However, from the percentages, it can be seen that the planes in FI were only having around 50% attributes of an ideal slip plane that was a bit low. Though FI may not be deforming plastically, this plane analysis can be utilised to understand the exposed face when fractured.

Up to now, the rigidity of FI has been described through elasticity, crystal chemistry and the attributes of slip planes, next the influence of dislocation energy towards preferred Burgers vector, was discussed.

Table 7-5 Rank of slip plane according to multiple attributes decision-making analysis. The probable slip planes are (110) with deviation from the ideal condition by 42% and (011) with 43%. The least to slip was (001) with 77% deviation.

	FI	
Rank	*Alternatives*	*% Optimum*
1	(110)	58
2	(011)	57
3	(111)	55
4	(101)	54
5	(002)	48
6	(010)	46
7	(100)	38
8	(001)	23

7.2.2   Paracetamol Form I Burgers vector calculations

The summary of calculated Burgers vector was shown in two subsections, first for the geometrical based and secondly when dislocations were introduced.

7.2.2.1 Geometrical-based Burgers vector

Initially, Burgers vector was calculated based on crystal geometry and results were given in Table 7-6. The most striking result was that the top three magnitudes were given by the crystal unit cell parameters. FI is a primitive crystal system, therefore, the preferred Burgers vector was the shortest unit cell parameters that were [100] with 7.09x10Å. The calculation generated all probable list of Burgers vector for the primitive crystal system. Firstly, in narrowing the list of Burgers vector generated, the farthest distance taken was double the values of the largest unit cell parameters. In the case of FI, the largest unit cell parameter was in the direction of [001] that is 11.59Å. There was 20 Burgers vector fell under this group. Secondly, this study did not consider any partial Miller indices. Following this second pass, there was only seven Burgers vector available for consideration and these were presented in Table 7-6. The same Burgers vector screening approach will be used for analysing the next four paracetamol systems. List of Burgers vector in decreasing magnitude was [100] < [010] < [001] < [110] < [101] < [011] < [111].

Potentially, displacement propagates in crystal with the help of defects, particularly dislocations. Considering the presence of dislocations, the list of Burgers vector was refined. The availability of dislocations energy was the ideal case during deformation of crystal. Dislocation in an anisotropic crystal was directly related to the elastic tensor.

7.2.2.2 Dislocation influence on Burgers vector

Dislocation energy was calculated using the Burgers vector presented in Table 7-6 with the elastic tensor of FI was taken from Table 6-5 in chapter 6. The anisotropy impact on the dislocation energy factor (K) was shown through polar plot of three dimensional (100), (010) and (001) planes with regards to Burgers vector. This continuum analysis was represented by Figure 7-3 with the K values were summarised in Table 7-6. From the polar plot, it was evident that the K values were varying with directionality (Figure 7-3). These variations relate to the elastic tensor anisotropy behaviour as mentioned in the earlier section. With this variations, the preferred Burgers vector will be dependent on the minimum K. Moreover, few of the Burgers vector namely, [100] and [010] were having a uniform distribution of the K values while the other were fluctuating. However, for each of the Burgers vector, there will be one minimum K value that was taken for calculating the dislocation energy.

Table 7-6 Range of dislocation energy factor (K) with varying Burgers vector (BV). The range of Burgers vector with the respective [100],[010] and [001] axial directions.

BV	Magnitude BV(Å)	Magnitude BV^2(Å)^2	K(GPa)			$K(BV)^2$ $(evnm^{-1})$
			[100]	[010]	[001]	
[100]	7.09	50.28	8.09	9.02	4.83	1.52-2.83
[010]	9.21	84.84	3.00	4.10	4.26	1.59-2.26
[001]	11.59	134.49	3.78	6.26	4.51	2.50-5.26
[011]	14.81	219.33	4.44	3.40	3.05	4.18-6.08
[101]	12.74	162.34	6.45	3.00	6.67	3.04-6.76
[110]	11.62	135.12	4.05	5.58	3.55	2.99-4.71
[111]	15.72	247.18	4.09	5.74	5.06	6.32-8.86

The dislocation energy computed was summarised together with the energy coefficient values were presented in Table 7-6. The range of K for all Burgers vector was in between 3.05 to 9.02GPa that is well below 10GPa. The resulting dislocation energies were seen fairly low with less than 5GPa for all Burgers vector. The Burgers vector preferability was depending on the distance. The influence of K was not obvious for FI as the rank of Burgers vector was the same as the initial geometrically calculated.

The calculated line dislocation energy was well below 10eVm-1. The K values were well related to the elastic tensor. Table 7-8 compares the Burgers vector values calculated by two different considerations, geometrical and dislocation energy. The refined list of Burgers vector was [100], [010], [001], [110], [101], [011], and [111]. [100] was calculated as the primary Burgers vector which agrees with the dislocation direction identified by Finnie et.al [20] for FI by using micro hardness indentation technique.
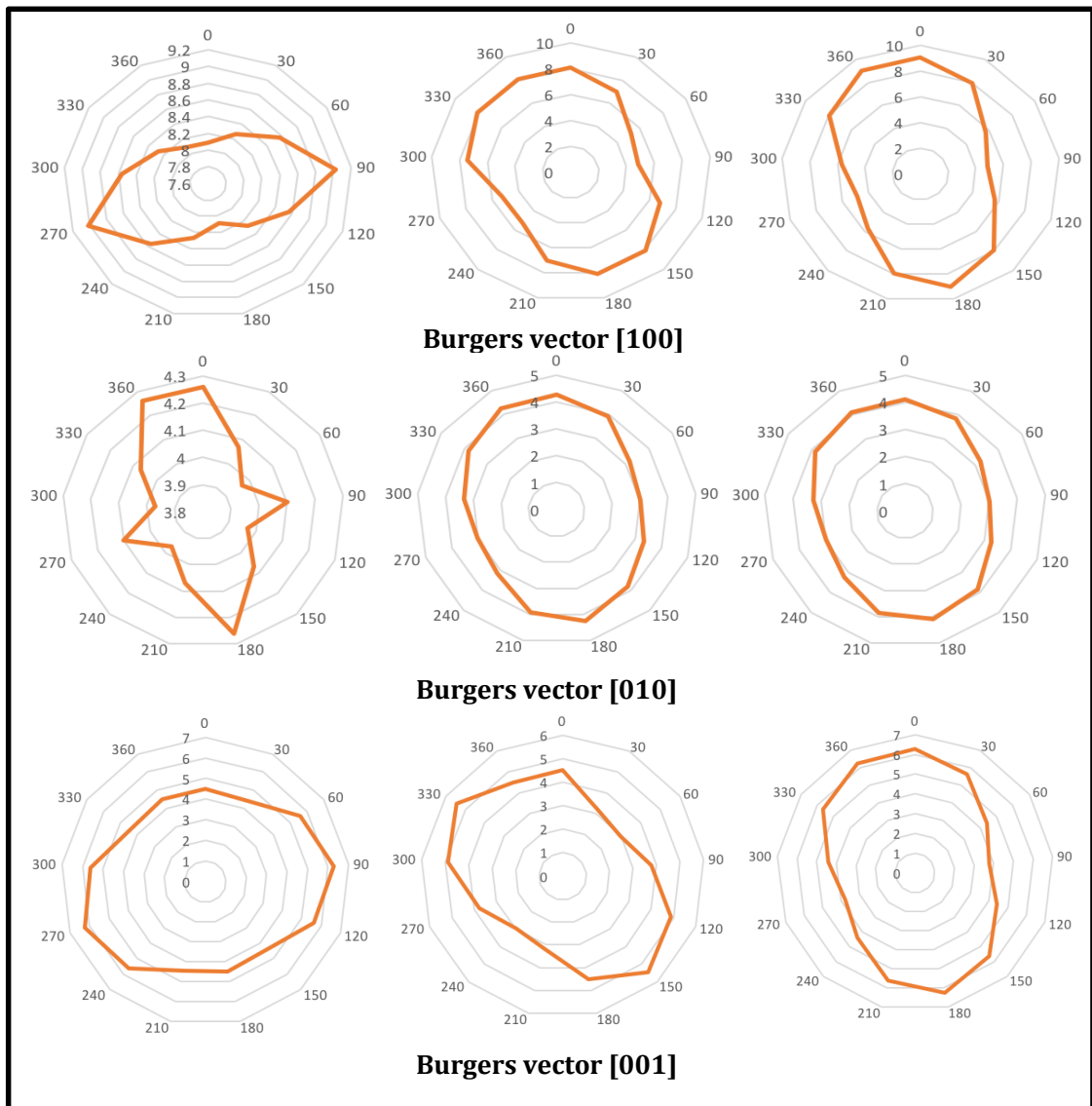
Figure 7-3 The dislocation energy factor continuum with regards to Burgers vector for planes (100), (010) and (001). For all the K values were varying with an angle up to 360°. The anisotropic behaviour was evident from the polar plot. For all of the Burgers vector, one minimum energy factor can be obtained. For [100] and [010] the distribution of K factor was uniform compared to other Burgers vector. The scanning angles for [100] $\emptyset = 90 \; \theta = 90$ [010] $\emptyset = 0 \; \theta = 90$ and [001] $\emptyset = 90 \; \theta = 0$

220

Burgers vector [110]

Burgers vector [111]

Burgers vector [101]

Burgers vector [011]
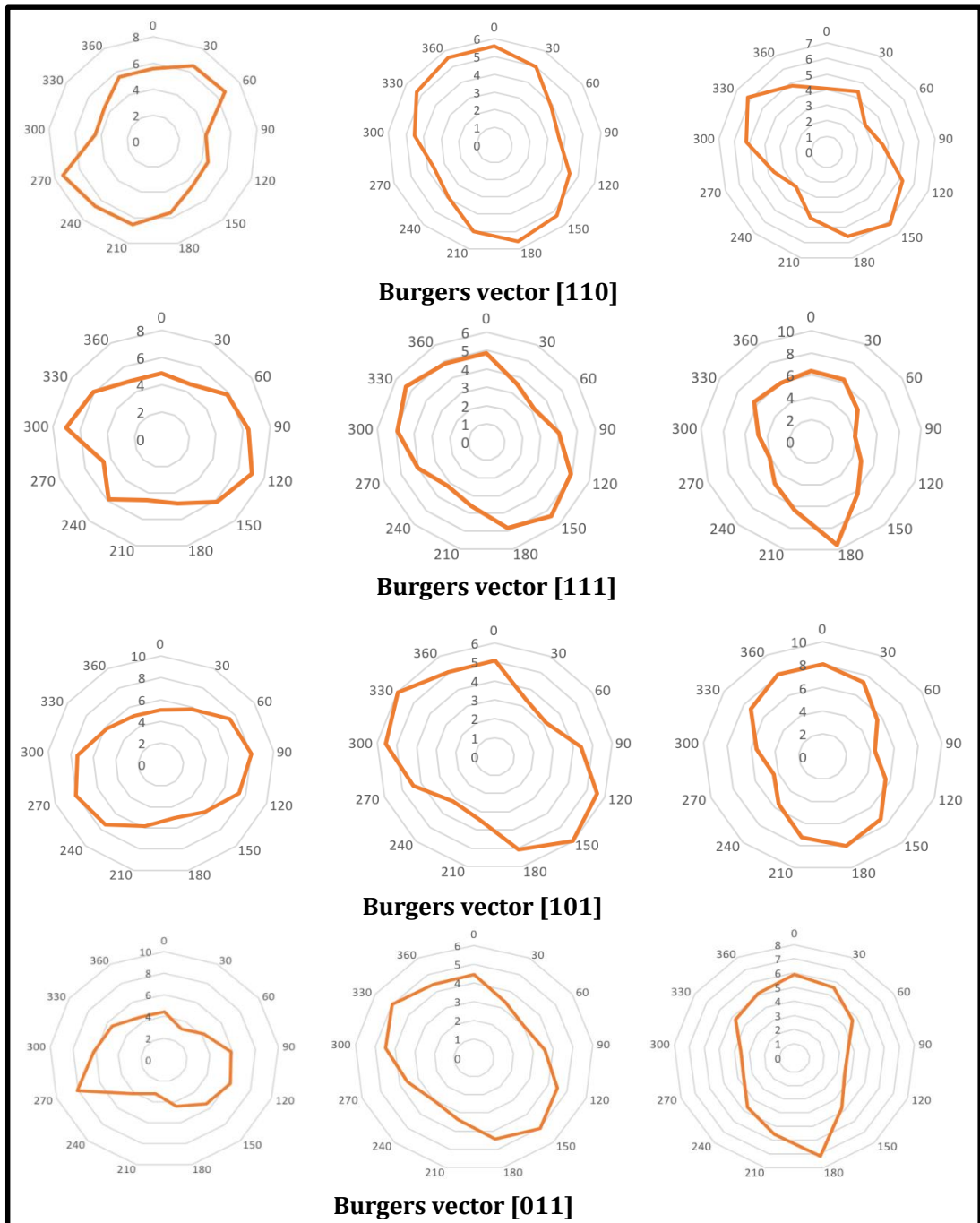
From the dislocations analysis, the identification of direction for potential edge and screw dislocations can be determine based on the line directions. List of probable line directions that are parallel and perpendicular to each Burgers vector was presented in Table 7-7- and were illustrated by stereographic projection in the appendix A2. From the list in Table 7-7, it can be seen that the Burgers vector parallel to unit cell axis were predicted to favour edge dislocations. In short, Table 7-7 provide a list of 23 potential dislocations for FI consisting

of edge and screw. The mixed dislocations were not included because of the complexity to characterise the right angle to differentiate the mixed from the pure edge and screw.

Table-7-7 Type of dislocation is showing the angle with respect to a particular Burgers vector. For each respective line directions, the scanning angle ∅ and angle θ at which the K value was identified were also given

		FI				
BV	LV	Angle ∅°	Angle θ°	K (GPa)	Kb^2(eVm^{-1})	Type
[100]	[100]	90	0	8.09	2.54	Screw
	[010]	0	90	9.02	2.83	Edge
	[102]	90	144	7.96	2.50	Edge
[010]	[010]	0	90	4.10	2.17	Screw
	[001]	0	0	4.26	2.25	Edge
	[100]	90	90	3.00	1.59	Edge
[001]	[001]	90	0	4.51	3.78	Screw
	[100]	90	90	3.78	3.17	Edge
	[010]	0	90	6.26	5.25	Edge
[110]	[110]	45	90	3.55	2.99	Screw
	[00-1]	90	180	3.55	4.70	Edge
	[-210]	45	0	5.58	4.70	Edge
	[100]	90	0	4.05	4.70	Edge
[101]	[101]	90	45	3.00	3.04	Screw
	[100]	45	90	6.45	6.53	Edge
	[010]	90	45	3.00	3.04	Edge
[011]	[011]	0	45	3.40	4.65	Screw
	[02-1]	0	90	5.87	8.03	Edge
	[-100]	90	180	4.44	6.08	Edge
[111]	[111]	45	45	4.09	6.31	Screw
	[010]	45	90	5.74	8.44	Edge
	[110]	45	0	4.83	7.45	Edge
	[012]	90	144	5.34	8.23	Edge

Table 7-8 Comparison of Burgers vector according to two approaches, geometrical and by considering dislocation energy

Rank	*Burgers vector (Geometrical)*	*Burgers vector (Dislocation Energy)*
1	[100]	[100]
2	[010]	[010]
3	[001]	[001]
4	[110]	[110]
5	[101]	[101]
6	[011]	[011]
7	[111]	[111]

7.2.3 Predicted mechanical behaviour of paracetamol Form I

Taking together the result from the top four potential slip planes which were (110), (011), (111) and (101) and Burgers vector [100], only (011) was active with the primary Burgers vector. FI did not have active slip system with planes (110), (111) and (101) because the Burgers vector did not lie within the plane based on the dot product (Weiss-zone law) calculations. Furthermore, though that (011) was active, the plane only met 57% characteristics of ideal slip plane. The negative finding correlates well to the rigid condition of FI as its' primary slip system was not active. Also, FI is not cleaving at a specific plane based on the test using strongest intermolecular interactions direction, which in this case was [100]. Therefore, FI was said to be stiff and tend to be brittle. Paracetamol FI was taken as the reference structure because it is the most stable form. The brittle behaviour of FI will be further justified through compaction measurements in the following chapter.

In short, the rigidity of FI was evidence based on the elastic tensor and corrugated crystal packing. Because of FI corrugated packing arrangements, there was less number of potential slip plane hence slip systems. Besides that, for FI the significance of dislocations energy was not obvious for classifying the preferred Burgers vector. This may be due to the fact that the magnitude of each potential Burgers vector also the K values was marginal difference. For this instance, the proposed model successfully predicts the slip behaviour of FI. In the successive section, the FII mechanical behaviour will be evaluated in a similar manner as FI.

7.3 Prediction of the mechanical properties for paracetamol Form II

This section contains the mechanical properties prediction of second polymorphs of paracetamol, Form II (FII). FII was reported to show better tabletability compared to the stable form, FI [15]. Improved tabletability was regarded to be caused by flat layers of molecules in FII crystallographic packing. Therefore, it is the objective of this section to predict the characteristics that contribute to deformation of FII besides the flat positioned of the molecules in the crystallographic packing.

7.3.1 Paracetamol Form II slip plane characterisations

There were eight slip plane candidates characterised as presented in Table 7-9. The rugosity for each respective slip plane candidates was between 1.83 and 9.38. The rugosity was fairly low because the flat herringbone pattern of FII. The flat position decreases the distance deviation between the slip plane candidate and atoms in a unit cell. Plane (110) has the lowest rugosity follows by (200) plane. Plane (200) was qualitatively identified as the easiest plane to slip with a minimal obstacle.

The lowest surface energy calculated was for (200) with 42 mJ/m^2 follows by (111) plane with 45 mJ/m^2. The (200) plane has the highest attachment energy and follows by the (111) plane as given in Table 7-9. The high attachment relates to the strong interaction with incoming face during crystallisation providing the region with ease to slip. The calculated surface energy was in the same magnitude to the literature value. Heng and Williams (2006)[12] studied the wettability of FI and FII while by doing so, they measured the contact angle for dominating crystal face giving the surface energy of each face. The calculated (001) surface energy was ≈64% more than the measured value. While there is no direct relation between the rugosity and surface energy, both characteristics are useful for representing the roughness of specific plane.

As seen in Table 7-9, the percent of hydrogen bond breaking was very low for all planes with values below 1.0%. The percent for hydrogen breaking was low as no inter-planar hydrogen bonding was observed in FII agreeing with the intermolecular analysis done. The low percent for hydrogen breaking of each plane shows that FII was soft materials compared to FI that was much rigid.

Table 7-9 FII surface mechanical properties characteristics. The rugosity was between 1.83 and 9.38 and for surface energy between 80.00 to 142.50 mJ/m². The percent for hydrogen bond breaking is very low with values for all slip plane candidates below 1.0%

		FII		
Plane	Rugosity	Surface energy (mJ/m²)	Surface energy (Literature)[12]	% H-bond breaking
(100)	3.69	58.00	-	0.50
(010)	6.45	97.00	71.1	0.40
(001)	9.38	142.50	51.8	0.33
(110)	1.83	50.00	71.9	0.41
(101)	2.38	54.00	-	0.54
(011)	4.44	80.00	-	0.31
(111)	2.52	47.00	-	0.53
(200)	1.90	42.00	-	0.50

7.3.1.1 Interlocking representations

The interlocking representation for all slip plane candidates graphically (Figure 7-4), demonstrated that only two planes were ever ready for a slip that was (100) and (200). Both were from the same family with (200) was having half d-spacing from (100). No interlocking for both planes was anticipated agreeing with the qualitative and other slip plane characterisation analysis. Inspection on (200) plane showed that no molecules were sticking out of plane also intermolecular contact forming between the layers.
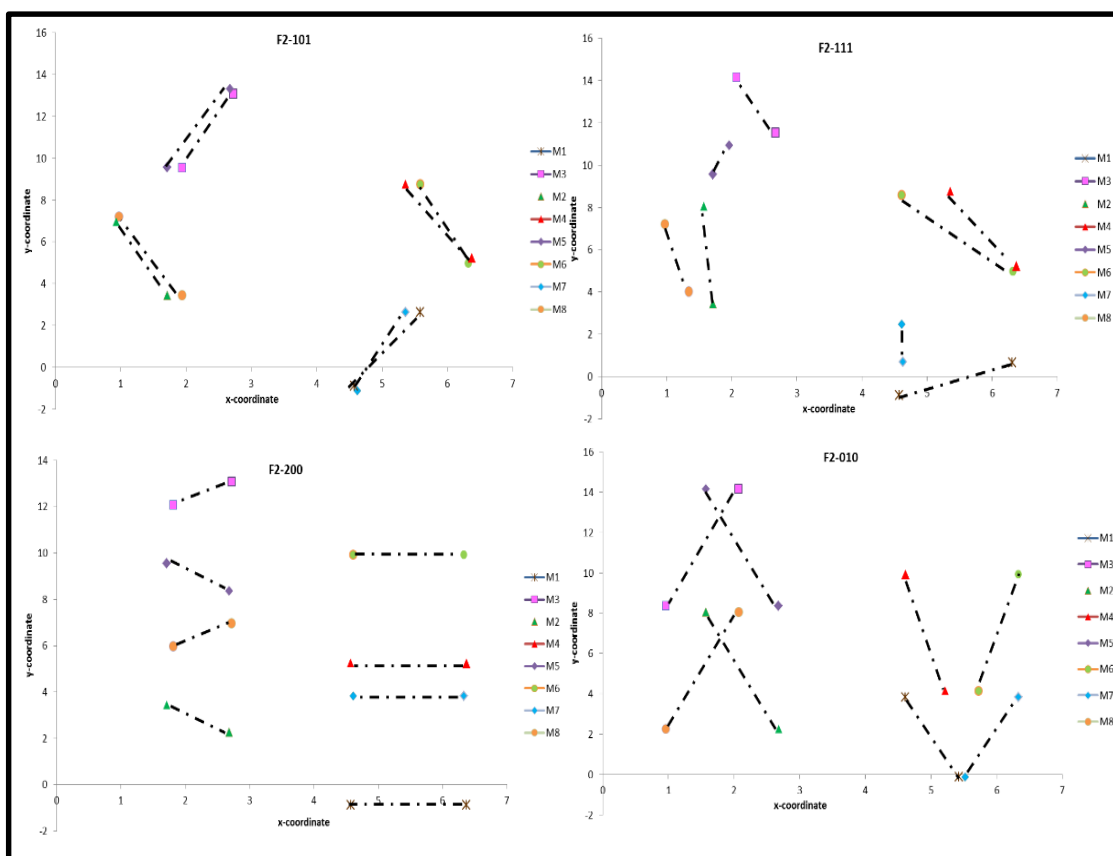
Figure 7-4 Projection of molecules in a unit cell onto respective candidates slip plane. Each connected lines were representing distance between the maximum and minimum atom in every molecule considered. Two points plotted for each were the x and y coordinates for respective atoms that have the maximum and minimum distance. A candidate slip plane was interlocking when the projected lines are crossing each other. It can be seen that (100) and (200) were not interlocked
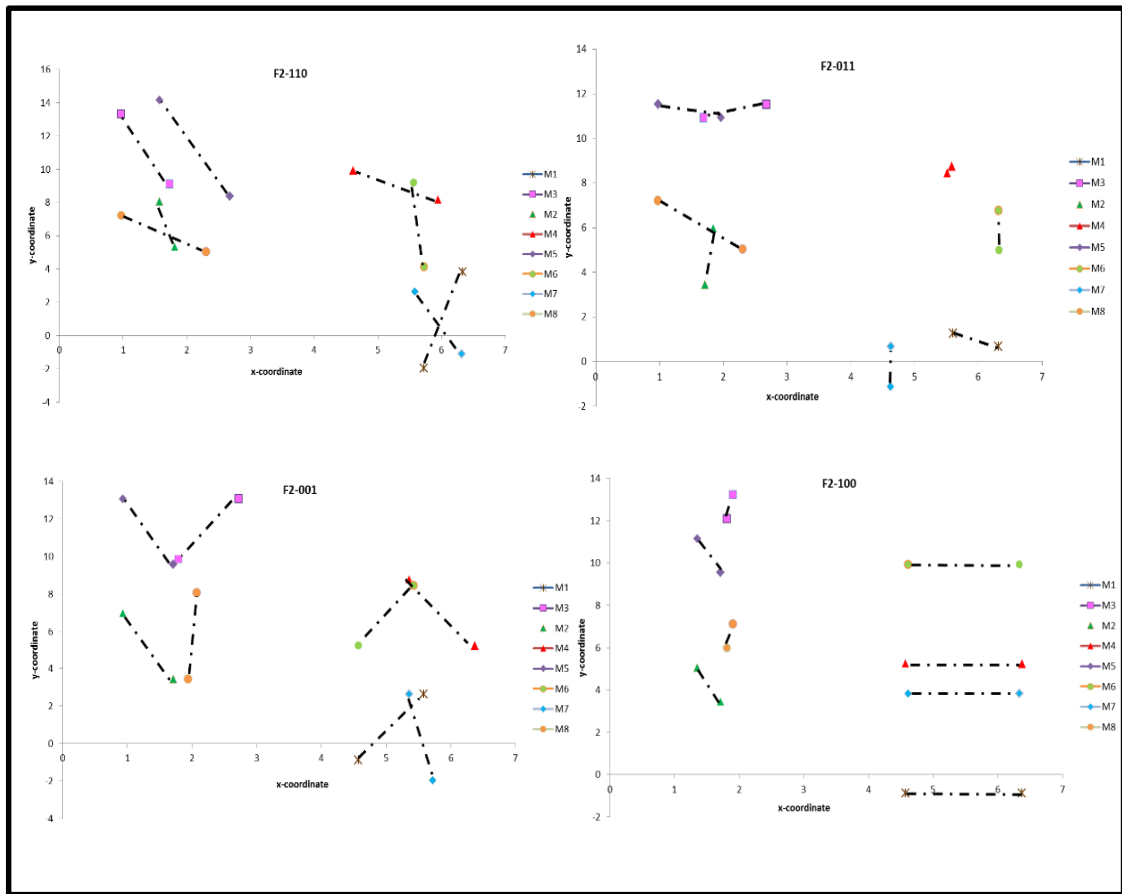
7.3.1.2   Multiple attribute decision-making calculations (MADM)

Normalised values of attributes calculated earlier were presented in Table 7-10. If surface energy is taken as the main factor for preferred slip plane, plane (200) was the best candidate. In contrast, if rugosity was the most importance, two planes were the obvious choice namely (110) and (200). While if interlocking, (100) and (200) were the best choice. Finally, in the case of hydrogen bond breaking, the most probable was (011) plane. From this hypothetical importance for preferred slip plane properties, it was identified that (200) was the only plane satisfying more than one ideal attributes of a slip plane.

Table 7-10 Normalised values for all attributes calculated earlier. Each attribute consists of values in the range 0-1.0 making it in the same dimension for comparison

Attributes/ Alternatives	FII			
	Surface E	Rugosity	Interlock of slip planes	H-bond breaking (%)
(100)	0.27	0.27	0.00	0.39
(010)	0.43	0.48	0.41	0.31
(001)	0.65	0.70	0.41	0.26
(110)	0.23	0.14	0.41	0.32
(101)	0.25	0.18	0.41	0.43
(011)	0.36	0.33	0.41	0.24
(111)	0.20	0.19	0.41	0.42
(200)	0.19	0.14	0.00	0.40

All attributes were weighted with the same importance that was 0.25. The weighted normalised attributes were given in Table 7-11 to show the best and worst scenario to be a slip plane. For the surface energy, the best condition was 0.05, gained by (111) and (200) while the worst was 0.16 for (001). Similarly, for the rugosity, the best was 0.04 for (200) and worst was 0.17 for (001). For the hydrogen bond breaking the best was 0.06 that were gained by (001) and (011). From the above results, (200) seem to score most of the best scenario of a slip plane.

Table 7-11 Weighted-normalised attributes with respect to the alternatives to give the best and worst values in relation to the ideal behaviour of a slip plane

Attributes/ Alternatives	FII			
	Surface E	Rugosity	Interlock of slip planes	H-bond breaking (%)
(100)	0.07	0.07	0.00	0.10
(010)	0.11	0.12	0.09	0.08
(001)	0.16	0.17	0.09	0.06
(110)	0.06	0.03	0.09	0.08
(101)	0.06	0.04	0.09	0.11
(011)	0.09	0.08	0.09	0.06
(111)	0.05	0.05	0.09	0.10
(200)	0.05	0.04	0.00	0.10

The positive and negative separation were calculated for all attributes and were given in Table 7-12. The positive separation had values ranging from 0.040 to 0.21 while the negative was 0.20 to 0.05. From the list, the lowest value for positive separation and highest values for negative separation was for the plane (200). The difference of the negative to positive was calculated against the total values giving the final rank of the slip plane.

Table 7-12 Positive and negative separation values of attributes with regards to achieving the optimum condition for slip plane. These separation analyses were carried out with respect to slip plane candidates

Attributes/ Alternatives	Surface Energy	Rugosity	Interlock of planes	H-bond breaking	Squared of sum	Positive separation
FII (positive separation)						
(100)	3.07E-04	1.47E-03	0.00E+00	1.48E-03	3.26E-03	5.71E-02
(010)	3.24E-03	8.02E-03	1.04E-02	3.51E-04	2.20E-02	1.48E-01
(001)	1.28E-02	2.07E-02	1.04E-02	2.46E-05	4.39E-02	2.10E-01
(110)	3.92E-05	1.53E-05	1.04E-02	4.29E-04	1.09E-02	1.04E-01
(101)	1.41E-04	1.99E-04	1.04E-02	2.14E-03	1.29E-02	1.14E-01
(011)	1.60E-03	2.73E-03	1.04E-02	1.05E-06	1.47E-02	1.21E-01
(111)	4.03E-07	2.79E-04	1.04E-02	1.97E-03	1.27E-02	1.13E-01
(200)	7.51E-06	2.64E-05	0.00E+00	1.52E-03	1.56E-03	3.94E-02

Attributes/ Alternatives	Surface Energy	Rugosity	Interlock of planes	H-bond breaking	Squared of sum	Negative separation
FII (negative separation)						
(100)	8.55E-03	1.03E-02	1.00E-02	1.34E-04	2.90E-02	1.70E-01
(010)	2.82E-03	2.55E-03	4.16E-06	9.77E-04	6.35E-03	7.97E-02
(001)	9.96E-06	1.47E-05	4.16E-06	2.03E-03	2.06E-03	4.54E-02
(110)	1.08E-02	1.85E-02	4.16E-06	8.58E-04	3.01E-02	1.74E-01
(101)	9.63E-03	1.58E-02	4.16E-06	1.37E-05	2.55E-02	1.60E-01
(011)	4.90E-03	7.69E-03	4.16E-06	2.40E-03	1.50E-02	1.22E-01
(111)	1.20E-02	1.52E-02	4.16E-06	3.21E-05	2.72E-02	1.65E-01
(200)	1.27E-02	1.82E-02	1.00E-02	1.21E-04	4.10E-02	2.03E-01

The rank of preferred slip plane was given in Table 7-13. The preferred slip plane for FII was (100). The full list in the decreasing importance were 100 > 101 > 111 > 110 > 011 > 010 > 001. (001) was shown to be the least likely preferred slip plane based on the attributes tested. It has the biggest deviation from the ideal condition with 72%.

Table 7-13 Rank for preferred slip plane for FII. Showing the most probable was for (100) with 25% deviation from the ideal condition

Rank	Alternatives	% Optimum
FII		
1	(100)	75
2	(101)	62
3	(111)	59
4	(110)	58
5	(011)	50
6	(010)	35
7	(001)	18

7.3.2 Paracetamol Form II Burgers vector calculations

FII is a primitive crystal, therefore, it will have Burgers vector without any halving. In a similar way to FI, the results were divided into two, geometrical and dislocations-based Burgers vector to show the variation of the preferability.

7.3.2.1 Geometrical-based Burgers vector

The list of geometrical based Burgers vector was presented in Table 7-14. The shortest magnitude was 7.29 Å in the direction of [100]. The largest unit cell parameter for FII was [001] with the magnitude of 17.58Å. The final list of Burgers vector for further study were seven and was presented in Table 7-14. In decreasing order of significance, the Burgers vector was [100]> [010]> [110]> [001]> [101]> [011] > [111]. As the magnitude of distance increases, the probability of slip displacement to take place decreases.

7.3.2.2 Dislocations influence on Burgers vector

Calculated dislocations energies were presented as a polar plot to show the continuum of the energy factor. The dislocation energy coefficients (K) in Table 7-14 showed the dependency towards the elastic components of FII and also showing the anisotropic properties of the dislocations based on the three-dimensional directions, [100], [010] and [001]. The range of dislocations energy corresponding to specific Burgers vector according to the variation in energy factor was also given in Table 7-14. The energy factor for [100] and [010] were seen to be distributed uniformly in the three axial directions compared to the other Burgers vector.
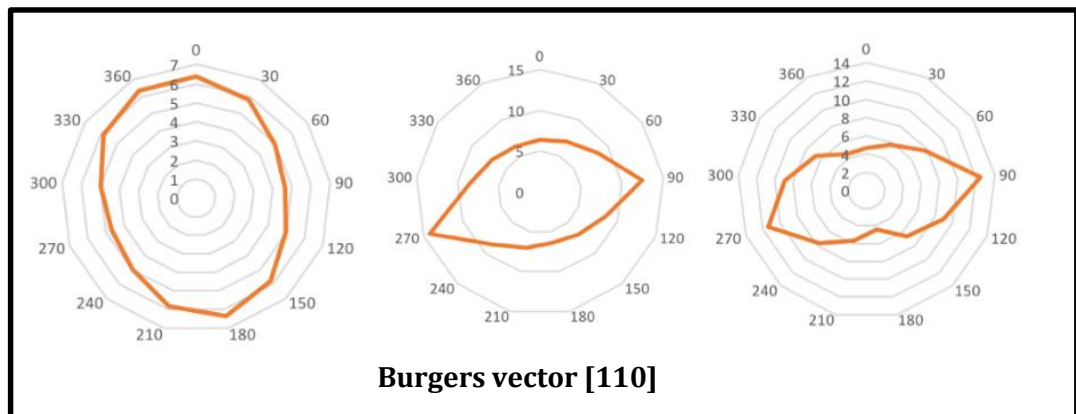
Burgers vector [110]

Figure 7-5 Polar plot representing the dislocation energy factor K for F2 viewing through [100], [010] and [001] directions. The Burgers vector scanning angle were for [100] $\emptyset = 90$ $\theta = 90$ [010] $\emptyset = 0$ $\theta = 90$ and [001] $\emptyset = 90$ $\theta = 0$. Uniform distributions was observed for Burgers vector [100] and [010]

Burgers vector [111]

Burgers vector [101]

Burgers vector [100]

Burgers vector [010]

Burgers vector [001]
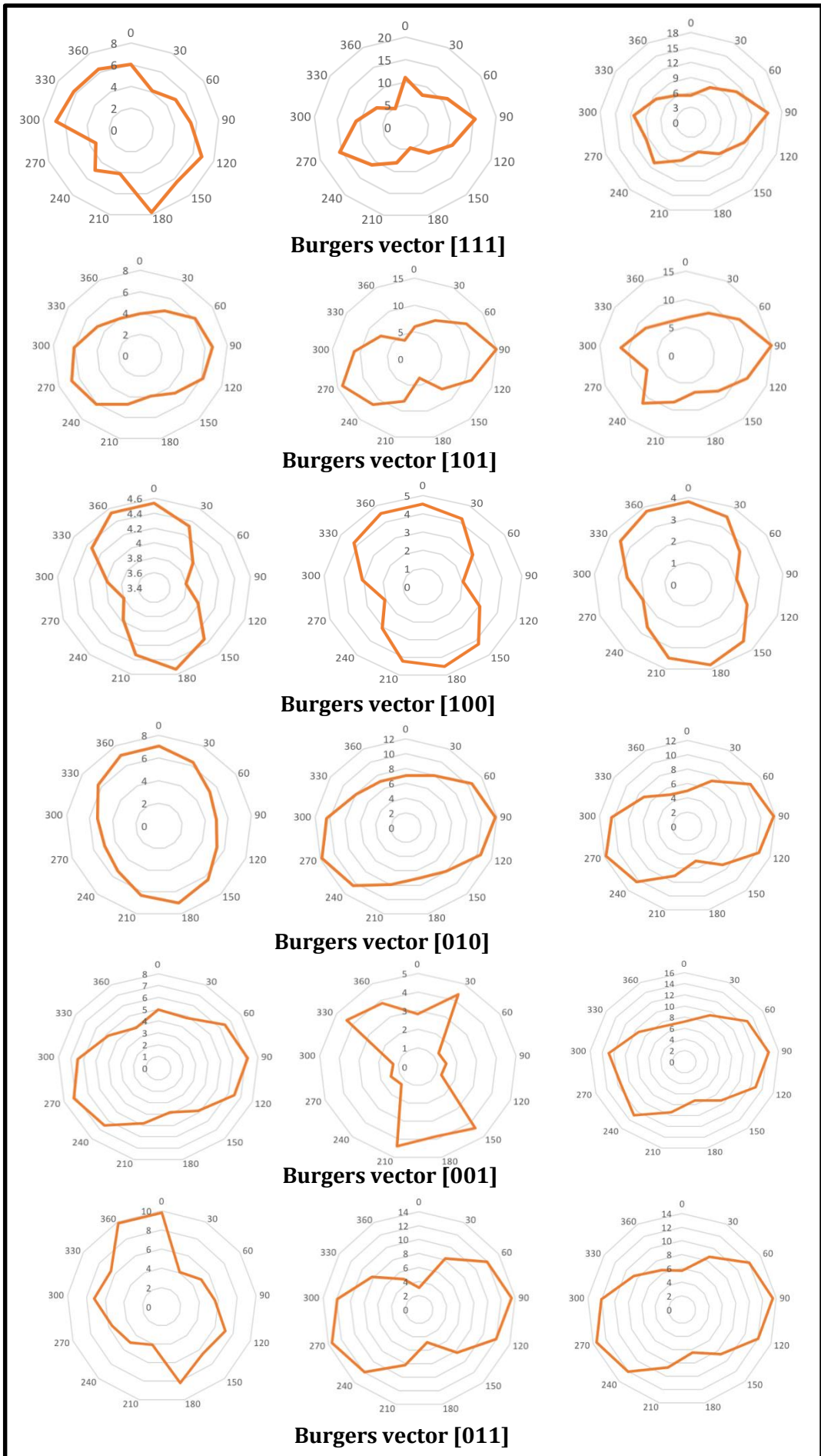
Burgers vector [011]

Moreover, from the polar plot, it can be seen that the K values varied significantly for the three axial directions. The lowest line dislocations energy was 0.68 $eVnm^{-1}$ in the direction of [100]. Line dislocations energy based Burgers vector was much preferred as it reflects closest the deformation in real crystal. The least direction for dislocations was [011] with 13.93 $eVnm^{-1}$.

Table 7-14 Calculated Burgers vector based on geometrical Burgers vector calculated by considering crystal geometry only. The smallest magnitude of Burgers vector was 7.29 Å in the direction of [100]. Dislocation energy coefficient (K) and resulting line dislocation energy was showing the dependency towards Burgers vector magnitude. Type of dislocation was predicted based on the angle between dislocation line and Burgers vector. The final line dislocation energy seems to be increasing as the Burgers vector magnitude increases.

BV	Magnitude BV(Å)	Magnitude BV²(Å)²	K(GPa)			$K(BV)^2$ $(evnm^{-1})$
			[100]	**[010]**	**[001]**	
[100]	7.29	53.22	4.53	3.80	2.05	0.68-1.51
[010]	12.20	148.94	4.97	11.76	7.02	4.62-10.94
[110]	14.22	202.15	4.66	6.36	6.70	5.88-8.46
[001]	17.58	309.13	3.85	7.19	8.50	7.4-16.41
[101]	19.04	362.34	5.46	10.03	4.28	9.69-22.70
[011]	21.40	458.06	5.63	13.52	6.97	16.11-38.69
[111]	22.61	511.28	4.36	7.52	5.66	13.93-24.02

From the continuum, the type of dislocations can be predicted. Appendix A3 presents the stereographic projection for determining the scanning angle of dislocation's line for the edge and screw. Table 7-15 lists the 17 potential edge and seven screw dislocations in FII at respective angle $\emptyset$ and θ. From the analysis, Burgers vector [100] was characterised to undergo edge dislocations.

Table 7-15 List of potential edge and screw dislocations in FII. The analysis produced 17 potential edge dislocations with regards to the Burgers vector

BV	Dislocation line			K (GPa)	Kb²(eVm⁻¹)	Type
	LV	Angle ∅°	Angle θ°			
[100]	[100]	90	0	4.53	1.51	Screw
	[010]	0	90	3.80	1.26	Edge
	[021]	35	90	3.37	1.12	Edge
	[001]	90	90	2.05	0.68	Edge
	[011]	55	90	2.78	0.92	Edge
[010]	[010]	0	90	11.76	10.94	Screw
	[001]	90	90	7.02	6.53	Edge
	[100]	180	90	4.97	4.62	Edge
	[102]	101	90	1.16	1.08	Edge
[001]	[001]	90	90	8.50	16.42	Screw
	[100]	270	90	3.85	7.44	Edge
	[010]	0	90	7.19	13.89	Edge
[110]	[110]	45	90	6.70	8.46	Screw
	[001]	90	90	6.70	8.46	Edge
	[312]	125	90	8.65	10.93	Edge
[101]	[101]	45	90	10.02	22.69	Screw
	[010]	0	90	10.03	22.71	Edge
[011]	[011]	0	45	4.38	12.54	Screw
	[100]	180	90	5.63	16.12	Edge
	[0-21]	90	90	13.51	38.67	Edge
	[1-21]	103	90	13.22	37.84	Edge
[111]	[111]	45	45	7.52	24.03	Screw
	[0-21]	114	90	11.70	37.38	Edge
	[121]	281	90	12.25	39.14	Edge

Table 7-16 presented the new order of preferred Burgers vector. Primary Burgers vector based on the lowest dislocation energy was [100]. Decreasing order of preferred Burgers vector was [100] > [010] > [110] > [001] > [101] > [111] and [011]. From the results, there was only one Burgers vector alternated that was [011]. The minimum different observed was related to the huge magnitude difference between the axial component, with the [100] was approximately half of the [010] and [001]. Therefore, effects of dislocations were not clearly seen because the K values were in the same range 2 to 9GPa. For this instance, the magnitude of Burgers vector was significantly influencing the line dislocations energy.

Table 7-16 Preferred Burgers vector for a slip to take place based on two approaches, geometrical consideration, and line dislocation energy. For both lists, [100] was the shortest Burgers vector hence becomes the primary Burgers vector

Rank	Burgers vector (Geometrical)	Burgers vector (Dislocation Energy)
1	[100]	[100]
2	[010]	[010]
3	[110]	[110]
4	[001]	[001]
5	[101]	[101]
6	[011]	[111]
7	[111]	[011]

7.3.3 Predicted mechanical behaviour for paracetamol Form II

From the analysis of slip plane and Burgers vector, it can be suggested that there was an association between the molecular crystallographic packing of FII to successfully predict the slip deformation. Different packing pattern, create different deformation environment, specifically, the slip plane attributes. There was one obvious slip plane that was (200). The quantitative representation of slip plane interlocking and rugosity further support the prediction. An interesting finding was the ideal slip plane (200) was not an active slip system with the primary Burgers vector [100]. Therefore, FII will not plastically deform at the first instance. However, taking the strongest intermolecular interactions direction, namely hydrogen bond that was created in the [010] gave a zero dot product. Therefore, FII was suggested to undergo cleaving with the strong in-plane interactions to drive the displacements.

Joiris et.al (1998) [17] reported the compaction behaviour of FII was contributed by the compressibility of the system more than the compactibility. In their study, it was observed that FII underwent fracture at low pressure and plastic behaviour at high pressure. Therefore, the predicted cleaving behaviour agrees well with the experimental measurements whereby, the ease of FII to cleave at (200) will create a new surface for interparticle interactions that can increase the compressibility performance. The following section will explore the influence of having co-former structure towards the mechanical behaviour of FI.

7.4 Prediction of the mechanical properties for paracetamol co-crystals: Paracetamol-Theophylline

Paracetamol-Theophylline (PTHEO) co-crystal was observed to create a layered-like crystallographic pattern. The nature of PTHEO crystallographic pattern was suggested to improve the mechanical properties of paracetamol hence produce a better tablet. The theophylline molecule was introduced to form co-crystal. This section will present the predicted mechanical properties of PTHEO.

7.4.1 Paracetamol-Theophylline slip plane characterisations

The lowest rugosity of PTHEO was 3.16 for (101), and the highest was 8.87 for (10-1) given in Table 7-17. The lowest surface energy was 41.69mJ/mol for (001) plane, and the highest was 118.11mJ/mol for (10-1). The surface energy of PTHEO by taking the morphological important faces was $76.43 mJ/m^2$ was comparable to a similar co-crystal molecule, theophylline-nicotinamide (THEO-NIC) dispersive surface energy measured by the inverse gas chromatography[21] which was $69.79 mJ/m^2$. It was appreciated that the bulk surface energy will be slightly smaller in comparison to small size samples therefore explains the $6 mJ/m^2$ difference between calculated. The hydrogen bond breaking was easy for all slip plane candidates because, the energy was below 1%. The small percentage was related to the total hydrogen bond interactions in a unit cell of PTHEO calculated in the earlier section.

Table 7-17 PTHEO surface mechanical properties characteristics. The rugosity was between 3.16 and 8.87 and for surface energy between 41.69 and 97.27 mJ/m². The percent for hydrogen bond breaking was very low with values for all slip plane candidates below 1.0%

Plane	Rugosity	Surface energy (mJ/m²)	% H-bond breaking
(100)	5.08	69.48	0.73
(010)	8.52	97.27	0.57
(001)	5.99	41.69	0.65
(110)	4.15	69.48	0.67
(101)	3.16	76.43	0.55
(011)	3.42	83.37	0.84
(111)	7.48	90.32	0.71
(10-1)	8.87	34.72	0.89

7.4.1.1   Interlocking representations

The interlocking representation for all slip plane candidates graphically (Figure 7-6), demonstrated that three planes were not interlocked that were (101), (011) and (110). The interlocking representation agrees with the qualitative analysis which has (101) as the potentially slip plane established as the molecules were arranged flat as seen in Figure 6-17shown in chapter 6.
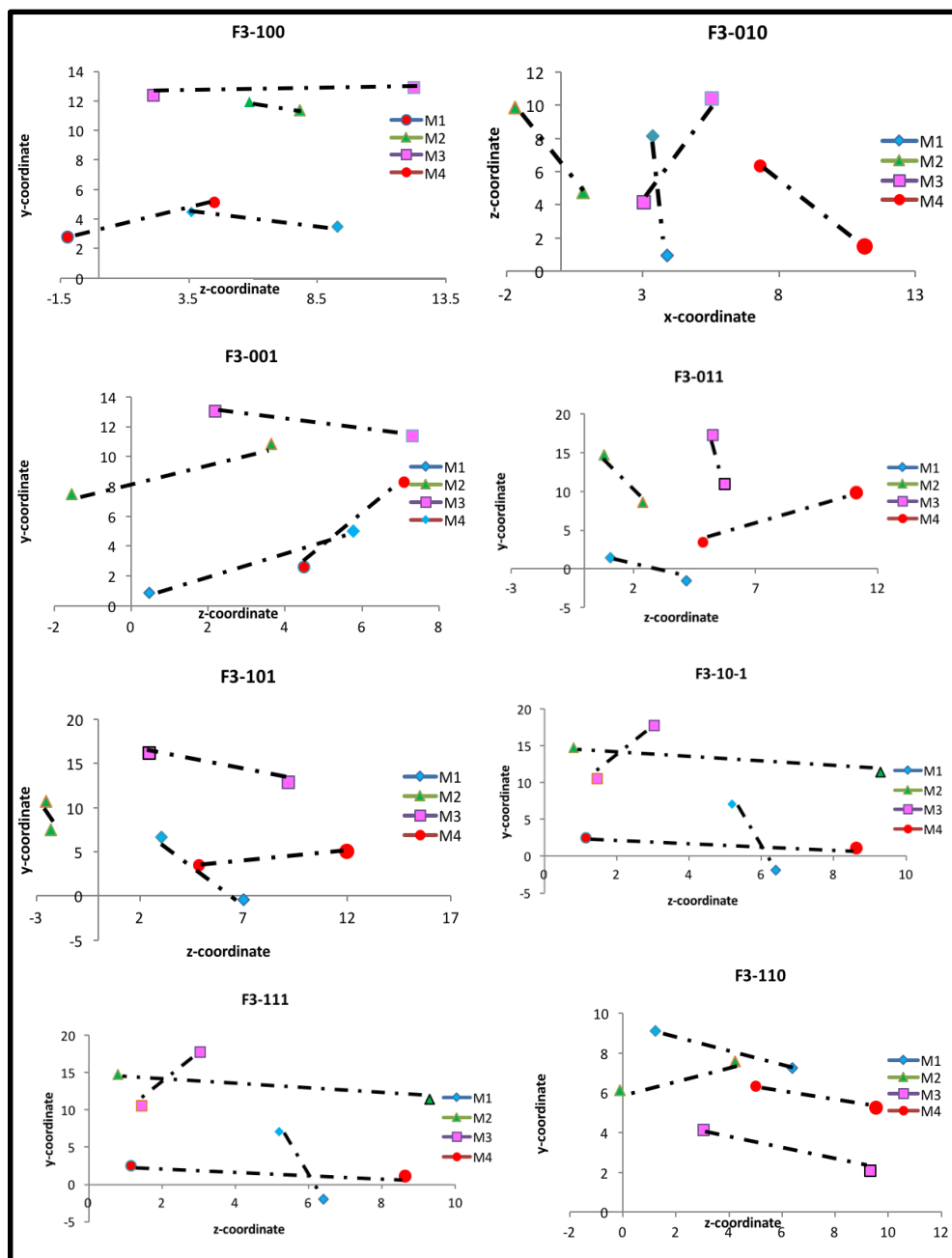
Figure 7-6 PTHEO interlocking representations showing projection of molecules in a unit cell onto plane normal. The non-interlock planes were (101), (011), and (110)

7.4.1.2 Multiple attribute decision-making calculations (MADM)

The multiple dimensions of the surface attributes calculated in prior subsections were compared as normalised values and presented in Table 7-18. From the analysis, the (101) was seen to have the lowest rugosity and hydrogen bond breaking also not interlocking. For surface energy, the best condition was at 0.04, and the worst was 0.10 as given in Table 7-19. Similarly, for rugosity the best condition was 0.05 and worst 0.13. For energy to break hydrogen bond, the best was 0.07 and worst was 0.11.

Table 7-18 Normalised values for all the attributes making it in the same dimension between 0 and 1.0

Attributes/ Alternatives	PTHEO			
	Surface E	Rugosity	Interlock of slip planes	H-bond breaking
(100)	0.29	0.29	0.38	0.37
(010)	0.41	0.49	0.38	0.29
(001)	0.18	0.34	0.38	0.33
(110)	0.29	0.24	0.00	0.34
(101)	0.32	0.18	0.00	0.28
(011)	0.35	0.19	0.00	0.42
(111)	0.38	0.43	0.38	0.36
(10-1)	0.25	0.51	0.38	0.45

Table 7-19 Weighted-normalised attributes with respect to the alternatives to give the best and worst values in relation to the ideal behaviour of a slip plane

Attributes/ Alternatives	PTHEO			
	Surface E	Rugosity	Interlock of slip planes	H-bond breaking (%)
(100)	0.07	0.07	0.09	0.09
(010)	0.10	0.12	0.09	0.07
(001)	0.04	0.09	0.09	0.08
(110)	0.07	0.06	0.00	0.08
(101)	0.08	0.05	0.00	0.07
(011)	0.09	0.05	0.00	0.11
(111)	0.10	0.11	0.09	0.09
(10-1)	0.06	0.13	0.09	0.11

The positive separation analysis showed clearly that (101) plane was closest to the ideal condition with smallest values, 0.042 and largest negative separation of 0.139. The farthest from the ideal slip plane conditions was (10-1). The ratio between the negative separation to the total (positive and negative) represented the final rank of potential slip plane and given in Table 7-21.

Table 7-20 Positive and negative separation (TOPSIS) values of attributes with regards to achieving the optimum condition for slip plane. These separation analyses were carried out with respect to slip plane candidates.

Attributes/ Alternatives	Surface E	Rugosity	Interlock of planes	H-bond breaking	Squared of sum	Positive separation
			PTHEO (positive separation)			
100	1.13E-03	5.02E-04	8.90E-03	4.52E-04	1.10E-02	1.05E-01
010	3.97E-03	5.10E-03	8.90E-03	1.56E-06	1.80E-02	1.34E-01
001	1.71E-05	1.25E-03	8.90E-03	1.27E-04	1.03E-02	1.01E-01
110	1.13E-03	8.37E-05	8.90E-03	1.89E-04	1.03E-02	1.01E-01
101	1.67E-03	2.46E-05	0.00E+00	1.56E-06	1.70E-03	4.12E-02
011	2.33E-03	1.57E-06	8.90E-03	1.23E-03	1.25E-02	1.12E-01
111	3.09E-03	3.21E-03	8.90E-03	3.52E-04	1.56E-02	1.25E-01
10-1	5.08E-04	5.84E-03	8.90E-03	1.70E-03	1.70E-02	1.30E-01

Attributes/ Alternatives	Surface E	Rugosity	Interlock of planes	H-bond breaking	Squared of sum	Negative separation
			PTHEO (negative separation)			
100	3.18E-03	3.32E-03	1.88E-05	3.52E-04	6.87E-03	8.29E-02
010	7.30E-04	7.33E-05	1.88E-05	1.50E-03	2.32E-03	4.82E-02
001	7.37E-03	1.99E-03	1.88E-05	8.27E-04	1.02E-02	1.01E-01
110	3.18E-03	5.02E-03	1.88E-05	6.89E-04	8.91E-03	9.44E-02
101	2.41E-03	7.22E-03	8.10E-03	1.70E-03	1.94E-02	1.39E-01
011	1.74E-03	6.60E-03	1.88E-05	2.50E-05	8.39E-03	9.16E-02
111	1.18E-03	5.47E-04	1.88E-05	4.52E-04	2.20E-03	4.69E-02
10-1	4.55E-03	1.28E-05	1.88E-05	1.56E-06	4.59E-03	6.77E-02

The (101) plane was the best choice with 77% attributes of an ideal slip plane. The least to be a slip plane was (10-1) with 4.7%. PTHEO distinctive preferred slip plane was (101) as the other planes were showing equal or less than 50% attributes of slip plane.

Table 7-21 Rank for preferred slip plane for PTHEO. Showing the most probable was for (101) with 23% deviation from the ideal condition

PTHEO		
Rank	Alternatives	% Optimum
1	(101)	77
2	(001)	50
3	(110)	48
4	(011)	45
5	(100)	44
6	(111)	27
7	(010)	26
8	(10-1)	4.7

7.4.2 Paracetamol-Theophylline Burgers vector calculations

PTHEO is a primitive crystal, therefore, it will have Burgers vector without any halving. In a similar way to FI and FII, the results were divided into two, geometrical and dislocations-based Burgers vector to show the variation of the preferability.

7.4.2.1 Geometrical-based Burgers vector

The list of geometrical based Burgers vector is presented in Table 7-22. The shortest magnitude was 9.62 Å in the direction of [100]. The largest Burgers vector being considered was [111] with 21.96Å. The final list of Burgers vector for further study were seven and was presented in Table 7-22. In decreasing order of significance, the Burgers vector was [100]> [001]> [101]> [010]> [110]> [011] > [111].

7.4.2.2 Dislocations influence on Burgers vector

The dislocation energy coefficients (K) in Table 7-22 showed the dependency towards the elastic components of PTHEO and also showing the anisotropic properties of the dislocations based on the three-dimensional directions, [100], [010] and [001]. The smallest K value was 1.91 for [101] in the dislocation line direction of [001]. However, the smallest dislocation energy was $1.96 eVnm^{-1}$ for [001] with dislocation line direction of [001]. The difference because of the magnitude of Burgers vector [101] was larger than [001]. Range of dislocations energy for each Burgers vector were also given in Table 7-22.

Table 7-22 Calculated Burgers vector based on geometrical Burgers vector calculated by considering crystal geometry only. The smallest magnitude of Burgers vector was 9.62 Å in the direction of [100]. Dislocation energy coefficient (K) and resulting line dislocation energy was showing the dependency towards Burgers vector magnitude. Type of dislocation was predicted based on the angle between dislocation line and Burgers vector. The final line dislocation energy seems to be increasing as the Burgers vector magnitude increases

BV	Magnitude BV(Å)	Magnitude BV²(Å)²	K(GPa)			$K(BV)^2$
			[100]	**[010]**	**[001]**	$(eVnm^{-1})$
[100]	9.62	92.54	5.30	6.68	8.19	3.06-4.73
[001]	11.33	128.37	3.67	5.62	2.44	1.96-4.35
[101]	14.17	200.79	2.37	4.11	1.91	2.40-5.16
[010]	15.72	247.12	5.51	2.23	9.12	3.44-14.08
[110]	18.43	339.66	5.49	5.28	5.22	11.20-19.12
[011]	19.38	375.58	5.13	4.11	7.72	9.64-18.11
[111]	21.96	447.75	4.73	5.96	7.32	13.23-20.47
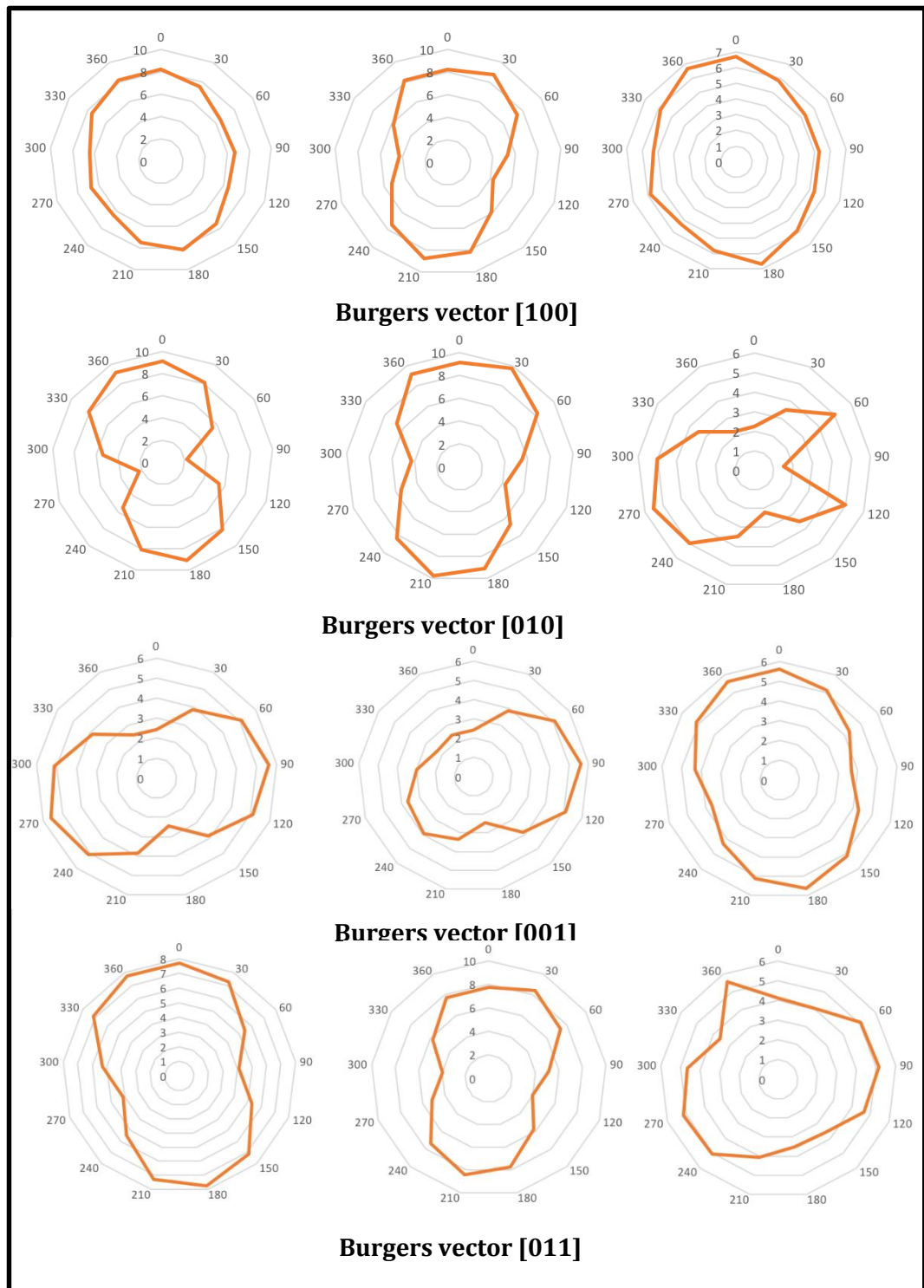
Figure 7-7 Polar plot representing the dislocation energy factor K for PTHEO viewing through [100], [010] and [001] directions. The Burgers vector scanning angle were for [100] $\emptyset = 90$ $\theta = 90$ [010] $\emptyset = 0$ $\theta = 90$ and [001] $\emptyset = 90$ $\theta = 0$. Uniform distributions was observed for Burgers vector [100] and [010]

239

Burgers vector [110]

Burgers vector [111]
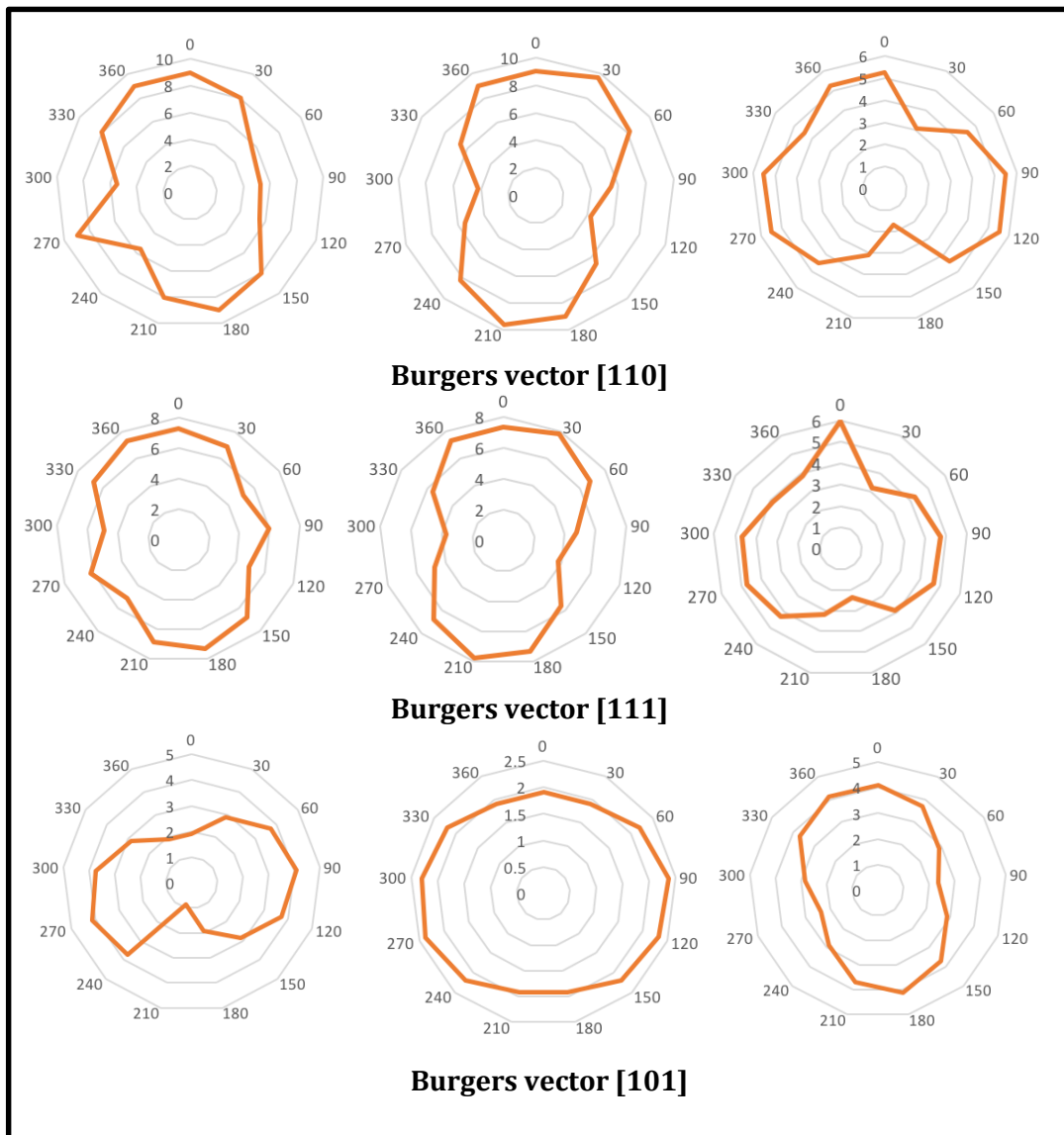
Burgers vector [101]

The energy factor for PTHEO was seen to be distributed uniformly in the three axial directions as shown in the polar plot (Figure 7-7). For all of the Burgers vector, the K values were varying from approximately 2 to 10GPa. From the K continuum analysis, 16 potential edge and seven screw dislocations were characterised. The position angles for the dislocation line with respect to the Burgers vector were given in Table 7-23 together with the potential dislocations type. It was obvious that for [111] and [011] that were having a large magnitude of Burgers vector, the dislocations energy was large therefore, these two directions were the least to displace.

The final rank of Burgers vector was given in Table 7-24. Now, the rank of Burgers vector according to increasing dislocations energy is [001] < [101] < [100] < [010] < [011] < [110] < [111]. The primary Burgers vector for PTHEO was [001].

Table 7-23 List of potential edge and screw dislocations in PTHEO. The analysis produced 16 potential edge dislocations with regards to Burgers vector. It was evidence that the large magnitude of Burgers vector [011] and [111] resulted in a large dislocations energy

BV	Dislocation line			K (GPa)	$Kb^2(eVm^{-1})$	Type
	LV	Angle $\emptyset°$	Angle $\theta°$			
[100]	[100]	90	0	5.30	3.06	Screw
	[010]	0	90	6.68	3.86	Edge
	[02-1]	340	88	6.16	3.56	Edge
	[01-1]	324	86	5.51	3.19	Edge
[010]	[010]	0	90	2.23	3.44	Screw
	[001]	90	90	9.12	8.51	Edge
	[100]	90	90	5.51	14.08	Edge
	[-102]	68	90	5.24	8.09	Edge
[001]	[001]	90	90	2.44	1.96	Screw
	[-120]	17	89	5.42	4.51	Edge
	[010]	0	90	5.62	4.35	Edge
[110]	[110]	45	90	3.80	8.06	Screw
	[001]	270	87	5.22	11.08	Edge
	[-212]	45	86	4.26	9.04	Edge
[101]	[101]	45	90	3.30	4.14	Screw
	[010]	0	90	4.11	5.16	Edge
[011]	[011]	0	45	6.61	15.51	Screw
	[100]	4	87	5.13	12.53	Edge
	[0-12]	90	89	5.21	12.04	Edge
	[-1-12]	71	88	5.34	12.22	Edge
[111]	[111]	45	45	7.08	19.80	Screw
	[-1-13]	90	88	4.88	13.64	Edge
	[01-2]	287	89	4.71	13.17	Edge

Table 7-24 Preferred Burgers vector for a slip to take place based on two approaches, geometrical consideration, and line dislocation energy. [001] was the shortest Burgers vector following dislocation energy hence becomes the primary Burgers vector

Rank	Burgers vector (Geometrical)	Burgers vector (Dislocation Energy)
1	[100]	[001]
2	[001]	[101]
3	[101]	[100]
4	[010]	[010]
5	[110]	[011]
6	[011]	[110]
7	[111]	[111]

7.4.3 Predicted mechanical behaviour for Paracetamol-Theophylline

The slip system of PTHEO was recognised as inactive because the calculated primary Burgers vector [001] was not in the predicted slip plane (101). The strongest intermolecular interaction, in this case, hydrogen bond which was created in the [010] direction was used to provide the displacement energy. In short, PTHEO has a prominent slip plane, namely (101) with 77% ideal attributes while other candidates were below 50%. The rank of Burgers vector showed differences between the geometrical-based and dislocations energy relating to the K factors and the magnitudes. The cleaving behaviour of PTHEO will be governed by the (101) characteristics.

7.5 Study of the mechanical properties for paracetamol hydrates: Paracetamol Trihydrates

The influence of three water molecules towards the FI was studied. Paracetamol Trihydrates (PTRI) was heavily hydrogen bonded and from the elastic calculations showed to be the softest amongst the other selected paracetamol solid forms. The mechanical properties prediction of PTRI is presented in the following subsections.

7.5.1 Paracetamol Trihydrates slip plane characterisations

The lowest rugosity of PTRI was 2.28 for (110), and the highest was 11.55 for (001) given in Table 7-25. The lowest surface energy was 41.69mJ/mol for (100) plane, and the highest was 118.11mJ/mol for (011). There were obvious variations of the rugosity values for PTRI that was related to the positions of H_2O making the PTRI corrugated. The hydrogen bond breaking was difficult for all slip plane candidates because, the energy was above 50%. The small percentage was related to the total hydrogen bond interactions in a unit cell of PTRI calculated in the earlier section.

Table 7-25 PTRI surface mechanical properties characteristics. The rugosity was between 2.28 and 11.55 and for surface energy between 41.69 and 118.11mJ/m². The percent for hydrogen bond breaking was very high with values for all slip plane candidates above 50%

Plane	Rugosity	Surface energy (mJ/m²)	% H-bond breaking
(100)	3.70	41.69	65.85
(010)	6.82	83.37	63.71
(001)	11.55	55.58	55.42
(110)	2.28	104.22	77.14
(101)	2.50	104.22	81.35
(011)	4.02	118.11	98.00
(111)	2.47	104.22	90.50

7.5.1.1 Interlocking representations

The interlocking representations for all slip plane candidates graphically (Figure 7-8), demonstrated that all planes were interlocked. The interlocking representation agrees with the qualitative analysis which has (010) as the potentially slip plane. This interlocking analysis indicated that PTRI had a corrugated structure that was reflected only one non-interlocking plane.
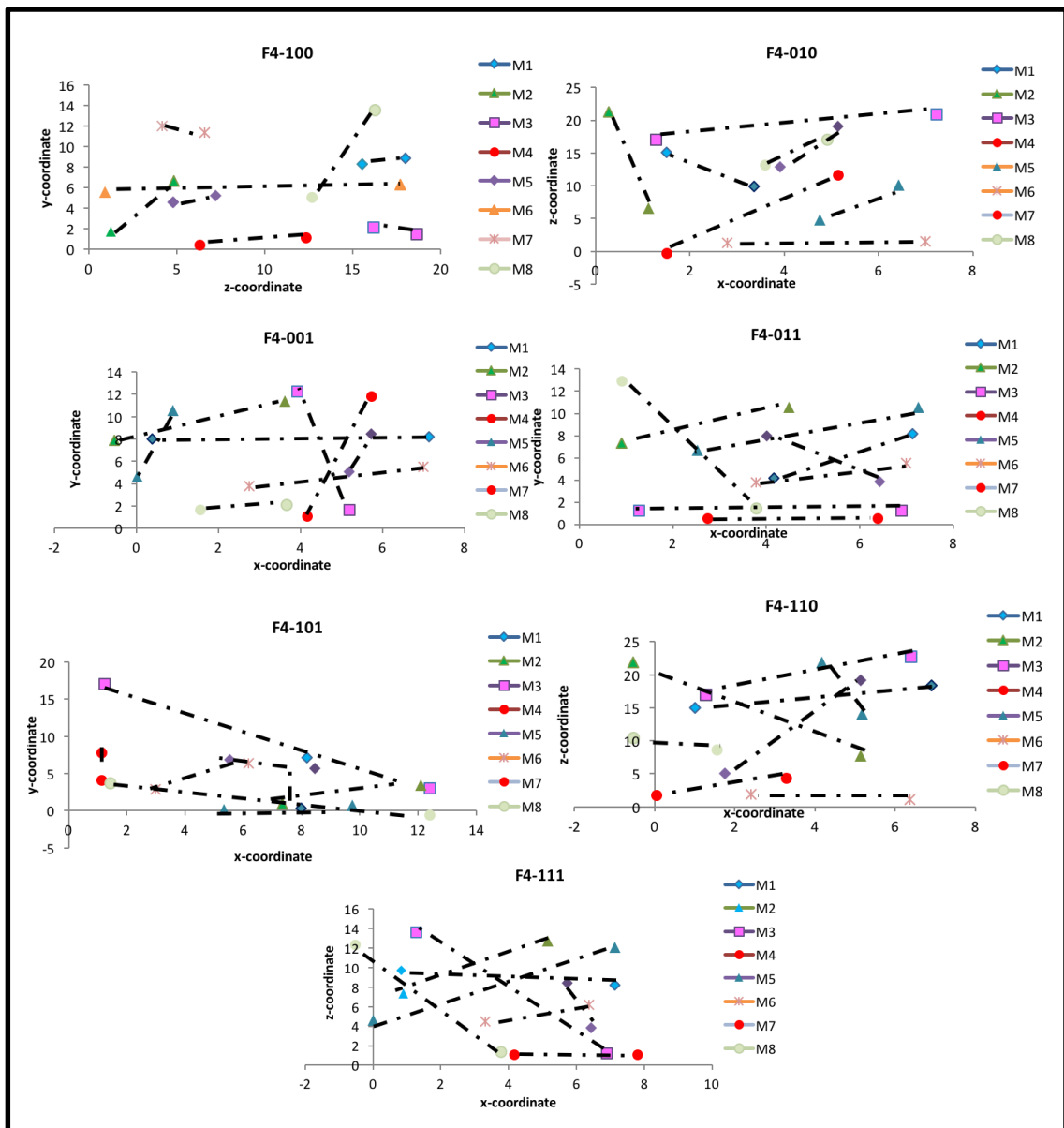
Figure 7-8 Slip plane candidates interlocking representation for PTRI. There was only one plane did not interlock, (010). PTRI was seem to have corrugated crystal packing

243

7.5.1.2 Multiple attribute decision-making calculations (MADM)

The multiple dimensions of the surface attributes calculated in prior subsections were compared as normalised values and presented in Table 7-26. From the analysis, the (110) was seen to have the lowest rugosity. For surface energy, the best condition was at 0.04, and the worst was 0.12 as given in Table 7-26. Similarly, for rugosity the best condition was 0.04 and worst 0.19. For energy to break the hydrogen bond, the best was 0.07 and worst were 0.12. The weighted-normalised values of attributes described the heavily hydrogen bonded impact that leads to slightly corrugated packing with there was no obvious plane have significantly better attributes than the other.

Table 7-26 Normalised values for all the attributes making it in the same dimension between 0 and 1.0

Attributes/ Alternatives	PTRI			
	Surface E	Rugosity	Interlock of slip planes	H-bond breaking
(100)	0.17	0.25	0.41	0.32
(010)	0.35	0.45	0.00	0.31
(001)	0.23	0.77	0.41	0.27
(110)	0.43	0.15	0.41	0.38
(101)	0.43	0.17	0.41	0.40
(011)	0.49	0.27	0.41	0.48
(111)	0.43	0.16	0.41	0.44

Table 7-27 Weighted-normalised attributes with respect to the alternatives to give the best and worst values in relation to the ideal behaviour of a slip plane

Attributes/ Alternatives	PTRI			
	Surface E	Rugosity	Interlock of slip planes	H-bond breaking (%)
(100)	0.04	0.06	0.10	0.08
(010)	0.09	0.11	0.00	0.08
(001)	0.06	0.19	0.10	0.07
(110)	0.11	0.04	0.10	0.09
(101)	0.11	0.04	0.10	0.10
(011)	0.12	0.07	0.10	0.12
(111)	0.11	0.04	0.10	0.11

The positive separation analysis showed in Table 7-28, the (010) plane was closest to the ideal condition with smallest values, 0.079 and largest negative separation of 0.106. The farthest from the ideal slip plane conditions was (011). The ratio between the negative separation to the total (positive and negative) represented the final rank of potential slip plane and given in Table 7-29.

Table 7-28 Positive and negative separation (TOPSIS) values of attributes with regards to achieving the optimum condition for slip plane. These separation analyses were carried out with respect to slip plane candidates

PTRI(positive separation)						
Attributes Alternatives	**Surface E**	**Rugosity**	**Interlock of planes**	**H-bond breaking**	**Squared of sum**	**Positive separation**
(100)	9.99E-06	1.29E-04	1.04E-02	8.84E-05	1.06E-02	1.03E-01
(010)	2.14E-03	3.98E-03	0.00E+00	6.41E-05	6.19E-03	7.87E-02
(001)	3.08E-04	2.00E-02	1.04E-02	4.59E-06	3.07E-02	1.75E-01
(110)	4.61E-03	1.49E-04	1.04E-02	5.98E-04	1.58E-02	1.26E-01
(101)	4.61E-03	7.32E-05	1.04E-02	8.76E-04	1.60E-02	1.26E-01
(011)	6.77E-03	2.77E-04	1.04E-02	2.50E-03	2.00E-02	1.41E-01
(111)	4.61E-03	8.19E-05	1.04E-02	1.66E-03	1.68E-02	1.29E-01
PTRI (negative separation)						
Attributes/ Alternatives	**Surface E**	**Rugosity**	**Interlock of planes**	**H-bond breaking**	**Squared of sum**	**Negative separation**
(100)	7.54E-03	4.71E-03	1.45E-04	9.36E-04	1.33E-02	1.15E-01
(010)	1.91E-03	2.87E-04	8.10E-03	1.02E-03	1.13E-02	1.06E-01
(001)	5.25E-03	3.78E-03	1.45E-04	1.78E-03	1.10E-02	1.05E-01
(110)	4.89E-04	8.50E-03	1.45E-04	2.42E-04	9.38E-03	9.68E-02
(101)	4.89E-04	7.84E-03	1.45E-04	1.08E-04	8.58E-03	9.26E-02
(011)	5.96E-05	4.01E-03	1.45E-04	9.98E-05	4.32E-03	6.57E-02
(111)	4.89E-04	7.93E-03	1.45E-04	5.78E-07	8.56E-03	9.25E-02

The (010) plane was the best choice with 57% attributes of an ideal slip plane. The least to be a slip plane was (011) with 32%.

Table 7-29 Rank for preferred slip plane for PTRI. Showing the most probable was for (010) with 43% deviation from the ideal condition

PTRI		
Rank	**Alternatives**	**% Optimum**
1	010	57
2	100	53
3	110	44
4	101	42
5	111	42
6	001	37
7	011	32

7.5.2   Paracetamol trihydrates Burgers vector calculations

Paracetamol trihydrates (PTRI) is a primitive crystal, therefore, it will have Burgers vector without any halving. The results were divided into two, geometrical and dislocations-based Burgers vector to show the variation of the preferability.

7.5.2.1   Geometrical-based Burgers vector

The list of geometrical based Burgers vector is presented in Table 7-30. The shortest magnitude was 7.53 Å in the direction of [100]. The largest Burgers vector being considered was [111] with 27.13 Å. The final list of Burgers vector for further study were seven and was presented in Table 7-30. In decreasing order of significance, the Burgers vector was [100]> [010]> [110]> [001]> [101]> [011] > [111].

7.5.2.2   Dislocations influence on Burgers vector

The dislocation energy coefficients (K) in Table 7-30 demonstrated the anisotropic properties of the dislocations based on the three-dimensional directions, [100], [010] and [001]. The smallest K value was 1.69GPa for [100] in the dislocation line direction of [010] giving a dislocation energy of $0.06 evnm^{-1}$. The largest K value given in Table 7-30 was 6.45GPa for Burgers vector [001] with line dislocation of [001]. Range of dislocations energy for each Burgers vector were also given in Table 7-30.

Table 7-30 Calculated Burgers vector based on geometrical Burgers vector calculated by considering crystal geometry only. The smallest magnitude of Burgers vector was 7.53 Å in the direction of [100]. Dislocation energy coefficient (K) and resulting line dislocation energy was showing the dependency towards Burgers vector magnitude. Type of dislocation was predicted based on the angle between dislocation line and Burgers vector. The final line dislocation energy seems to be increasing as the Burgers vector magnitude increases

BV	Magnitude BV(Å)	Magnitude $BV^2 Å)^2$	K(GPa)			$K(BV)^2$ $(evnm^{-1})$
			[100]	[010]	[001]	
[100]	7.53	56.70	5.97	1.69	2.26	0.60-2.11
[010]	13.36	178.49	2.13	1.96	4.26	2.19-4.75
[110]	15.34	235.32	2.09	4.95	2.92	3.07-7.28
[001]	22.38	500.86	5.67	2.13	6.45	6.66-20.18
[101]	23.61	557.43	4.95	2.09	5.67	7.28-19.74
[011]	26.06	679.54	2.07	4.32	2.92	8.79-18.34
[111]	27.13	736.62	2.67	2.67	3.08	12.29-14.17

Burgers vector [100]

Burgers vector [010]

Burgers vector [001]
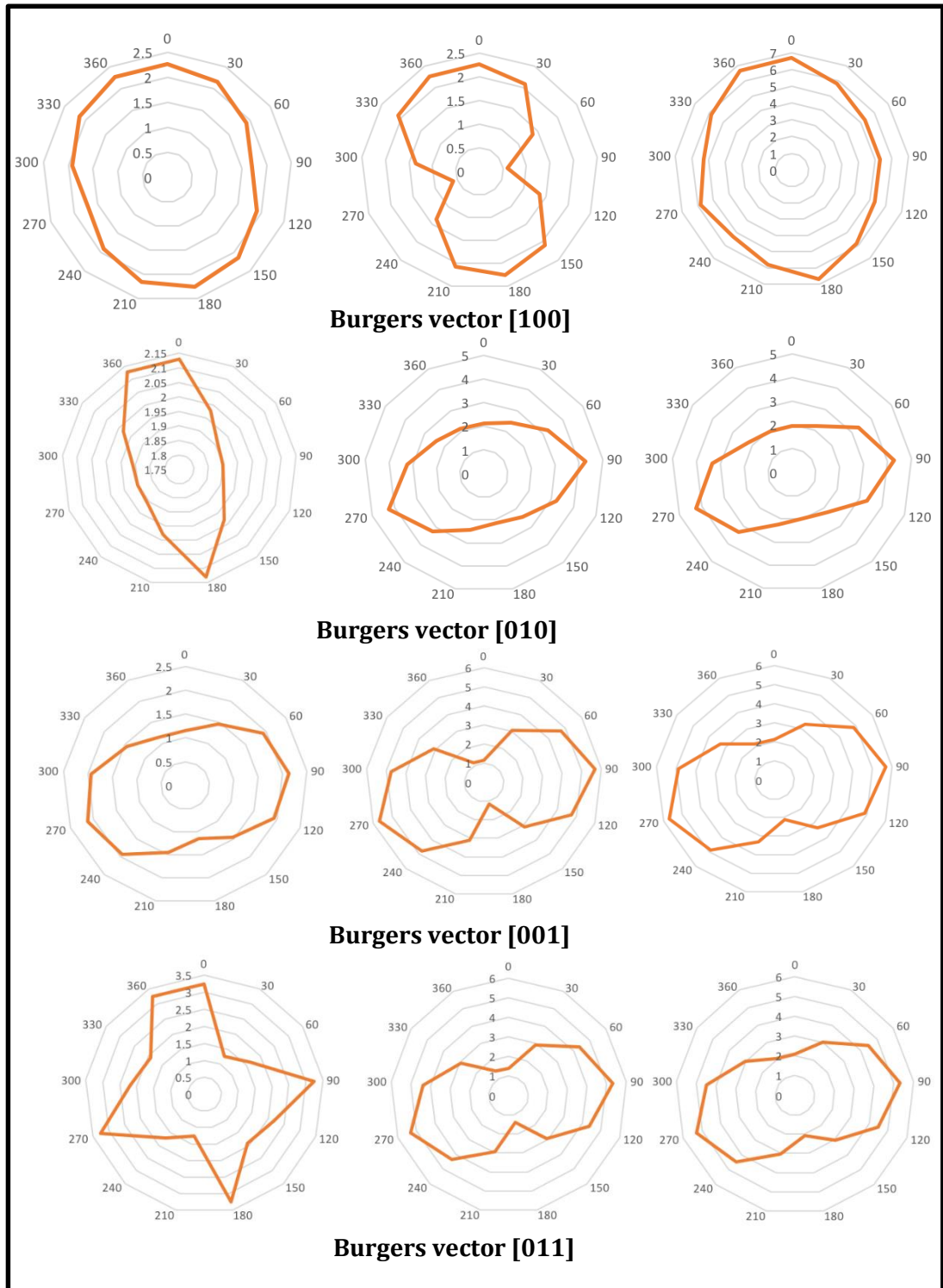
Burgers vector [011]

Figure 7-9 Polar plot representing the dislocation energy factor K for PTRI viewing through [100], [010] and [001] directions. The Burgers vector scanning angle were for [100] $\emptyset = 90$ $\theta = 90$ [010] $\emptyset = 0$ $\theta = 90$ and [001] $\emptyset = 90$ $\theta = 0$. Uniform distributions was observed for Burgers vector [100] and [010]

Burgers vector [110]

Burgers vector [111]
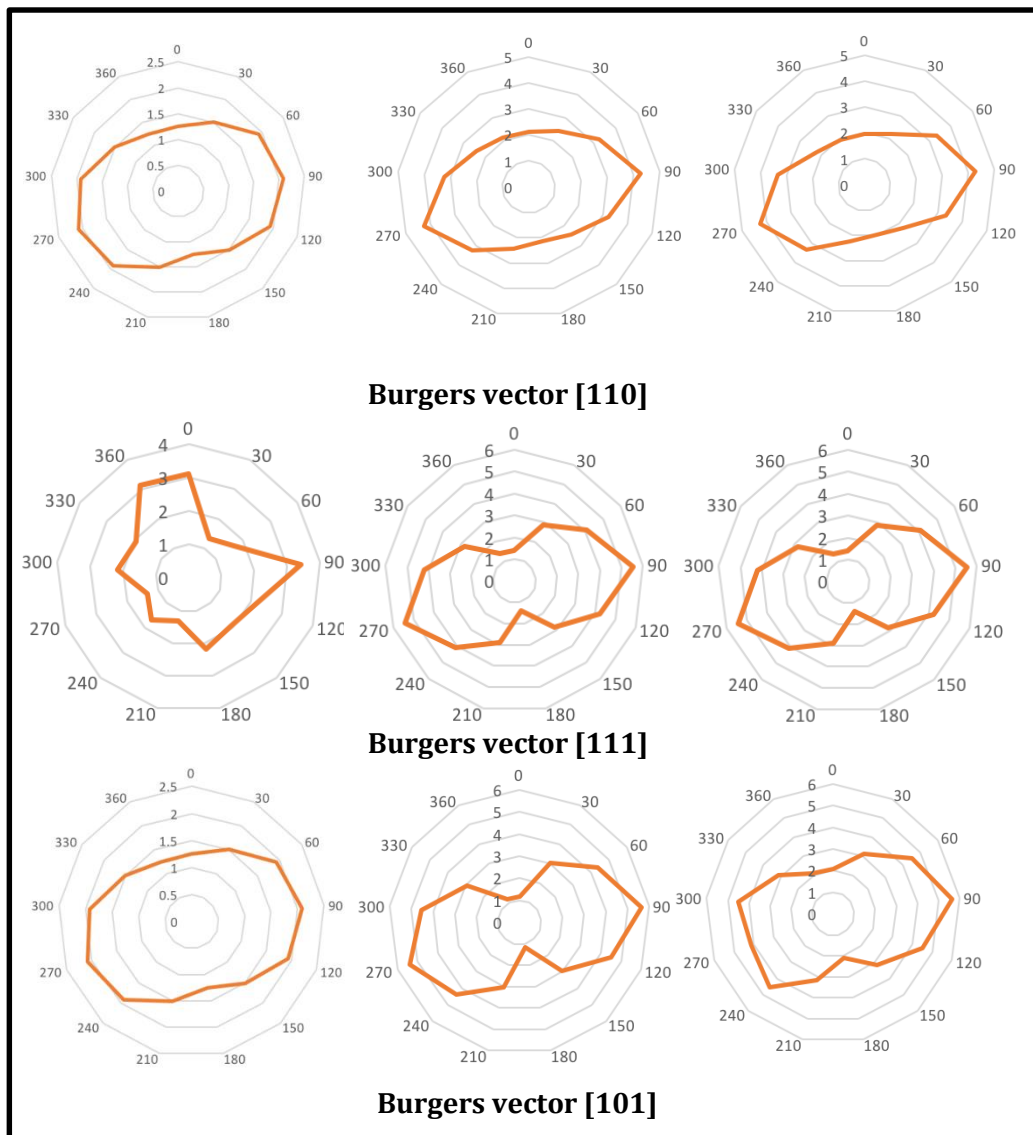
Burgers vector [101]

The energy factor for PTRI was seen to be distributed uniformly in all directions except for two plot namely Burgers vector [011] and [111] for dislocation line of [100] that were showing evidence variation as shown in the polar plot (Figure 7-9). For all of the Burgers vector, the K values were varying from approximately 2 to 7GPa. From the K continuum analysis, 13 potential edge and seven screw dislocations were characterised. The position angles for the dislocation line with respect to the Burgers vector were given in Table 7-31 together with the potential dislocations type. The stereographic projection to determine the angle for an edge is given in Appendix A5. It was obvious from Table 7-31 for [111] and [011] the dislocations energy was large therefore, these two directions were the least to displaced.

248

The final rank of Burgers vector was given in Table 7-32. Now, the rank of Burgers vector according to increasing dislocations energy is [100] < [010] < [110] < [001] < [101] < [011] < [111]. The primary Burgers vector for PTRI is [100].

Table 7-31 List of potential edge and screw dislocations in PTRI. The analysis produced 13 potential edge dislocations with regards to Burgers vector. It was evidence that the large magnitude of Burgers vector [011] and [111] resulted in a large dislocations energy

		PTRI				
BV	Dislocation line			K (GPa)	Kb²(eVm⁻¹)	Type
	LV	Angle ∅°	Angle θ°			
[100]	[100]	90	0	5.97	2.11	Screw
	[010]	0	90	1.69	0.60	Edge
	[001]	90	90	2.26	0.80	Edge
	[011]	59	90	1.01	0.36	Edge
[010]	[010]	0	90	1.96	2.19	Screw
	[001]	90	90	4.26	4.75	Edge
	[100]	180	90	1.96	2.19	Edge
	[102]	99	90	4.11	4.58	Edge
[001]	[001]	0	1	6.45	20.18	Screw
	[100]	270	90	5.67	6.66	Edge
[110]	[110]	45	90	6.45	9.48	Screw
	[001]	90	90	5.67	4.29	Edge
[101]	[101]	45	90	5.67	19.74	Screw
	[010]	0	90	2.09	7.28	Edge
	[001]	90	90	5.67	19.74	Edge
[011]	[011]	0	45	1.42	6.03	Screw
	[100]	180	90	2.07	8.79	Edge
[111]	[111]	45	45	3.43	15.78	Screw
	[-2-21]	90	88	4.82	22.18	Edge
	[-131]	124	89	4.21	19.37	Edge

Table 7-32 Preferred Burgers vector for a slip to take place based on two approaches, geometrical consideration, and line dislocation energy. The [100] was the shortest Burgers vector hence becomes the primary Burgers vector

Rank	Burgers vector (Geometrical)	Burgers vector (Dislocation)
1	[100]	[100]
2	[010]	[010]
3	[110]	[110]
4	[001]	[001]
5	[101]	[101]
6	[011]	[011]
7	[111]	[111]

7.5.3 Predicted mechanical behaviour for Paracetamol Trihydrates

The slip system of PTRI was identified as active because the calculated primary Burgers vector [100] was in the predicted slip plane (010). By having an active slip system, PTRI was predicted to undergo plastic deformation. However, the result need to be treated with cautious as the predicted slip plane was only having 57% ideal attributes. Nonetheless, the predicted active plastic deformation correlates well with the calculated elastic tensor in earlier section 6.3.2. It was suggested, the hydrogen bond provides strength and directionality for PTRI during deformation. The rank of Burgers vector showed no differences between the geometrical-based and dislocations energy relating to the K factors and the magnitudes.

7.6 Study of the mechanical properties of paracetamol salts: Paracetamol Hydrochloride Monohydrate

The Paracetamol Hydrochloride Monohydrate (PHM) system was reported to have 2MPa yield strength, that was double the FI [18] resulting to better tabletability. This section attempted to predict the behaviour of the PHM through molecular and crystallographic modelling. This section results hope to add the knowledge of the paracetamol salts which was scarce with only six structures identified at the moment in the CCDC database [19].

7.6.1 Paracetamol Hydrochloride Monohydrate slip plane characterisations

The lowest rugosity of PHM was 1.66 for (101), and the highest was 8.43 for (110) given in Table 7-33. The low rugosity for (101) showed the clearance for the plane to slip under stress. The lowest surface energy was 20.84mJ/mol for (111) plane, and the highest was 243.18mJ/mol for (100). For the hydrogen bond breaking, the results were given as yes, for breaking hydrogen bond or no for otherwise. The current state of the mechanical properties prediction program used for calculating the amount of the hydrogen bond breaking was under development for salts system. For PHM, all planes tested were breaking hydrogen bonds.

Table 7-33 PHM surface mechanical properties characteristics. The rugosity was between 1.66 and 8.43 and for surface energy between 20.84 and 243.18 mJ/m². The percent for hydrogen bond breaking was very low with values for all slip plane candidates below 1.0%

Plane	Rugosity	Surface energy (mJ/m²)	H-bond breaking
(100)	3.94	243.18	Yes
(010)	4.19	55.58	Yes
(001)	3.24	83.37	Yes
(110)	8.43	118.11	Yes
(101)	1.66	48.64	Yes
(011)	7.66	104.22	Yes
(111)	6.21	20.84	Yes

7.6.1.1   Interlocking representations

The interlocking representations for all slip plane candidates graphically (Figure 7-10), demonstrated that five planes were not interlocked that were (100), (010), (001), (011) and (101). The observations agree well with the qualitative observations in section 6.8.1
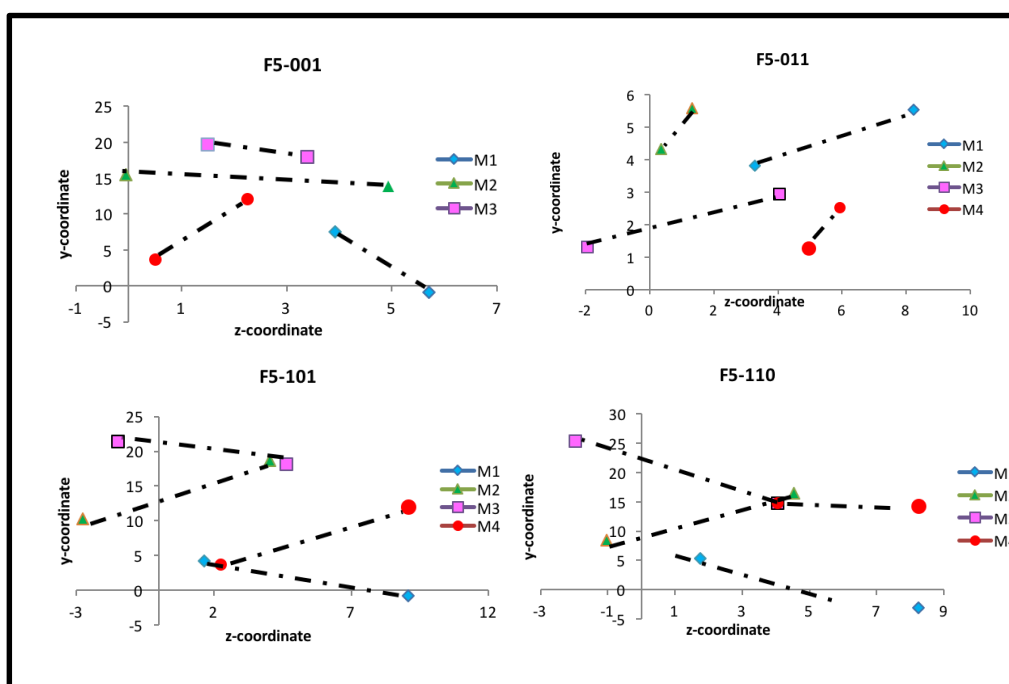
Figure 7-10 The interlocking representations for PHM. There were five planes that were not interlocked. From the numbers of non-interlocked planes, PHM was suggested to have non-corrugated crystal packing. The plot was the projection of molecules in a unit cell onto plane normal

F5-100 — **F5-010** — **F5-111**
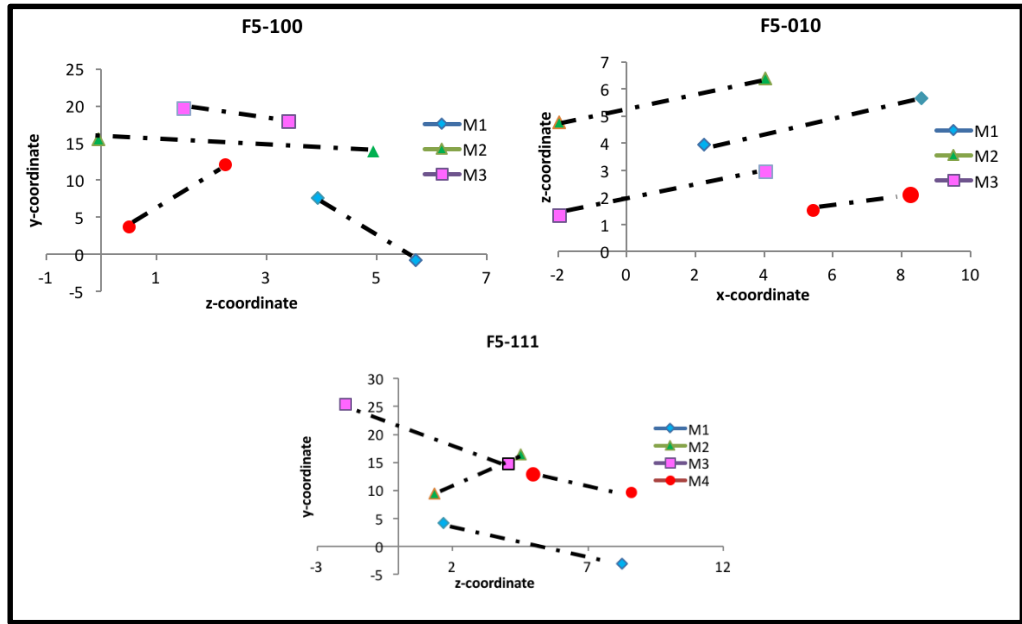
7.6.1.2 Multiple attribute decision-making calculations (MADM)

The multiple dimensions of the surface attributes calculated in prior subsections were compared as normalised values and presented in Table 7-34. Now, the values were in the same dimension hence it can be compared fairly. Values were given in the range between 0 and 1. From Table 7-34, it can be seen that the surface energy had the highest value with 0.78 while the interlock was the smallest. Table 7-35 provide the weighted normalised values to rank the planes according to the importance of the attributes.

Table 7-34 Normalised values for all the attributes making it in the same dimension between 0 and 1.0

Attributes/ Alternatives	PHM			
	Surface E	Rugosity	Interlock of slip planes	H-bond breaking
(100)	0.78	0.27	0.00	0.38
(010)	0.18	0.29	0.00	0.38
(001)	0.27	0.22	0.00	0.38
(110)	0.38	0.58	0.71	0.38
(101)	0.16	0.11	0.00	0.38
(011)	0.33	0.52	0.00	0.38
(111)	0.07	0.42	0.71	0.38

Table 7-35 Weighted-normalised attributes with respect to the alternatives to give the best and worst values in relation to the ideal behaviour of a slip plane

Attributes/ Alternatives	PHM			
	Surface E	Rugosity	Interlock of slip planes	H-bond breaking
100	0.20	0.07	0.00	0.09
010	0.04	0.07	0.00	0.09
001	0.07	0.06	0.00	0.09
110	0.09	0.14	0.18	0.09
101	0.04	0.03	0.00	0.09
011	0.08	0.13	0.00	0.09
111	0.02	0.11	0.18	0.09

The positive separation analysis in Table 7-36 showed clearly that (101) plane was closest to the ideal condition with smallest values, 0.096 and largest negative separation of 0.266. The farthest from the ideal slip plane conditions was (110). The ratio between the negative separation to the total (positive and negative) represented the final rank of potential slip plane and given in Table 7-37. (101) the plane was matching 73% of ideal slip plane attributes.

Table 7-36 Positive and negative separation values of attributes with regards to achieving the optimum condition for slip plane. These separation analyses were carried out with respect to slip plane candidates

Attributes/ Alternatives	PHM (positive separation)					
	Surface E	Rugosity	Interlock of planes	H-bond breaking	Squared of sum	Positive separation
100	3.08E-02	1.39E-03	0.00E+00	8.90E-03	4.11E-02	2.03E-01
010	6.08E-04	1.72E-03	0.00E+00	8.90E-03	1.12E-02	1.06E-01
001	2.21E-03	6.40E-04	0.00E+00	8.90E-03	1.17E-02	1.08E-01
110	5.61E-03	1.30E-02	3.14E-02	8.90E-03	5.89E-02	2.43E-01
101	3.64E-04	2.80E-06	0.00E+00	8.90E-03	9.27E-03	9.63E-02
011	4.06E-03	1.01E-02	0.00E+00	8.90E-03	2.31E-02	1.52E-01
111	1.06E-05	5.77E-03	3.14E-02	8.90E-03	4.61E-02	2.15E-01
Attributes/ Alternatives	PHM (negative separation)					
	Surface E	Rugosity	Interlock of planes	H-bond breaking	Squared of sum	Negative separation
100	2.10E-05	5.29E-03	3.24E-02	1.88E-05	3.77E-02	1.94E-01
010	2.41E-02	4.69E-03	3.24E-02	1.88E-05	6.12E-02	2.47E-01
001	1.77E-02	7.18E-03	3.24E-02	1.88E-05	5.73E-02	2.39E-01
110	1.10E-02	1.49E-05	7.26E-06	1.88E-05	1.11E-02	1.05E-01
101	2.59E-02	1.25E-02	3.24E-02	1.88E-05	7.08E-02	2.66E-01
011	1.35E-02	8.62E-05	3.24E-02	1.88E-05	4.60E-02	2.15E-01
111	3.36E-02	1.16E-03	7.26E-06	1.88E-05	3.48E-02	1.86E-01

Table 7-37 Rank for preferred slip plane for PHM. Showing the most probable is for (101) with 73% of the slip plane ideal condition

	PHM	
Rank	Alternatives	% Optimum
1	(101)	73
2	(010)	70
3	(001)	69
4	(011)	59
5	(100)	50
6	(111)	46
7	(110)	30

From the slip plane characterisations, PHM seems to have multiple planes that potentially can slip. The top three planes were only having small difference amongst them. The identification of the direction for slip represented by the Burgers vector will be presented next.

7.6.2 Paracetamol Hydrochloride Monohydrate Burgers vector calculations

PHM is a primitive crystal, therefore, it will have Burgers vector without any halving. The result in this subsection will be presented in the same manner as the previous four subsections (7.2 to 7.5).

7.6.2.1 Geometrical-based Burgers vector

The list of geometrical based Burgers vector was presented in Table 7-38. The shortest magnitude was 6.25Å in the direction of [100]. The largest Burgers vector being considered was [111] with 23.90Å. The final list of Burgers vector for further study were seven and was presented in Table 7-38. In decreasing order of significance, the Burgers vector was [100]> [001]> [101]> [010]> [110]> [011] > [111].

7.6.2.2 Dislocations influence on Burgers vector

The dislocation energy coefficients (K) in Table 7-38 demonstrated the anisotropic properties of the dislocations based on the three-dimensional directions, [100], [010] and [001]. The smallest K value was 1.91GPa for [001] in the dislocation line direction of [001] giving a dislocation energy of $0.60 evnm^{-1}$. The largest K value given in Table 7-38 was 8.46GPa for Burgers vector [010] and [110] with line dislocation of [001]. Range of dislocations energy for each Burgers vector were also given in Table 7-38. These calculated

values reflect that PHM was having a large variation of dislocation energy. The representations for dislocation energy factor K, were illustrated in Figure 7-11.

Table 7-38 Calculated Burgers vector based on geometrical Burgers vector calculated by considering crystal geometry only. The smallest magnitude of Burgers vector was 6.25Å in the direction of [100]. Dislocation energy coefficient (K) and resulting line dislocation energy was showing the dependency towards Burgers vector magnitude. Type of dislocation was predicted based on the angle between dislocation line and Burgers vector. The final line dislocation energy seems to be increasing as the Burgers vector magnitude increases

| BV | Magnitude BV(Å) | Magnitude BV^2(Å)^2 | K(GPa) | | | $K(BV)^2$ |
			[100]	[010]	[001]	$(evnm^{-1})$
[100]	6.25	39.0625	2.95	3.57	8.05	0.72-1.96
[001]	7.07	49.9849	4.04	3.25	1.91	0.60-1.26
[101]	9.44	89.1136	2.99	3.22	5.33	1.66-2.97
[010]	21.96	482.2416	4.43	3.62	8.46	10.91-25.49
[110]	22.83	521.2089	4.42	2.76	8.46	8.98-27.55
[011]	23.07	532.2249	4.42	3.43	8.39	11.40-27.89
[111]	23.9	571.21	4.41	2.58	8.42	9.21-30.04

Burgers vector [110]
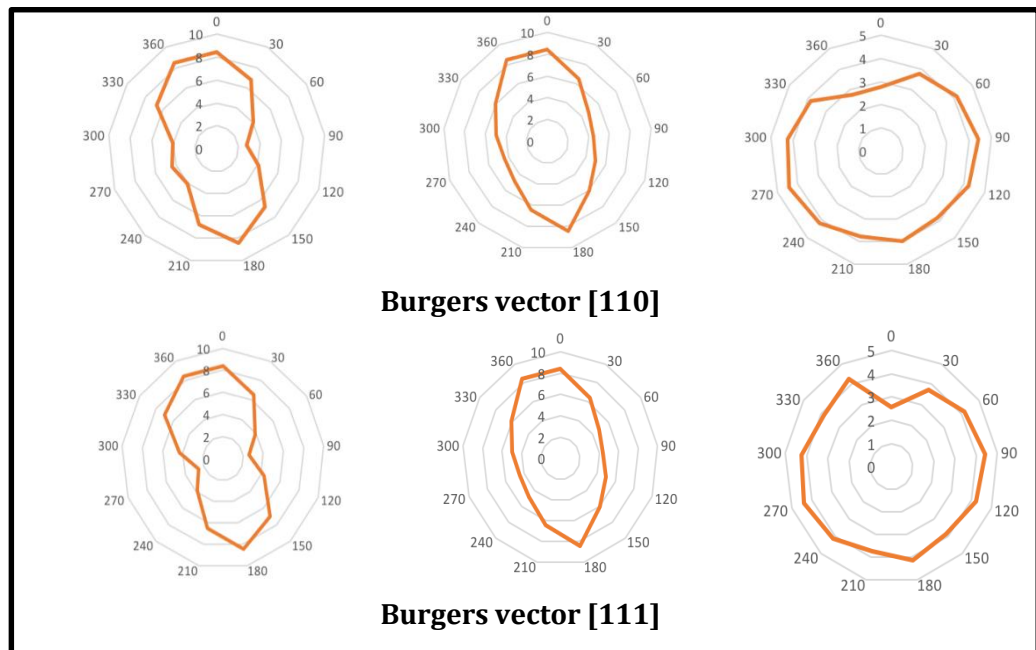
Burgers vector [111]

Figure 7-11 Polar plot representing the dislocation energy factor K for PHM viewing through [100], [010] and [001] directions. The Burgers vector scanning angle were for [100] $\emptyset = 90\ \theta = 90$ [010] $\emptyset = 0\ \theta = 90$ and [001] $\emptyset = 90\ \theta = 0$. Uniform distributions was observed for Burgers vector [100] and [010]

Burgers vector [100]

Burgers vector [010]

Burgers vector [001]

Burgers vector [011]
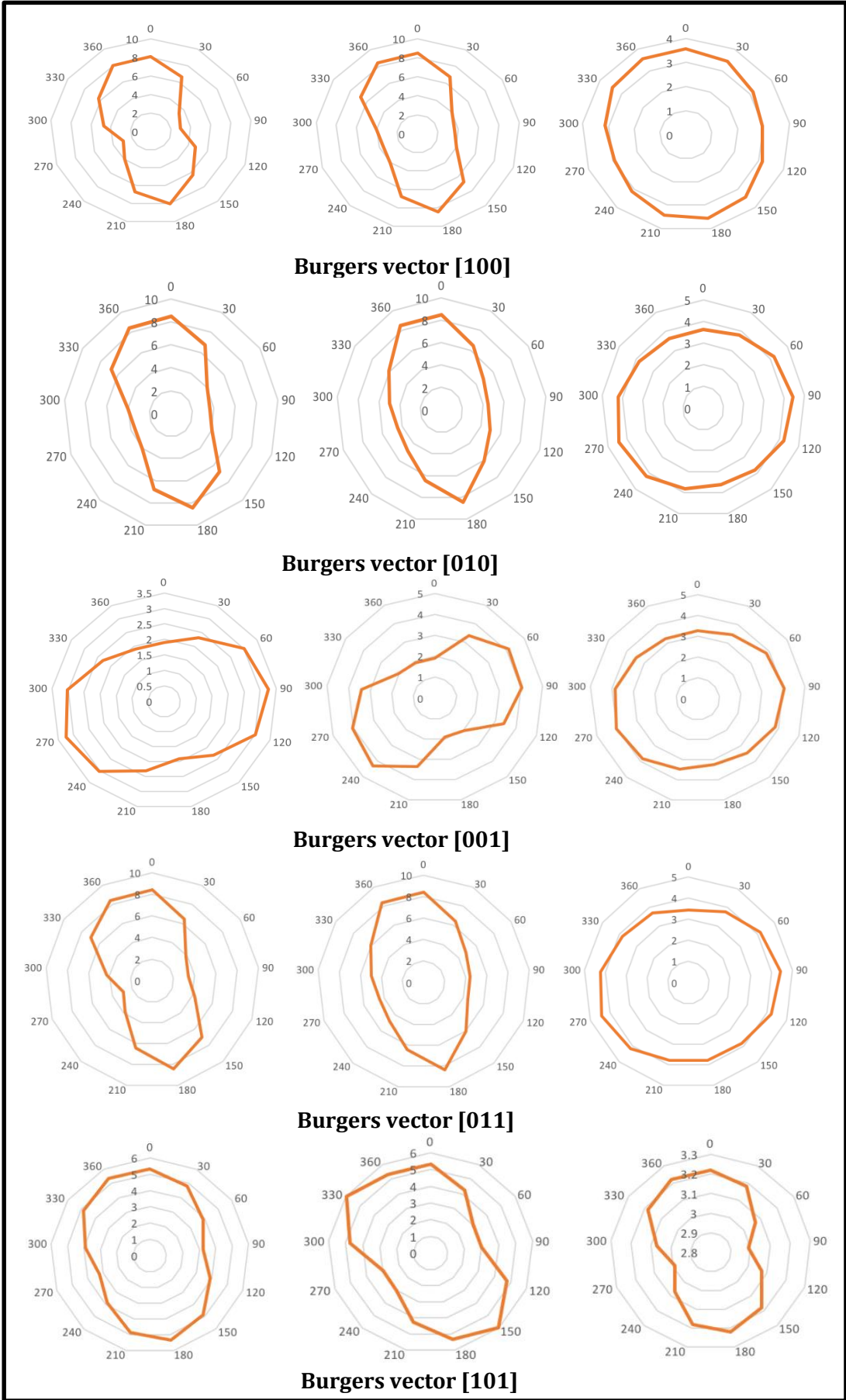
Burgers vector [101]

The energy factor for PHM was seen to be distributed uniformly in all directions as seen in Figure 7-11. For all of the Burgers vector, the K values were varying from approximately 2 to 9GPa. From the K continuum analysis, 13 potential edge and seven screw dislocations were characterised. The position angles for the dislocation line with respect to the Burgers vector were given in Table 7-39 together with the potential dislocations type. It was obvious from Table 7-39 for [111] and [011] the dislocations energy were large . Therefore, these two directions were the least to displaced.

The final rank of Burgers vector was given in Table 7-40. Now, the rank of Burgers vector according to increasing dislocations energy was [001] < [100] < [101] < [110] < [111] < [010] < [011]. The primary Burgers vector for PHM is [001].

Table 7-39 List of potential edge and screw dislocations in PHM. The analysis produced 14 potential edge dislocations with regards to Burgers vector. It was evidence that the large magnitude of Burgers vector [011] and [111] resulted in a large dislocations energy

	PHM					
BV	Dislocation line			K (GPa)	$Kb^2(eVm^{-1})$	Type
	LV	Angle $\emptyset°$	Angle $\theta°$			
[100]	[100]	90	0	2.95	0.72	Screw
	[010]	0	90	3.57	0.87	Edge
	[01-1]	343	88	3.56	0.87	Edge
	[02-1]	350	89	3.56	0.87	Edge
[010]	[010]	0	90	3.62	10.91	Screw
	[-100]	7	90	3.64	10.97	Edge
	[001]	180	90	8.46	25.49	Edge
	[-102]	66	90	4.28	12.89	Edge
	[-101]	50	90	4.07	12.26	Edge
[001]	[001]	0	1	1.91	0.60	Screw
	[010]	270	90	3.25	1.01	Edge
	[-110]	15	88	3.31	1.03	Edge
[011]	[011]	0	45	4.89	16.26	Screw
	[-100]	6	88	3.6	11.97	Edge
[101]	[101]	45	90	3.22	1.79	Screw
	[-111]	23	87	3.16	1.76	Edge
	[-212]	41	86	3.03	1.69	Edge
[110]	[110]	90	45	4.42	14.39	Screw
	[00-1]	270	88	4.45	14.49	Edge
[111]	[111]	45	45	4.41	15.74	Screw
	[-101]	52	88	3.98	14.20	Edge

Table 7-40 Preferred Burgers vector for a slip to take place based on two approaches, geometrical consideration, and line dislocation energy. The [001] was the shortest Burgers vector following dislocation energy, hence becomes the primary Burgers vector

Rank	Burgers vector (Geometrical)	Burgers vector (Dislocation)
1	[100]	[001]
2	[001]	[100]
3	[101]	[101]
4	[010]	[110]
5	[110]	[111]
6	[011]	[010]
7	[111]	[011]

7.6.3 Predicted mechanical behaviour for Paracetamol Hydrochloride Monohydrate

The slip system of PHM was identified as inactive because the calculated primary Burgers vector [001] was not in the predicted slip plane (101). The strongest interaction in PHM was in the direction of [010] therefore making the direction in-plane. The in-plane interaction provides the driving force to pull the (101) plane in the same direction of the hydrogen bond. The PHM was predicted to undergo cleaving. Hence, potentially the better tabletability strength poses by PHM relates to the cleaving behaviour.

7.7 Conclusions

Arriving from the mechanical properties prediction of all five paracetamol solid forms it was observed that the diversity of solid forms contributed to the fracture, cleavage or plastic behaviour as summarised in Table 7-41. It was learnt that to predict the mechanical properties of molecular system pose quite a challenge as the intermolecular interactions and types component consisted in the crystal have to impact on the crystal packing. Hence, the different molecular system will behave differently. From the prediction of mechanical properties, the two main factors governing the predictions were intermolecular interactions and the dislocation energy. The reason was, the intermolecular interactions may have changed the crystal packing arrangements hence relate to the rugosity, interlocking and surface energetics which were the criteria for characterising ideal slip plane. Moreover, the amount of energy to break the hydrogen bonds that formed within crystals indicates barrier for slip plane.

The best example to show the effects of intermolecular interactions on the prediction was PTRI. PTRI has an extensive network of hydrogen bond that reduce the ideality of the

potential slip plane. For PTRI, though, it may undergo plastic deformation, the predicted preferred slip plane (010) only behaving with 57% of ideal attributes. This was similar to the FI slip plane properties that fractured. However, the presence of the extensive network of hydrogen bond in PTRI seems to be responsible towards its' flat-stacking crystal packing arrangements that promote slip. Similarly, in the PHM the dipole-dipole moment together with the hydrogen interactions contribute to the rearrangement of the molecules within the crystal packing.

Other than the intermolecular interactions, dislocations energy was identified to significantly change the slip directions for a system with unit cell components that were far apart in magnitude. This was obvious for PHM, whereby the [010] was approximately three times larger than the [100] and [001]. Because of the great difference in the [010] direction, the rank of preferred Burgers vector was swapped considerably when classifying based on dislocation energy. From the PTRI and PHM, the impact of intermolecular interactions and dislocation energy were evidence. In short, in characterising the slip systems comprising slip plane and direction there is no one component which was superior to the other, as the slip plane may have less ideality but it has an active slip with the primary Burgers vector.

Table 7-41 Summary for the prediction of mechanical properties of the five solid forms of paracetamol. For the elastic tensor, the lowest of axial and diagonal components were given. Similarly, the dislocation energy, only the smallest was provided. The predicted mechanical behaviour given showed probable fracture, plastic or cleaving

Solid forms	Dislocation energy ($eVnm^{-1}$)	% as slip plane	Predicted behaviour
FI	1.52	58	Fracture
FII	0.68	84	Plastic/Cleaving
PTHEO	1.96	77	Cleaving
PTRI	0.60	57	Plastic
PHM	0.60	73	Cleaving

The stiffness of FI was related to its' corrugated crystal packing. The corrugated structure increased the rugosity and interlock of planes that limit the numbers of potential slip systems. The Burgers vector rank, between the geometrical and dislocation-based, were not showing any different. This was suggested to be due to the magnitude of each geometrical Burgers vector, and the K values were marginal difference. The FI was predicted to fracture because of its corrugated structure the inactive slip system.

Conversely, the crystal packing of FII was seen to be flat layers stacking along the [010] direction. This particular flat plane was identified as (200) the ideal slip plane for FII. For

FII, the preferred slip plane was obvious by having 84% ideal attributes compared to the least to slip that only have 18%. Similar to FI, the Burgers vector rank, changed slightly. FII was predicted to undergo cleaving at first instance and plastic deformation later. This mechanical behaviour coincides with compaction data obtained by Joiris et.al. [17] that observed cleaving at low pressure and plastic behaviour at high pressure.

The molecular packing of PTHEO was creating wavy sheets of planes with distinct diagonal layers seen in the [010] direction. The preferred slip plane was recognised as (101). In this instance, it was obvious that PTHEO preferred plane be (101) with 77% ideal attributes that were far apart from the second preferred (001) with 50%. While the least probable to be a slip plane was (10-1) with 4.7% only. The Burgers vector showed the influence of K values because the unit cell components were in similar magnitude. The Burgers vector rank was rearranged substantially. The PTHEO was predicted to undergo cleaving as the preferred slip plane was not active with the primary Burgers vector. Likewise, for PTRI and PHM, the predicted mechanical behaviour was plastic and cleaving with behaviour as described in early of this section.

In brief, the proposed prediction model effectively characterised the mechanical behaviour for the five selected solid forms of paracetamol. However, there is still need to have the experimental validation for the PTRI as there were no experimental measurements to validate the prediction. For FII and PHM, there were literature results for compaction for comparison. The predicted mechanical behaviour for FI and PTHEO will be assessed in the next chapter.

References

[1]   S. Datta, D.J. Grant, Crystal structures of drugs: advances in determination, prediction and engineering, Nature Reviews Drug Discovery. 3 (2004) 42–57.

[2]   P. Di Martino, A. Guyot-Hermann, P. Conflant, M. Drache, J. Guyot, A new pure paracetamol for direct compression: the orthorhombic form, International Journal of Pharmaceutics. 128 (1996) 1–8.

[3]   M. Haisa, S. Kashino, H. Maeda, The orthorhombic form of p-hydroxyacetanilide, Acta Crystallographica Section B: Structural Crystallography and Crystal Chemistry. 30 (1974) 2510–2512.

[4]   E. Boldyreva, High-pressure polymorphs of molecular solids: when are they formed, and when are they not? Some examples of the role of kinetic control, Crystal Growth & Design. 7 (2007) 1662–1668.

[5]   S.L. Mayo, B.D. Olafson, W.A. Goddard, DREIDING: a generic force field for molecular simulations, The Journal of Physical Chemistry. 94 (1990) 8897–8909. doi:10.1021/j100389a010.

[6]   R. Roberts, The elasticity, ductility and fracture toughness of pharmaceutical powders., 1991.

[7]   G.M. Day, S.L. Price, M. Leslie, Elastic constant calculations for molecular organic crystals, Crystal Growth & Design. 1 (2001) 13–27.

[8]   Y.V. Nelyubina, I.V. Glukhov, M.Y. Antipin, K.A. Lyssenko, "Higher density does not mean higher stability" mystery of paracetamol finally unraveled, Chemical Communications. 46 (2010) 3469–3471.

[9]   H.A. Garekani, J.L. Ford, M.H. Rubinstein, A.R. Rajabi-Siahboomi, Highly compressible paracetamol: I: crystallization and characterization, International Journal of Pharmaceutics. 208 (2000) 87–99.

[10] G. Perlovich, T.V. Volkova, A. Bauer-Brandl, Polymorphism of paracetamol, Journal of Thermal Analysis and Calorimetry. 89 (2007) 767–774.

[11] I. Rosbottom, K. Roberts, R. Docherty, The solid state, surface and morphological properties of p-aminobenzoic acid in terms of the strength and directionality of its intermolecular synthons, CrystEngComm. 17 (2015) 5768–5788.

[12] J.Y. Heng, D.R. Williams, Wettability of paracetamol polymorphic forms I and II, Langmuir. 22 (2006) 6905–6909.

[13] Y. Feng, D.J.W. Grant, Influence of crystal structure on the compaction properties of n-alkyl 4-hydroxybenzoate esters (parabens), Pharmaceutical Research. 23 (2006) 1608–1616.

[14] M.H. Shariare, F.J.J. Leusen, M. de Matas, P. York, J. Anwar, Prediction of the Mechanical Behaviour of Crystalline Solids, Pharmaceutical Research. (2011) 1–13.

[15] G. Nichols, C.S. Frampton, Physicochemical characterization of the orthorhombic polymorph of paracetamol crystallized from solution, Journal of Pharmaceutical Sciences. 87 (1998) 684–693.

[16] J.Y. Heng, A. Bismarck, A.F. Lee, K. Wilson, D.R. Williams, Anisotropic surface energetics and wettability of macroscopic form I paracetamol crystals, Langmuir. 22 (2006) 2760–2769.

[17] E. Joiris, P. Di Martino, C. Berneron, A.-M. Guyot-Hermann, J.-C. Guyot, Compression behavior of orthorhombic paracetamol, Pharmaceutical Research. 15 (1998) 1122–1130.

[18] S.R. Perumalla, L. Shi, C.C. Sun, Ionized form of acetaminophen with improved compaction properties, CrystEngComm. (2012).

[19] D. Trzybiński, S. Domagala, M. Kubsik, K. Woźniak, Solid-State Analysis of Monohydrated Halide Salts of Paracetamol,, Crystal Growth & Design,. (n.d.).

[20] S.Finnie, K.V.R.Prasad, D.B.Sheen and J.N.Sherwood, Microhardness and dislocation identification studies on paracetamol single crystals, Pharmaceutical Research, 18 (2001). 674-681

[21] A.Alhalaweh, W.Kaialy, G.Buckton, H.Gill, A.Nokhodchi and S.P.Velaga, Theophylline cocrystals prepared by spray drying: physicochemical properties and aerosolization performance, AAPS Pharmscitech, 14 (2013). 265-276

Chapter Eight

Influence of Solid Form Properties on the Tabletability of Microcrystals of Paracetamol

This chapter presents the empirical measurements of powder flowability, compactibility and particle size distribution. These results were compared with the computational predictions in earlier chapters

Chapter 8. Influence of Solid Form Properties on the Tabletability of Microcrystals of Paracetamol

8.1 Introduction

The variation of crystal habit and solid forms impact significantly towards powder tabletting process [1]. The common crystal habits are diamond, tubular, needle and plate-like. Diverse solid forms constructed with different crystallographic pattern results in different stability also compressibility. Often, the crystallographic pattern can be observed as corrugated or flat layer [3]. These types of the pattern have been described previously by Summers et.al (1976) [4] are related to the ability of the powder to withstand pressure during tabletting process.

The aim of this chapter is to validate the predicted mechanical properties of the five solid forms of paracetamol through experimental studies. To validate, the particulates properties in solid pharmaceutical dosage during the manufacturing process particularly flowability and compressibility were evaluated. As part of this industrial research collaboration, few components of this chapter were carried out at Pfizer Ltd that is the compaction and rings shear tests, which are not available at the University of Leeds. Two summer students were also assisting the attempts for crystallising the metastable forms and co-crystals.

The flow diagram in Figure 8-1 represents the general layout of this chapter. This chapter consists of two case studies, first was looking into the effects of solvent and second was evaluating the influence of different solid forms on the tabletability of the microcrystals. Following this theme, initially, the results for the characterisation of microcrystals was presented that followed by the particle size distributions and habit appreciations. Subsequently, the compaction and flow measurements were presented. Finally, the conclusions were drawn according to the results obtained from the experimental observations.
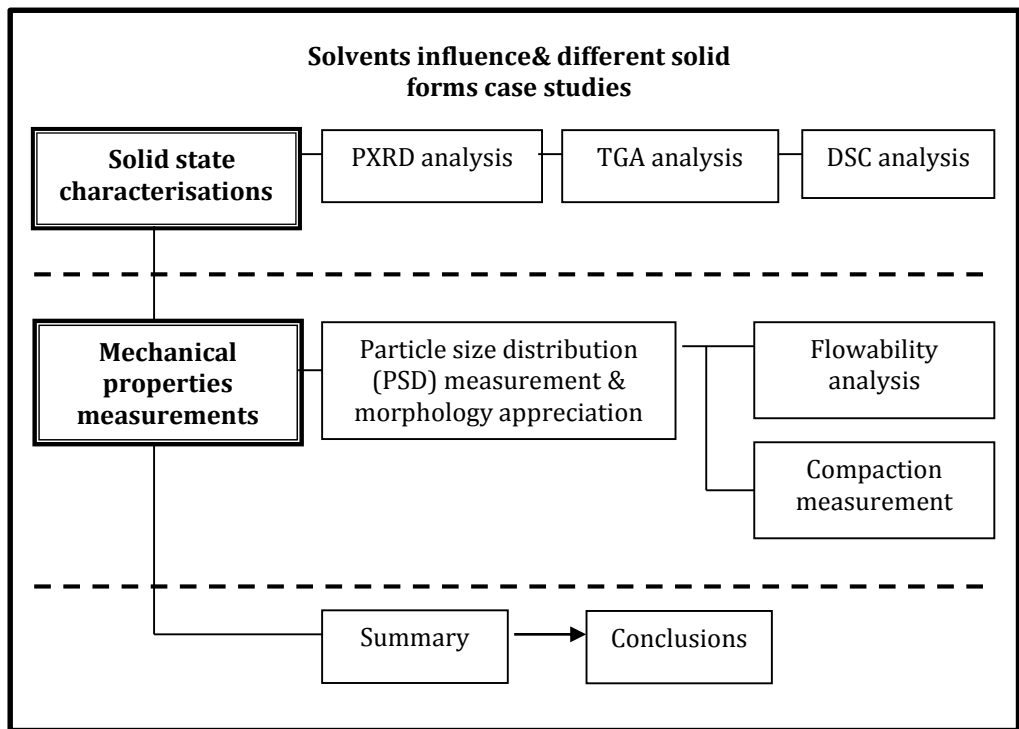
Figure 8-1 The flow for this experimental result chapter follows that, the identification of structure, the thermal analysis, the particle size distribution measurements, flowability analysis and finally compaction measurement. Conclusions was drawn from both the solid state and mechanical properties measurements

8.2 Effects of solvent on the tabletability

Initially, three analytical tests were carried out to ensure that microcrystals are the stable form of paracetamol (FI). The tests include X-ray powder diffraction (PXRD), differential scanning calorimetry (DSC) and thermogravimetric analysis (TGA). Following these analyses, the measurements of mechanical property were presented.

8.2.1 Powder X-ray diffraction (PXRD) pattern

The PXRD evaluation provides a fingerprint for crystal system that is useful for crystal structure determination and identification. The FI PXRD reference pattern (from CSD[1]) was labelled as (FI-simulated) given in Figure 8-2. Few small peaks were missing in the raw sample pattern but did not result in phase change and also in the allowable range. All the main peaks of the reference pattern were detected, confirming that the raw sample used was the same stable paracetamol polymorph (FI).
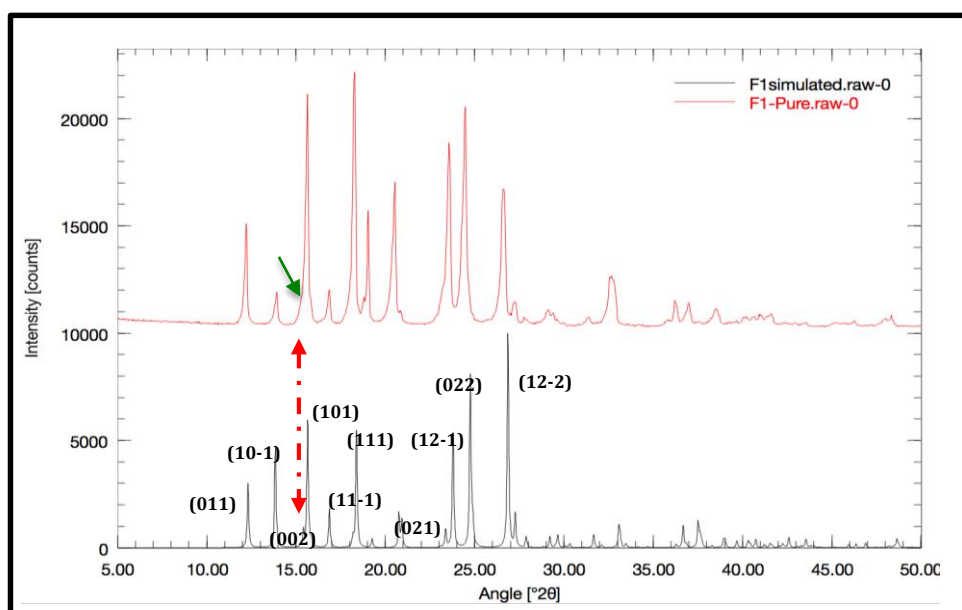
Figure 8-2 PXRD pattern of the raw materials and the simulated pattern obtained from the CSD. Diffracted pattern confirms that the starting material was the stable form of paracetamol

Similarly, for the crystallised FI in FI-MeOH (FI-MeOH) showed few peak differences compared to the simulated pattern as presented in Figure 8-3. It was observed that at 23.6° for FI-Ace the peak seems to be weak compared to the simulated. A small shoulder peak at 26.6° was seen in both FI-MeOH and FI-Ace and was not in the simulated pattern. It was perceived as impurities caused peak broadening. The peaks were also shifted by 0.2° that was related to the difference of experiments temperature; this study was at room temperature, and the reference was at -173℃. There was a new peak observed at 37.1°for the FI-Ace. The extra peak was seen to match a peak in the FII pattern. However, other main peaks of FI-Ace are matching the FI pattern. Hence the additional peak was proposed to be impurities and not solid state transformation. Slight differences may have related to the way samples were ground and packed on the sample plate for analysis. The samples may tend to be at preferred orientation. Besides that, the slight difference between the FI-MeOH and FI-Ace samples may well be caused by the solvent effects that roughened the surfaces of crystals. Regardless of the little peak differences, all the major peaks of the simulated pattern were met by both samples. Therefore, confirms that both crystallised batches were the stable polymorphic forms.
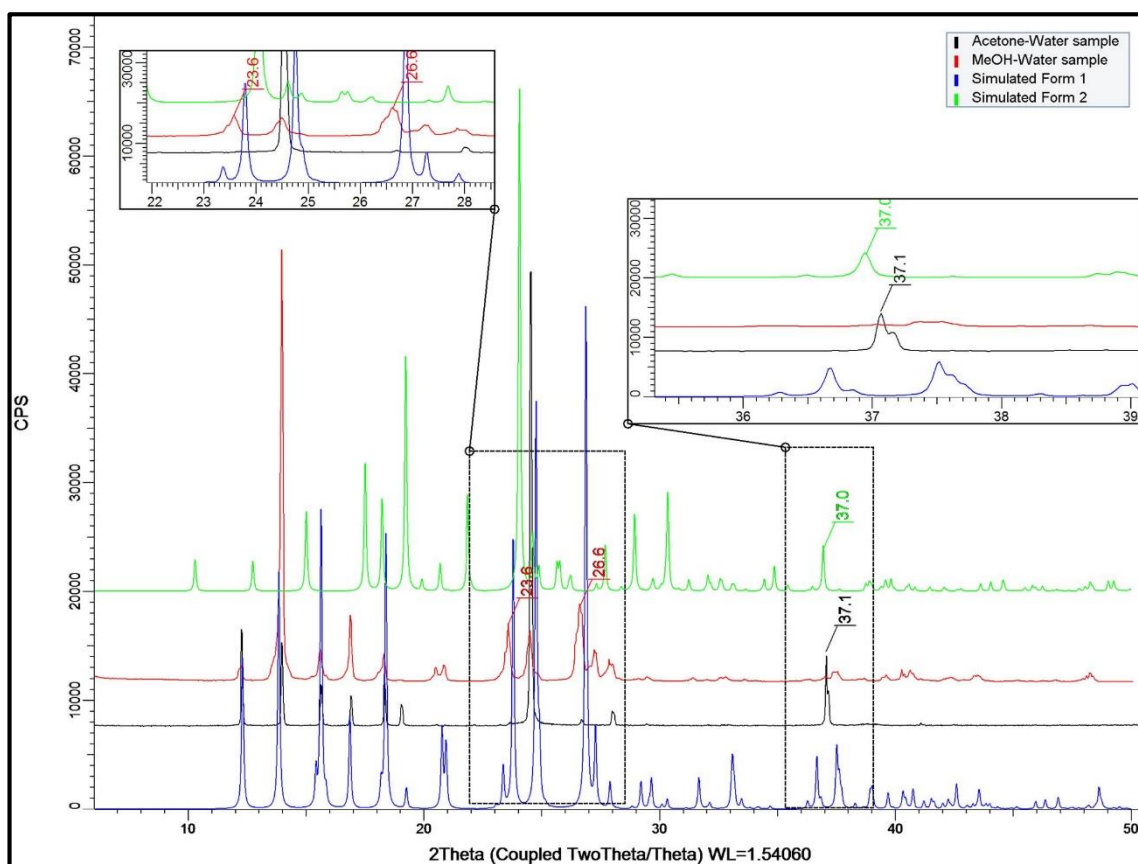
Figure 8-3 PXRD pattern comparison of the paracetamol stable (FI) and metastable (F2) simulated, FI-MeOH and FI-Ace crystallised samples. Few allowable peaks were observed that does not involve solid state transformation

8.2.2 Thermal analysis (differential scanning calorimetry and thermogravimetric analysis)

The differential scanning calorimetry (DSC) thermograms in Figure 8-4 represent the FI-MeOH and FI-Ace thermal analysis. The FI-Ace was observed to have one distinct endothermic peak at 171.74°C with melting enthalpy of 180.02J/g (27.21kJ/mol). The enthalpy was agreeing well with the value of literature which was obtained using DSC, 185J/g (27.96) [5]. The endothermic peak signifies the melting of pure FI. Likewise, the thermogravimetric analysis (TGA) showed a negligible weight loss of 0.02% at 140.06°C verifying that the FI-Ace sample was purely FI.
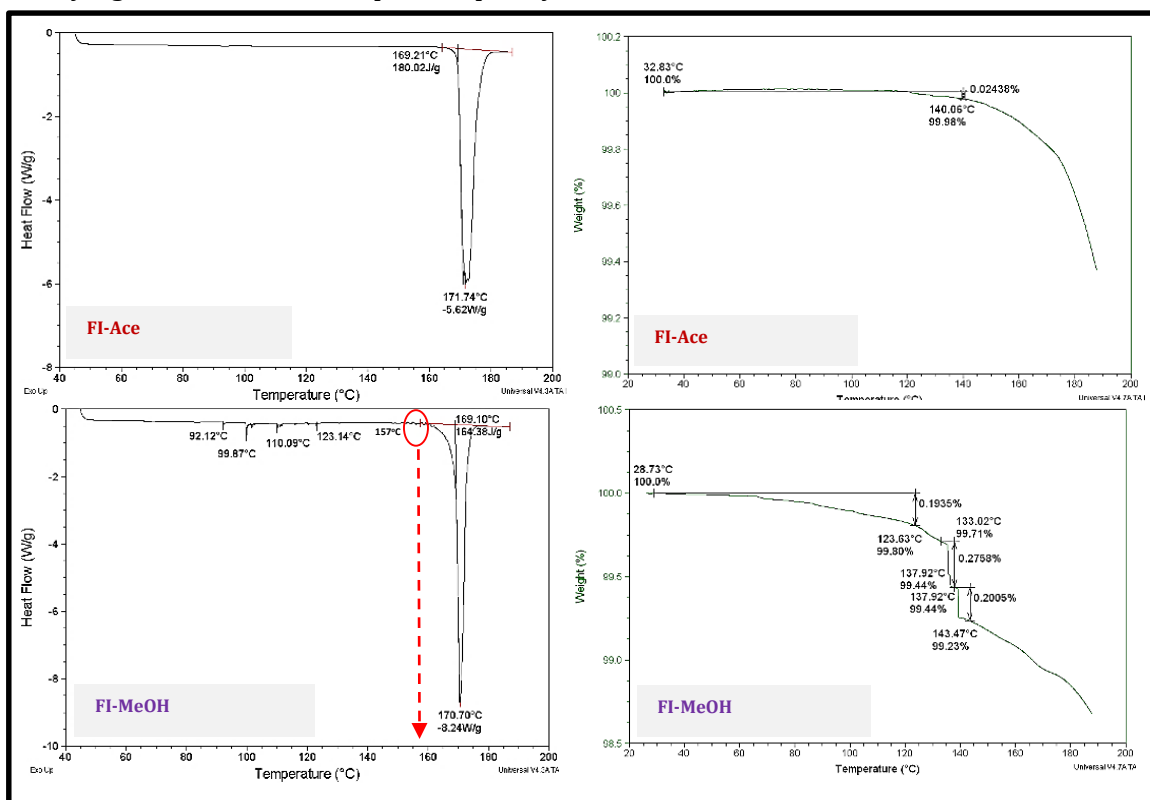
Figure 8-4 The DSC thermogram and TGA plot for two samples. The FI-Ace sample was showing single endothermic peak and agreeing well with the TGA result of only 0.024% weight loss. The FI-MeOH sample showed one major peak and four weak peak between 90-130ºC. Similar observation can be seen from the TGA plot displaying significant drop at two point, between 130-150ºC

In contrary, the FI-MeOH thermograms' showed five endothermic peaks between 90°C to 170°C, with one that was significant at 170.70°C. The peak observed at 92.12°C, and 99.87°C was the evaporation of the MeOH entrapped in the samples during crystallisation. The peak at 110.09°C was believed to be the conversion of the metastable form III (F3) to form II (FII). Because the value obtained in this study was well within the range of previously attained transition temperature by DSC (120°C)[6] and PXRD (102°C) [7]. The next peak at 123.14°C was the transition of FII to the stable FI. A weak peak observed at 157°C was the melting of

non-converted FII [5]. Nevertheless, the PXRD did not detect the different transitions distinguished in the DSC thermogram. Therefore, it was proposed that the variations in the DSC results were purely influenced by the temperature during the measurements that may induce the formation of the metastable forms, but then converted back to FI. This occurrence showed the sensitivity of the FI-MeOH towards temperature. The transition events observed in the DSC thermogram was further reflected in the TGA plot. There was weight loss at two temperatures namely, 137.92 and 143.47^{o}C. The two weight loss may well be affected by the solvent evaporation. Nonetheless, it is worthwhile to note that the weight loss was minuscule between 0.2 to 0.3%. Therefore, no solid phase transformations occurred, and the FI-MeOH was still the stable form.

The thermal analyses particularly the TGA showed a potential of solvent-masking at the particle's surface based on the small weight loss of less than 0.3% which was reflecting the ease to detach from the FI surface. The ease of detachment was speculated as the effects of two polar protic solvents, methanol and water were loosely bound at the surface when competing to bind with the FI during the crystallisation process. Water and methanol are both known to be highly polar solvents in comparison to acetone which is mildly polar. The hydroxyl (-OH), amine (-NH) and carbonyl (=O) groups in the FI provide the polar site while the alkane (-CH) as the non-polar ever ready for intermolecular interactions (Figure 8-5). The presence of polar solvents encourage interactions of both polar and non-polar sites at FI hence improves the solubility of the system namely the solute-solvent interactions.
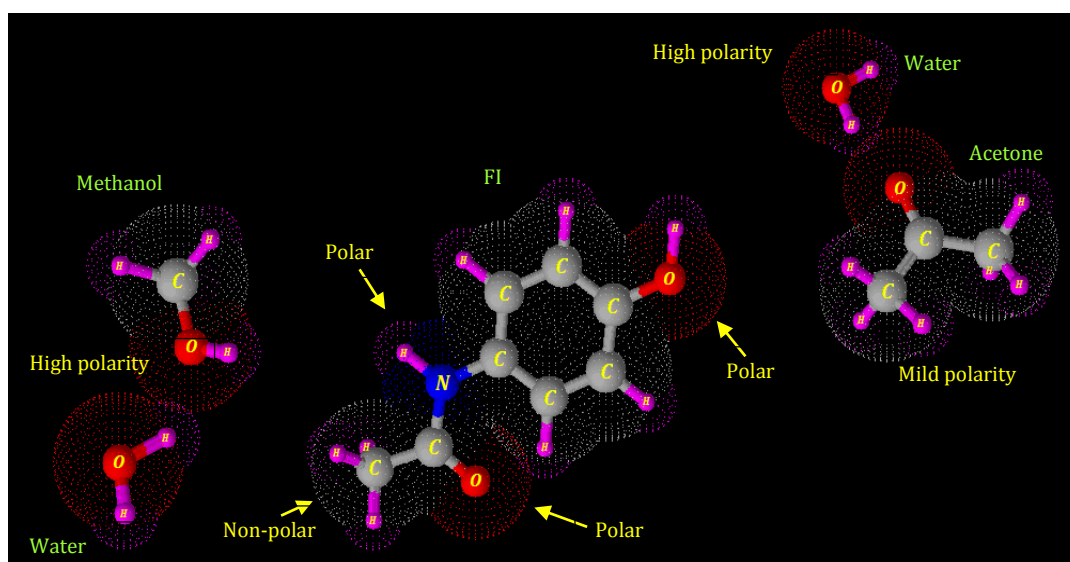
Figure 8-5 The FI potential interaction between the methanol, water and acetone solvent. The potential site of interactions at FI were labelled to be as polar or non-polar

Conversely, the presence of two polar solvents will create competitions of solute-solvent or solvent-solvent. In the case of FI-MeOH and FI interactions, the solvent-solvent dominates, therefore, explains the loosely bound solvent on the surface which easily evaporated [8]. Observation of similar interaction between solvent-solutes indicated that the surface chemistry plays a significant role in describing the final crystal properties, for example, habit and solubility of a particular system [9,10]. However, to support this speculation, the mass spectroscopy analysis need to be done to confirm the particular compounds that were lost in the thermogravimetric analysis.

8.2.3 Mechanical properties measurement

As mentioned earlier in chapter three, the commonly measured physical properties for describing the compactibility were the secondary factor, namely size and habit of the particles. These two physical characteristics are impacting the flowability and compactibility of particles.

8.2.3.1 Particle size distributions analysis

The FI-MeOH samples were distributed between 465 and $1466\mu m$ as shown in Figure 8-7. The mean size for the samples was $909\mu m$. The FI-Ace samples were distributed between 537 and $1301\mu m$ with mean size of $959\mu m$. It was noted that both samples were having similar a size distribution with only $\approx 100\mu m$ difference for the smallest and largest size (D10 and D90). These alike distributions between both samples were resulted from the antisolvent crystallisation approach. By creating supersaturation conditions instantaneously by the addition of pre-chilled water promotes the formation of fresh nuclei instead of growth of available primary nuclei [11,12]. Additionally, the sudden reduction of supersaturation shortens the induction time for formation of fresh nuclei resulting in particle sizes below $1000\mu m$.

8.2.3.2 Crystal habit observation

The stable polymorph of paracetamol (FI) that was recrystallised using methanol-water mixture formed an octogonal thin plate crystal (Figure 8-6). Though there were plenty of primary crystals can be observed, it tends to aggregate together forming clusters (Figure 8-10). The agglomerations appeared to be soft hence, can be easily separated by shaking slowly. From the scanning electron microscopy (SEM) micrographs shown in Figure 8-10, it was observed that for the FI-MeOH samples, the overlapping occurred at a

preferred face as highlighted in red. The face was seen to be the slow growing face that was having a large surface area exposed. Referring to the predicted morphology of FI, the exposed face was identified to be (101). The overlapping of crystals on the (101) face was following the arrangements of molecules in crystal bulk, that were stacking parallel to (101) along the [010] direction. This observation agrees with the observation by Naumov et.al (1997) [13] that also point out that the layers were held together by the van der Waals interactions.

The shape of the crystal samples was described further using aspect ratio. As seen in Figure 8-8 the aspect ratio measured by the circle of equal projection area (EQPC) and the FERET diameter (diameter of two parallel tangential lines) were not further apart, with only 0.02 difference. The similarity was because of the crystal shape that did not have an extreme difference in their dimension. Based on the distribution, the FI-MeOH samples were mainly having an aspect ratio of 0.83.
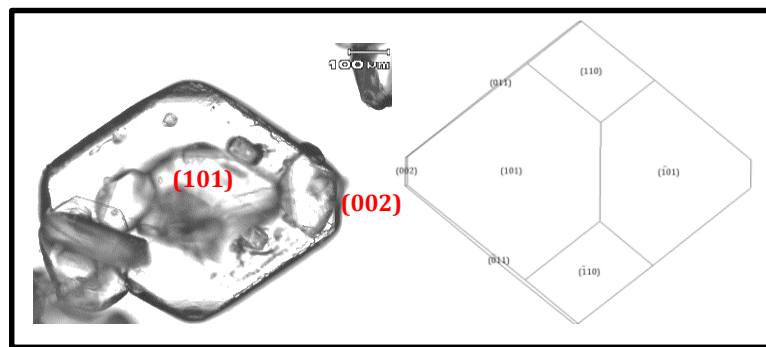
Figure 8-6 FI-MeOH face indexing based on centre to face distant and interfacial angles
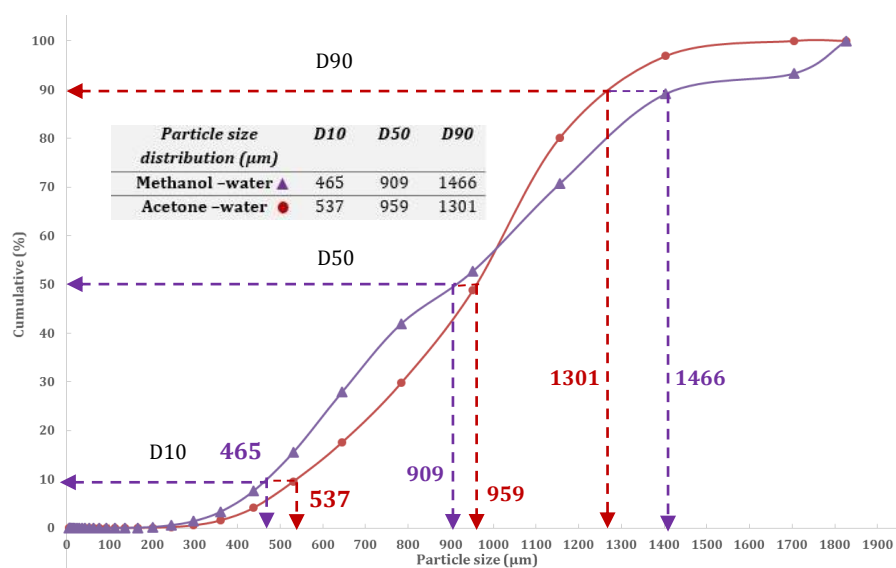
Figure 8-7 The cumulative percent of particle size distribution for the two batches of FI. The particle sizes for both batches were having the similar size range with only $\approx 100\mu m$ difference for D10 and D90

Aspect ratio	(D10)	(D50)	(D90)
FERET	0.49	0.66	0.81
EQPC	0.51	0.68	0.83
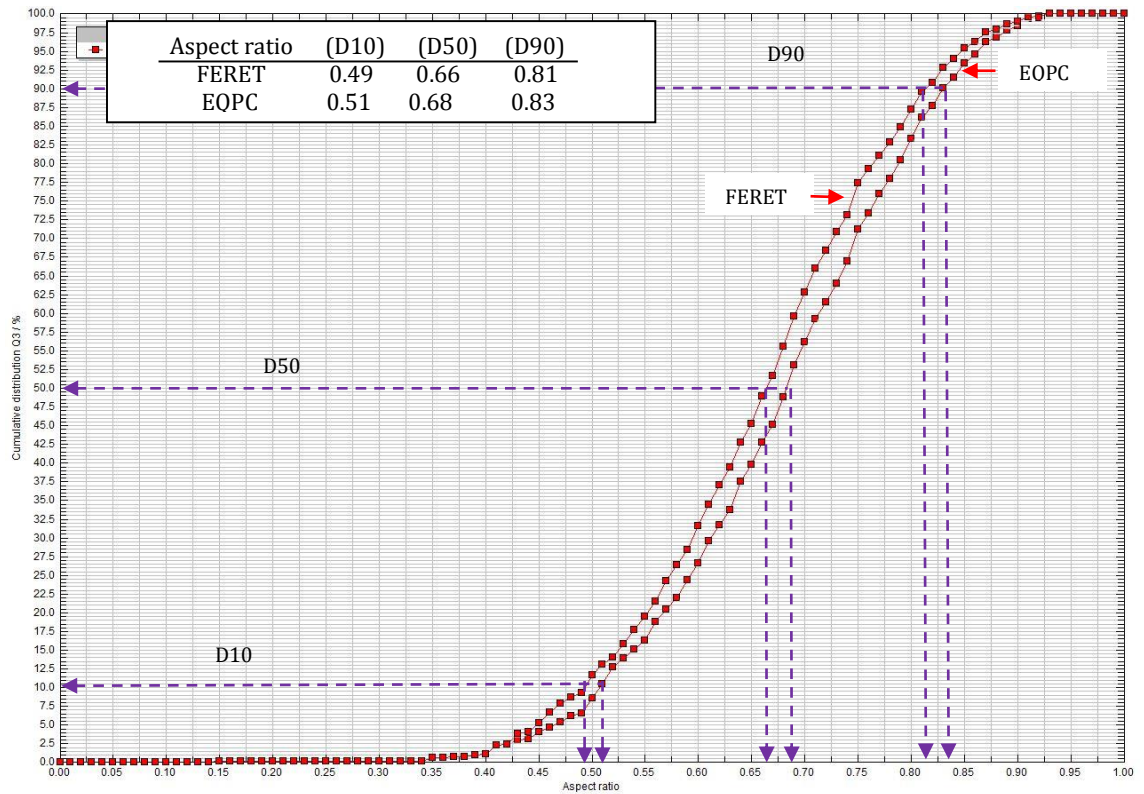
Figure 8-8 The aspect ratio distribution of FI-MeOH to describe the habit of samples. The shape was resembling sphere with 90% of the samples were having 0.81 to 0.83 aspect ratio with 1.0 as sphere

Aspect ratio	(D10)	(D50)	(D90)
FERET	0.58	0.72	0.84
EQPC	0.60	0.74	0.86
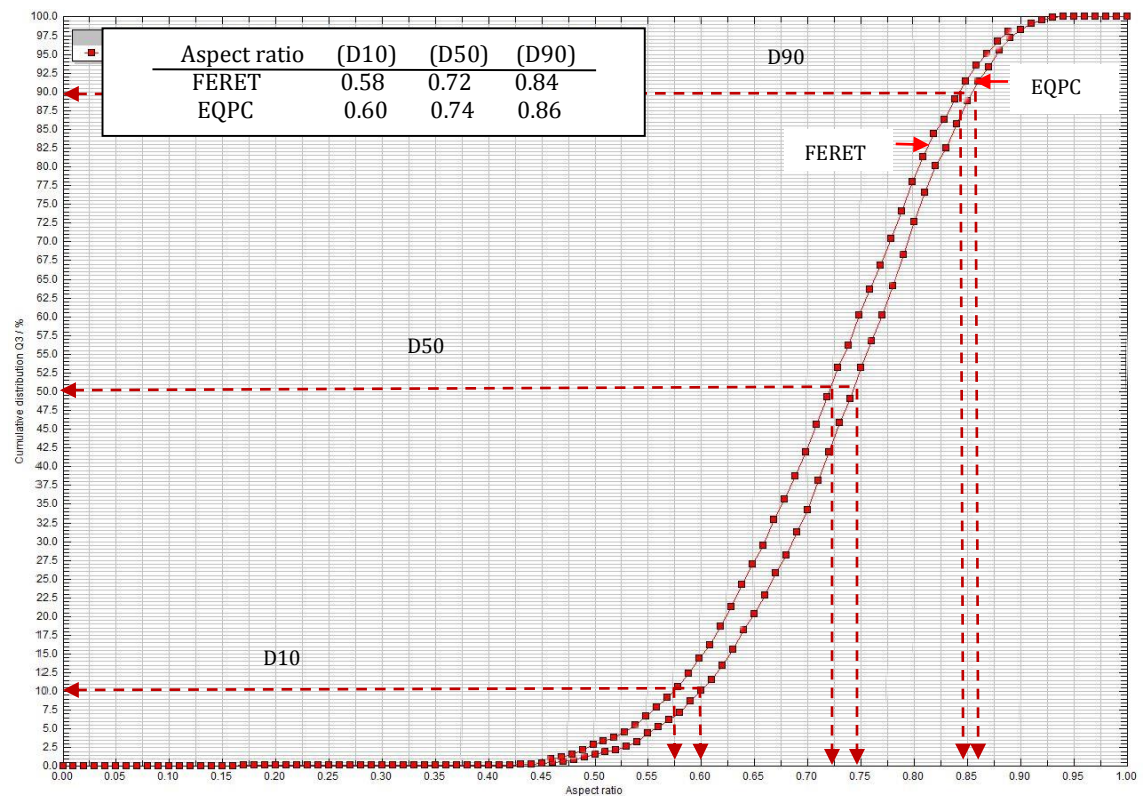
Figure 8-9 The aspect ratio distribution of FI-Ace to describe the habit of samples. The shape was resembling sphere with 90% of the samples were having 0.84 to 0.86 aspect ratio with 1.0 as sphere

272
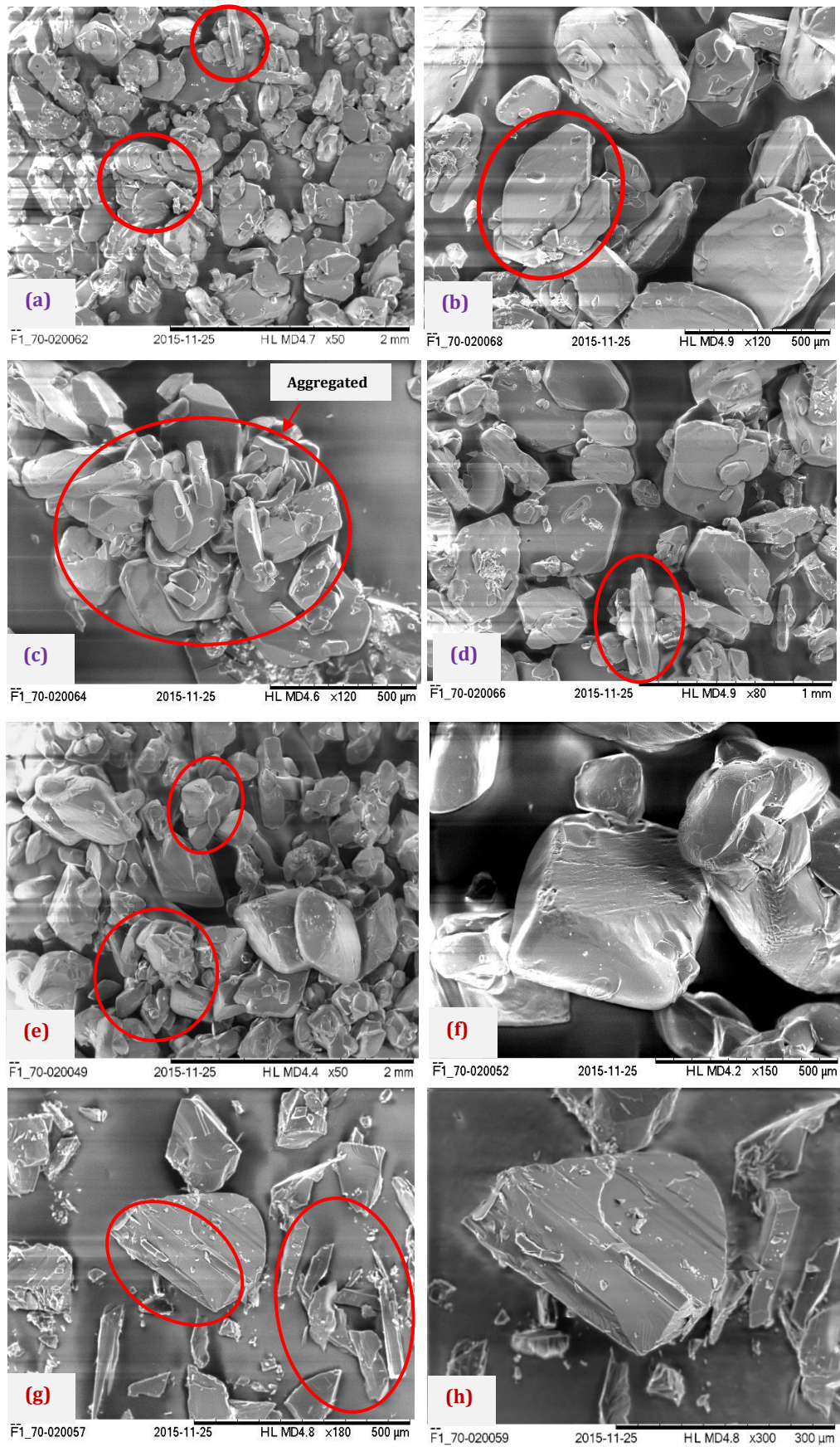
Figure 8-10 Scanning electron microscopy (SEM) micrographs for (a-d) FI-MeOH (e-g) FI-Ace samples.   Roughed surfaces were observed in both batches with aggregated crystals highlighted in red

The sample that was recrystallised in the acetone-water mixture produced an equant diamond-like crystal that is bulkier than the plate-shaped. The FI-Ace batch produced large and hard-agglomerates. The hard-agglomerations make it difficult to break. The agglomerated crystals formed a flower pattern as seen in Figure 8-11. Furthermore, as depicted in Figure 8-11, the surrounding crystals were cemented to one core at seemly the same orientation. The agglomeration was also observed previously by Granberg et.al (1999) [14] that observed an increase in crystals agglomeration in binary solutions in comparison to pure solvents. They suggest that the hard agglomerates were resistant to disruption during mixing of the solution. By manual pressing the crystals will put an amount of pressure for the agglomerates to dissociate before fracture took place. SEM micrographs presented in Figure 8-10 (g and h) showed the surface of FI-Ace crystals after fractured. The fracture was seen to take place not at any defined face.
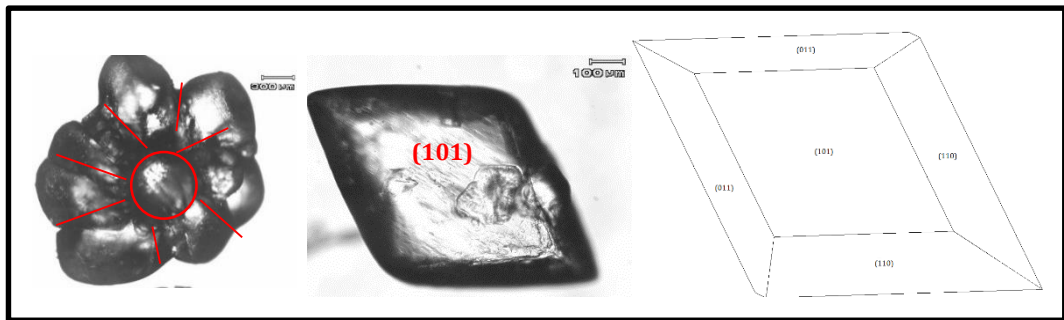
Figure 8-11 FI-Ace crystal face indexing following centre to face distant and interfacial angle

From Figure 8-9 it was perceived that the habit has a maximum aspect ratio of 0.86 which further relate to the diamond habit it has with four near to equal sides. The FI-Ace samples were shown to be more sphere than the FI-MeOH. The roundness was comprehensible based on the FI-MeOH samples that have octagon shape rather than the diamond-like that only have four sides. Hence, based on the particle size and habit analysis of the two batches were not distinctively different. Besides that, the surface chemistry for both samples that was described in chapter six was suggested to dictate the orientation of the agglomerates. The flowability and compactibility for both were expected to be comparable, with the FI-Ace behaving slightly better by being bulkier compared to the FI-MeOH samples.

8.2.3.3 Flow analysis

The powder flow is essentially affected by particle size, habit and surface chemistry as mentioned in chapter three. By plotting the major principal stress to the unconfined yield strength will give the flow function (FF_c) representations. Figure 8-12 represents the FF_c for FI-MeOH and FI-Ace which, showed a positive linear relationship and the measurement values were given in Table 8-1. The positive slope was representing the direct proportionality between amounts of force needed to initiate flow and the normal stress that is consolidating the powder. The samples were very cohesive as established from Figure 8-12 which had the FF_c below 2 corresponding to the Jenike's [15] rank. Surprisingly, the FI-MeOH had slightly better flow though it has a platy habit. Therefore, the density-corrected flow function is useful to demonstrate the flow properties of similar size and shape samples.

Figure 8-13 showed the density-corrected flow function that demonstrated the FI-Ace had a bulkier habit which alternates its' flow function line to be better than the FI-MeOH samples. This observation corresponds well with the better flow that can be attained by particles with larger density. Besides density, the particles size influence was shown by having the plot of the unconfined yield strength slope to the size distributions. The particle size distribution is directly related to the powder flowability [16] as seen in Figure 8-14. As the size increases, the slope steepness decreases, showing a better flow. The steepness of slope shows the amount of pressure needed to initiate flow.

Table 8-1 The ring shear measurements for FI-MeOH and FI-Ace samples. The values of unconfined yield strength for FI-Ace were lower than the FI-MeOH samples

Samples	Run	Bulk density (g/cm³)	Major principal stress (Pa)	Unconfined yield strength (Pa)
FI-MeOH	1	0.58	1017	2747
	2	0.59	1018	2687
	3	0.59	1537	2725
	4	0.59	2058	2708
	5	0.59	2617	2715
FI-Ace	1	0.69	1020	931
	2	0.69	1020	968
	3	0.69	1540	1372
	4	0.69	2061	1798
	5	0.69	2620	2188
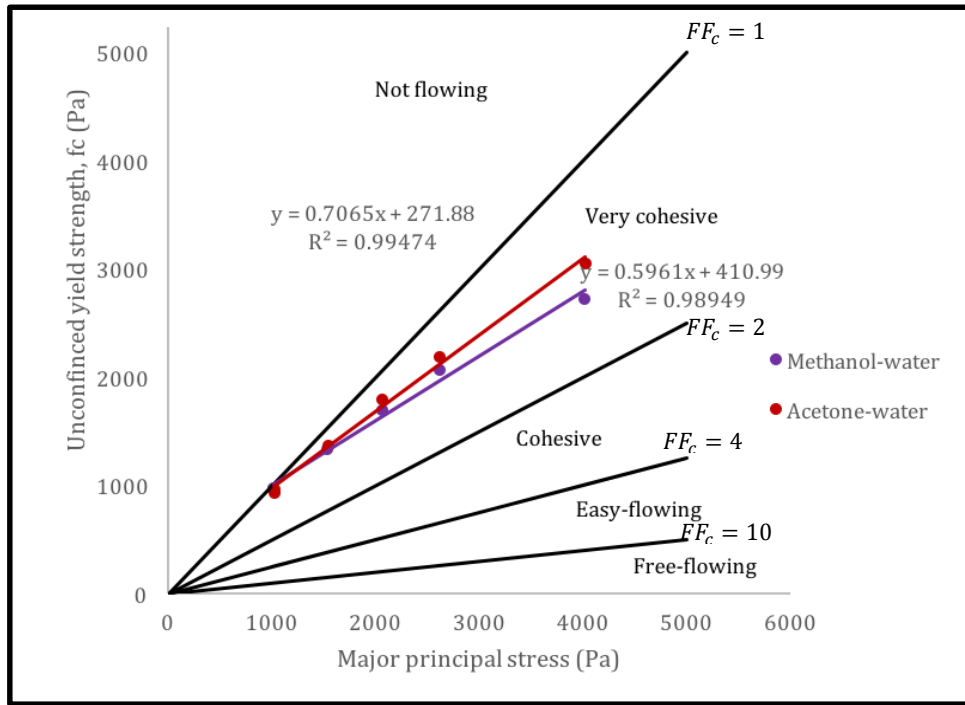
Figure 8-12 Flow function of FI-MeOH samples that was plotted against the Jenike's [15] flow rank
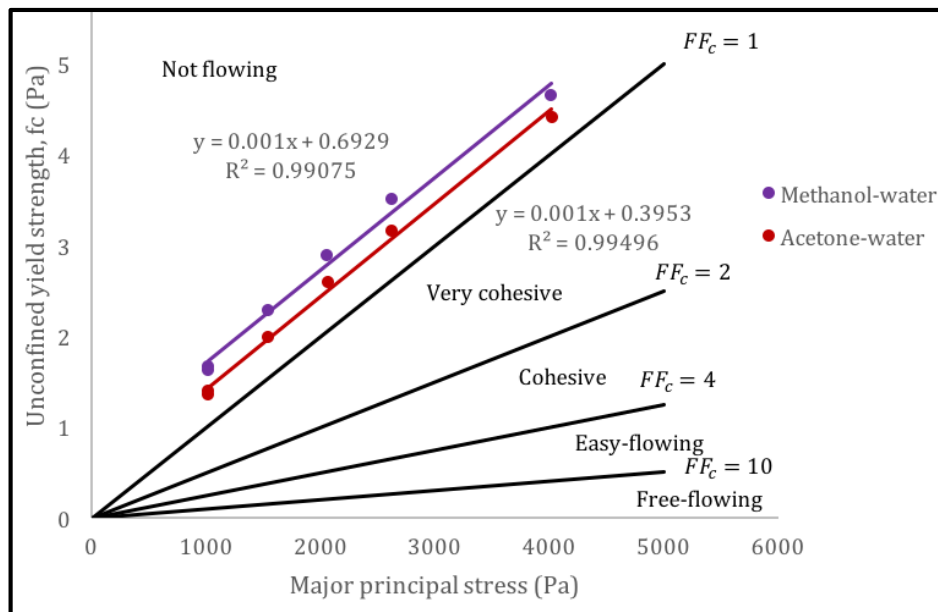
Figure 8-13 The density-corrected flow function plot of FI-MeOH and FI-Ace samples. The flow function line was alternate when density was taken into considerations. Bulkier samples with improve density showed a better flowability

From Figure 8-14, the larger particles size (D90) had a slope of -9×10^{-5} compared to the mean (D50) and small size (D10) with 3×10^{-4} and 2×10^{-4} respectively. The linear regression equations and the corresponding slopes were shown in Table 8-2.
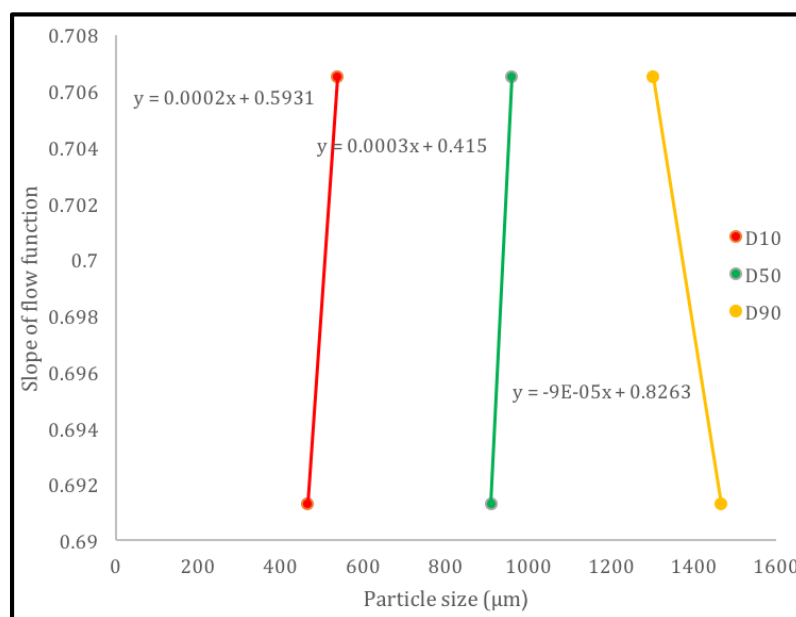
Figure 8-14 The relation between the particle size distributions with flow was reflected by the steepness of the flow function slope. Steeper slope relates to poor flow

Table 8-2 Linear regression equations for the flow function

Samples	Linear regression equations	Regression values (R^2)
FI-MeOH	$y = 0.596x + 410.99$	0.99
FI-Ace	$y = 0.707x + 271.88$	0.99

Deducing from the above analysis, though the size and habit of both FI samples were similar the flow can be differentiated by considering the density influences. Moreover, the effect of particles size on powder flowability was exhibited by observing the flow function slope steepness. Though both samples were very cohesive and potentially not flowing, the FI-Ace samples were behaving a little better than the FI-MeOH in this instances. The poor flow exhibited suggested that better-flowing excipients are needed if APIs with similar habit are to undergo direct compression.

8.2.3.4 Tabletability measurements

Table 8-3 showed the results of compaction measurements carried out. The tensile strength was observed to be directly proportional to the compression stress. Moreover, the solid fractions seemed to reduce as the tabletting cycle increases. The solid fractions are describing the amount of solid in the tablet, whereby the standard value for pharmaceutical tablets is 0.85 [17].

The mean tensile strength of the FI-Ace was 25% higher compared to the FI-MeOH samples, with 0.17 MPa. The tabletability performance was taken as the tensile strength in relation to compression stress. This tabletability as mentioned in chapter three can be further elaborated through compressibility and compactibility.

The tabletability of the FI-Ace samples was better with 75.51MPa compared to the FI-MeOH with 47.98MPa. Initially, the plot in Figure 8-15 showed a direct proportionality of tensile strength to compression stress for both samples. At this initial section, the FI-Ace had better tensile strength at any compression stress. At 37.33MPa, both lines intersect, and the FI-Ace plot seems to level off at a tensile strength of 0.19MPa while the FI-MeOH keep increasing. The rationale for the tabletability difference observed was related to the bulky-equant and platy octogonal habit samples. The habit effects to the tabletability can further be described by the compactibility and compressibility plots. By having the compressibility and compactibility plot, the influence of interparticle bonding area and strength towards tabletability can be distinguished
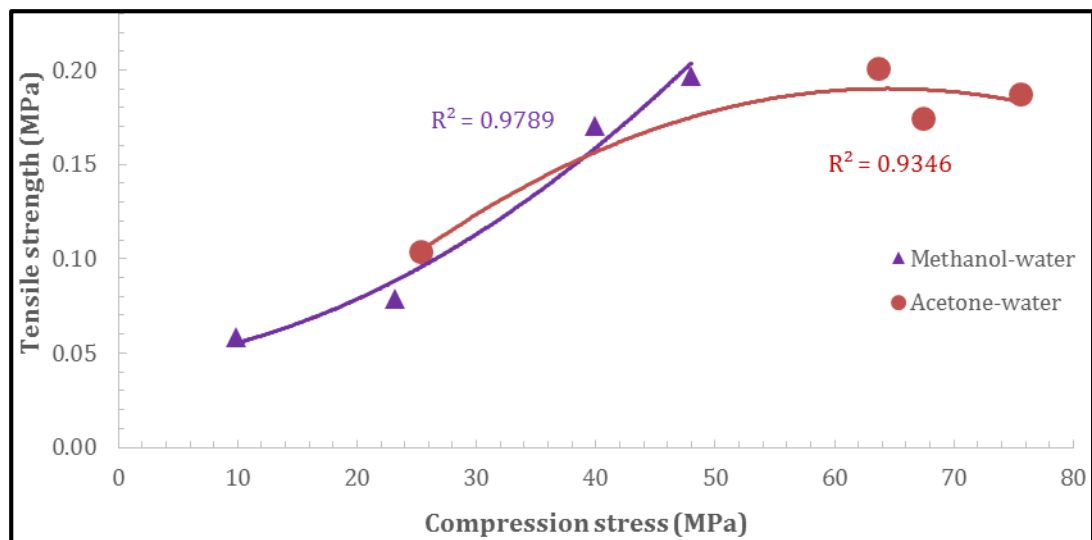
Figure 8-15 Tabletability of FI-MeOH and FI-Ace samples. The tabletability was related to the crushing force, force needed for tablet to fail with the compression stress. The FI-Ace have better tabletability with higher tensile strength

Table 8-3 The compaction measurement data according to cycle. The apparent density was the bulk density ratio to true density. The solid fraction shows the extent of powder in tablet or densification. The tensile strength was measured by tablet failure based on diametral compression

Samples	Cycle	Mean compression stress (MPa)	Standard deviations (MPa)	Mean crush force (N)	Standard deviations (N)	Mean weight (mg)	Standard deviations (mg)	Mean thickness (mm)	Apparent density	Tensile strength (MPa)	Solid fraction
FI-MeOH	1	47.98	4.28	6.83	0.58	156.2	1.47	2.76	1.1	0.20	0.89
	2	39.88	15.29	5.97	3.09	153.3	6.72	2.78	1.1	0.17	0.87
	3	23.15	3.03	2.83	0.35	153.8	2.41	2.86	1.1	0.08	0.84
	4	9.89	7.08	2.20	0.14	153.7	3.18	2.99	1.0	0.06	0.81
FI-Ace	1	75.51	2.52	6.30	0.66	155.5	0.36	2.68	1.2	0.19	0.91
	2	67.44	12.07	5.97	0.60	156.6	3.20	2.72	1.1	0.17	0.91
	3	63.61	7.44	7.00	2.86	159.0	2.12	2.77	1.1	0.20	0.90
	4	25.28	2.72	3.70	1.25	155.5	2.84	2.84	1.1	0.10	0.86

8.2.3.5 Compressibility

Figure 8-16 (a) presents the compressibility which describes the ability of the powder to accommodate the compression stress. At any compression stress, FI-Ace samples had a better solid fraction. For instance, taking compression pressure of 40MPa, the solid fraction for FI-Ace was 0.88 and FI-MeOH are 0.87. The highest solid fraction achieved for FI-Ace samples was 0.91. The ability of the FI-Ace samples to accommodate the compression pressure through volume reduction showed the available bonding surface area which correlates with the smaller particle size compared to the FI-MeOH. The larger surface relates to more amount of particles that can be packed into a tablet of fixed volume hence demonstrating a higher densification.

The equant habit of the FI-Ace samples will allow for better particles arrangement in the tablet die reducing void. The octogonal platy shape will create a void in between the particles when being filled into the tablet die with the assumption that the particles will arrange themselves at preferred orientation. Figure 8-17 depicts the void presence in between particles. The amount of available void relates to the solid composition of samples hence to the densification of the tablet that gave the greater solid fraction for FI-Ace samples.

8.2.3.6 Compactibility

Another key analysis to describe tabletability is the compactibility of the tablet. The compactibility relates to the bonding strength of tablet to stay intact after decompression. A greater solid fraction will have an adverse impact on the tensile strength. The decrease in tensile strength was exhibited by the FI-Ace samples as shown in Figure 8-16 (b). For example, at a solid fraction of 0.88, the FI-MeOH samples had the higher tensile strength (0.17 MPa) displaying the strong interparticle bond interactions. The strong bonding interactions of FI-MeOH samples were suspected to be given by the dominant face exposed.

A study by Sun and Grant (2001) [28], emphasised on the existence of favoured orientation for two habit which was platy and prisms during tabletting of L-lysine monohydrochloride dihydrate (LMH). They found out that the platy crystals orientation was at the (001) face, that was a slip plane. They suggested that by favouring (001), the compactibility of the platy crystals were increased hence contributed to the LMH tabletability performance. This outcome was a little different from current study though the habits were similar. The best explanation was because of the absence of slip planes in FI. The presence of slip systems

promotes the deformation to take place favouring the direction of slip and seemly improves the strength of the microcrystals.

Based on the compressibility and compactibility evaluations, the positive tabletability of FI-Ace samples was contributed by its compressibility behaviour instead of compactibility. Therefore, effects of equant and platy habit FI showed that the total area available for bonding between the particles supersede the bonding strength. Because both microcrystals were the same forms, hence explains the same strength. The impact of physicochemical properties of different habit was not dominant and did not govern during compaction of the tablet.
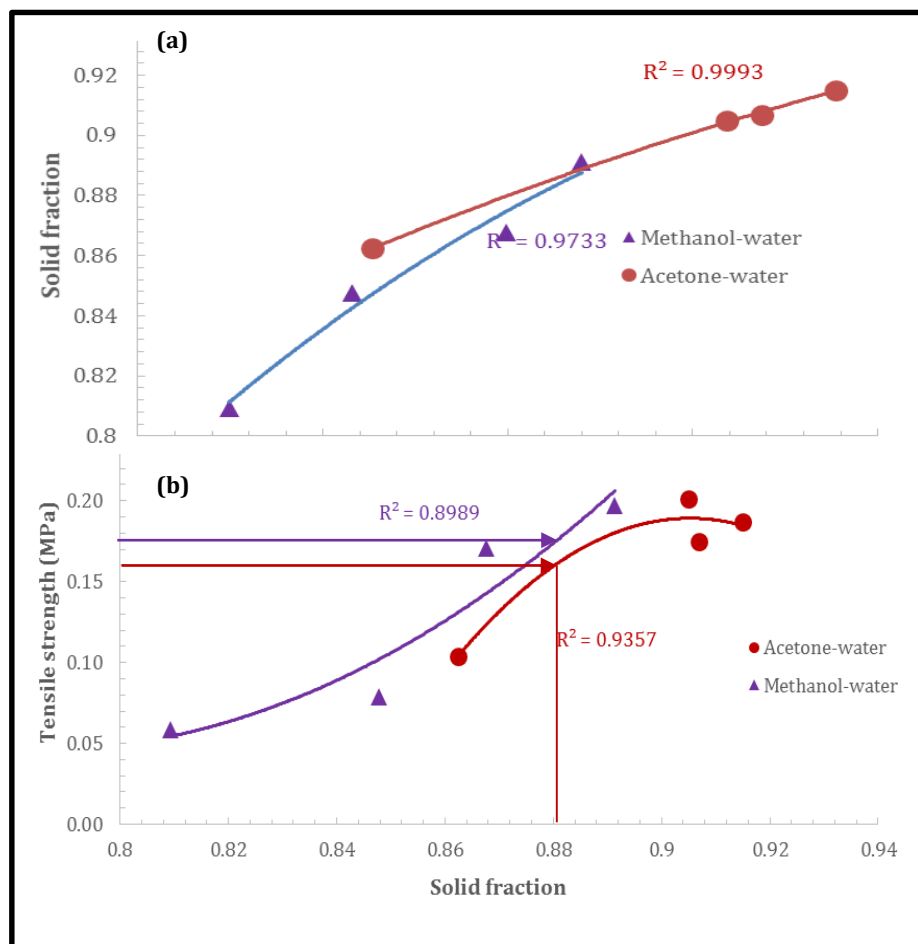
Figure 8-16 a) Compressibility of tablet relating the compression stress to the solid fraction. High compression pressure with high solid fraction result in better compressibility. b) Compactibility shows the interparticle strength of FI-MeOH and FI-Ace samples. It relates the ability to form tablet with certain amount of force with the effect of densification
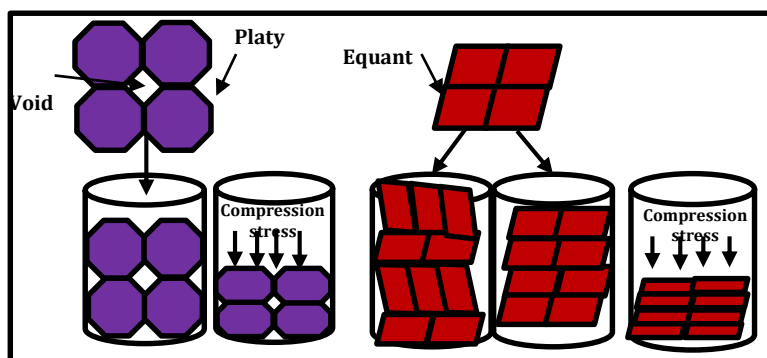
Figure 8-17 Schematic showing the habit effects during filling of powder into tablet die showing better packing ability for the equant shape. By having more amount of powder, the density increases and more solid fraction under compression stress

Figure 8-18 showed the maximum crushing limit for the platy and equant habit. The slope of the platy habit was steeper compared to the equant habit. The crushing strength of the platy habit was achieved at a compression force of 2.3kN that was half of the equant habit. The equant habit was showing better compression force because of its ability to rearrange better in the tablet die giving more space for volume reduction (Figure 8-17). This compressibility was evident by having the plot of apparent density on compression pressure (Figure 8-19). The platy habit was shown to have the small range of density compared to the equant.
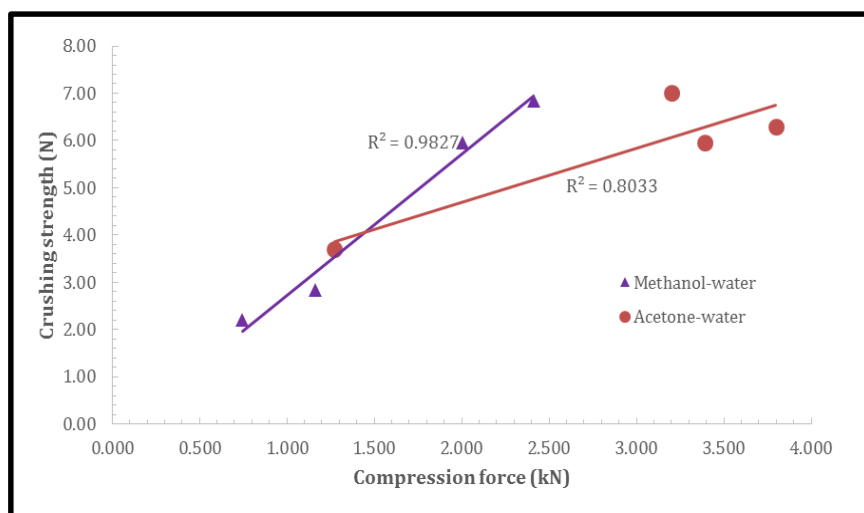
Figure 8-18 Tablet limiting force between two habits of FI. The equant habit showed higher compression force limit with similar crushing force compared to the platy habit. Apparent density with respect to the compression stress
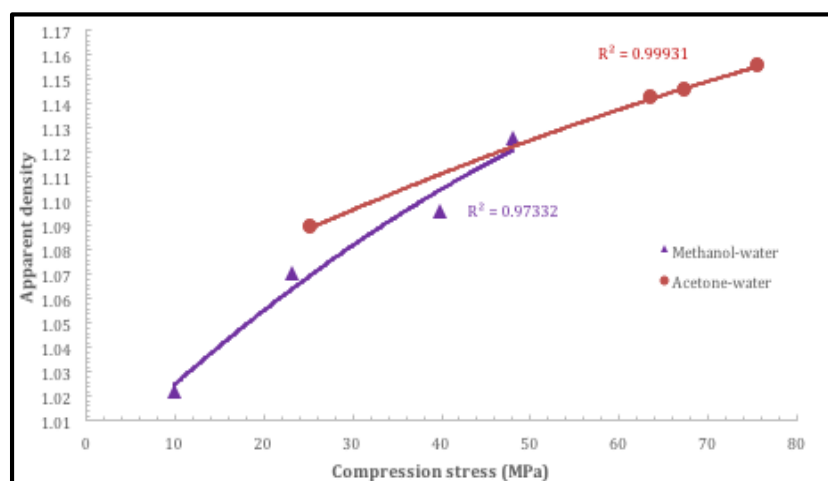
Figure 8-19 Plot of apparent density relation to compression stress. The platy habit was having better density at low pressure while equant habit at the higher compression stress

8.2.4   Summary

Table 8-4 presents the summary of properties for this section. The habit similarity with only 0.02 difference of aspect ratio and sphericity between the platy (FI-MeOH) and equant (FI-Ace) microcrystals resulted in only slightly different for the tabletability. Likewise, it can be seen that the limit of crushing force for both was similar $\approx 7N$. However, the equant habit needed double the compression force of the platy habit before crushing. The highest limit of the compression force of the equant habit was 4kN. The higher compression force achieved was related to the total numbers of bond created from the larger surface area that the equant habit and reflected by the improved compressibility. The same crushing force was directly proportional to the tensile strength, giving both microcrystals the maximum strength of $\approx 0.19MPa$. Paracetamol was identified as brittle according to the Rowe and Roberts (1995) [27] mechanical properties classifications.

Table 8-4 Summary of the properties measured from the two different habit. The FI-Ace was shown to have more positive results than the FI-MeOH. The different habit was showing slightly different mechanical properties which relate larger surface area for interparticle interactions

Characteristics	FI-MeOH	FI-Ace
Particle size distribution	$465\text{-}1466\mu m$	$537\text{-}1301\mu m$
Habit / mean bulk density	Platy/0.59	Equant/0.69
Flowability	FF_c<1	FF_c<1
Tabletability(Tensile strength)	0.18MPa	0.19MPa
Compressibility (solid fraction)	0.82	0.92
Compactibility (Tensile strength/ solid fraction)	4.5	5.1

8.3 Influence of different solid forms on the mechanical properties

Another factor that influences the mechanical properties during tabletting is different solid forms. The effects of co-crystals to improve the tabletting behaviour of paracetamol FI were studied and presented in this section. FI-Ace samples were selected based on its marginally better mechanical properties shown in the previous section for comparison with one of the paracetamol co-crystals, paracetamol-theophylline (PTHEO).

8.3.1 Powder x-ray diffraction

The outcome of PXRD analysis for paracetamol-theophylline (PTHEO), paracetamol and theophylline are shown in Figure 8-20. The crystallised PTHEO was the same structure as obtained in the literature [18]. An obvious difference was at a 2θ angle of 26.49°. There was 0.5° peak shift observed for the crystallised PTHEO samples. The shift was because of the different temperature used to solve the structure, whereby the literature was solved at 180℃, and this study structure was at 25℃. All the other main peaks were the same showing no phase changes and confirming that it was the same form.
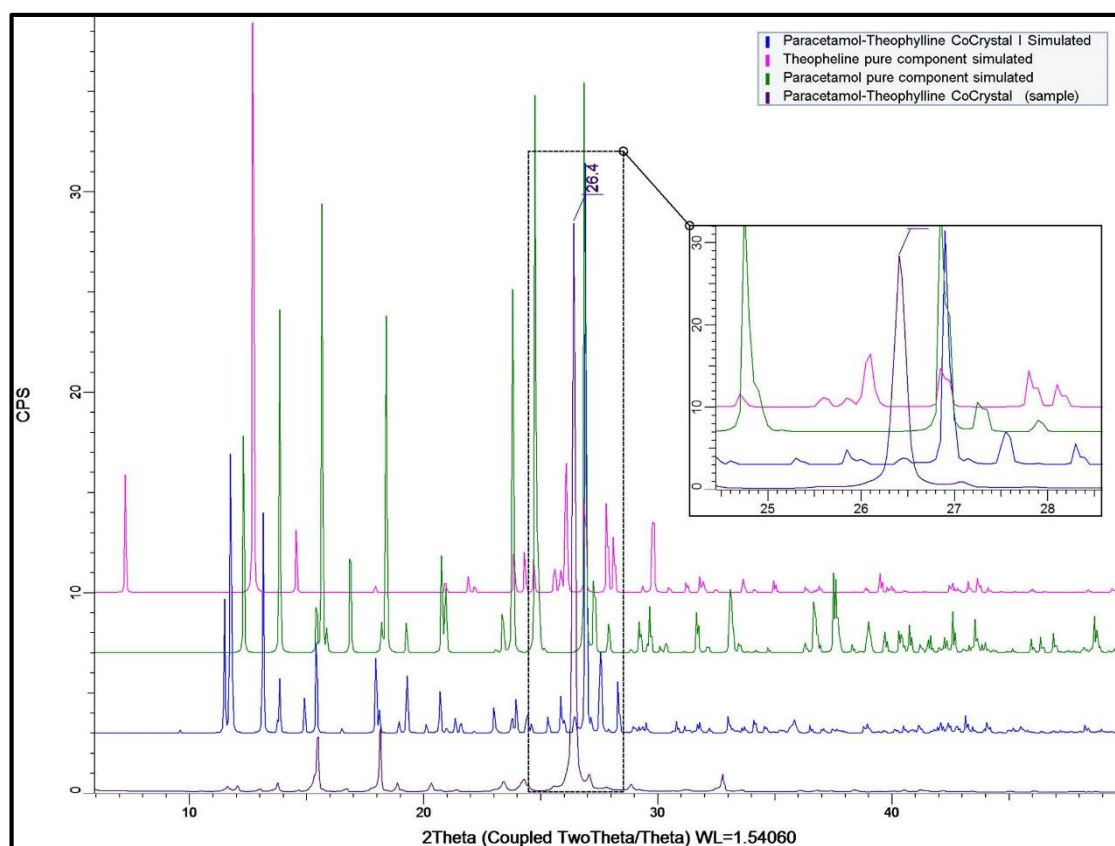
Figure 8-20 PXRD patterns of crystallised PTHEO compared to the simulated co-crystal and pure component of paracetamol and theophylline

8.3.2 Thermal analysis

The DSC thermogram of PTHEO showed one strong endothermic peak at 172.17°C, which was the melting temperature. The melting enthalpy was 105.70 J/g. This observation was agreeing with the literature value of 171°C with only 1°C difference, as shown in Figure 8-21 (a). The TGA plot showed 1.24% weight loss (Figure 8-21(b)). The small amount of weight loss was suggested to be from the solvent evaporation that was suspected to be at the surface of the samples. Moreover, the weight loss was identified to start at 64°C, which was the boiling point of methanol and end at 100°C, the boiling point of water. The degradation started to take place at 220°C as seen in both the DSC and TGA thermograms.
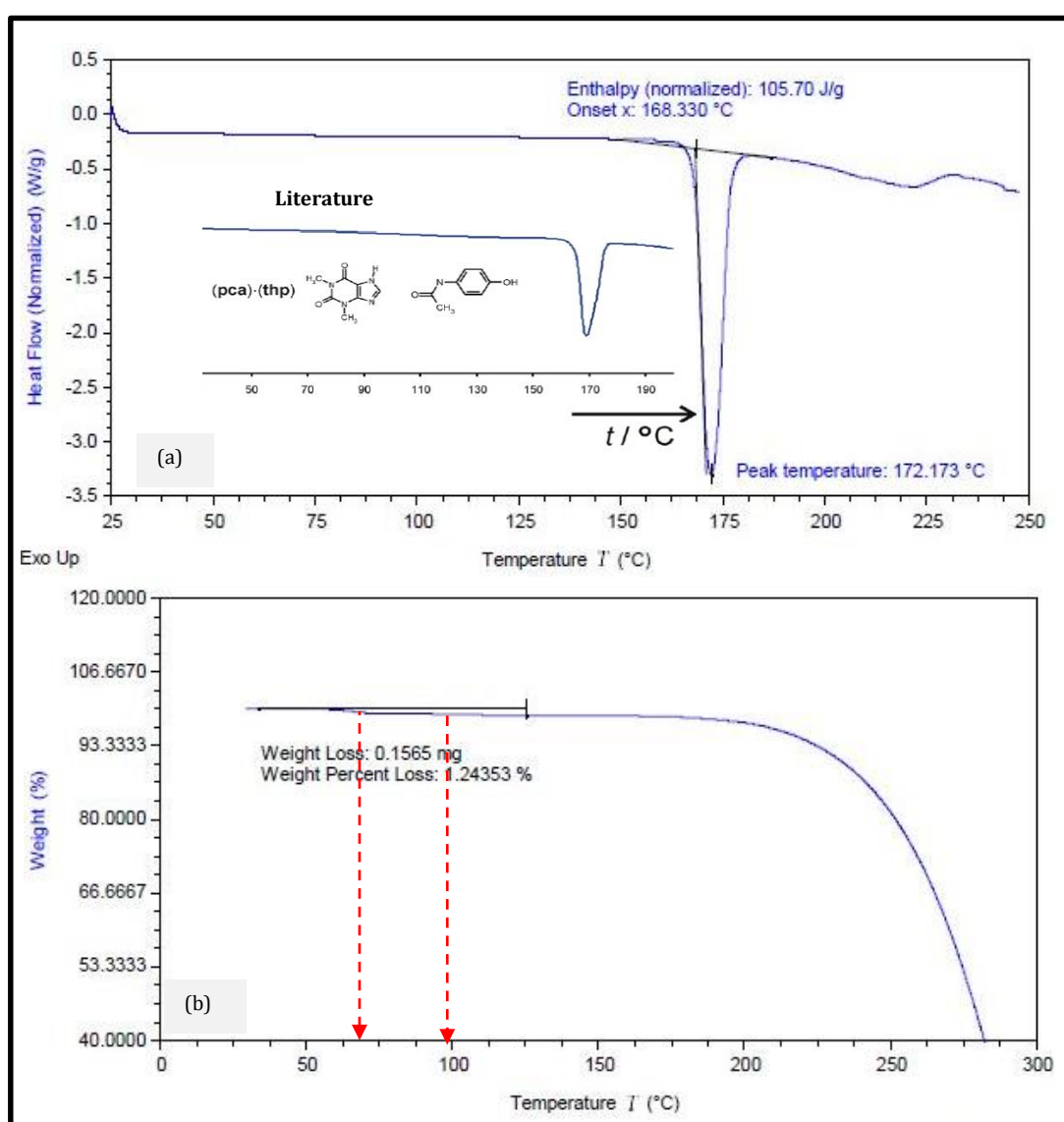
Figure 8-21 Thermal analysis for PTHEO a) DSC thermogram showing one strong endothermic peak b) TGA thermogram showing 1.24% weight loss

8.3.3 Mechanical properties measurement

The related properties that are influencing the compaction of PTHEO are measured. The PTHEO was hypothesised to have improved compaction performance compared to the FI.

8.3.3.1 Crystal habit appreciation

The isolated PTHEO showed a platy-hexagonal habit as illustrated in Figure 8-22 (a-b). There were a lot of primary crystals observed with minimal agglomerations (Figure 8-22 (c)). Interestingly, by applying small pressure on the crystals, it will start to cleave at a particular face as displayed in Figure 8-22 (d). While doing so, the crystals were seen to be soft and easily cleaved. The indexed faces showed three dominant faces, (10-1), (011) and (101). The biggest face was (10-1). The SEM micrographs confirmed the cleaving behaviour of PTHEO. The PTHEO cleaving manner was shown in Figure 8-23. Likewise, the PTHEO surface was observed to contain defects at the centre of the dominant face (Figure 8-23 (a)). It was showing a screw-like pattern, whereby the circuit was getting smaller as it gets deeper into the crystal.
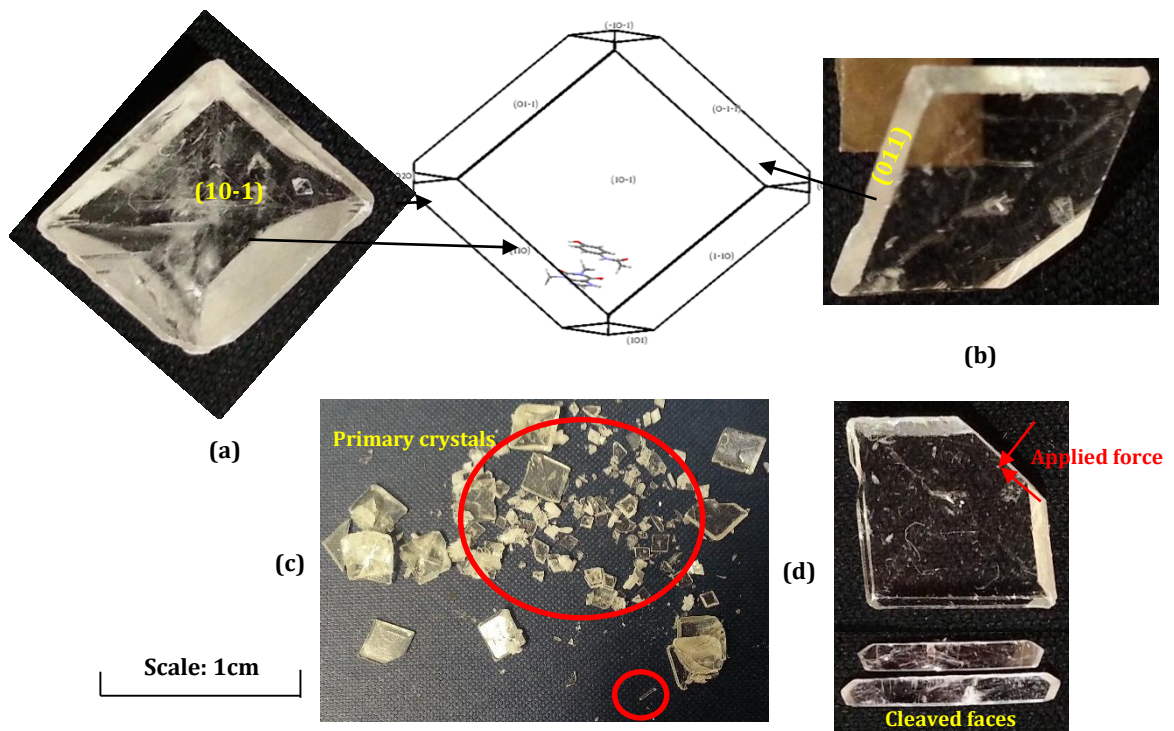
Figure 8-22 PTHEO crystals with platy habit. a) Crystal isolated from the sonication crystallisation b) Tilted crystal exposing the side face c) Cleaved crystal faces showing specific cleavage face that was not the morphological importance
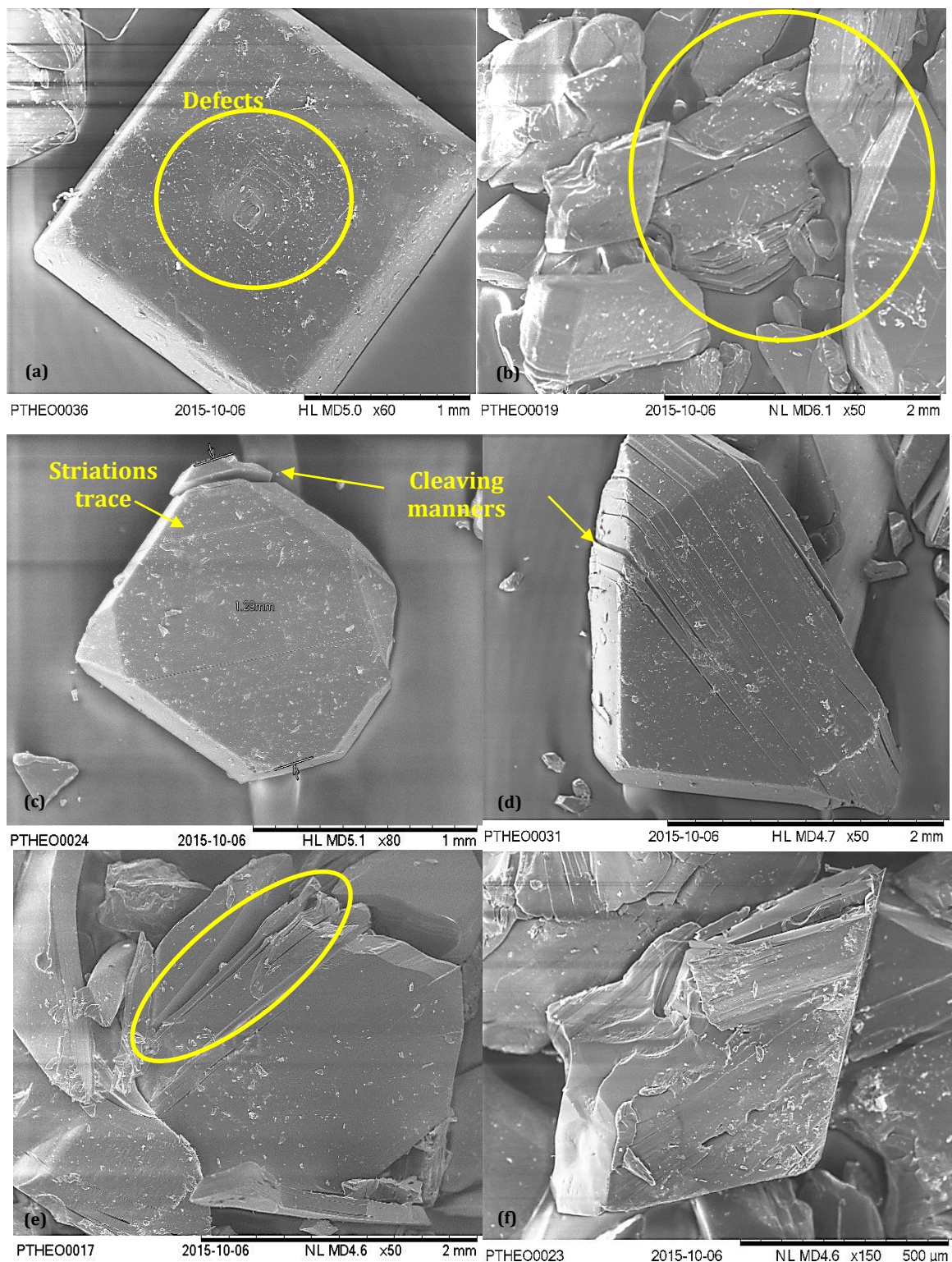
Figure 8-23 SEM micrographs for PTHEO with a) Habit of PTHEO b-f) PTHEO deformation observations showing the cleaving behaviour and cleavage plane. Striation traces were observed where cleave of faces took place. Figure e showed the ease of the cleaving

The cleavage face was predicted to be (101) habit face. The cleaving was observed to follow the striations exhibited by PTHEO as seen in Figure 8-23 (c). PTHEO cleaving behaviour was agreeing with the predicted mechanical behaviour in this study. Though the primary burgers vector was inactive, the strongest intermolecular bond, in this instance the hydrogen bond, was in-plane. The hydrogen-bond network that was formed in-plane being the driving force for the cleaving to take place in the (101) face along the [010] direction. The strong in-plane bonds, create enough force to displace the plane and was retaining the plane from breaking in different directions. The knowledge of potential cleave or slip systems hence provides insight into preferred orientation during processing namely milling and tabletting.

8.3.3.2 Particle size distribution measurement

Based on the direct observation, the crystal size was determined to be approximately 1 cm. The large size crystals were milled to get better distributions and also to get the appropriate size to meet the lens equipment limit. Ball milling was used to comminute PTHEO into the acceptable size of ~6mm. PXRD was carried out to ensure that the milled samples did not transform into different forms. The milled samples were shown to preserve the solid forms of the start materials as seen in Figure 8-24 with all the main peaks were seem to match the unmilled pattern. As expected, the milled crystal was positioned at its' preferred orientation, based on the strength of (103) peak with the other major peak seems to be reduced in strength. The PXRD pattern attained then confirms the observation of SEM.
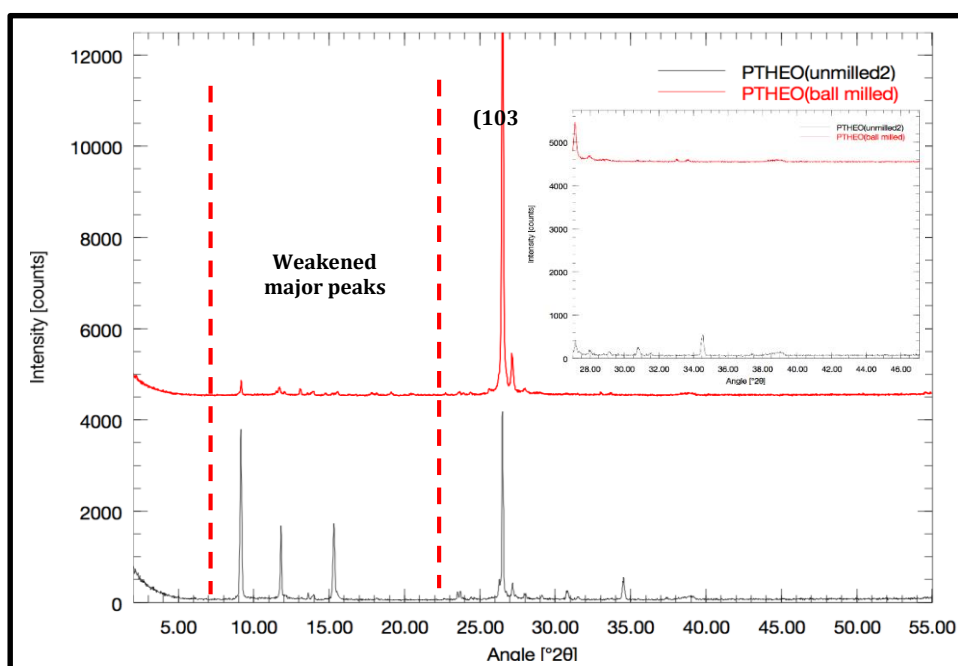
Figure 8-24 PXRD patterns of unmilled and milled PTHEO confirming no phase transformation after milling. PTHEO exhibited preferred orientation face of (103)

The particle size of the milled PTHEO was ranging between the smallest, 10µm and the largest 580µm as shown in Figure 8-25. The mean size was 124µm. The milled samples had a greater total surface area in comparison to the unmilled. The milled samples were expected to provide more area for interparticle bond creation. The exposed cleavage face was supposed to govern the behaviour during tabletting and flowability of PTHEO instead of the dominant faces. The effect of size will be further accessed with flowability and tabletting performance.
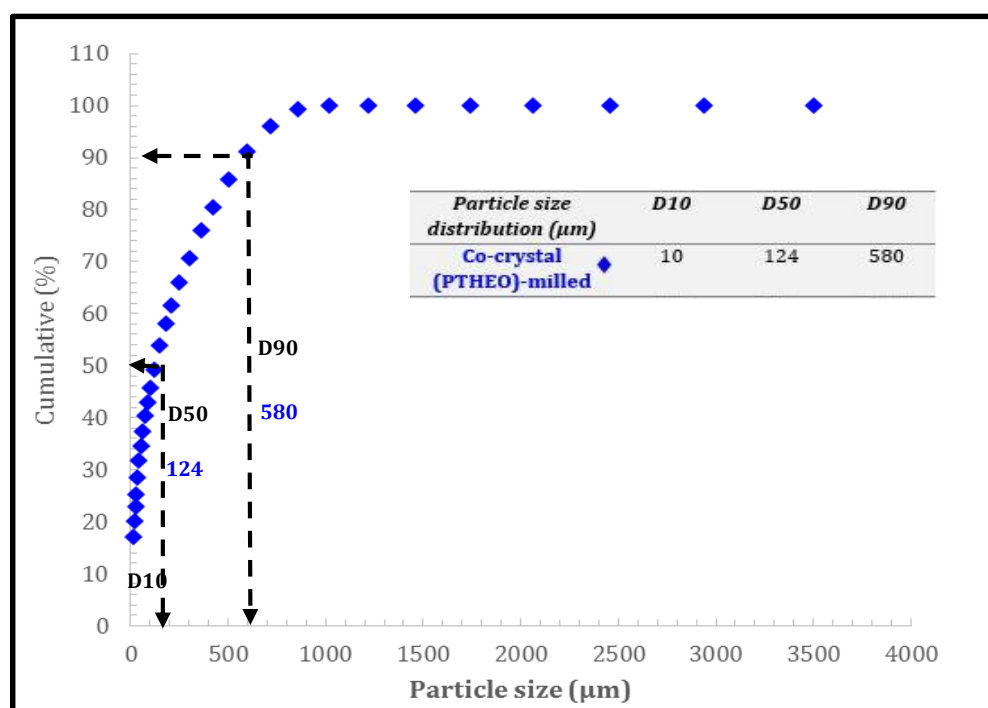
Figure 8-25 Particle size cumulative distribution of PTHEO showing the range of size between 10 and 580µm

8.3.3.3 Flow analysis

From Figure 8-26 (a), PTHEO flow seemed to be in between the 'not flowing' and 'very cohesive' region suggesting that the PTHEO was not flowing well. The poor flow was related to the particles size and platy habit of PTHEO. The measure of flow as mentioned in chapter three is the point at which powder starts to fail or plastically deformed. When the particle size gets smaller, the individual contact area becomes limited. When the principal external pressure is acting on the small contact area, the pressure is contained locally making the particle highly active. The highly active individual particle is then excited to the neighbouring particle to stabilise by forming interparticle interactions, in this instance the

cohesion. The amount of cohesive forces increases as the particle get smaller. The simple force-pressure relationship is best to represent the cohesiveness of small particle. Figure 8-27 depict the schematic of particle interactions under stress. The strong cohesive forces will increase the amount of strength needed for flow to begin, particularly the unconfined yield strength hence the flow. The effect of size can be evident because the FI-Ace samples have bigger particles.
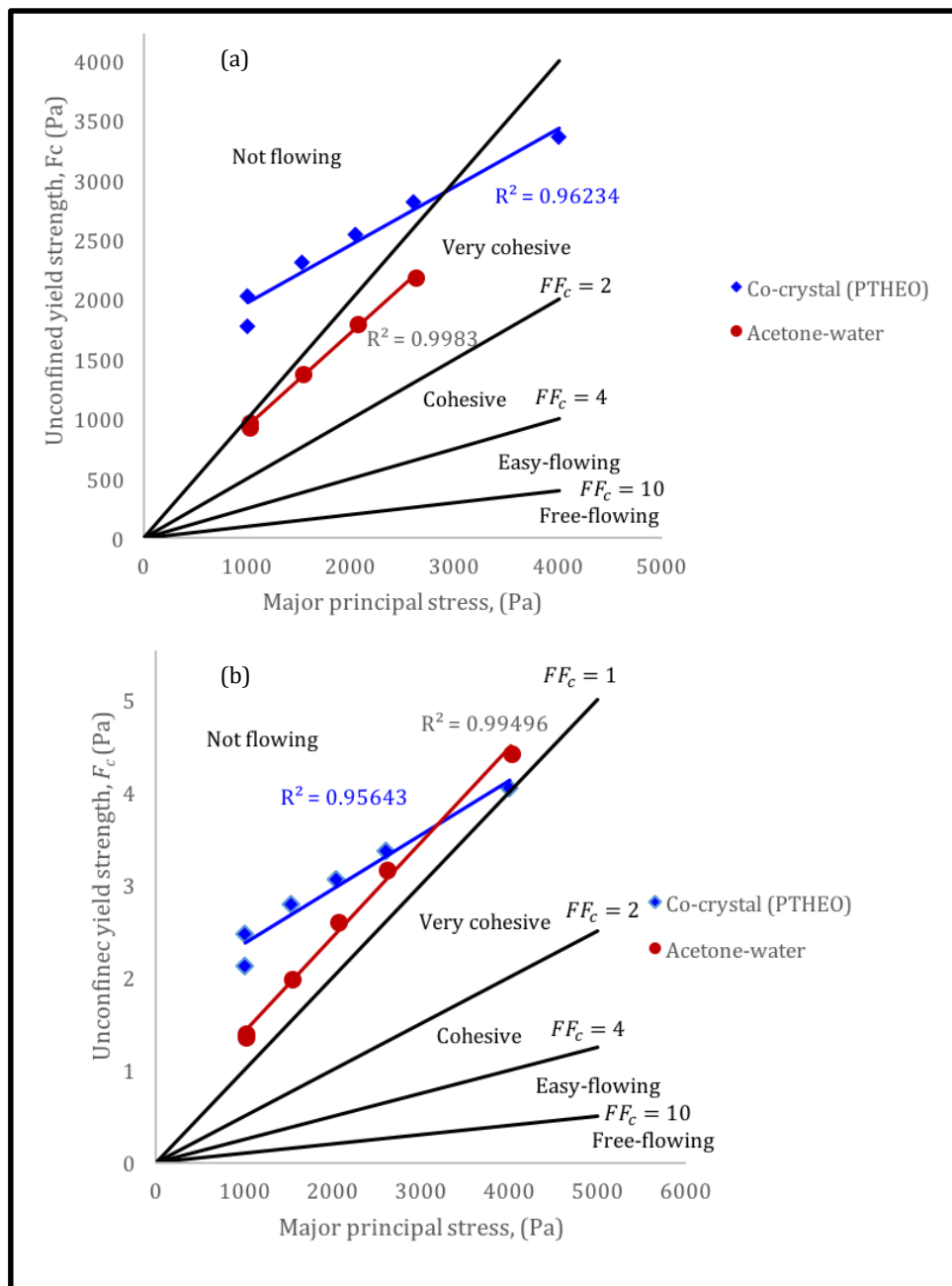
Figure 8-26 a) The flow function plot for PTHEO. The size influences were shown in comparison to FI-Ace samples. b) The flow function corrected to bulk density. PTHEO, which has lower bulk density, was having poor flow compared to the FI-Ace samples

$$P_{principal} = \frac{F_{cohesive/adhesive}}{A_{contact}}$$
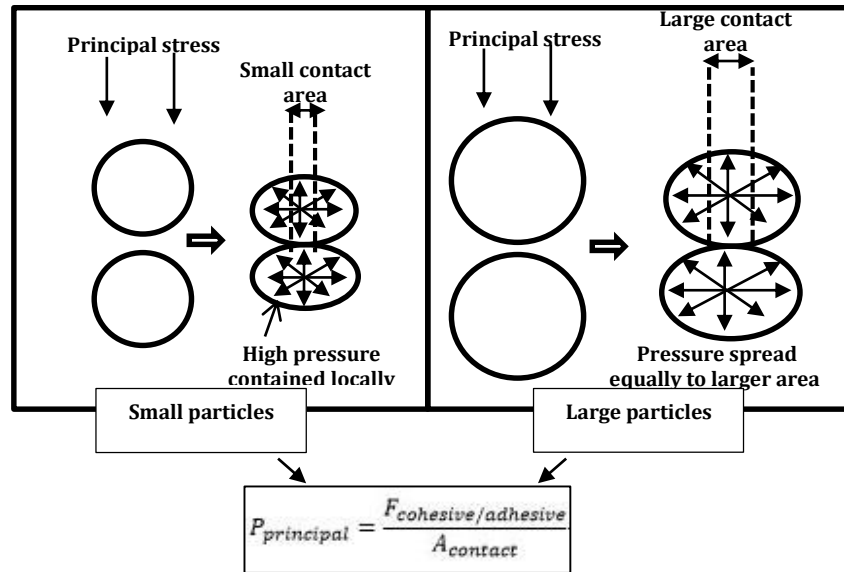
Figure 8-27 Different particle size contact area description which explains the increase of cohesive forces for small size due to the pressure contained locally within the individual particles

The effects of bulk density were also evident as seen in Figure 8-26(b). The measured bulk density values for PTHEO were given in Table 8-5. The mean bulk density was 0.83. It can be seen that the flow of FI-Ace was better compared to the PTHEO because of it was bulkier.

Table 8-5 Measured flow properties of PTHEO. The mean bulk density was 0.83

Samples	Run	Bulk density (g/cm³)	Major principal stress (Pa)	Unconfined yield strength (Pa)
PTHEO	1	0.82	1002	2029
	2	0.84	1002	1777
	3	0.83	1523	2306
	4	0.83	2042	2547
	5	0.84	2602	2820

Further influence of particle size was presented in Figure 8-28. The representation of particle size distribution with regards to the slope of flow function demonstrated the impact of particle size on flow. The maximum size (D90) was shown to have a smaller slope and slanting clockwise which indicates better flow. The linear regression of PTHEO flow function was presented in Table 8-6. The slope was determined to be 0.487 with regression value of 0.96.
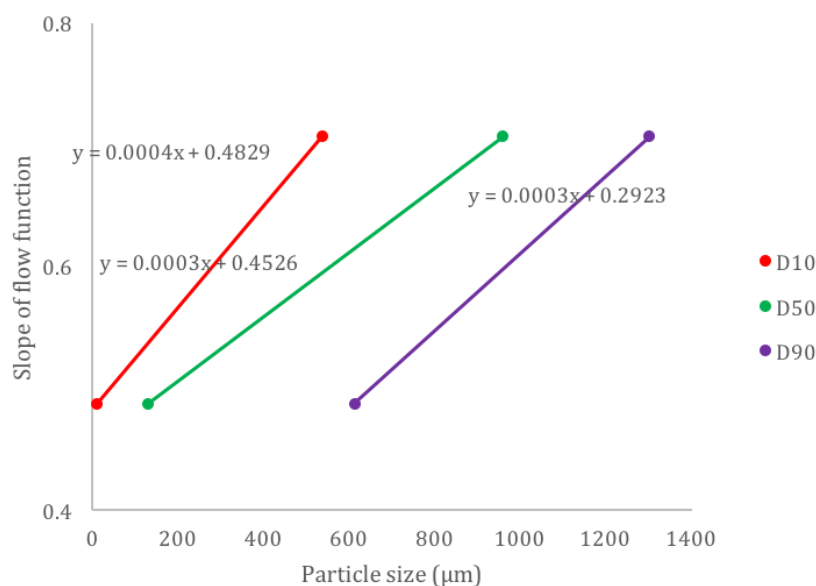
Figure 8-28 Flow function relationship with respect to particle size distributions. The milled powder is flowing better when the line rotates clockwise

Table 8-6 Linear regression of PTHEO flow function

Samples	Linear regression equations	Regression values (R^2)
PTHEO	$y = 0.487x + 1485.6$	0.96

In this section, it was obvious that the bulky behaviour of FI-Ace caused the system to have slightly better flow compared to the PTHEO. Moreover, the smaller size of PTHEO (10-580μm) was implied to promote cohesive interactions. The cohesiveness of PTHEO is proposed to provide greater strength between particles during tabletting. Next, the tabletability behaviour for PTHEO was described and compared to the FI-Ace.

8.3.3.4 Tabletability measurements

Tabletability in Figure 8-29 represents the ability of PTHEO to withstand stress during tabletting. At any compression stress, PTHEO exhibited better tensile strength than FI-Ace samples. The better tabletability of PTHEO was prominent looking at Figure 8-29, with the FI-Ace samples were grouped at lower tensile strength. For instance, at 50MPa compression stress, PTHEO had a tensile strength of 30MPa while FI-Ace was 20MPa. The tensile strength that is resulting from the compression stress implicates the amount of stress needed to form a tablet. The factor governing the tabletability can be determined based on compressibility and compactibility analysis.
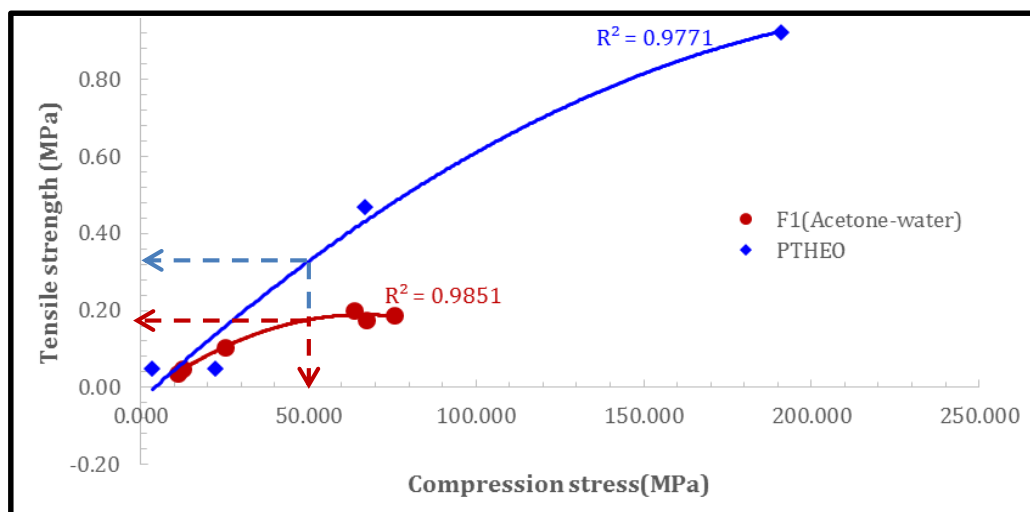
Figure 8-29 Tabletability of PTHEO compared to FI-Ace samples. Significant difference can be observed for PTHEO. Better tabletability was observed for PTHEO that leads to determination of total surface area ready to create bond or strength of particles

8.3.3.5 Compressibility

The compressibility as described in the earlier section is related to the total surface area of interactions, therefore, related to particle size. The compressibility of PTHEO was shown in Figure 8-30 (a). The PTHEO was compressing better at low stress up to 25MPa when the line intercept with FI-Ace samples where from this point forward, the compression of FI-Ace powder was better. Nevertheless, the compressibility of FI-Ace and PTHEO was a marginal difference. The compressibility is vital to ensure that homogeneity of the tablet. It is essential because, during the tabletting process, the window for particles to form bonds is short. Therefore, large surface area promotes the interactions and avoids the weight variation. The negative compressibility performance of PTHEO was not the factor that governs the tabletability.

The habit of the cleavage face of PTHEO was another possible factor that gave less compressibility. The cleavage face (101) was having a needle-like habit as observed in Figure 8-22 (d) affects the way powder was compacted in the tablet die. The needle shape will expose a large surface area of the (101). The (101) have a strong intra-planar hydrogen bond which makes it difficult to break the face into smaller size hence, reduce the true contact area[19]. The less solid fraction can be attained from a needle-like habit crystals. Figure 8-30 (b) showed the schematic diagram of the needle-like cleaved (101) face of PTHEO when packed into the tablet die and the possible manner of PTHEO fracture.

293
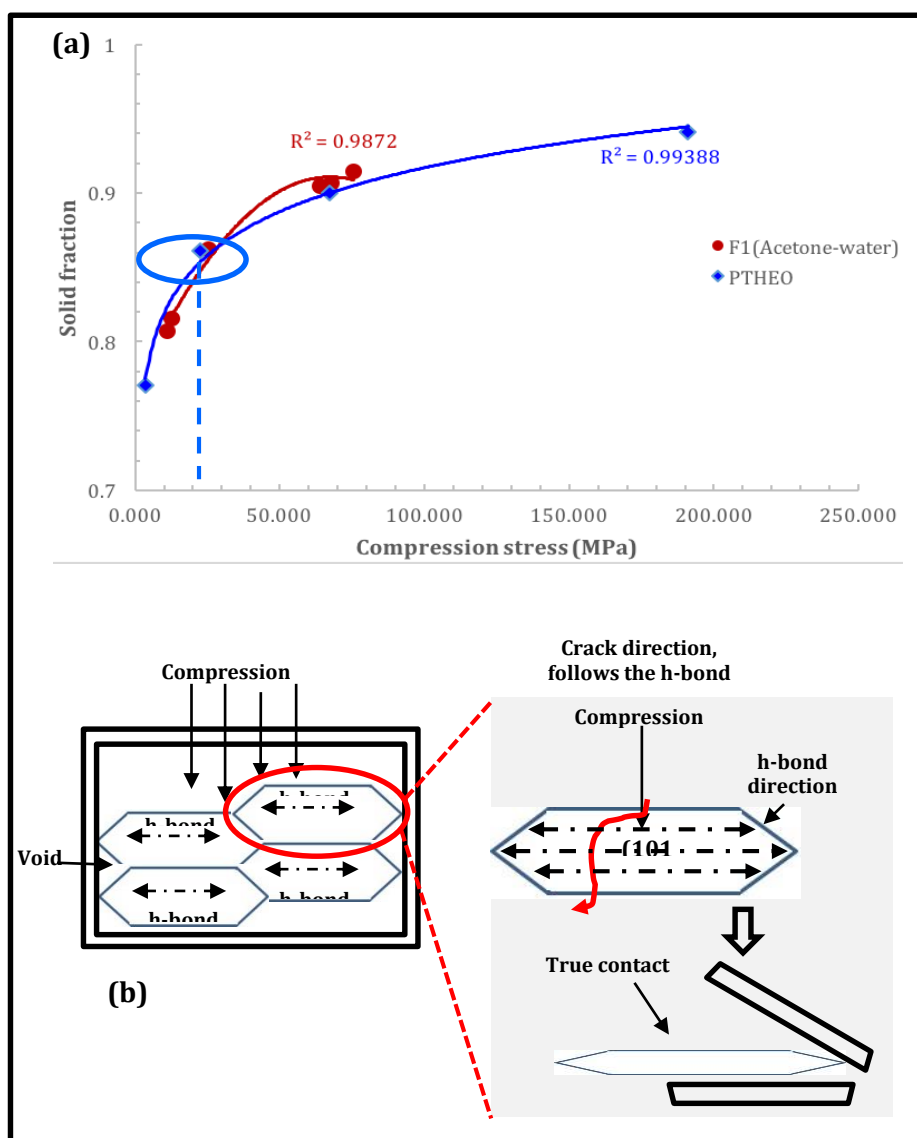
Figure 8-30 a) The compressibility plot of PTHEO against FI-Ace samples. The FI-Ace was having better compressibility compared to the PTHEO. b) Schematic of probable fracture face of PTHEO which contribute towards the decrease of compressibility of PTHEO. The strong intra-planar hydrogen bonds promote cleaving according to its' bonding directions. The true contact area was still low because of the minima surface area

8.3.3.6 Compactibility

The PTHEO samples demonstrated prominent compactibility compared to the FI-Ace samples. The tensile strength of PTHEO was increasing when compared to FI-Ace mixture which was increasing proportionally (Figure 8-31). Superior compactability of PTHEO correlates to the cohesion forces between particles as acknowledged to impact the flow properties. The cohesion interactions between particles were strengthened by the strong intra-planar hydrogen bonding that was governing the direction of PTHEO deformation during tabletting. The amount of interparticle and interplanar of PTHEO cleavage plane

294

interactions were providing the bond strength for PTHEO to stay intact during compression and after decompression. The positive compactibility of PTHEO overcome the negative compressibility hence explains the explicit tabletability strength.
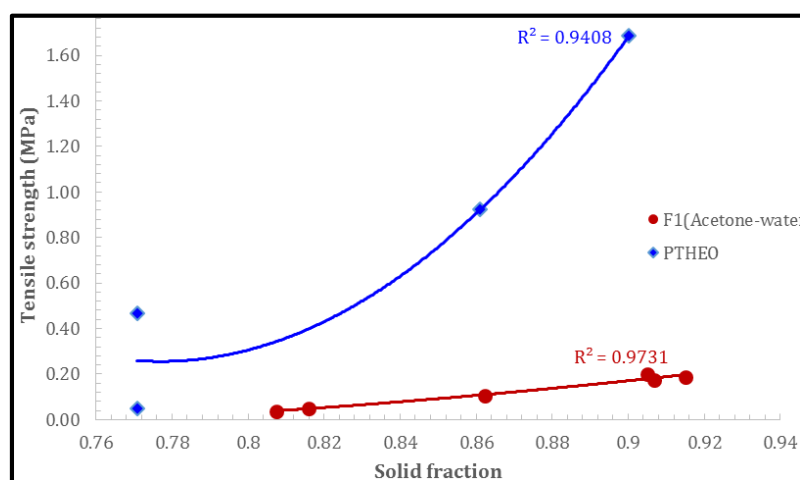
Figure 8-31 Compactibility of PTHEO in comparison to the FI-Ace samples. PTHEO was showing significantly better compactibility showing the larger amount of bond strength

The high compactability of PTHEO reflects the extent of tensile strength it has. The relation between compression and crushing force represents the limit for tablet strength before failing. PTHEO was displaying great strength with the ability to withstand up to 15kN compression force before start to fail as shown in Figure 8-32 (a). The limiting force was corresponding to the compatibility performance of PTHEO. The ability of PTHEO to cleave as described earlier relates to the crystal packing of an individual particle as described in chapter seven. The layering of molecules promotes cleaving to takes place easily and increase the amount of bond strength. Conversely, the FI-Ace samples were poorly behaving with the small range of compression force, less than 5kN with corresponding less than 10N crushing force. The poorly behaving of FI-Ace samples because of the molecular packing stiffness. The crystal packing of FI-Ace was corrugated that will interlock under pressure. The minimal crushing force coinciding the predicted deformation behaviour of FI in the previous chapter.
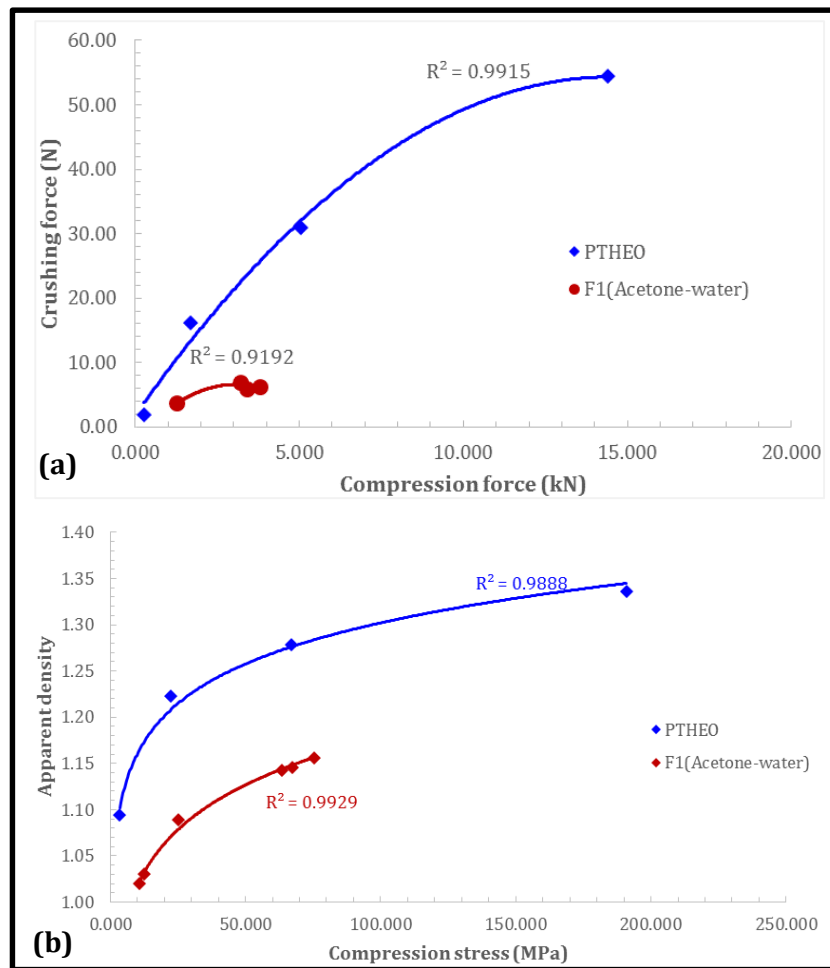
Figure 8-32 The plot of limiting force for PTHEO and FI. PTHEO was obviously having better strength with crushing force up to 55N with compressive force of 15kN. FI samples was having poor strength with crushing force lower than 10 N. b) Apparent density of PTHEO and FI. PTHEO was showing better apparent density at any point of compression stress

The flow and compaction properties were also affecting the apparent density of the tablet to ensure no weight variation in a tablet. As observed in Figure 8-32(b), the apparent density of PTHEO was increasing with compression stress. The highest apparent density for PTHEO was 1.35 at compression stress of 200MPa. The apparent density of PTHEO agrees with the observed compactibility and tabletability performance characterised. Table 8-7 summarised the mechanical properties studied of two paracetamol solid forms, namely co-crystal (PTHEO) and polymorph 1 (FI). The co-crystal (PTHEO) improves the tabletability by having better strength and softer than FI. Moreover, the observed tabletability and flowability were in agreement with the predicted cleaving behaviour in this study. Therefore, the relation between the experimental measurement, it can be understood that by knowing the single particle behaviour, the bulk properties can be determined. The PTHEO was exhibiting better apparent density at any point of compression stress compared to the FI that relates to the strength that PTHEO possess to stay intact after decompression.

8.3.4 Summary

Huge differences were seen with the mechanical properties of FI-Ace and PTHEO (Table 8-7). Though the flowability for both was similar which was not flowing, the tensile strength of PTHEO with 0.90MPa was four times stronger than FI-Ace. The tabletability of for PTHEO was given by its compactibility instead of compressibility. This striking difference in strength was related to the presence of cleavage plane of (101) in PTHEO. The flow for PTHEO was impacted by its smaller size (10-580μm).

Table 8-7 Summary of mechanical properties of two solid forms, namely co-crystal (PTHEO) and FI. The co-crystal was showing better properties relating to the crystallographic packing of an individual particle

Characteristics	PTHEO	FI
Particle size distribution	10-580µm	537-1301µm
Habit / mean bulk density	Platy	Equant
Flowability (*ff$_c$*)	*ff$_c$* <1	*ff$_c$* <1
Tabletability (tensile strength)	0.9MPa	0.2MPa
Compressibility (solid fraction)	0.88	0.9
Compactibility (Tensile strength/ solid fraction)	2	0.22

8.4 Attempts to crystallise the three other solid forms of paracetamol

It has been the objectives of this study to crystallise and compare the mechanical properties of five solid forms of paracetamol consisting of two polymorphs, co-crystals, hydrates and salts. Nonetheless, throughout the duration of this study, only two solid forms were successfully being crystallised more than 100 grams. Both were investigated and characterised which were presented earlier. The attempt to crystallise the salts (PHM) according to the method by Perumalla et.al [20] was unsuccessful. Nevertheless, it was learnt that the gradual addition of hydrochloric acid to protonate the paracetamol need to be done carefully as the window between crystallising the salts, and the stable form is small.

8.4.1 Paracetamol Trihydrates

Efforts to crystallise the paracetamol trihydrate (PTRI) by slow cooling to 0°C [21] in water resulted in the stable paracetamol polymorph (FI). Though the study has a similar observation as McGregor et.al [21] for the habit transformation, from needle to block-like (Figure 8-34) but the DSC and PXRD analysis (Figure 8-33) confirmed that samples were the stable polymorph. The final isolated crystals were a mixture of needle-like and block

habit. Looking into the micrographs of PTRI, it was perceived that the surface was rough, and some inclusions were seen. The availability of three water molecules creates an extremely active condition and thermally unstable. The failure to obtain the PTRI was suspected to be caused by the efficiency of equipment cooling rate and also the temperature during isolations. Moreover, by exposing the crystals to room condition promote dehydrations which rapidly transform the PTRI to FI [22].

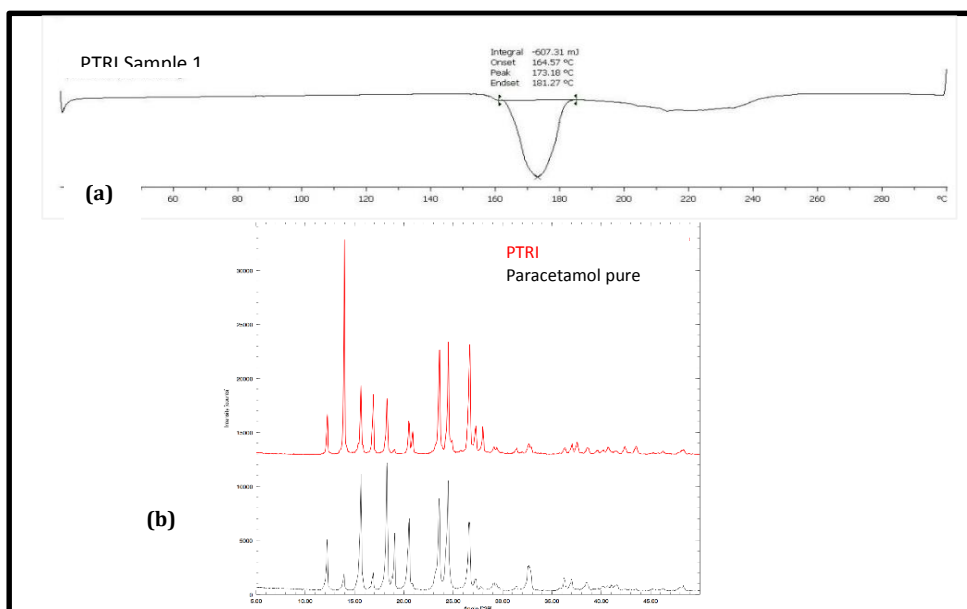**Figure 8-33 a) DSC thermogram showing one strong endothermic peak at 173.4ºC corresponding to the FI enthalpy. b) PXRD pattern showing fit of major peaks therefore confirmed that the structure was FI**
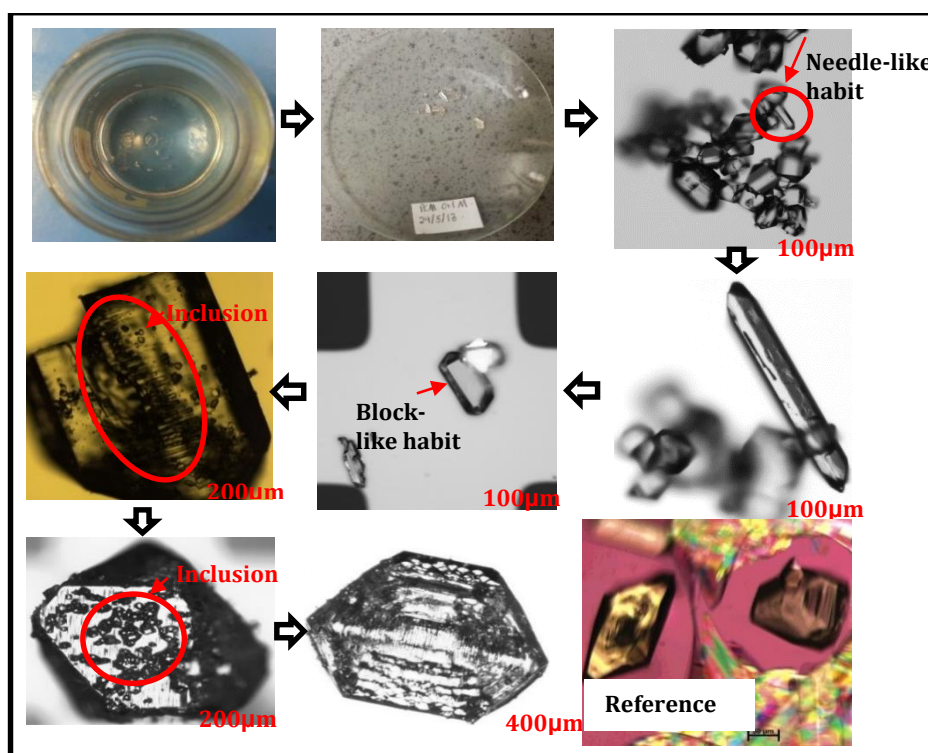

Figure 8-34 PTRI crystals when isolated and when viewed under light microscopy. The surface of the crystals were observed to have solvent inclusions and roughened. Reference picture taken from Peterson et.al [22]

8.4.2 Metastable paracetamol Form II

More work was focusing on crystallising the metastable form of paracetamol, Form II (FII). Multiple approaches as acquired from the literature were adopted namely, swift cooling [23], seeding crystallisation [5], slow cooling [24,25], anti-solvent and by using the co-former compound. Even so, the FII was unable to be isolated as a pure component. The FII can easily by melt using DSC, but the efforts to replicate the process using solution crystallisation were unsuccessful. From the extensive effort to crystallise FII, three approaches which are the anti-solvent, co-former and melt were showing fruitful results.

8.4.2.1 Anti-solvent

By using chilled distilled water (0°C) as the anti-solvent for a saturated methanol-paracetamol solution at 40°C, it seemed to isolate FII successfully. Needle-like crystals started to form 15 minutes after adding the chilled distilled water. It is important to note the temperature for isolation of crystals to ensure that it is within the metastable range of the stable form. In this study, the isolation temperature was at -1°C. DSC test was carried out on the same day showed the identification of FII as seen in Figure 8-35(b), with one strong peak at 157.95°C same as obtained by Nichols et.al [5]. Nevertheless, a test done after a week showed an endothermic peak at 171.33°C (Figure 8-35 (c)). The crystals suspected not properly dry. Traced of moisture promote the transformation of FII to FI at room temperature. The PXRD was carried out after a week because of the accessibility of the unit. Hence, the PXRD result obtained showed the stable form pattern (Figure 8-36).
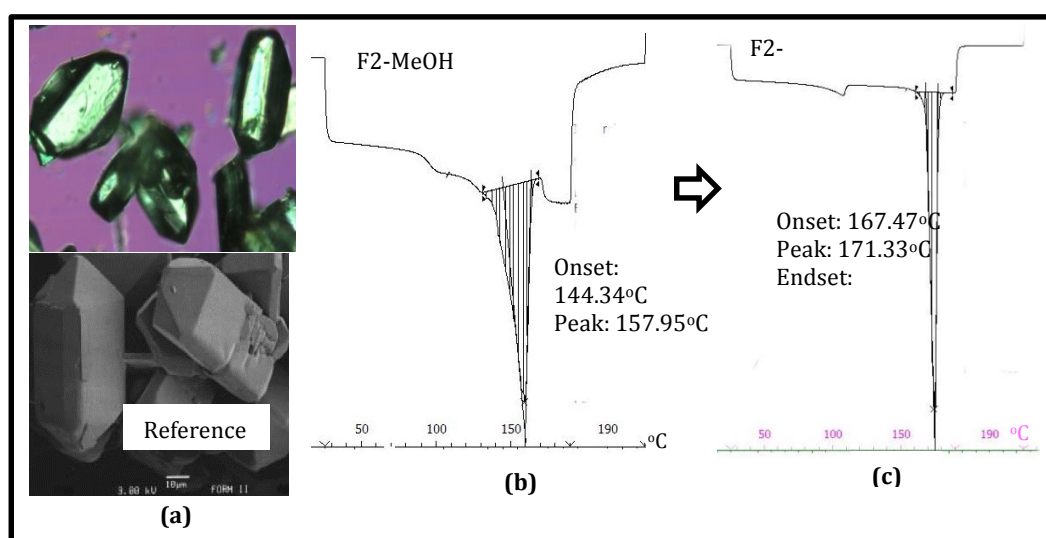

Figure 8-35 a) Micrograph of F2 isolated when the crystals started to form. The crystals showed needle-like b-c) DSC thermograms of the sample on the same day and after a week showing the transformation of F2-FI
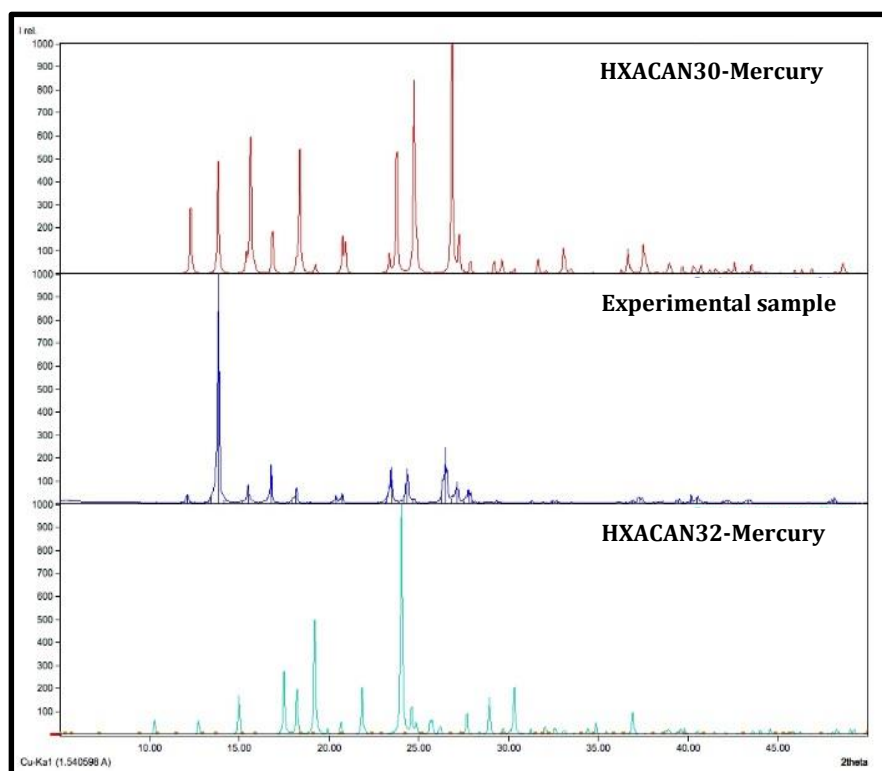
299

Figure 8-36 The PXRD pattern confirming that the sample already transformed into FI. Reference micrograph was taken from Nichols et.al [5]

8.4.2.2 Paracetamol Form II from melt

A scoopful of FI was melted on a microscope and quenched cooled using a pre-cooled aluminium block led to the formation of FII. The FII from melt was used as seeds for solution crystallisation. Though seeds of pure FII were utilised in the solution crystallisation, it was still challenging to isolate pure FII. Figure 8-37 (a) represents the thermogram analysis. The thermogram showed a mixture of the sample by having two strong endothermic peaks which are at 170°C referring to the stable form (FI) and a weak peak at 157°C referring to the metastable form (FII).

Conversely, PXRD result was showing only pure FII without any trace of FI. Two PXRD tests were carried out. The first was done on the same day the seeds were produced. The seeds were then kept for a week at room temperature before running another PXRD test to observe any phase changes during storage. Figure 8-37(b) represents the PXRD analysis. The contradicting results between DSC and PXRD might be caused by the thermal effects during the DSC tests, and this suggests that paracetamol polymorphs are sensitive to thermal changes. The process of crystallisation was conducted in a free-FI environment to ensure no trace of FI present which will promote the rapid transformation of FII.
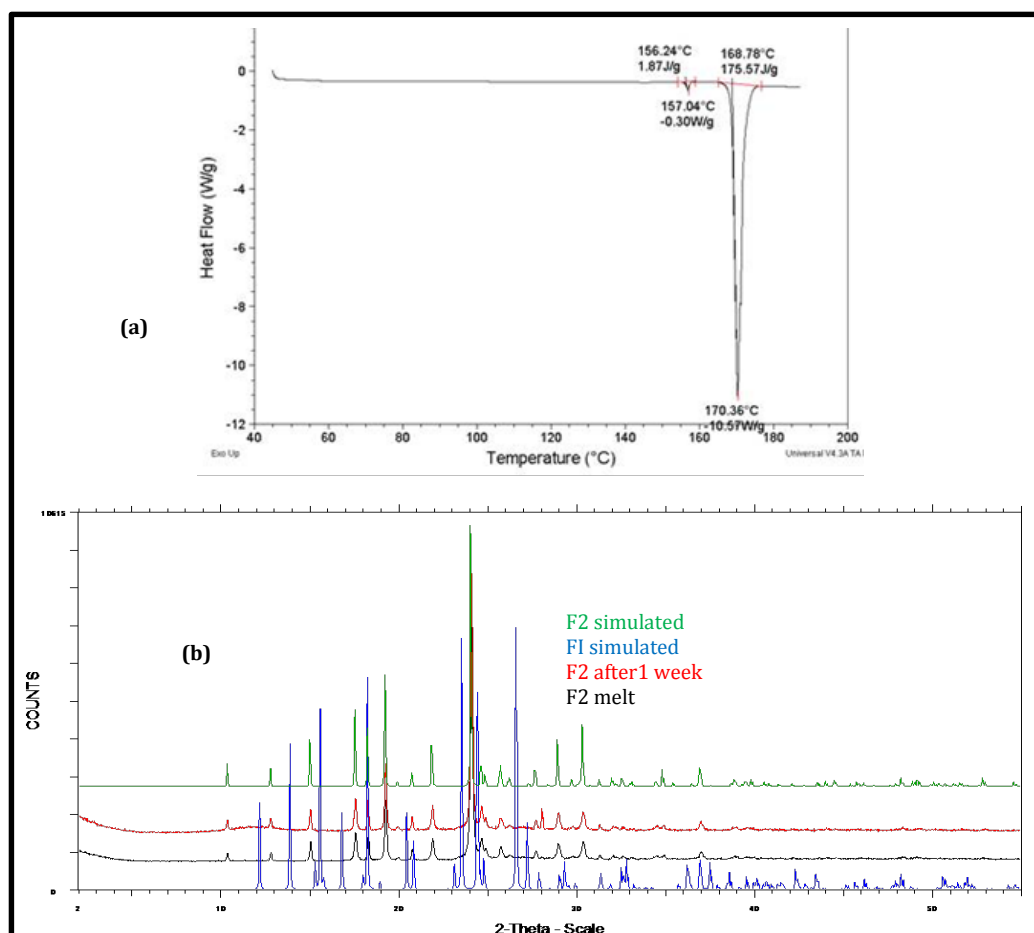
Figure 8-37 a) DSC thermograms of F2 from melt showing two endothermic peaks that were identified as FI (169°C) and F2 (157°C) b) The PXRD patterns showing F2 tested on the same day, after a week, simulated and FI simulated

8.4.2.3 Paracetamol Form II formation during co-crystallisation

While trying to crystallise the co-crystal (PTHEO) from solution, the FII was observed to form alongside the theophylline. Analysis of the DSC thermogram showed an endothermic peak at 157-158°C and another strong peak at 267-270°C associated with the melting of FII and theophylline respectively (Figure 8-38 (c)). Accordingly, the PXRD confirms the mixture of samples as seen in Figure 8-38 (a). Hypothetically, the presence of theophylline decreases the transformation rate of FII to FI. In this instance, theophylline was seen to provide stability to the FII by acting as impurities. Lancaster et.al observed the similar condition while performing co-crystallisation of progesterone [26]. Nevertheless, a separation process was needed to isolate pure FII from the mixture samples. Therefore, further analysis will be of interest to understand more the effect of theophylline in providing stability to FII.

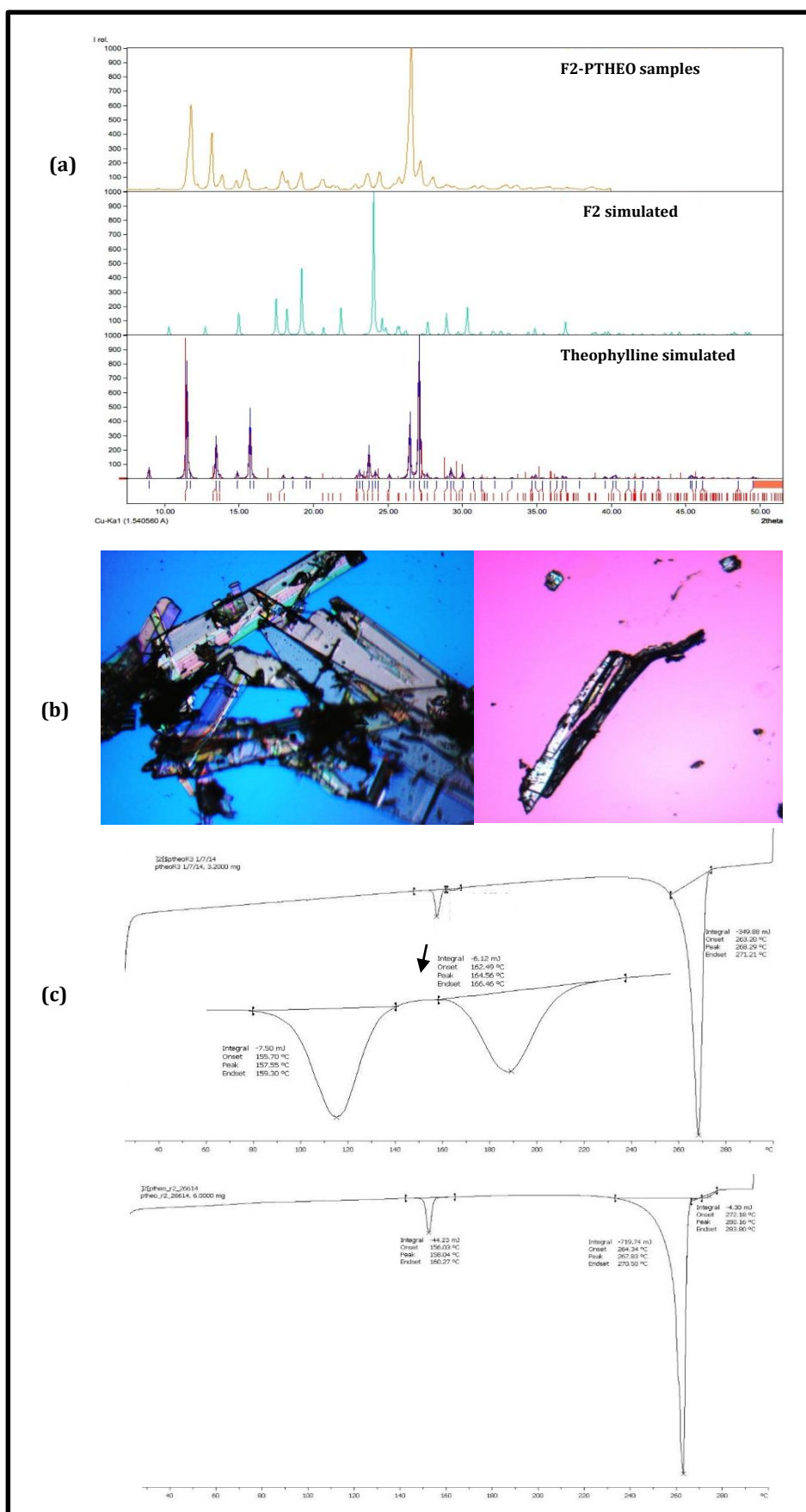**Figure 8-38 a) PXRD patterns of mixture of F2 and theophylline, F2 and theophylline simulated. The crystallised samples showed to be a mixture of both F2 and theophylline. b) Crystals micrographs of suspected F2 c) DSC thermograms of samples**

8.5 Conclusions

This chapter was set to validate the predicted mechanical properties in of diverse paracetamol solid forms in chapter six. Though five solid forms were selected for the case studies, only two solid forms namely Form I (FI), and co-crystals (PTHEO) were managed to be crystallised and presented here. Several attempts were carried out to grow the other solid forms that are Form II (FII), trihydrates and salts at which the results were included. The two main sections of this chapter were trying to observe the influence of habit and different forms of paracetamol microcrystals on mechanical properties particularly compactibility.

For the first case study, the compactibility and flowability of FI were relatively affected by the platy and equant habit as the habit was not extremely different. The tabletability of FI in this instance was given governed by compressibility hence the total surface area ready for the inter-particle bond is vital. The tensile strength of FI tablets was in the range of 0.18 to 0.19MPa for compression pressure of 40 to 80MPa. In the second case study, the co-crystals (PTHEO) was showing significantly better tabletability compared to FI therefore agreeing with the predicted cleaving properties of PTHEO in the earlier chapter. Moreover, the tensile strength of PTHEO was considerably higher than FI, with 0.9MPa with compression stress of 200MPa. Likewise, the limiting force for PTHEO was five times larger than FI.

Deducing from this observation then the elucidation of solid forms deformation materials, therefore, need to be done based on the molecular structure rather than the physical properties [28]. It was obvious that, though the habit was different, the tensile strength was similar, suggesting that the physical differences of microcrystals not change the strength of the same solid forms. The same crushing force suggested that habit differences did not effect the crushing strength of the FI tablet and tabletability was not entirely depending on the strength of materials, as preferred orientation during tabletting has an influence on the force.

Another obvious observation was when there are potential slip systems; the tabletability will favour compactibility rather than compressibility. Compactibility was favoured was because of the plastic behaviour that can undergo more compression force before crushing. The presence of slip systems or cleavage then increases the strength of microcrystals. In this instances, APIs with similar properties with FI was perceived not to be a good APIs to undergo direct compressions or dry granulations, but suitable for wet granulations. On the

contrary, APIs that are behaving like PTHEO is suitable to directly compressed or dry granulations because the strong bond strength can replace the hydrogen bond created by water molecules to keep the tablet intact after decompressions.

Arriving from both case studies, the impact of different solid forms was major compared to habit. However, different observation might be obtained if the habit is extremely different for instance needle-like to platy. This chapter than successfully showed the prediction of single particle deformation behaviour is reliable for understanding the powder properties. Consequently, the combination of crystallographic properties seems to be a reliable predictor of solid form deformations in this instances.

Correspondingly, it can be seen that the different solid forms showed more influence on the tabletability compared to varying habit. In this line, the molecular and crystallographic properties were showing the major impact on the tensile strength of materials. Therefore, molecular-based predictions are reliable to understand the tabletting behaviour of microcrystals. Moreover, the tabletting behaviours can be improved through the formation of co-crystals with layered molecular positions.

References:

[1] S. Jain, Mechanical properties of powders for compaction and tableting: an overview, Pharmaceutical Science & Technology Today. 2 (1999) 20–31.

[2] S. Patel, A.M. Kaushal, A.K. Bansal, Compression physics in the formulation development of tablets, Critical Reviews™ in Therapeutic Drug Carrier Systems. 23 (2006).

[3] G.R. Desiraju, Designer crystals: intermolecular interactions, network structures and supramolecular synthons, Chemical Communications. (1997) 1475–1482.

[4] M. Summers, R. Enever, J. Carless, The influence of crystal form on the radial stress transmission characteristics of pharmaceutical materials, Journal of Pharmacy and Pharmacology. 28 (1976) 89–99.

[5] G. Nichols, C.S. Frampton, Physicochemical characterization of the orthorhombic polymorph of paracetamol crystallized from solution, Journal of Pharmaceutical Sciences. 87 (1998) 684–693.

[6] P. DiMartino, P. Conflant, M. Drache, J.P. Huvenne, A.M. GuyotHermann, Preparation and physical characterization of forms II and III of paracetamol, Journal of Thermal Analysis. 48 (1997) 447–458.

[7] M.A. Perrin, M.A. Neumann, H. Elmaleh, L. Zaske, Crystal structure determination of the elusive paracetamol Form III, Chemical Communications. (2009) 3181–3183.

[8] K. Kachrimanis, S. Malamataris, Crystallization of Paracetamol from Ethanol-water Solutions in the Presence of Polymers, Journal of Pharmacy and Pharmacology. 51 (1999) 1219–1227.

[9] C.Sudha and K.Srinivasan, Understanding the effect of solvent polarity on the habit modification of monoclinic paracetamol in terms of molecular recognition at the solvent/crystal interface, Crystal Research and Technology, 49 (2014). 865-872.

[10] A.R.Granberg and A.C.Rasmuson, Solubility of paracetamol in binary and ternary mixtures of water+acetone+toluene, Journal of Chemical & Engineering Data, 45 (2000). 478-483.

[11] J.W. Mullin, Crystallization, Butterworth-Heinemann, 2001.

[12] D.J.A. Ende, Chemical engineering in the pharmaceutical industry: R & D to manufacturing, John Wiley & Sons, 2011.

[13] D.Y. Naumov, M. Vasilchenko, J. Howard, The monoclinic form of acetaminophen at 150K, Acta Crystallographica Section C: Crystal Structure Communications. 54 (1998) 653–655.

[14] R.A. Granberg, D.G. Bloch, Å.C. Rasmuson, Crystallization of paracetamol in acetone-water mixtures, J. Cryst. Growth. 198 (1999) 1287–1293.

[15] A.W. Jenike, A measure of flowability for powders and other bulk solids, Powder Technology. 11 (1975) 89–90.

[16] H. Hou, C.C. Sun, Quantifying effects of particulate properties on powder flow properties using a ring shear tester, Journal of Pharmaceutical Sciences. 97 (2008) 4030–4039.

[17] P. Narayan, B.C. Hancock, The relationship between the particle properties, mechanical behavior, and surface roughness of some pharmaceutical excipient compacts, Materials Science and Engineering: A. 355 (2003) 24–36.

[18] S. Karki, T. Frivsvci'c, L. Fábián, P.R. Laity, G.M. Day, W. Jones, Improving mechanical properties of crystalline solids by cocrystal formation: new compressible forms of paracetamol, Advanced Materials. 21 (2009) 3905–3909.

[19] W. Hong-Guang, Z. Ru-Hua, Compaction behavior of paracetamol powders of different crystal shapes, Drug Development and Industrial Pharmacy. 21 (1995) 863–868.

[20] S.R. Perumalla, L. Shi, C.C. Sun, Ionized form of acetaminophen with improved compaction properties, CrystEngComm. (2012).

[21] P.A. McGregor, D.R. Allan, S. Parsons, C.R. Pulham, Preparation and crystal structure of a trihydrate of paracetamol, Journal of Pharmaceutical Sciences. 91 (2002) 1308–1311.

[22] M.L. Peterson, D. McIlroy, P. Shaw, J.P. Mustonen, M. Oliveira, Ö. Almarsson, Crystallization and transformation of acetaminophen trihydrate, Crystal Growth & Design. 3 (2003) 761–765.

[23] C. Sudha, K. Srinivasan, Supersaturation dependent nucleation control and separation of mono, ortho and unstable polymorphs of paracetamol by swift cooling crystallization technique, CrystEngComm. 15 (2013) 1914–1921.

[24] J.Y. Heng, D.R. Williams, Wettability of paracetamol polymorphic forms I and II, Langmuir. 22 (2006) 6905–6909.

[25] M. Mikhailenko, Growth of large single crystals of the orthorhombic paracetamol, J. Cryst. Growth. 265 (2004) 616–618.

[26] R.W. Lancaster, P.G. Karamertzanis, A.T. Hulme, D.A. Tocher, T.C. Lewis, S.L. Price, The polymorphism of progesterone: Stabilization of a "disappearing"polymorph by co-crystallization, Journal of Pharmaceutical Sciences. 96 (2007) 3419–3431.

[27] R.C Rowe and R.J. Roberts, The mechanical properties of powder, Journal of Drugs and Pharmaceutical Sciences, 71 (1996) 283-322

[28] CC. Sun and J.W. Grant, Influence of crystal shape on the tabletting performance of L-lysine monohydrochloride dihydrate, Journal of Pharmaceutical Sciences, 9 (2001), 569-579

[29] R.E. Gordon and S.I. Amin, Crystallization of ibuprofen, US patent (1984) 4,476,248

[30]   S. Sun, J.R. Mitchell, W. MacNaughtan, T.J. Foster, V. Harabagiu, Y.song and Q.Zheng, Comparison of the mechanical properties of cellulose and starch films, Journal of Biomacromolecules, vol.11 no.1 (2009), 126-132

Chapter Nine

Conclusions and Suggestions for Future Work

This chapter presents the summary for major findings of this study. Included together are the review of the aims and objectives. The chapter finishes with suggestions for future work

Chapter 9   Conclusions and Suggestions for Future Work

9.1   Conclusions for this study

This chapter is divided into three subsections following the order of the goals for this chapter. Firstly, the aim of this chapter is to bring together all the main findings. The summary of each case study has been provided separately at the end of section for each chapter. Secondly, to contrast them with the aims and objectives of this study. Lastly, deducing from the findings, this chapter also included the prospective future work to improve the mechanical prediction approach.

This study makes it possible to comprehend the slip system behaviour for a range of solid organic forms namely polymorphs, co-crystals, hydrates and salts. Besides that, this study too elucidates the behaviour of two forms that are related by nitrate esters. By now, the key components for slip system are obvious, that are slip plane with ideal behaviour and Burgers vector with low dislocation energy.

9.1.1   Slip plane characterisations

A novel approach for characterising the rugosity of slip plane was proposed by exploiting the plane equation. By utilising the proposed approach for characterising slip planes for all seven solid forms, particularly PET[1], PETN[2], F1[3], F2[4], PTHEO[5], PTRI[6] and PHM[7] assist in better mechanical properties prediction. Moreover, from the rugosity evaluation, the interlock of planes can be characterised quantitatively. Both the rugosity and quantitative characterisation of interlock planes are imperative attributes of ideal slip plane.

Drawing from the ideal attributes of slip plane described in section 5.5, this study was able to perceive interrelation between the complexity of organic crystallographic packing with ease for slippage. The PET and PETN that have only two molecules in a unit cell have 94% and 82% potential respectively to be a slip plane. Moreover, the layered molecule arrangements within the crystal packing scored another point and make it closer to the optimum attributes for slip plane.

Similar analysis that was done on fairly complicated system paracetamol form I (F1) and its four solid forms, polymorph FII (F2), co-crystal (PTHEO), trihydrate (PTRI) and salt (PHM) gave comparable percentage of optimum attributes for preferred slip plane to PET and

PETN. For F2, PTHEO and PHM that have obvious layered positions, gained 84%, 77% and 73% of optimum attributes. However, for PTRI, though it was predicted to undergo cleaving, the preferred slip plane was behaving with 57% of optimum attributes that was 1% lower than F1, that is brittle. The contradicting observation for PTRI highlight the influence of components involve to build the unit cell.

From the analysis of the seven solid forms, namely PET, PETN, F1, F2, PTHEO, PTRI and PHM lead to a preliminary rank for associating slip planes to the deformation behaviour. The lower boundary for preferred slip or cleavage plane is 60%. An exception must be considered for solid forms with extreme hydrogen bond network as this may contribute to the significant amount of hydrogen bond breaking energy. Apart from the extreme cases, the prediction for slip plane seems to work sensibly.

9.1.2 Burgers vector identifications

This study managed to demonstrate the influence of dislocation energy towards the slip direction specifically Burgers vector. The smallest dislocation energy for PET, PETN, F1, F2, PTHEO, PTRI and PHM for primary Burgers vector was low, approximately $1 eVnm^{-1}$. The anisotropy influence of the molecular systems was evident through the dislocation energy factor (K) continuum analysis and elastic components calculation. Computation of the elastic tensor showed the possibility of using shearing components ($C_{44} - C_{66}$) to describe stiffness of solid forms. By considering the potential dislocations, now the calculated Burgers vector will show the influence of individual solid form elastic energetics.

9.1.3 Crystal chemistry and lattice energetics influence

In this study, the crystal intermolecular interactions particularly hydrogen bond exhibited versatile function. In the case of PTRI, the large amount of more than 60% hydrogen bond network provides strong intraplanar strength, which gave the systems' flexibility. Though PTRI is an active slip system with the primary Burgers vector, the significant amount of hydrogen bond network may halt the displacement. Therefore, the interplay between inter and intraplanar hydrogen bond strength was important for plastic deformation to take place in PTRI. Nonetheless, the predicted result needs to be treated with caution because it still needs experimental validation.

Conversely, from the study of PET, F2, PTHEO and PHM, the intermolecular interaction was highlighted to provide displacement force when the primary Burgers vector was not in-

plane. The strong intraplanar hydrogen bond observed in PET, F2, PTHEO and PHM was parallel to the preferred slip plane hence propagates cleaving. Another obvious influence of intermolecular interaction is for PETN. PETN was evaluated to have van der Waals interaction. The weak strength of van der Waals was seen to promote the plastic deformation of PETN.

It is useful to elucidate the crystal chemistry of molecular forms considering the different effects of the hydrogen bond to promote cleaving and provide flexibility during plastic deformation. By having the elucidation, the impact for prediction of mechanical properties can be improved.

9.1.4 Contrasting predicted mechanical properties with tabletability measurements

The flowability and tabletability measurements showed that PTHEO had better tabletability under pressure. The tensile strength for PTHEO was 0.9MPa compared to F1 with 0.2MPa. The tabletability of PTHEO was contributed by compactibility. The strength for compactibility was provided by cleavage plane of (101) that was aligned parallel facing the punch when contrasting the observation with the predicted mechanical properties. The (101) plane had strong in-plane hydrogen bond. The strong hydrogen bond holds the plane together from breaking apart and promotes displacement parallel to the hydrogen bond direction.

Though F1 is stiffer than PTHEO based on the elastic tensor computation, the higher tensile strength obtained by PTHEO was regarded to be caused by the ease of cleaving for (101). Moreover, the (101) was observed to be the preferred orientation for PTHEO hence exposing the plane facing the punch during compaction. Gathering from the difference of tabletability behaviour between F1 and PTHEO, the presence of cleavage or slip plane offers improvement of tensile strength hence potentially suitable for direct compression. Likewise, by having a solid form that has similar predicted crystallographic properties as F1 and PTHEO, the tabletability of compounds per se can be estimated.

9.2 Re-review of the original thesis aims and objectives

This study was set to explore six objectives that were given in section 1.2. Addressing the first, second and fourth objectives, seven solid forms (PET, PETN, F1, F2, PTHEO, PTRI and PHM) that bear multitude molecular and crystallographic properties were selected. From

the PET and PETN case studies, a mechanical properties prediction model was developed. The model comprises attributes to predict slip system with the ability as describes below:

1. Proposed a quantitative rugosity and interlock of planes computation. Besides that, it also brings together the surface and hydrogen bond breaking energy to enhance the mechanical properties prediction. Because this is the first time rugosity and interlock of slip planes were analysed in this manner, there is still room for improvement, for instance, the selection of limit to describe overlapping of the molecule.
2. Integrates the crystal's elastic energetics by calculating dislocation energy for the quantification of the slip direction (Burgers vector).
3. Exploits the crystal chemistry to explain the cleaving of planes

The diverse paracetamol solid forms were utilised to explore the adaptability of the model with hydrates, salts, and co-crystals. Moreover, paracetamol was routinely used to study solid forms for direct compression.

Addressing the third, fifth and sixth objectives, the developed model effectively predicts the potential mechanical properties behaviour of the selected solid forms. However, only two solid forms of paracetamol were successfully being crystallised. This was related to a large amount of time was dedicated to obtaining the F2, which was metastable at room temperature. Though the attempts failed, knowledge gained during the process provides the basis for future work. The tabletability study for F1 and PTHEO showed a correlation with the predicted, brittle and cleaving behaviour. Though the flowability was not showing significance influence, because of the similarity of habit, the consequence was still apparent during compaction. The predicted molecular mechanical properties behaviour manifested through the tabletability analysis.

This study postulates the crystallographic parameters to describe the mechanical deformation are rugosity, interlock of planes, surface energy, intermolecular interactions and dislocations. These dimensions were able to be measured through multiple molecular modelling approaches. Moreover, the results of this study, provide preliminary guidance for understanding the mechanical properties of solid forms during tabletting. Thus, the proposed mechanical properties prediction model demonstrated the capability of molecular and crystallographic modelling to predict the mechanical properties of pharmaceutical particulates and so answer the research question raised in section 1.2. The capability of the model to predict the mechanical properties was bound to few limitations

namely steric hindrance and fewer data available to weight specific ideal attributes of slip plane. Though the results for the predictions were promising, continuous improvement of the model will further refine the accuracy and make it rigorous.

9.3 Suggestions for future work

It was highlighted that because of the time constraints few of the work carried out in this study were unable to be completed fully. Therefore, it is ideal to complete the following work:

1. Fitting of Dreiding force field to all five structures. This will provide insights on the influence of simultaneous fitting onto improvement of the elastic tensor.
2. Crystallisations of the polymorph F2, salts and hydrates. For the hydrates, it was learnt that it transformed immediately to anhydrous at room temperature, therefore for future work, perhaps a less hydrous system was selected for example monohydrate.
3. Extends the dislocations analysis to identify mixed dislocation.
4. Carry out hardness test namely nano-indentation to examine the single crystal mechanical properties

This study makes part of synthonic engineering research collaboration with Cambridge Crystallographic Data Centre and Pfizer Inc. Sandwich. Therefore, in the long run, it is anticipated that the model can be automated and integrated fully into Mercury-CSD as one of the modules.

Besides that, extensive measurements related to the surface energy and surface rugosity may fulfil the lack of information on the relative weighting factors to show the importance among the specific ideal slip plane attributes. Besides the experimental measurements, application of the developed prediction model to vast solid forms will provide a well of data that can be used to improve the accuracy of the model.

APPENDIX A

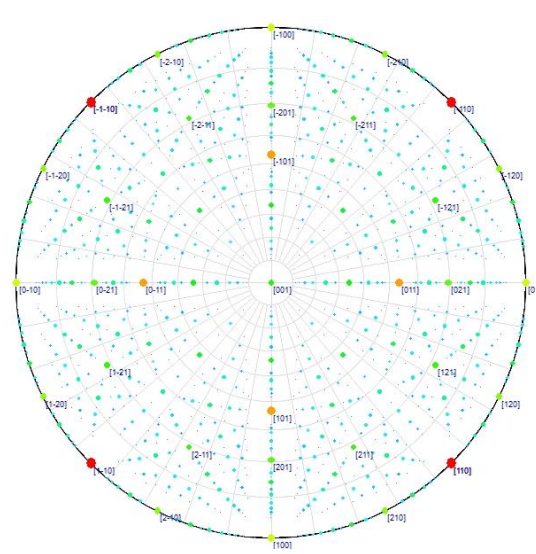# STEREOGRAPHIC PROJECTION

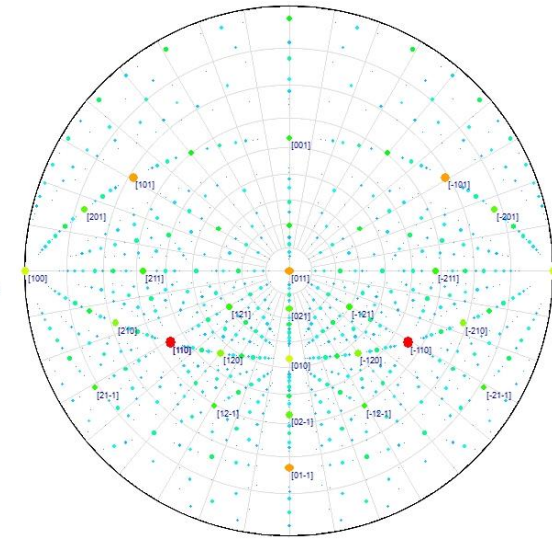## A1.Pentaerythritol Tetranitrate (PETN)
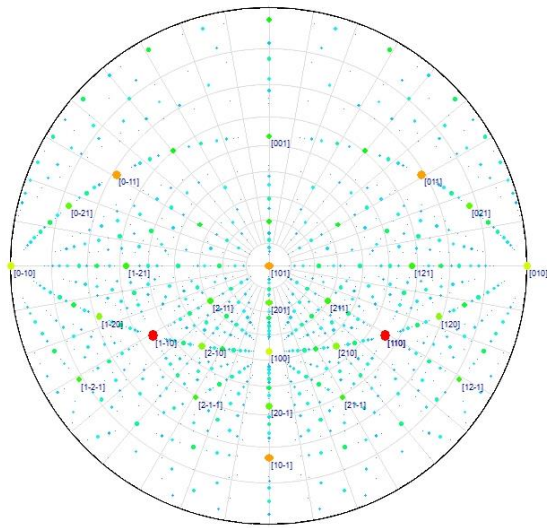

Burgers vector [100]
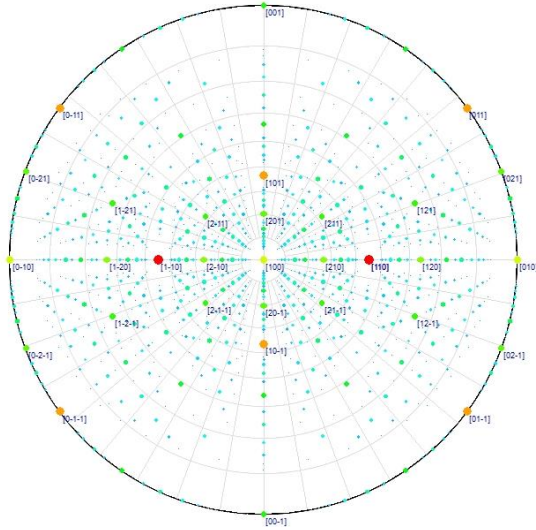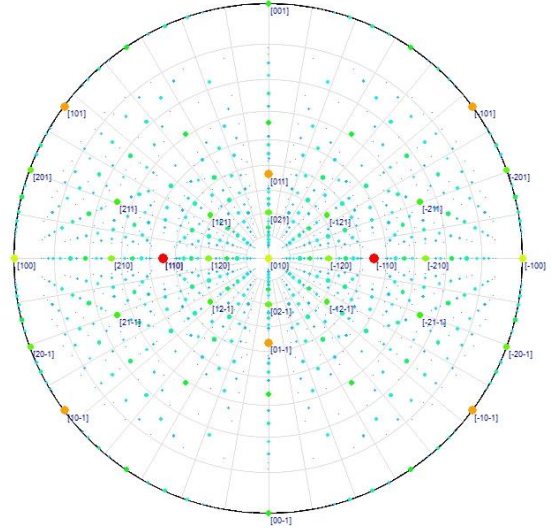
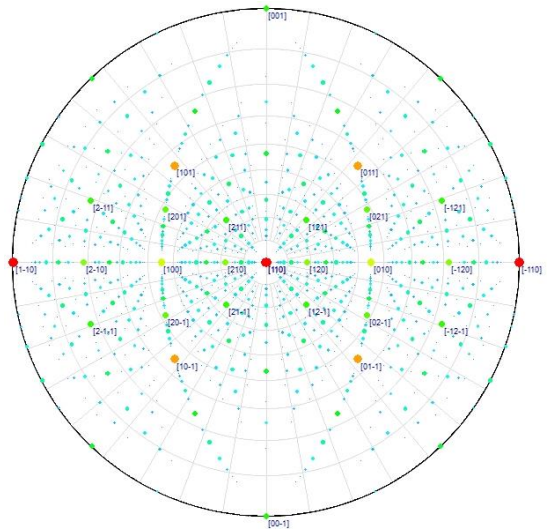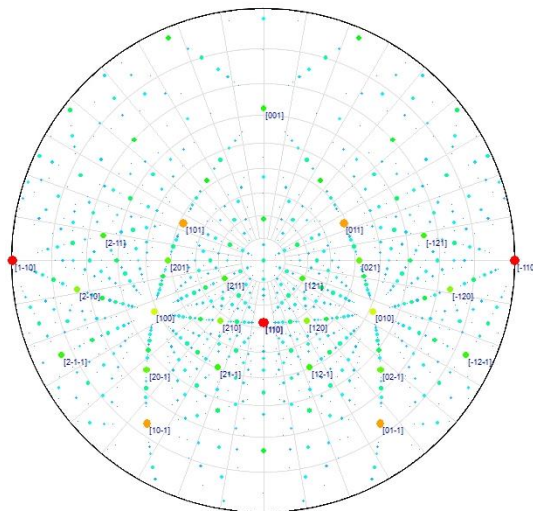Burgers vector [010]

Burgers vector [001]

Burgers vector [011]
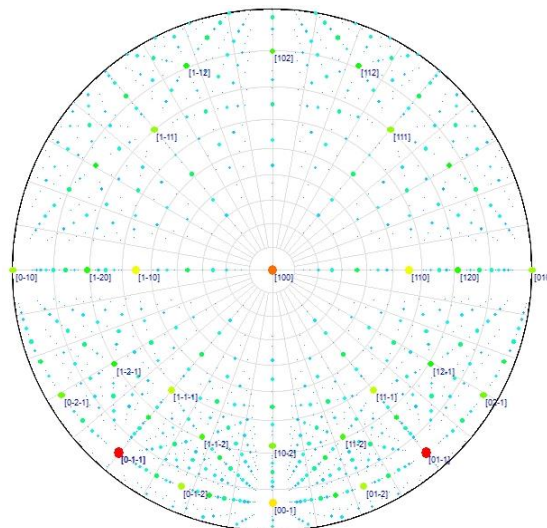
Burgers vector [101]
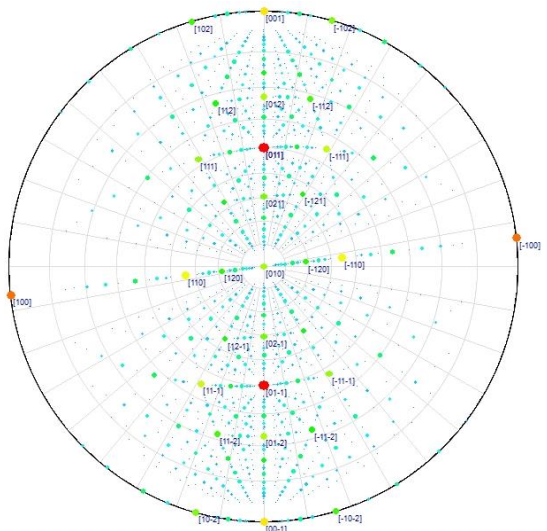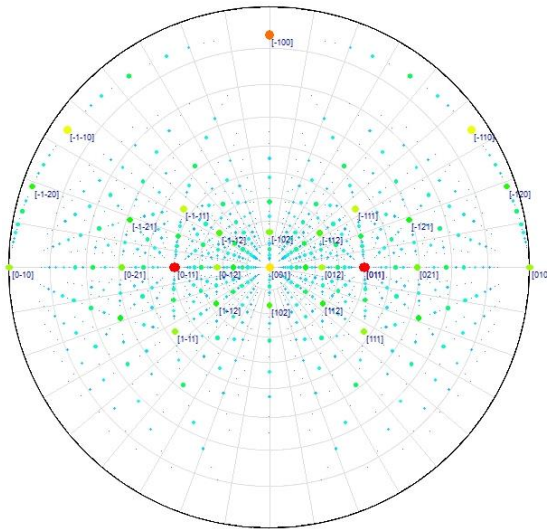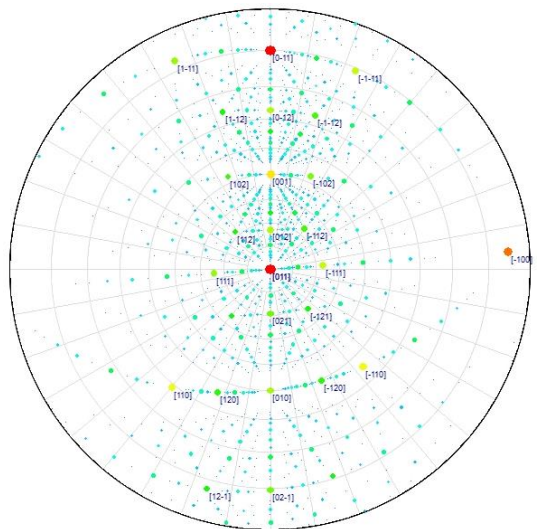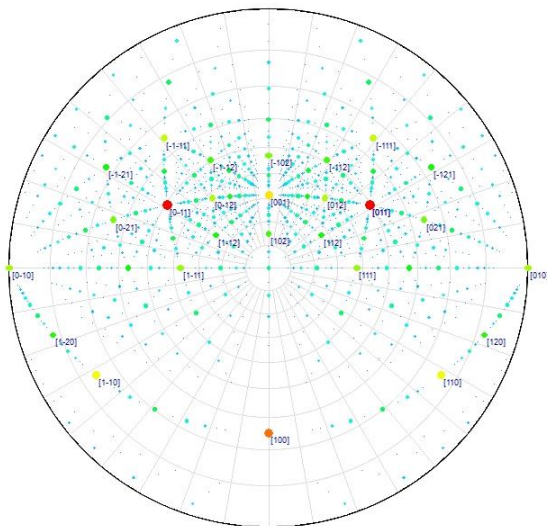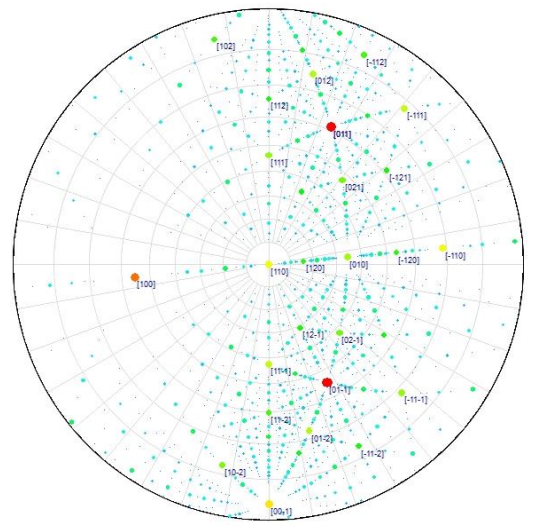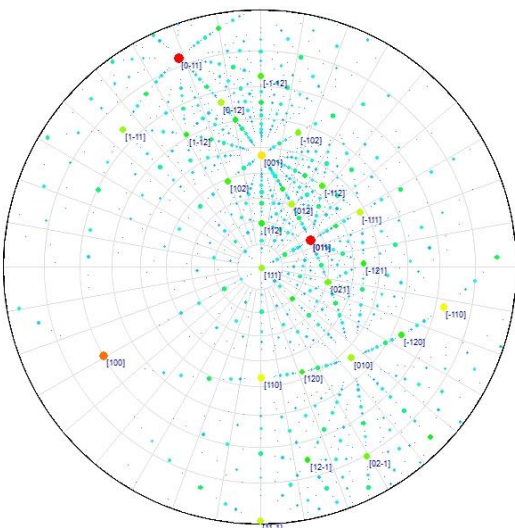

Burgers vector [110]

Burgers vector [111]

A2. Paracetamol Form I (F1

Burgers vector [100]

Burgers vector [010]

Burgers vector [001]

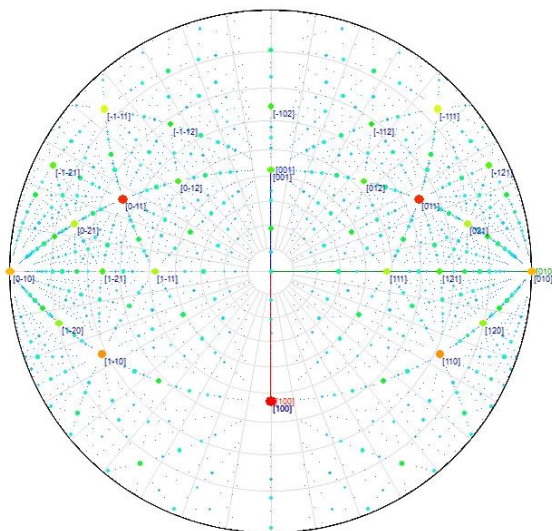Burgers vector [011]

Burgers vector [101]

Burgers vector [110]

Burgers vector [111]

A3. Paracetamol Form II (F2)

Burgers vector [100]

Burgers vector [010]

Burgers vector [001]

Burgers vector [011]

Burgers vector [101]
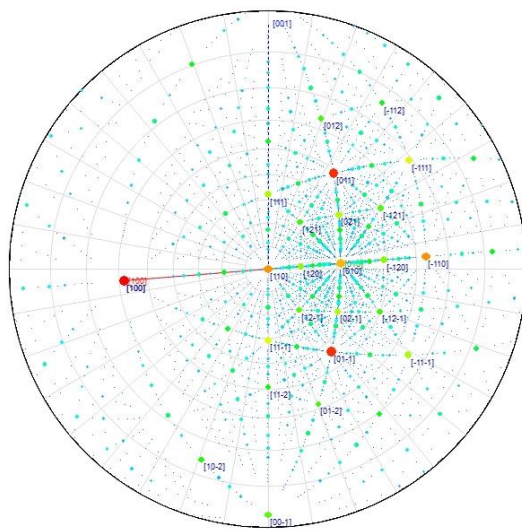

Burgers vector [110]

318

Burgers vector [111]

A4. Paracetamol Theophylline (PTHEO)

Burgers vector [100]

Burgers vector [010]

Burgers vector [001]

Burgers vector [011]

Burgers vector [101]
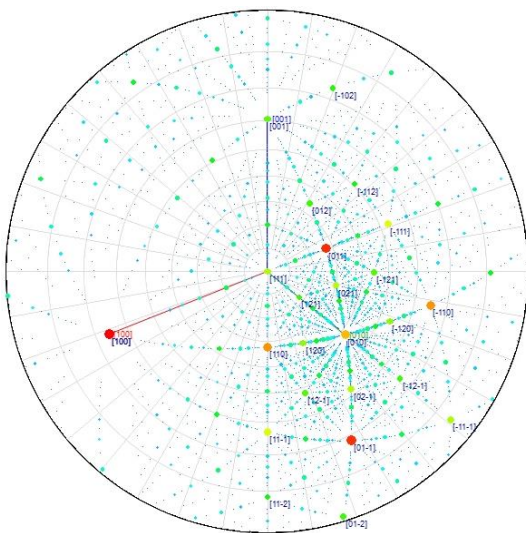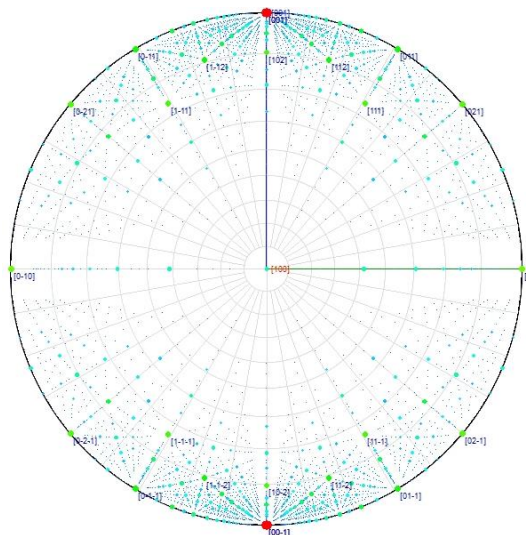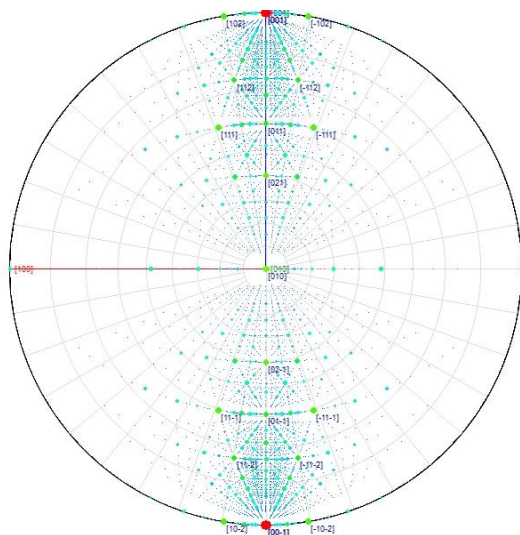

Burgers vector [110]

Burgers vector [111]

A5. Paracetamol Trihydrate (PTRI)

Burgers vector [100]

Burgers vector [010]

Burgers vector [001]

Burgers vector [011]

Burgers vector [101]

Burgers vector [110]

Burgers vector [111]

A5. Paracetamol Hydrochloride Monohydrate

Burgers vector [100]

Burgers vector [010]

Burgers vector [001]

Burgers vector [011]

Burgers vector [101]

Burgers vector [110]

Burgers vector [111]